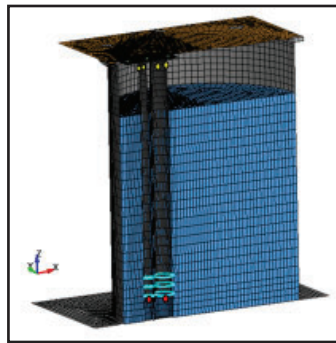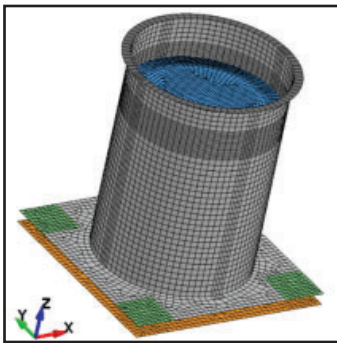# Physical and Numerical Simulations of Seismic Fluid-Structure Interaction in Advanced Nuclear Reactors

by
Faizan Ul Haq Mir, Ching-Ching Yu, Andrew S. Whittaker and Michael C. Constantinou

NOTICE

Physical and Numerical Simulations of Seismic Fluid-Structure Interaction in Advanced Nuclear Reactors

by

Faizan Ul Haq Mir,[1] Ching-Ching Yu,[2] Andrew S. Whittaker[3] and Michael C. Constantinou[4]

1. Graduate Student, Department of Civil, Structural and Environmental Engineering, University at Buffalo, The State University of New York
2. Postdoctoral Associate and former Graduate Student, Department of Civil, Structural and Environmental Engineering, University at Buffalo, The State University of New York
3. SUNY Distinguished Professor, Department of Civil, Structural and Environmental Engineering, University at Buffalo, The State University of New York
4. Samuel P. Capen Professor and SUNY Distinguished Professor, Department of Civil, Structural and Environmental Engineering, University at Buffalo, The State University of New York

Preface

MCEER was originally established by the National Science Foundation in 1986 at the University at Buffalo, The State University of New York, as the first National Center for Earthquake Engineering Research (NCEER). In 1998, it became known as the Multidisciplinary Center for Earthquake Engineering Research (MCEER), from which the current name, MCEER, evolved.

Comprising a consortium of researchers and industry partners from numerous disciplines and institutions throughout the United States, MCEER's mission expanded in the early 2000s from its original focus on earthquake engineering to one which addresses the technical and socioeconomic impacts of a variety of hazards, both natural and man-made, on critical infrastructure, facilities, and society.

This report describes physical and numerical experiments conducted to study seismic fluid-structure interaction, with a focus on liquid-cooled advanced reactors and the use of seismic isolation. The seismic design of advanced reactors will rely on the use of verified and validated numerical models capable of accurately capturing the interactions of the liquid coolant with the enclosing and submerged structural / mechanical components, and the isolation-system responses. Experiments to support validation of such numerical models of advanced reactors, base-isolated and conventionally supported, with a focus on fluid-structure interaction, are described in this report. Specifically, earthquake-simulator experiments generating datasets for: 1) hydrodynamic responses in a conventionally supported, fluid-filled vessel, 2) dynamic responses of components submerged in a conventionally supported vessel, and 3) hydrodynamic and isolation-system responses in a base-isolated, fluid-filled vessel are described. The commercial finite element package LS-DYNA is used for validation studies. The data from the experiments and the results of the validation studies are broadly applicable to the seismic response of liquid-filled vessels and submerged components, regardless of industry sector.

ABSTRACT

The seismic design of liquid-cooled advanced reactors, particularly those that operate at near atmospheric pressure, will need to consider the interaction of the liquid coolant with enclosing or submerged components. The vessels in these reactors are thin-walled, with limited seismic capacity, and seismic isolation has been proposed to enable their construction. Design and risk calculations for seismically isolated advanced reactors will rely on the use of verified and validated numerical models that can accurately capture the interactions of the liquid coolant, the vessel, and the submerged structural/mechanical components (fluid-structure interaction: FSI), and the isolation-system responses. Validation of such numerical models of advanced reactors, base-isolated and conventionally founded, with a focus on fluid-structure interaction, is addressed in this report.

This report describes physical experiments conducted to generate datasets for: 1) hydrodynamic responses in a conventionally supported fluid-filled vessel, 2) dynamic responses of components submerged in a conventionally supported vessel, and 3) hydrodynamic and isolation-system responses in a base-isolated, fluid-filled vessel. The experiments, executed on a six-degree-of-freedom earthquake simulator, used multi-directional seismic inputs with different intensities and frequency contents.

The data generated in the physical experiments are used to validate numerical models for seismic FSI analysis of base-isolated or conventionally supported vessels and submerged components. The Arbitrary Lagrangian Eulerian (ALE) solver in LS-DYNA is used for the validation studies. Recommendations for validating numerical models for fluid-filled advanced reactors, using the data provided in this report, are provided.

ACKNOWLEDGMENTS

TABLE OF CONTENTS

TABLE OF CONTENTS (CONT'D)

TABLE OF CONTENTS (CONT'D)

TABLE OF CONTENTS (CONT'D)

TABLE OF CONTENTS (CONT'D)

LIST OF FIGURES

LIST OF FIGURES (CONT'D)

LIST OF FIGURES (CONT'D)

LIST OF FIGURES (CONT'D)

LIST OF FIGURES (CONT'D)

LIST OF FIGURES (CONT'D)

LIST OF FIGURES (CONT'D)

LIST OF FIGURES (CONT'D)

LIST OF FIGURES (CONT'D)

LIST OF TABLES

LIST OF TABLES (CONT'D)

LIST OF TABLES (CONT'D)

SECTION 1

INTRODUCTION

1.1 Introduction

The quest for a clean energy source to meet both growing global energy demand and climate goals has driven recent interest in advanced nuclear power plants. Nuclear power plants have clear advantages over conventional fossil fuel plants in terms of greenhouse gas emissions. According to the U.S. Energy Information Administration (EIA), in 2019, power plants that run on coal, natural gas, and petroleum generated about 62% of the total electricity in the U.S. but accounted for 99% of CO_2 emissions related to electricity generation (EIA 2020). A 2011 report by the World Nuclear Association (WNA) compared lifecycle greenhouse gas emissions of different electricity generation sources (WNA 2011). The study included the construction and decommissioning phases of different electricity generating facilities. The study concluded that on a lifecycle basis, emissions of nuclear power plants are 30 and 15 times smaller than coal and natural gas plants, respectively. Emissions of nuclear power plants were found to be comparable to those from wind and hydroelectric plants. The perceived drawbacks attached to nuclear power plants include high risk associated with exposure to natural hazards or malevolent acts, overnight capital cost, and long lead time to construct.

The design of next generation nuclear reactors, referred to as advanced reactors or Generation IV (Gen IV) reactors[1], is focused on the development of prototype reactors that are safe and economically competitive. The Generation IV International Forum[2] focuses on advanced reactors that have clear advantages, in terms of deployment cost, time to construct, operating temperature and pressure, fuel efficiency, and safety, compared to the reactors in use today (GIF 2002). The Gen IV reactor types are: gas-cooled fast reactor (GFR), lead-cooled fast reactor (LFRs), molten salt reactor (MSR), supercritical-water-cooled reactor (SCWR), sodium-cooled fast reactor (SFR), and very high temperature reactor (VHTR). Some of these advanced reactor types (LFR, MSR, and SFR) operate at near atmospheric pressure. Table 1.1 list the operating temperatures and pressures for the different types of reactors. For reference, the operating

---

[1]Several generations (Gen) of nuclear reactors are identified. Gen I reactors are not in operation at the time of this writing. Most operating reactors were built in the 1970s and are referred as Gen II reactors. Reactors built after the late 1990s are referred as Gen III and III+ reactors. The classification is loose and reflects advancements in efficiency and safety.

[2] Generation IV international forum is an international co-operation framework, established in the U.S. in 2000, seeking to develop and coordinate necessary research for the deployment of Generation IV nuclear reactors in 2030s.

temperature and pressure of a conventional pressurized water reactor (PWR) is also included. (PWRs constitute about two-thirds of existing nuclear power plants in the U.S.)

Table 1.1. Operating conditions (typical) for Gen IV reactor types

Reactor type	Temperature (ºC)	Pressure (atm)	Source
PWR	315	150	(WNA 2020)
GFR	850	90	Park (2017)
LFR	550	1	Pioro and Duffey (2019)
MSR	750	1	Pioro and Duffey (2019)
SCWR	500 – 625	250	Naidin *et al.* (2009)
SFR	500 -550	1	GIF (2020)
VHTR	700 – 950	70	Zhang (2016)

Figure 1.1 presents a cutaway view of a typical lead-cooled fast reactor supported at its head (top) on a reinforced concrete structure. The reactor comprises a vessel filled with molten lead coolant and a steam generator, and houses internal components such as fuel assemblies, pumps, and decay heat removal (DHR) equipment. A safety (guard) vessel is provided around the reactor vessel to contain the coolant in the event of an accident. Advanced reactors that operate at a low pressure (e.g., LFR, MSR, and SFR) provide an opportunity to use thin-walled reactor vessels and internal equipment and thus are advantageous from a cost standpoint.
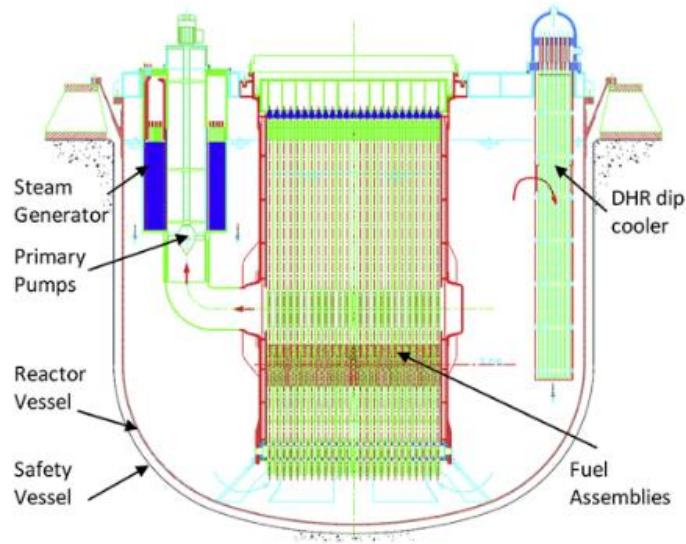
Figure 1.1. European lead cooled fast reactor, ELFR, adapted from Fig. 1 in Alemberti et al. (2014)

Thin-walled vessels also provide the advantage of not having to deal with extreme through-thickness thermal gradients (Benson *et al.* 2012). However, the downside to using a thin-walled vessel is that its seismic capacity is substantially smaller than a thick-walled counterpart. This reduction in capacity can be offset by using seismic isolation (described in Section 1.3). Explicit, accurate numerical modelling of the interaction between the contained fluid, the thin-walled vessel, and the internal components (referred to as fluid-structure interaction: FSI) will be key to seismic design and risk assessment calculations.

1.2   Design methods for seismic FSI analysis of reactors

Seismic FSI analysis of reactors in the operating fleet utilized analytical solutions and simplifying assumptions. Review of the literature suggested that designs of fluid-filled reactor vessels disregarded the presence of internal components and that of the submerged internal components ignored any interactions with the vessel. A simple mechanical analog for seismic analysis of a fluid-filled vessel, credited to Housner (1963), was referenced in consensus standards used in early nuclear engineering design practice (Thomas *et al.* 1963). The mechanical analog (described later in Section 2.2) represents the fluid response using two oscillators and disregards vessel flexibility. Later analytical solutions accounted for the flexibility of the vessel (Veletsos 1974; Veletsos 1984; Veletsos and Yang 1977) and were referenced in subsequent design standards.

Early design methods for submerged internal components relied on the use of *added mass* coefficients derived for simple geometries. An *added mass* coefficient represents a part of fluid mass that is assumed to

be attached to a submerged component for calculation of its frequency in the submerged state. Damping effects for a submerged component were estimated based on prescriptive guidelines or simple equations. Dong (1978) presents details of legacy design methods used in the nuclear industry for designing submerged components.

The simplified analytical solutions, introduced above, were derived for vessels and internal components having simple geometries and idealized boundary conditions, and unidirectional seismic inputs of small amplitude. In most cases, the fluid was considered ideal; that is, the effects of fluid compressibility and viscosity were ignored. The geometries and boundary conditions proposed for advanced reactor vessels and their internals are complex and generally not amenable to analytical solutions. Seismic design and qualification of advanced reactors must consider the interaction of the vessel, its internal components, and the contained fluid, for multi-directional design and beyond design basis earthquake shaking. Physical testing of advanced reactor vessels and their internal components for informing seismic design is not feasible because of their large size and cost of testing, leaving numerical modeling as the only plausible path for their seismic analysis, design, qualification, and risk assessment.

Numerical models used for seismic FSI analyses will have to be verified and validated. A model can be verified by comparing numerical results with those calculated using analytical solutions for similar (simplifying) assumptions. A verified model can be validated by comparing results of numerical solutions with physical test results. Yu and Whittaker (2021a) provides guidance on verification of numerical models. The focus of this report is validation of numerical tools for performing seismic FSI analysis of advanced reactors. Physical test data that could be used for validating numerical seismic FSI models for a wide range of shaking do not exist. Experiments carried out to generate such data and subsequent validation studies are described in this report.

1.3   Seismic isolation of liquid-filled vessels and nuclear reactors

Seismic isolation is a proven strategy for reducing seismic demands by shifting the fundamental period of the *supported* structure away from the dominant period range of earthquake ground motions. This is typically achieved in 2D by introducing horizontally flexible isolators in a horizontal plane, which is generally located at the base of the structure. Figure 1.2 presents a cross section of a sample 2D base-isolated reactor building. The reduction in seismic demands in the superstructure is accompanied by an increase in displacements (see Figure 1.3), nearly all of which is accommodated over the height of the isolators. The most popular 2D seismic isolation systems in the United States are composed of either Lead-Rubber (LR) (elastomeric) or friction pendulum (sliding) bearings. Three-dimensional isolation systems, based on coil-spring assemblies, are also viable and have been implemented in the U.S. and abroad.

Seismic isolation is a mature technology. Isolators have been implemented in more than 10,000 structures worldwide, including buildings, bridges, liquefied natural gas (LNG) tanks, off shore oil and gas platforms, and electric power equipment. The application of seismic isolation to nuclear structures has been limited to a few facilities in France and South Africa.

Recent studies (Lal *et al.* 2022) have demonstrated that the use of seismic isolation in advanced nuclear reactors can enable significant reductions in overnight capital cost (OCC) and levelized cost of electricity (LCOE) and enable standardization of equipment across sites of varying seismicity. A move towards standardization of equipment will require the use of numerical tools capable of performing integrated non-linear seismic analysis for multi-component earthquake shaking.
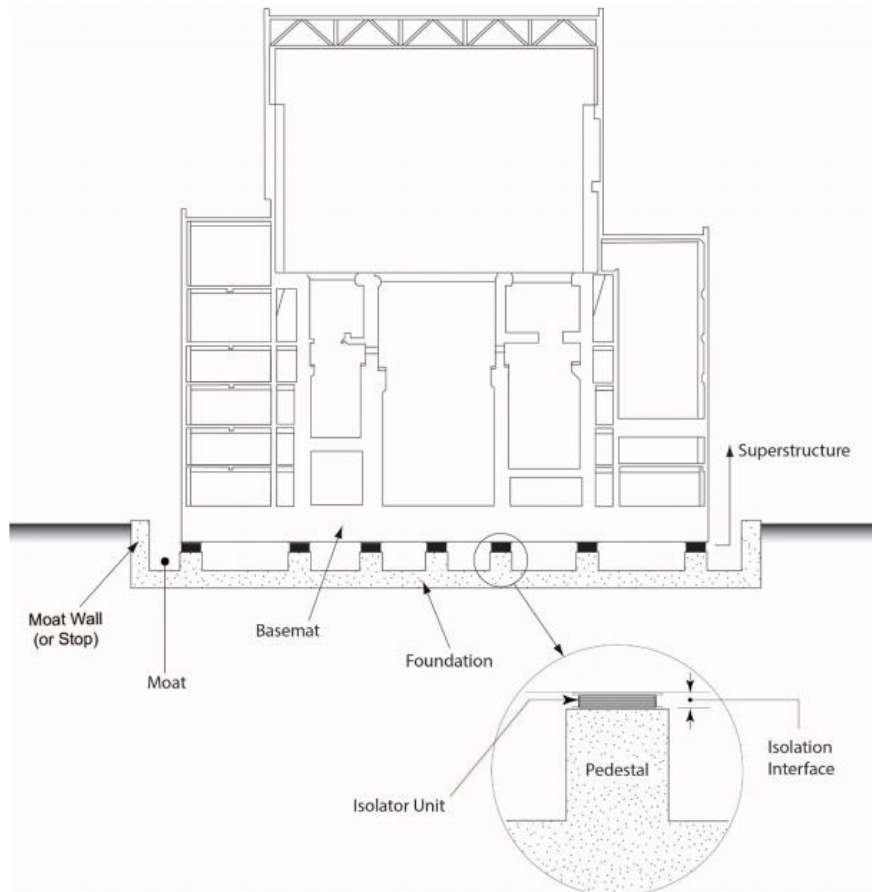
Figure 1.2. Cross section of a seismically isolated nuclear structure, adapted from Figure 3.1 in Kammerer *et al.* (2019)
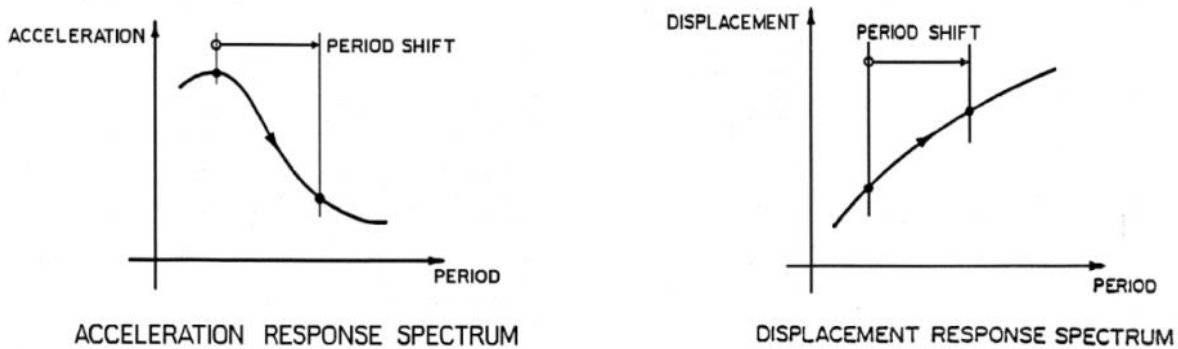
Figure 1.3. Effect of seismic isolation on spectral demands, adapted from Figure 3.2 in Kammerer *et al.* (2019)

Nearly all studies of FSI in seismically isolated, liquid-filled containers are numerical and utilize mechanical analogs to represent fluid behavior. The only experimental studies on seismically isolated, fluid-filled vessels were executed by Chalhoub and Kelly (1988) and Calugaru and Mahin (2009). These are discussed in detail in Section 2.3. Neither study involves collection and curation of all key fluid responses (e.g., wave height, hydrodynamic pressure, base shear, and base moment) for a seismically isolated, fluid-filled vessel subjected to multi-component earthquake shaking. The need for physical test data for fluid responses in an isolated vessel that could be used to validate integrated non-linear analysis tools motivated some of the experiments described in this report.

1.4   Objectives of the report

The goals of this report are: 1) to validate numerical tools for enabling reliable numerical seismic FSI analysis of fluid-filled vessels and submerged components in advanced nuclear reactors; and 2) to demonstrate the efficacy of seismic isolation in mitigating seismic demands in advanced reactor vessels. These goals are achieved by meeting three objectives:

1. Generating experimental data for hydrodynamic responses (in a fluid-filled vessel) and submerged-component responses for multiple components of earthquake shaking, considering conventional base-support conditions and multiple choices of isolation systems.

2. Generating experimental data for hydrodynamic responses in a base-isolated, fluid-filled vessel subjected to multiple components of earthquake shaking.

3. Validating numerical models for seismic FSI analysis of reactor vessels, seismically isolated and conventionally supported, and submerged internals, using data generated from experiments and to provide recommendations for validating numerical models for fluid-filled advanced reactors.

6

1.5   Organization of this report

This report is organized into eight sections, a list of references, and five appendices.

Section 2 reviews analytical and experimental studies on fluid-filled vessels, submerged components, and seismic isolation of fluid-filled vessels.

Section 3 presents details of experiments conducted on a fluid-filled vessel. Test results are compared with analytical predictions. The impact of seismic isolation on hydrodynamic responses is studied using earthquake-simulator inputs generated using a virtual isolation system.

Section 4 develops and validates numerical models for the fluid-filled vessel described in Section 3. The utility of the Lagrangian and the Arbitrary Lagrangian-Eulerian (ALE) solvers in LS-DYNA (LSTC 2017) are investigated and their limitations and possible applications are identified.

Section 5 describes experiments conducted on multiple submerged components. Inputs simulating multiple isolation systems are used to study the impact of seismic isolation on component responses.

Section 6 presents validation studies for seismic FSI responses of submerged components using the ALE solver in LS-DYNA.

Section 7 describes experiments conducted on a fluid-filled vessel seismically isolated using friction pendulum bearings. Numerical models, integrating FSI analysis and isolation system analysis are introduced (based on the models introduced in Section 4) and validated.

Section 8 summarizes the work, presents conclusions drawn from the experiments and validation studies and provides recommendations for developing validated numerical models for fluid-filled advanced reactors.

A list of references is provided after Section 8 and is followed by five appendices. Appendix A describes the calibration of the four five-channel load cells used in the experiments. Appendix B summarizes strategies explored for measuring wave height in experiments. Appendix C presents lists of input motions used in different test configurations described in this report. Appendix D describes tests for characterizing the friction pendulum bearings used in the experiments of Section 7 and Appendix E describes modifications to an existing analytical solution for hydrodynamic responses of a cylindrical vessel under rocking inputs.

SECTION 2
LITERATURE REVIEW

2.1   General

This section surveys the literature pertaining to the objectives of Section 1.4. Summaries of analytical and experimental studies dealing with analysis of fluid-filled containers are presented in Sections 2.2 and 2.3, respectively. Analytical and experimental studies dealing with submerged components are presented in Sections 2.4 and 2.5, respectively. Section 1.3 summarizes studies dealing with seismic isolation of fluid-filled containers.

Many of the studies that are described here parse the hydrodynamic responses in a dynamically excited container into impulsive and convective components. These two terms are defined here for later use. The *impulsive component* represents the effects of the part of the fluid that is assumed to move with the container or surfaces of submerged components as a rigidly attached mass. The *convective component* represents the effects of the part of the fluid that sloshes. The sloshing response may be further parsed into contributions from different modes.

2.2   Review of analytical studies for seismic analysis of fluid-filled vessels

The behavior of structures subjected to earthquake-induced fluid pressures was first studied in the early 1930s. Westergaard (1933) provided one of the first solutions for such a problem, wherein the dynamic pressure on a rectangular, vertical concrete dam subjected to horizontal acceleration (normal to the dam-water interface) was established (see Figure 2.1). The acceleration of the dam was assumed to be constant over its height and its response was approximated by a harmonic corresponding to the period of the dam (evaluated independently) and the peak ground acceleration. The resulting displacement was used as a boundary condition for simplified equations for the semi-infinite fluid domain (water, in this case) on the upstream side. The fluid was considered compressible and small deformations were assumed, allowing the application of equations used to model sound propagation in fluids (Lamb 1932). Westergaard approximated the hydrodynamic pressure distribution over the height of the dam by a parabola and provided coefficients for calculating hydrodynamic shear and moment at the base of the dam. A parabolic body of the fluid (water) was added to the dam (*added mass*) with no adjustment to strength, as shown in Figure 2.1.
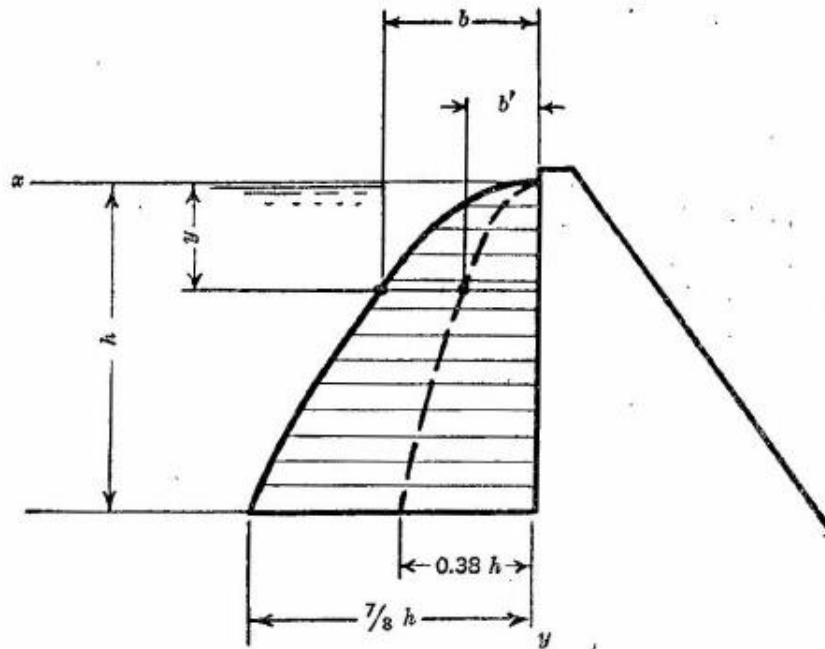
Figure 2.1. Body of water which may be considered to move with dam, dotted curve shows equivalent body of concrete, adapted from Fig. 3 in Westergaard (1933)

Hoskins and Jacobsen (1934) used an approach similar to that of Westergaard (1933) to evaluate dynamic impulsive pressure in a prismatic rectangular tank subjected to small amplitude, horizontal motions. Unlike Westergaard, who considered a channel of infinite length (as on the upstream in case of a dam) with a single barrier, a channel of finite length with synchronously moving barriers at both ends was considered. The fluid was assumed to be incompressible and the derived analytical solution was validated by results from an accompanying experimental investigation that used impulsive ground motions. Hoskins extended the work on rectangular tanks to evaluate the dynamic impulsive pressure for a cylindrical tank subjected to an impulsive earthquake loading. The work, although not published, is among the earliest attempts to evaluate the hydrodynamics of a cylindrical tank subjected to earthquake motions. Some results from this unpublished work, pertaining to the participation of water in the accelerated motion of a cylindrical tank, are presented in Appendix A of Morris (1938). Morris (1938) is summarized in Section 2.3.

Jacobsen (1949) presented a solution for hydrodynamic impulsive pressure in a rigid cylindrical vessel subjected to a small, horizontal, and unidirectional acceleration. The velocity of the rigid cylindrical vessel was used as a boundary condition for solving Laplace's equation for velocity potential (φ) in the enclosed

cylindrical fluid domain[3]. A zero fluid velocity in the vertical direction was assumed at the base of the vessel and a zero pressure was assumed at the initial free surface, essentially neglecting the effect of gravity waves (convective component). Jacobsen and Ayre (1951) subsequently conducted earthquake-simulator tests, subjecting tanks of different dimensions to small amplitude '*simple*' inputs: step motion and oscillatory motion. The authors concluded that the comparison of experimental results and theory (Jacobsen 1949) was good.

Research on fluid-filled tanks subjected to dynamic loads developed in parallel across a number of fields of engineering, including aeronautical, ocean, and civil. Graham and Rodriquez (1951) analyzed the response of fuel in a rectangular aircraft fuel tank for small amplitude translation, pitching and yawing motions. The obtained expressions for the resulting hydrodynamic force and moment were used to construct simple mechanical analogs (see Figure 2.2) for the modeling the fuel. The masses shown in Figure 2.2 represent fluid behavior in impulsive and multiple convective modes. Similar models were developed for civil engineering applications soon after, as discussed next. .
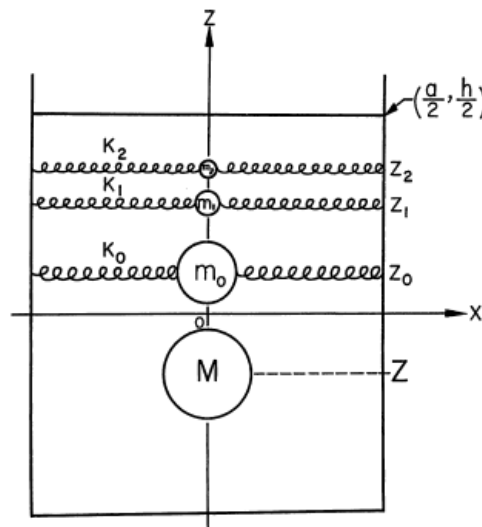
Figure 2.2. Mechanical analog representing response of fuel to horizontal and pitching motions of fuel tank, adapted from Figure 2 in Graham and Rodriquez (1951)

---

[3] Laplace's equation for velocity potential is: $\nabla^2 \varphi = 0$. The velocity potential φ is a function of space coordinates and time and is related to the components of liquid velocity and the resulting hydrodynamic pressure. The fluid velocity, V_n, in the direction of a generalized coordinate, n, is related to the velocity potential as: $V_n = -\partial\varphi/\partial n$. The hydrodynamic pressure, p, at a point is related to φ as: $p = \rho_l\,\partial\varphi/\partial t$, where ρ_l denotes the mass density of the fluid and t denotes time.

Housner (1954, 1957, 1963) evaluated the hydrodynamic responses of rigid tanks of different geometries subjected to small-amplitude, unidirectional, horizontal inputs using an approximate method, avoiding solution of the Laplace's equation. The work resulted in a simple mechanical analog for the analysis of rectangular and cylindrical tanks, which is still widely used with certain modifications. Figure 2.3b shows the mechanical analog for a base-supported cylindrical tank (Figure 2.3a) wherein two masses are considered. The impulsive mass, M_i, and the convective mass, M_c, are connected to the tank wall with rigid and flexible elements, respectively, at specified heights h_i and h_c above the base, such that they generate reactions at the base of the tank as would be exerted by the fluid pressure in the corresponding tank of Figure 2.3a.

(a) base-supported, rigid cylindrical tank of radius R, with fluid up to a height h, subjected to base excitation $\ddot{u}_g(t)$

(b) equivalent mechanical analog
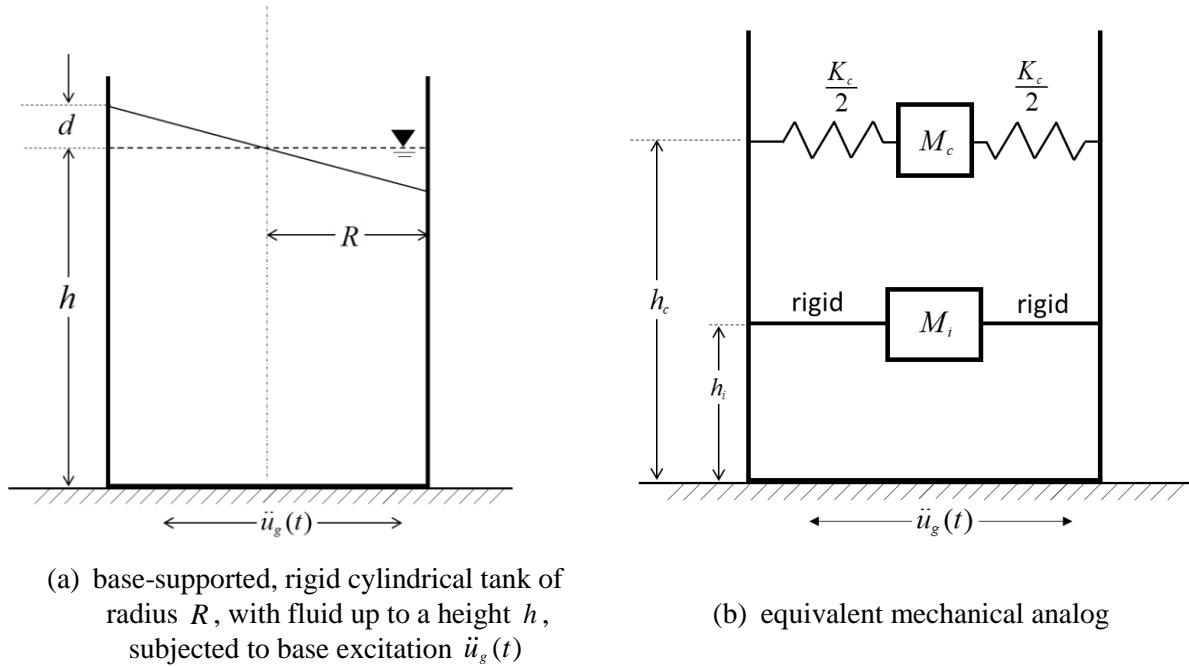
Figure 2.3. Housner's mechanical analog for a rigid cylindrical tank, reproduced from Fig. 1 in Housner (1963)

The equivalent system is specified by the following quantities (Housner 1963), where M is the total mass of fluid in the tank and g is the acceleration due to gravity:

$$M_i = M \frac{\tanh(1.7R/h)}{1.7R/h} \tag{2.1}$$

12

$$h_i = \frac{3}{8} h \left\{ 1 + \alpha \left[\frac{M}{M_c} \left(\frac{R}{h} \right)^2 - 1 \right] \right\} \tag{2.2}$$

$$M_c = M(0.6) \frac{\tanh(1.8h/R)}{1.8h/R} \tag{2.3}$$

$$h_c = h \left[1 - 0.185 \left(\frac{M}{M_c} \right) \left(\frac{R}{h} \right)^2 - 0.56\beta \frac{R}{h} \sqrt{\left(\frac{MR}{3M_c h} \right)^2 - 1} \right] \tag{2.4}$$

$$k_c = 5.4 \frac{M_c^2}{M} \frac{gh}{R^2} \tag{2.5}$$

where α and β are constants equal to 1.33 and 2.0 respectively, if base moments generated due to pressure acting on both the wall and the floor of the tank are to be determined. If base moments generated by pressure acting only on the wall are to be determined, the constants take the values of 0 and 1 respectively. The amplitude of the sloshing waves (d in Figure 2.3a) is related to the displacement amplitude (A_i) of the convective mass M_c by the following relationship:

$$d = \frac{0.63 A_i \left(\frac{k_c R}{M_c g} \right)}{1 - 0.85 \frac{A_i}{R} \left(\frac{k_c R}{M_c g} \right)} \tag{2.6}$$

Subsequent studies extended the analysis tools to account for the flexibility of the tank wall, since there was evidence from reconnaissance after the 1964 Alaska earthquake that hydrodynamic response quantities could be underestimated if wall flexibility was ignored. One of the earliest attempts to consider tank flexibility in the calculation of hydrodynamic forces on a base supported cylindrical tank was made by Edwards (1969). Edwards employed the finite element method for the dynamic analysis of a fluid-filled storage tank. The hydrodynamic effects were considered as an added mass matrix in the equation of motion for the coupled fluid-structure system.

Veletsos (1974) presented a simpler approach for evaluating the impulsive responses (pressure, shear force and moment at the base) in a flexible fluid-filled cylindrical tank. The method was based on the assumption that the fluid-filled tank vibrates as a single degree of freedom, such that the cross section remains circular at all times, with an assumed deflected shape along the height of the tank that could be prescribed. The system analyzed by Veletsos considered three deflected shapes, denoted $\psi(y)$, as shown in Figure 2.4. Veletsos and Yang (1977) improved the method presented in Veletsos (1974) and decoupled the impulsive response into multiple modes. Veletsos (1984) presented a comprehensive discussion on the analysis of

13

flexible and rigid base supported tanks and extended the analysis to include effects of vertical shaking and tank-foundation interaction.

(a) tank and fluid system considered

(b) deflected shapes (vibration modes) considered
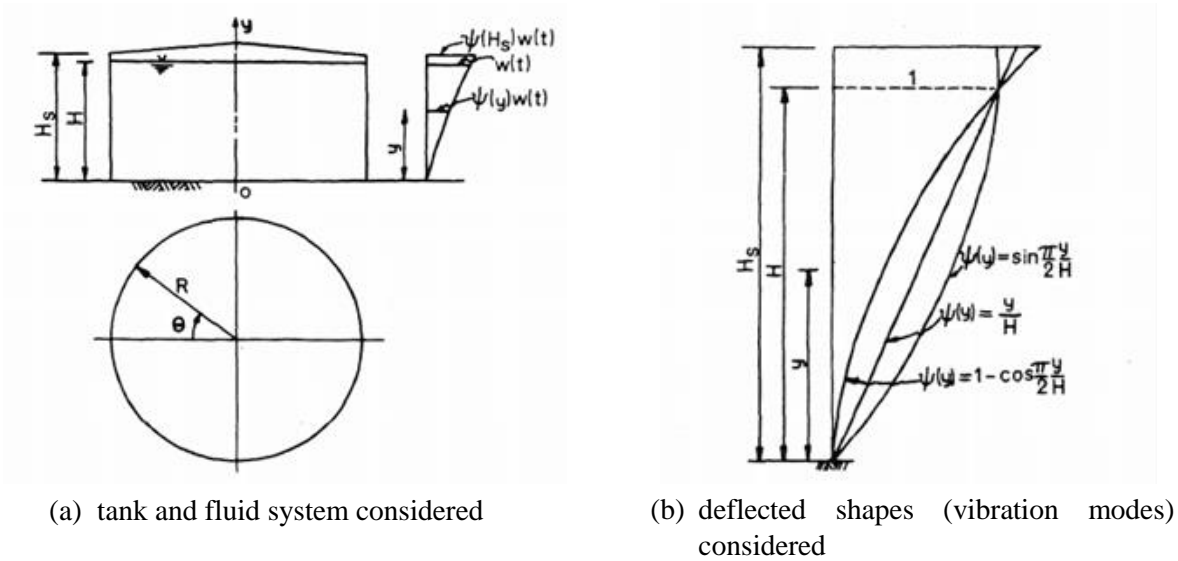
Figure 2.4. Analysis of a flexible fluid-containing cylindrical tank, adapted from Fig. 1 and Fig. 2 in Veletsos (1974); H_s and H are the tank and fluid heights, respectively; R is the tank radius; θ and y (and R) denote a cylindrical coordinate system; $w(t)$ denotes the displacement relative to ground of a section of the tank at the liquid level; and t denotes time

Haroun and Housner (Haroun and Housner 1981a; Haroun 1983; Haroun and Housner 1981b) conducted experimental and theoretical investigations into the dynamic behavior of ground-supported, flexible, cylindrical tanks. Their study involved a detailed theoretical treatment of the coupled fluid-shell system, an experimental investigation of the dynamic characteristics of full-scale tanks, and the development of a design procedure based on simplified analysis. The theoretical treatment involved a combination of the finite element method and an analytical solution of fluid pressure to calculate seismic responses of a cylindrical tank. The method enabled the calculation of the lateral and circumferential modes of a cylindrical, fluid-filled tank. Results from experiments, to be described in Section 2.3, were used to validate the analysis method. Haroun and Housner developed a three-mass mechanical analog that accounted for tank wall flexibility.

Veletsos and Tang (1987) presented exact solutions for the impulsive and convective responses of a fluid-containing, flexible, cylindrical tank subjected to a small amplitude rocking motion at the base. The response to a rocking acceleration, $\theta_g''(t)$, was evaluated by factoring the response to a lateral acceleration,

14

$u_g^{''}(t)$, if $u_g^{''}(t) = C\theta_g^{''}(t)$, where C is a constant length and t denotes time. A mechanical model for a laterally excited tank was extended to consider base rocking.

Malhotra *et al.* (2000) presented a two-mode mechanical analog, based on the work of Veletsos and Yang (1977) that could be used for the seismic analysis of flexible, base supported tanks subjected to a unidirectional, horizontal motion. Similar in format to the mechanical analog of Housner (1963), Malhotra's analog accounted for higher convective modes and flexibility of the tank wall. Figure 2.5 presents the mechanical analog: masses m_c and m_i representing the convective and impulsive modes, respectively, are located at heights h_c and h_i above the base, respectively. Expressions for the periods (or frequencies) of the two modes are provided in the study. Malhotra proposed damping ratios of 0.5% of critical for the convective mode, and 2% and 5% for the impulsive mode of steel and concrete tanks, respectively. Malhotra verified his analog by comparing results with those calculated using the solution presented in Veletsos and Yang (1977). The Malhotra analog is used in Eurocode 8 (CEN 2008) for seismic analysis of base supported tanks.
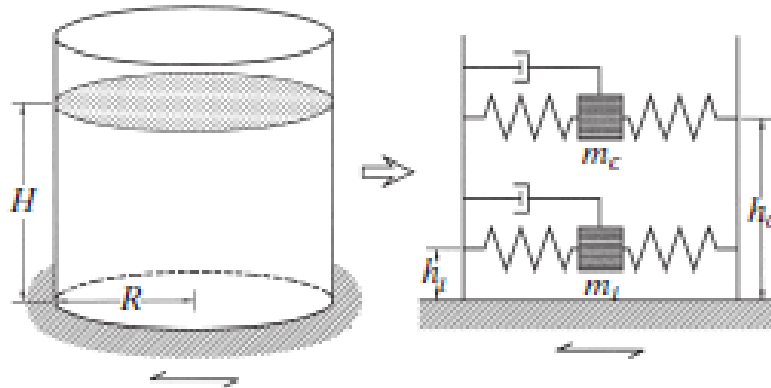
Figure 2.5. Two-mode mechanical analog, adapted from Fig.3 in Malhotra *et al.* (2000)

Yu and Whittaker (2020) extended the work of Veletsos (1984) on base-supported cylindrical tanks to derive solutions for head-supported flexible tanks. The hydrodynamic responses of a head-supported tank subjected to a small amplitude unidirectional, horizontal input were decoupled into modal contributions, and analytical solutions were provided for each mode. Analytical solutions for impulsive frequencies of the tank, hydrodynamic pressures, convective frequencies, wave heights, and reactions at the head support in each mode were provided. The responses were calculated for tanks with a wide

range of dimensions. The analytical solutions were used for verification of a numerical model of a fluid-filled head supported vessel (Yu *et al.* 2019).

Aslam *et al.* (1978) presented an experimental and analytical study of sloshing in annular, rigid tanks (see Figure 2.6). Laplace's equation was solved to derive closed-form expressions for convective frequencies, surface displacements, and hydrodynamic pressures in a base-excited annular tank. Results were compared with experimental data. Fujita *et al.* (1986) presented a similar analytical study and conducted experiments to validate solutions. Tang *et al.* (2010) extended the theory of Aslam *et al.* (1978) to develop closed form solutions for hydrodynamic base shear and base moment in base-excited, flexible annular tanks.
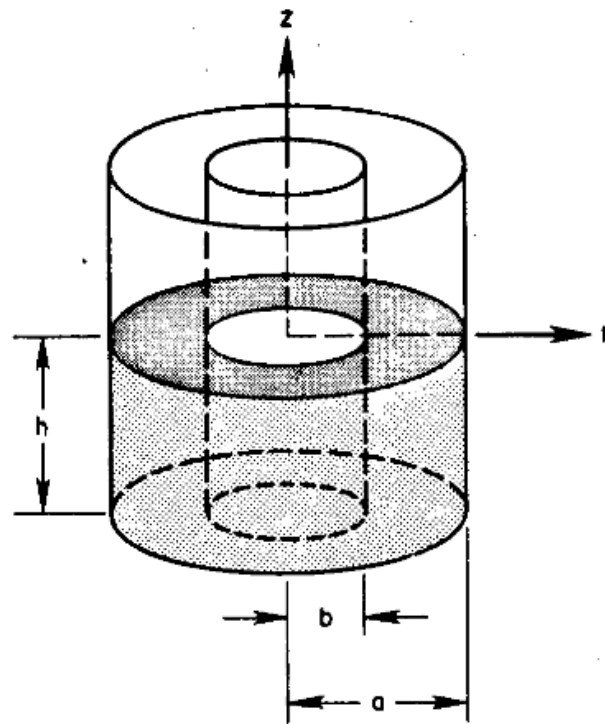
Figure 2.6.Annular tank, adapted from Fig.1 in Aslam *et al.* (1978)

2.3   Review of experimental studies for seismic analysis of fluid-filled vessels

Morris (1938) conducted an experimental investigation to study sloshing dynamics in cylindrical tanks; see Figure 2.7. The study used the classical hydrodynamics solutions (Lamb 1932) to interpret the experimental results. These experiments were among the first to investigate the behavior of fluid in cylindrical tanks subjected to earthquake shaking. Morris concluded that resonance between a ground motion input and wave motion (convective modes) was possible and that it could result in significant wave heights.

Figure 2.7. Cylindrical tanks on shaking table, adapted from Plate XXIV in Morris (1938)

Haroun (1983) investigated the dynamic behavior of base-supported, deformable, cylindrical, fluid-filled storage tanks. Ambient and forced vibration measurements were made of the natural frequencies and mode shapes for three water storage tanks with height-to-radius ratios between 2 and 3 and with different types of foundations. The first tank was anchored to a reinforced concrete slab on deep alluvium. The second tank was supported on a deep concrete ring but not anchored. The third tank was anchored to a thick slab supported on reinforced concrete caissons. The tanks were closed at their top by a head, termed here as *roof*. The focus of the experimental program was characterizing the dynamics of the fluid-shell system. Hydrodynamic responses such as sloshing were not investigated. A vibration generator was used to excite the tanks. Results from the experiments were used to validate theory presented by the author in the same study (described in Section 2.2 above). Haroun's comparison of experimental and theoretical predictions for lateral and circumferential modal frequencies confirmed the importance of considering foundation flexibility, hydrostatic pressure, and tank roof stiffness in a dynamic analysis.

Chalhoub and Kelly (1988) conducted an earthquake-simulator study on two fluid-filled tanks. One tank was attached directly to an earthquake simulator. The second tank was mounted immediately above the base of an isolated nine-story steel frame building model on the same simulator. The frame represented a prototype building at 1/4 length scale. Eight elastomeric bearings isolated the steel frame. Unidirectional inputs, including sinusoids and earthquake time series, were used for testing. Hydrodynamic pressure at tank walls, displacements and accelerations in the tank wall, and water surface displacements (wave height) were measured. The experimental results were used to validate theory developed by the authors that assumed linear fluid response. The experimental data showed reductions in hydrodynamic pressure, acceleration, and displacement of the tank walls due to seismic isolation. Wave heights were increased. The percentage change in response due to seismic isolation was dependent on the frequency content of the input motion.

Pal *et al.* (2001) conducted experiments on a water-filled, plexiglass cylindrical tank using a mechanically manipulated lathe machine as a shaking platform. See Figure 2.8 for details. The focus of the experiments was sloshing response. Bespoke capacitance probes recorded wave height (free surface displacements). The authors generated a three-dimensional finite element model assuming the fluid to be ideal and solving for velocity potential that satisfies the Laplace's equation at each point in the fluid domain. The velocity potential was considered as the unknown field variable and expressed in terms of finite element shape functions and time dependent nodal values of the variable. The authors claimed good agreement between experimental and numerical predictions of wave actions.
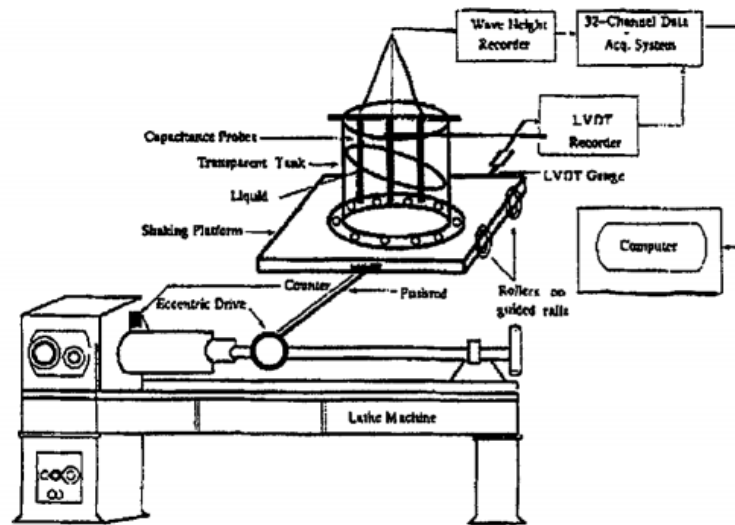
Figure 2.8. Test setup, adapted from Fig. 2 in Pal *et al.* (2001)

Calugaru and Mahin (2009) conducted earthquake-simulator tests on a cylindrical tank having a diameter and a height of 1.8 m. Triple Friction™ pendulum bearings were used to seismically isolate the tank. Experiments were performed using multi-directional inputs and different fill heights. Wave height and base reactions were recorded using parallel wire gages and load cells, respectively. Hydrodynamic pressures were not measured. The experimental data was used to validate a numerical model comprising Housner's analog (considering one convective mode) mounted atop a single Triple Friction™ pendulum bearing. Inclusion of higher convective modes (as additional spring-mass systems) in the analog improved the accuracy of the prediction for wave height but not for base shear. The authors reported first-mode type sloshing for the isolated experiments but *violent* sloshing for the fixed base tests.

Goudarzi and Sabbagh-Yazdi (2012) investigated non-linear sloshing in rectangular tanks subjected to unidirectional inputs. Experiments were performed on an acrylic rectangular tank, 0.96 m × 0.4 m in plan and 1.0 m in height. Wave height data were collected using ultrasonic wave gauges. Four fill heights (0.19 m, 0.33 m, 0.48 m and 0.62 m) were considered. Three harmonic excitations with frequencies less than, close to, and greater than the fundamental sloshing frequency of the contained fluid were imposed. The authors used the experimental wave-height data to validate a non-linear Volume of Fluid (NL-VOF) model in ANSYS (ANSYS 2017) and used an analytical solution for wave height derived in the study to verify a linear finite element model (utilizing FLUID79 elements). The applicability of the linear and non-linear solvers for prototype scale tanks was investigated in a parametric study considering six tanks with aspect ratios (ratio of height to length) ranging from 0.6 to 6. Non-linear effects (in wave height) were found to be significant for wide tanks, for which an increase of about 70% in maximum wave height due to non linearities was reported.

Sangsari and Hosseinzadeh (2014) conducted earthquake-simulator tests on a model of a cylindrical steel tank, with a diameter of 1.2 m, height of 1.25 m, and a wall thickness of 2 mm. The tank roof was conical. Different fill heights (0.6 m, 0.8 m, 1 m and 1.2 m) were used for testing. Unidirectional earthquake motions with a peak acceleration of 0.4g and a time scale corresponding to a 1/16 length scale were used for testing. The focus of the experiments was damping in the impulsive and convective modes. Instrumentation included accelerometers at the base and top of the tank and a camera for recording wave height. The results for different fluid heights and earthquake inputs indicated damping ratios in the range of 0.3% to 0.5% (of critical) for the convective mode and 1.1% (of critical) for the impulsive mode.

Park *et al.* (2016) conducted earthquake-simulator tests on a thin walled steel tank, with a radius, height, and wall thickness of 0.6 m, 1.75 m and 0.6 mm, respectively. Tests with unidirectional earthquake inputs were conducted with three fill heights: 97%, 89%, and 66%. Six pressure transducers and fifteen

accelerometers recorded responses. Figure 2.9 presents a photograph of the model and the instrumentation layout. The focus of the tests was to investigate beam-type and oval-type[4] vibrations of the tank wall for different fill heights. The authors reported a dominant second mode type (second mode in beam bending) vibration and noted that oval-type vibration modes in the circumferential direction were not significant. At locations of dominant impulsive response, the temporal variation (phase) of the hydrodynamic pressure and tank wall acceleration were similar. The hydrodynamic pressure at locations of dominant convective response was not influenced by tank wall acceleration.
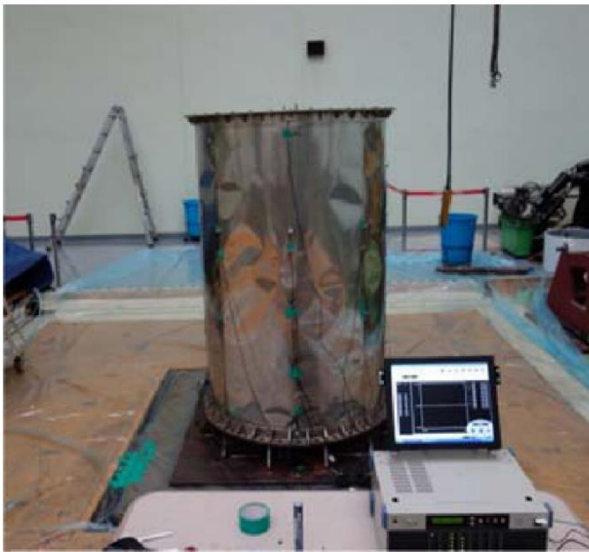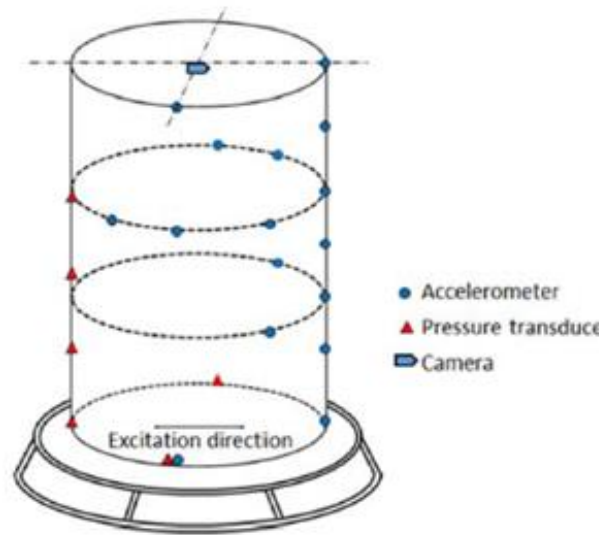
(a) tank model   (b) instrumentation used

Figure 2.9. Test setup, adapted from Figures 2 and 4 in Park *et al.* (2016)

Radnić *et al.* (2018) conducted earthquake-simulator experiments on three rectangular tanks, each with plan dimensions of 2.4 m × 0.8 m and a height of 1 m. The tanks differed in the thickness of a wall in the direction of excitation, referred to as the front wall, as identified in Figure 2.10. Front wall thicknesses of 1 mm and 2 mm (deformable), and 100 mm (rigid) were investigated. The remaining three walls in each tank were 100 mm thick. Instrumentation included ten pressure gauges arranged vertically on the front wall, two strain gauges installed on the front wall, two transducers to measure the displacements of the front wall and cameras to record the motion of the free surface. Harmonic excitation, a synthetically generated

---

[4] *Beam-type* vibrations are associated with the lateral deformation of the tank (similar to those in a cantilever beam) and *oval-type* vibrations are associated with circumferential deformations.

acceleration and a recorded earthquake acceleration, each with a peak of 0.1g, were used for testing. Although the authors drew a number of broad conclusions, context was missing. For example, the authors concluded that increasing the stiffness of the front wall leads to an increase in the hydrodynamic force on the wall. This outcome is a function of frequency content of the seismic input and is not correct in a general sense. In a subsequent study by the authors (Kusić *et al.* 2019), a numerical model, constructed using SPH (smoothed particle hydrodynamics) particles for the fluid and Lagrangian elements for the tank was used to predict hydrodynamic pressure on the front wall.

Figure 2.10. Test setup, adapted from Fig. 2 in Radnić *et al.* (2018)

Compagnoni and Curadelli (2018) conducted experimental and numerical investigations into the seismic response of base-supported, cylindrical, fluid-filled storage tanks. Instrumentation included an assembly of buoys and laser displacement sensor to measure wave height and an accelerometer for measuring the base acceleration. Figure 2.11 shows the test setup. Hydrodynamic pressures and base reactions were not recorded. The authors used correlation coefficient, difference in peak values, and difference in root mean square values to compare time series (of responses) obtained from the experiments and numerical analysis. A comparison of the experimentally recorded wave heights with those predicted by the simplified mechanical models proposed by Malhotra *et al.* (2000) and with finite element (FE) models developed in ANSYS indicated that the mechanical model underestimated wave height whereas the FE models yielded similar results. Analysis using the mechanical analog predicted greater base reactions than the FE model.
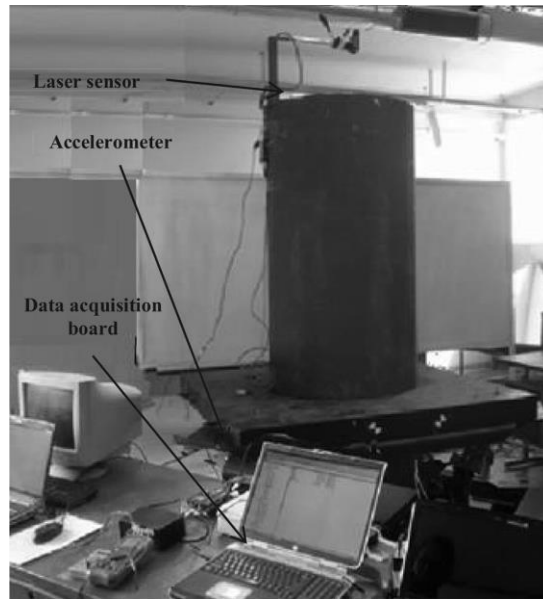
Figure 2.11. Test setup, adapted from Fig. 3 in Compagnoni and Curadelli (2018)

2.4   Review of analytical studies for seismic response of submerged internals

The dynamics of submerged structures and components has been the focus of studies, dating back to the 18th century (see Clough (1960)). It is well known that when a submerged component vibrates in a fluid, the displacements of the surrounding fluid result in fluid pressures that produce a hydrodynamic force acting on the structure. The dynamic characteristics (natural frequency and damping) of the vibrating structure are thus affected by the pressure. The component experiences effects that are equivalent to an increase in the apparent mass of the system (the *added mass effect*) and damping. The three-dimensional Navier-Stokes equations[5] could be used to derive solutions but simplifications are made for practical applications: the effects of viscosity and compressibility are neglected. In such cases, the incompressible potential flow theory[6] can be used to evaluate the added mass effects. (Added damping effects due to fluid cannot be evaluated using such an approach because fluid viscosity is ignored). Such an approach has been used in different fields of engineering (e.g., naval, mechanical, and civil) albeit for simple structural shapes.

---

[5] The governing equations for fluid dynamics include sets of momentum balance equations, mass balance equations and energy balance equations along with boundary conditions. These are referred to as the Navier-Stokes equations.

[6] Potential flow theory assumes incompressible and inviscid flow and the fluid behavior is governed by Laplace's equation, as described earlier. See footnote 3 in Section 2.2.

Keane (1963) performed an experimental and a theoretical investigation of a circular cantilevered rod vibrating in a cylindrical pipe. Several annular sizes were studied. The increase in the virtual mass (added mass, M_H) of the inner cylinder was shown as:

$$M_H = M_1 \left(\frac{((R_2 / R_1)^2 + 1)}{((R_2 / R_1)^2 - 1)} \right) \tag{2.7}$$

where R_1 and R_2 are the radii of the cantilevered rod and the cylindrical pipe, respectively, and M_1 is the mass of fluid displaced by the cantilevered rod.

Fritz (1972) analyzed the dynamics of a fluid-solid system comprising two rigid coaxial cylinders separated by a fluid annulus as shown in Figure 2.12. Assuming an incompressible and inviscid fluid and small displacements of the cylinders, Fritz used the potential flow theory to generate closed form expressions for added masses for the inner and outer cylinders. The added masses were expressed in terms of dimensions of the annulus and the density of the fluid.
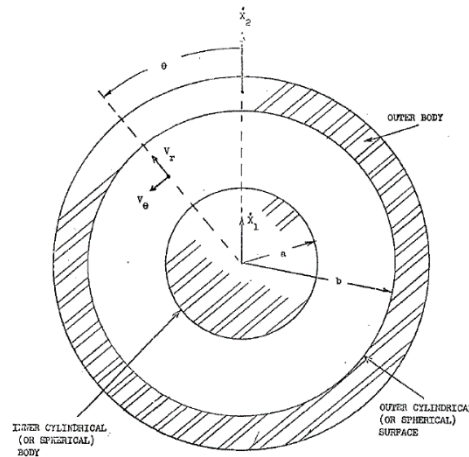
Figure 2.12. Two body system analyzed by Fritz (1972), adapted from Fig. 1 in Fritz (1972)

A body of work dealing with vibrations of multiple cylindrical components including parallel cylinders, concentric cylinders separated by fluid, a row of cylinders in an infinite fluid, and a group of cylinders in a fluid was produced by Chen and his co-workers at the Argonne National Laboratory in the 1970s. Chen (1975c) analytically studied the lateral vibration of two parallel circular cylinders vibrating in a fluid as shown in Figure 2.13. The equations of motion including fluid coupling were derived using the added mass approach, wherein the hydrodynamic forces were evaluated considering an ideal fluid. The author presented a closed form solution and an approximate solution for response in free vibration and considered a special

case of an elastic rod vibrating next to a rigid rod in a fluid. Expressions for the steady-state responses of the two cylinders subjected to harmonic excitations were presented. In-phase and out-of-phase modes of vibration, in which the rods vibrate in the same and opposite directions, respectively, were identified.
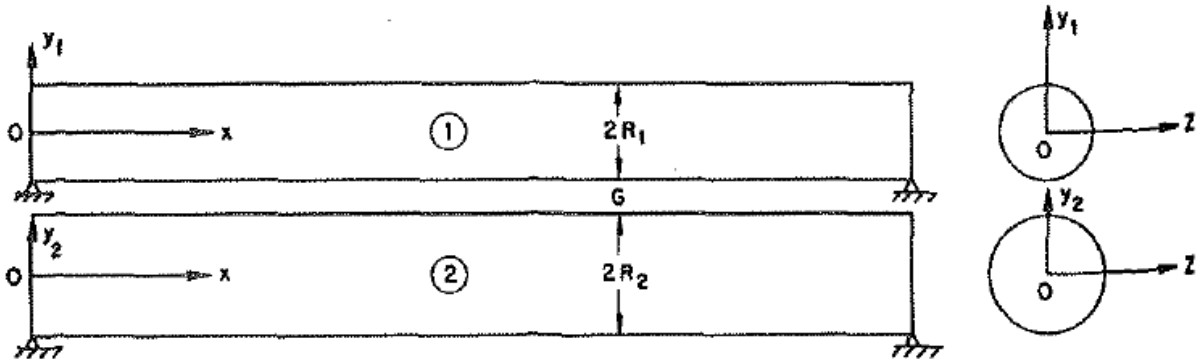
Figure 2.13. Two parallel circular cylindrical rods vibrating in a fluid, adapted from Fig.1 in Chen (1975c)

Chen *et al.* (1976) analyzed a long cylindrical rod undergoing small amplitude vibrations in a fluid confined by a cylindrical pipe, as shown in Figure 2.14. This system is similar to that analyzed by Fritz (1972) except that fluid is considered to be viscous. (A similar system, consisting of a finite length rod vibrating in a confined viscous fluid was analyzed by (Mulcahy 1980).) Chen *et al.* (1976) derived closed form solutions for added mass and damping for the vibrating rod. A series of experiments was also conducted for a rod vibrating in viscous fluids (water, mineral oil, silicone oil) and results were compared with analytical solutions. The authors note that the derived solutions should only be used if the flow around the vibrating cylinder is two-dimensional and axial flow can be neglected.
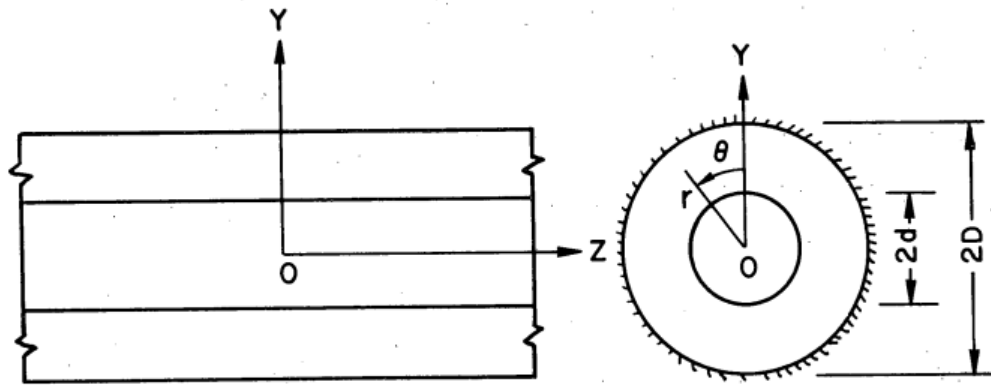
Figure 2.14. Cylinder vibrating in a fluid annulus, adapted from Fig. 1 in Chen *et al.* (1976)

Chen (1975a) analyzed the effects of surrounding fluid on the dynamic behavior of a row of circular cylindrical cylinders as shown in Figure 2.15. The hydrodynamic forces associated with cylinder motions were evaluated using the potential flow theory. The fluid velocity potential associated with the motion of a cylinder (say the *j*th cylinder in Figure 2.15) in one of the two directions (*x* or *y*, as identified in Figure 2.15) was evaluated considering all other cylinders to be stationary. The author refers to this potential field (due to one cylinder) as a *partial field*. Using the assumption of linearity, the total velocity potential field at a point in the fluid was thus evaluated as a summation of the *partial fields* generated by all cylinders. A closed form expression for total velocity potential field (φ) was obtained by using suitable velocity boundary conditions at the interfaces of the cylinders and the fluid. The fluid forces acting on cylinders were then evaluated using fluid pressure p calculated per $p = -\rho_l \, \partial\varphi/\partial t$ where ρ_l and t denote fluid density and time, respectively. The author presented a methodology for free and forced vibration analysis of the cylinder system, specifically identifying coupling modes in the vibration response of the cylinders. Chen (1975b) extended the work in Chen (1975a) to analyze arbitrarily located, parallel circular cylinders vibrating in an unconfined (infinite) fluid as shown in Figure 2.16. The analytical solutions were further extended to accommodate a group of cylinders vibrating in a confined fluid (Chung and Chen 1977), as shown in Figure 2.17. Added mass coefficients for different cylinders in the group were derived as a function of group geometry: gap between the inner and outer cylinders, and radii of the cylinders. Subsequently, experiments were performed to validate the proposed analytical solutions and these are described in Section 2.5.
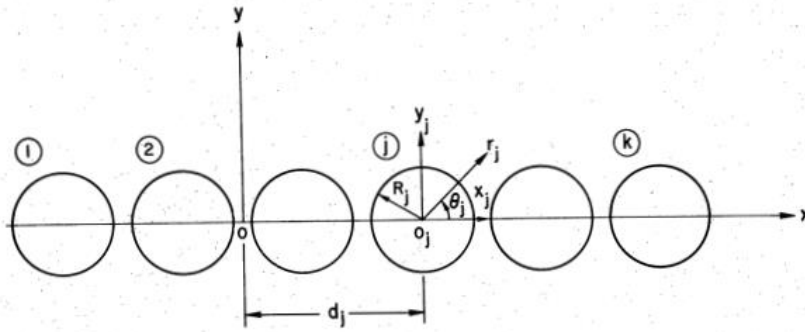
Figure 2.15. A row of circular cylinders vibrating in a fluid, adapted from Fig. 1 in Chen (1975a)
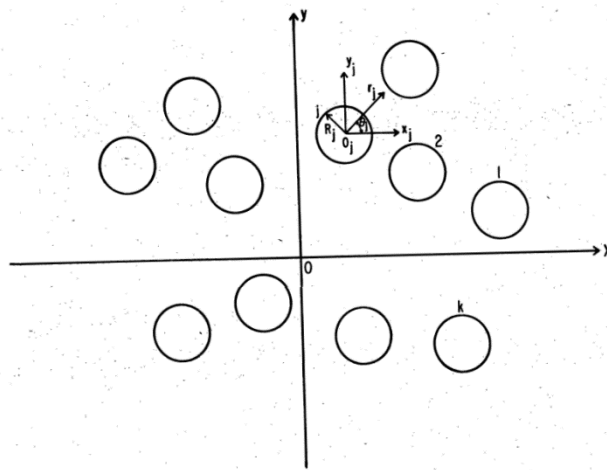
Figure 2.16. A group of circular cylinders vibrating in an infinite fluid, adapted from Fig. 1 in Chen (1975b)
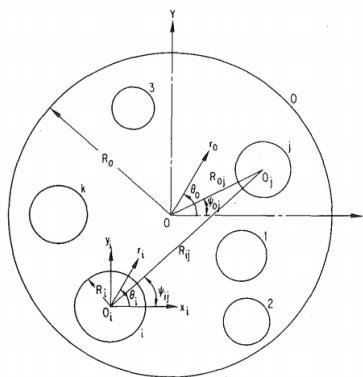
Figure 2.17. A group of circular cylinders vibrating in a fluid containing confining cylinder, adapted from Fig.1 in Chung and Chen (1977)

Chen and Rosenberg (1975) analyzed the dynamic behavior of two circular cylindrical shells separated by a narrow fluid gap as shown in Figure 2.18. The interaction of the shell system with the annular fluid couples the responses and leads to a fundamental natural frequency that is lower than that of the individual shells (filled with fluid). The authors considered the lateral, circumferential, and axial modes of the shells and derived an exact frequency equation for a general case (in terms of fluid properties) and an approximate closed form solution of the equation disregarding fluid compressibility.
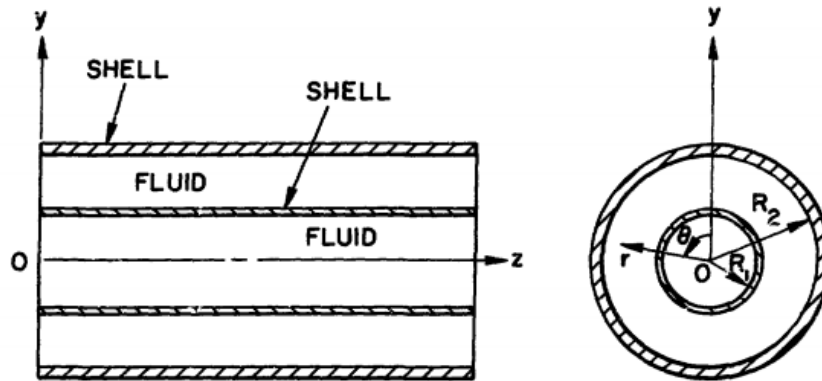
Figure 2.18. A coupled fluid-shell system, adapted from Fig. 1 in Chen and Rosenberg (1975)

Au-Yang (1976) analyzed the case of three fluid-filled, finite-length coaxial cylinders. The outer cylinder was assumed to be rigid and the inner cylinders were assumed to be flexible. The fluid was treated as compressible and inviscid. Results of analysis of one case, considering only one inner cylinder, were compared with experimental data. The author concluded that the agreement between theory and the experiment was good.

Dong (1978) presented a summary of methods used in the nuclear industry for the seismic design of individual and multiple submerged components. The report by Dong (1978) is referenced in ASCE/SEI 4 (ASCE 2017) that provides provisions and commentary for the seismic analysis of safety-related nuclear structures.

Williams (1986) presented an analytical solution for the dynamic response of a surface-piercing, vertical, circular cylinder of uniform flexural rigidity, fixed at the base and immersed in a compressible and infinite fluid domain undergoing small amplitude motion, as shown in Figure 2.19. The author neglected convective response in the analysis and modeled the partially-submerged cylinder as a one-dimensional beam.

27

Chilukuri (1987) conducted a finite element study using the computer program "USHA" for evaluation of added mass and fluid damping coefficients for the vibrations of a cylinder enclosed by a fluid-filled outer cylinder as shown in Figure 2.20. The author used nine-node, quadrilateral elements to model the fluid domain and solved the weak form of the governing Navier-Stokes equations for incompressible flow. The study reports that fluid damping coefficients increase with increasing vibration amplitude and that added mass coefficients may first decrease and then increase with an increasing vibration amplitude.
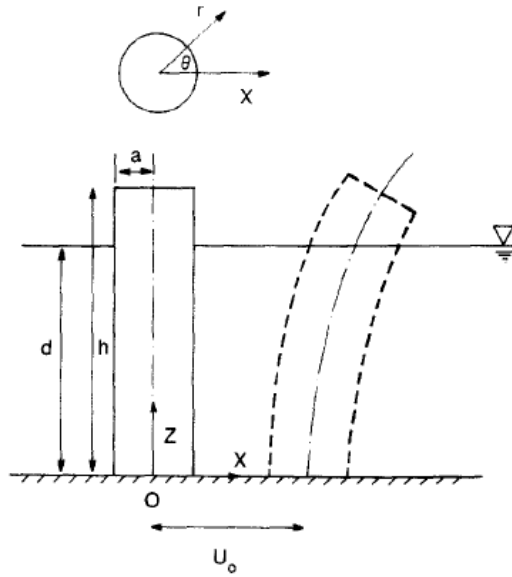
Figure 2.19. Fluid surface-piercing, vertical, circular undergoing small amplitude irrotational motion, adapted from Fig. 1 in Williams (1986).
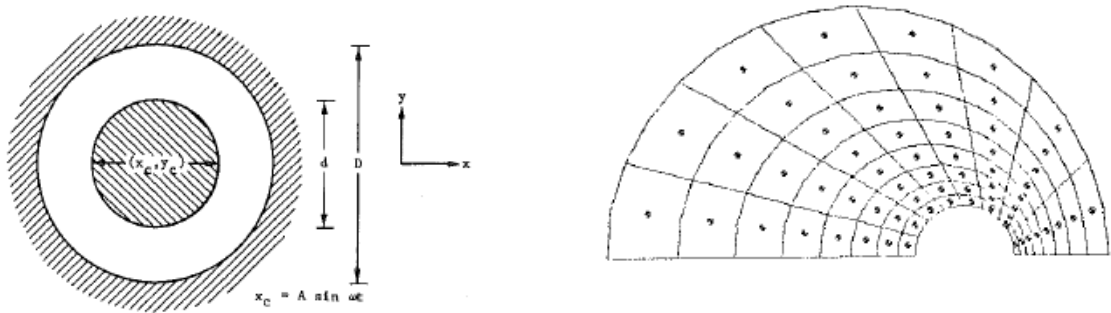
(a) cylinder within an annulus

(b) typical deformed mesh due to lateral motion of the cylinder

Figure 2.20. Vibrations of a cylinder within a fluid annulus using finite elements, adapted from Fig. 1 and Fig. 8 in Chilukuri (1987)

28

Jhung (1996) analyzed a lumped mass model (*stick* model) representative of reactor vessel internals and a core structure, with and without consideration of hydrodynamic effects. The author used the approach of Fritz (1972) to develop the hydrodynamic mass matrix for the submerged components and noted that seismic responses are greater when hydrodynamic effects are considered.

Mitra and Sinhamahapatra (2007) presented a finite element study addressing the seismic response of base-mounted, rectangular components submerged in a rectangular vessel, as shown in Figure 2.21. The vessel and the submerged component were considered to be rigid. The authors described a pressure-based, finite element formulation that was used to solve for the hydrodynamic responses to seismic excitations and presented parametric studies to investigate the effect of the height, width, and location of the submerged component. The authors reported a reduction in the fundamental sloshing frequency with an increase in the ratio of the height of the submerged rectangular block to the water depth. The peak amplitude of wave motion near the vessel wall decreased with increasing height of the submerged component. Increasing the height of the submerged component, led to a decrease (increase) in hydrodynamic pressure on the tank wall (component). The maximum amplitude of the waves was not significantly affected by the location of the submerged component (centered and off-center) for the cases considered.
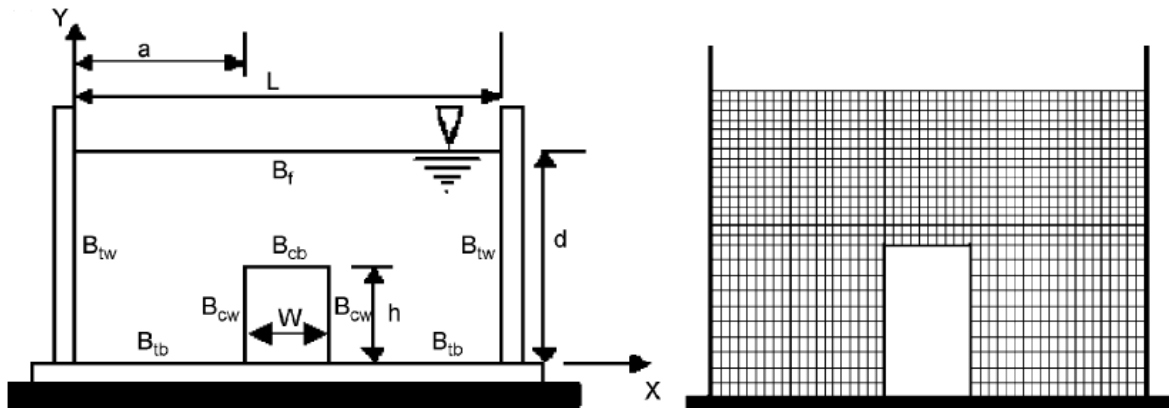
Figure 2.21. Submerged component in a rectangular tank and the mesh used for analysis, adapted from Fig. 1 in Mitra and Sinhamahapatra (2007)

Frano and Forasassi (2009) performed a finite element analysis of an experimental reactor (eXperimental Accelerator Driven System, XADS) considering internal components and their interactions with the liquid lead coolant. The authors performed eigen value analyses (with and without the coolant), sloshing analyses, and buckling analyses. Frano and Forasassi concluded that the frequencies of the internal components

reduced significantly in the presence of the coolant and that the sloshing response is influenced by the presence of internal components.
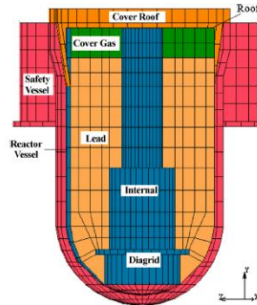
Figure 2.22. Finite element model, adapted from Fig. 3 in Frano and Forasassi (2009)

Yamada *et al.* (2018) validated two numerical models for evaluation of the dynamic response of fuel assemblies in a boiling water reactor. The first was a three dimenional model with acoustic elements for simulation of fluid behavior (Model A). The second utilized beam elements with added mass representing the fluid (Model B). Numerical predictions of deflection time series of fuel assemblies were compared with data from a test performed in 1986, as shown in Figure 2.23. The input excitation in the test (and the numerical models) was an artificially generated motion with frequency content in the range of 3 to 12 Hz. The full scale set-up, as shown in Figure 2.24, included 368 fuel assemblies, control rods and their drive mechanisms (Watabe *et al.* 1989). The specimen was tested for a combination of horizontal and vertical accelerations. Two earthquake inputs were used for testing and the structural integrity of the internals and control rod scrammability were verified for different intensities of both motions (Sato *et al.* 1989).

(a) numerical results   (b) test results
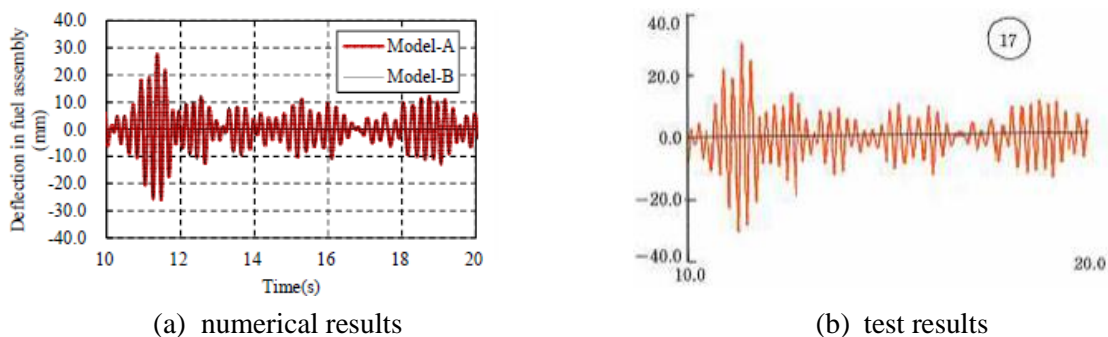
Figure 2.23. Deflection of fuel assembly in under seismic excitation, numerical and experimental results, adapted from Figure 8 in Yamada *et al.* (2018)
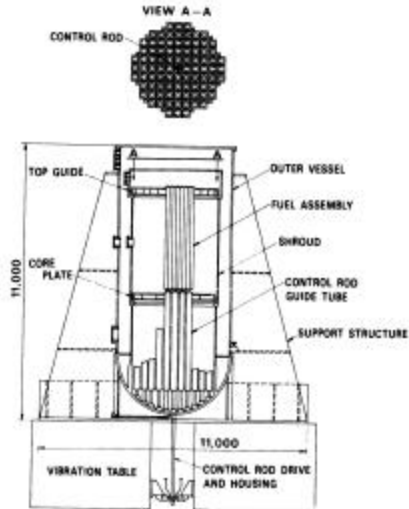
Figure 2.24. Test specimen, adapted from Fig. 1 in Watabe *et al.* (1989)

2.5   Review of experimental studies for seismic response of submerged internals

Clough (1960) conducted an experimental study to evaluate added mass for simple, prismatic structures subjected to earthquake ground motion. He tested two series of models on a one-dimensional earthquake simulator. The first series consisted of rigid prismatic aluminum members having different cross-sections mounted horizontally on flexible *legs*, as shown in Figure 2.25. The second series consisted of tests of flexible vertical cantilever columns of different cross sections. The test specimens were attached to the earthquake simulator and surrounded by a fluid (water) that was contained using ply wood walls at the perimeter of the earthquake simulator. The fundamental frequencies of the submerged components were identified. Tests were also conducted in air with additional masses attached to the component to achieve the same natural frequency as in the submerged state. Clough reported added mass coefficients (defined as the ratio of the added mass to the mass of water displaced by a right circular cylinder with a diameter equal to the maximum transverse dimension of the model) for the tested specimen.
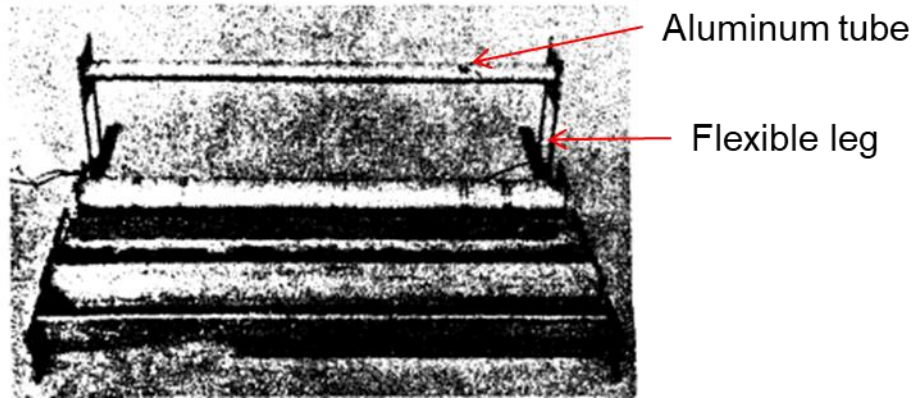
Figure 2.25. Horizontal aluminum tubes used for testing, adapted from Fig. 2 in Clough (1960)

Lindholm *et al.* (1965) performed an experimental study on cantilever plates in air and water, and compared results with theoretical predictions obtained from beam theory and thin plate theory, both modified to include added masses calculated using a hydrodynamic theory. The authors studied the vibration of plates with ratios of width to length of between 0.5 and 5, and thickness-to-width of between 0.009 and 0.124. An empirical factor, correcting for the influence on added mass of plate aspect ratio and thickness, was introduced. The authors concluded that the dynamic characteristics of the horizontally vibrating plate are only affected if the depth of immersion was less than about one-half of the plate span. The dynamic characteristics of a partially immersed vertical plate were dependent on the immersion depth and the mode of vibration.

Chen *et al.* (1977) conducted experiments on different submerged tube arrays with different patterns and gaps between adjacent tubes to validate solutions for frequencies and mode shapes developed by Chen and his co-workers, as discussed in section 2.4. Four series of tube arrays were tested. The arrangements of the tubes were: (1) five tubes in a row with the gap to tube radius ratio equal to 2.0, 1.0, and 0.25; (2) three-tube arrays in staggered arrangements with gap to tube radius ratio equal to 2.0, 1.0, and 0.5; (3) seven-tube arrays in staggered arrangements with gap to tube radius ratio equal to 1.5, 1.0, and 0.4; and. (4) a four-tube array in a square pattern with a gap to tube radius ratio of 0.5. The fourth series was tested under five different conditions: (a) fully submerged in a large water domain, (b) partially submerged in water; (c) near a rigid flat wall; (d) contained in a rigid circular cylinder; and (e) fully submerged in a fluid of high viscosity (mineral oil). The arrangements used in the four series are shown in Figure 2.26 and some tested elements are shown in Figure 2.27. An electromagnetic shaker was used to excite the tubes in the submerged state. Tube acceleration time series were measured to obtain frequencies of the tubes and the mode shapes of the arrays. The authors concluded that the experimental data and analytical predictions were in good agreement.
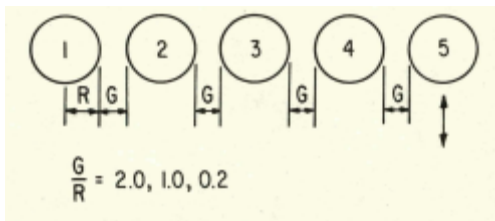
(a) five tube row
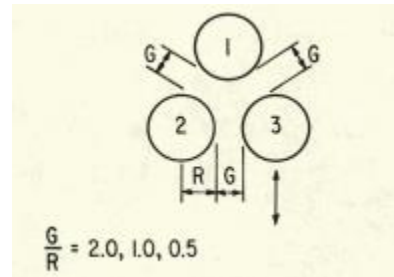
(b) three tube array
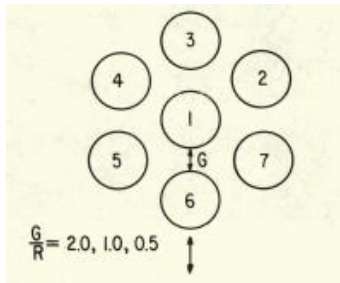
(c) seven tube array
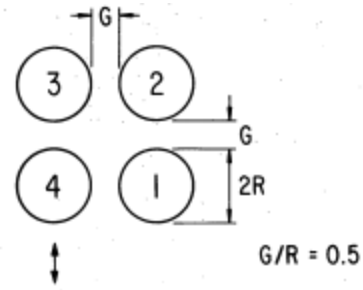
(d) four tube array

Figure 2.26. Tested tube arrays, adapted from Fig.2 in Chen *et al.* (1977)
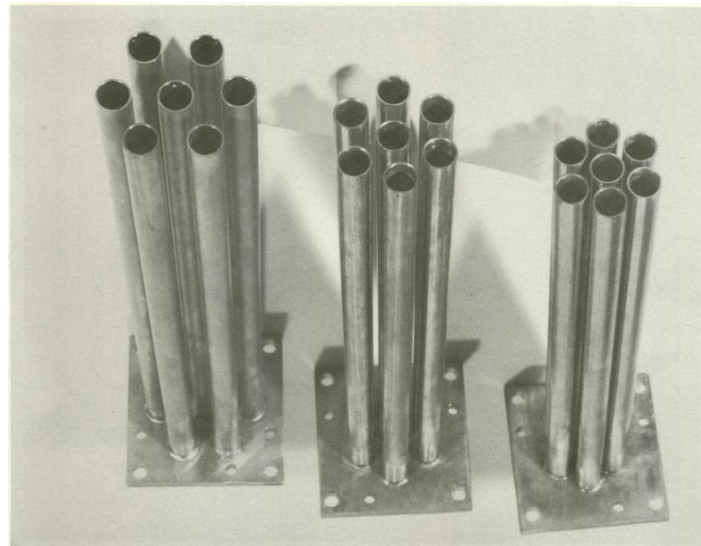
Figure 2.27. Tested seven-tube arrays, adapted from Fig.3 in Chen *et al.* (1977)

Moretti and Lowery (1976) evaluated added mass for a submerged, transversely vibrating tube. The vibrating tube was surrounded by rigid tubes in hexagonal and square arrays with pitch-to-diameter ratios ranging from 1.25 to 1.5, as shown in Figure 2.28. The vibrating tube was supported by reproducible boundary conditions whereas the surrounding tubes were rigidly attached at multiple locations along their

length (see Figure 2.29). Moretti and Lowery presented experimental data and derived added mass coefficients for the vibrating cylinder and different pitch-to-diameter ratios. The added mass coefficients for the vibrating tube decrease with increasing pitch-to-diameter ratio in both arrays. The coefficients for the hexagonal array were greater than for the square array in most cases.
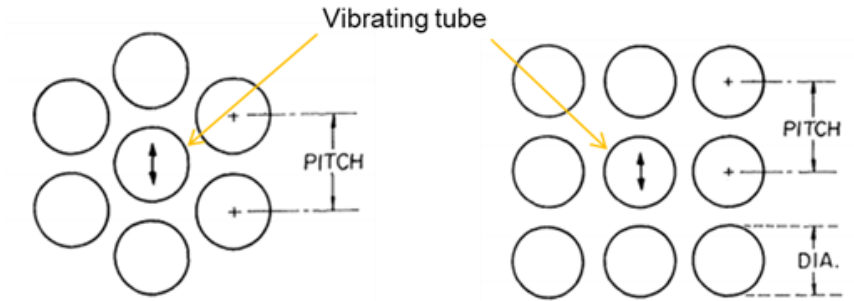
Figure 2.28. Experimental geometries, adapted from Fig. 1 in Moretti and Lowery (1976)
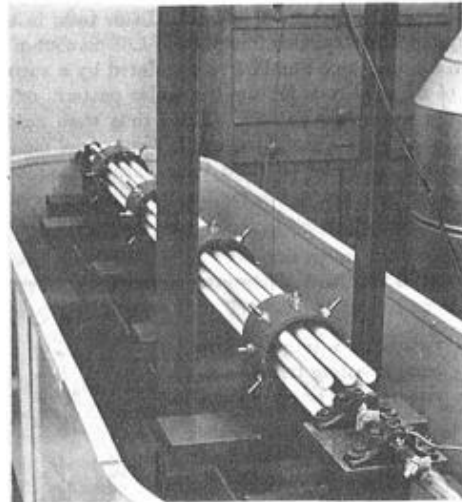
Figure 2.29. Experimental apparatus, adapted from Fig. 3 in Moretti and Lowery (1976)

Maheri and Severn (1992) performed experiments to evaluate added masses for three, base-supported, cylindrical steel models, as shown in Figure 2.30. Experiments were conducted with the models containing water or surrounded by water. The natural frequencies of the cylinders were evaluated numerically using FE software based on a Eulerian formulation in which the fluid motion is expressed by a pressure variable. The authors concluded that for multi-degree-of-freedom systems, the added mass is a function of the geometry of the body, the density of the fluid, and the modal properties. (Namely, the added mass calculated for the first mode should not be used for analysis of higher modes.)
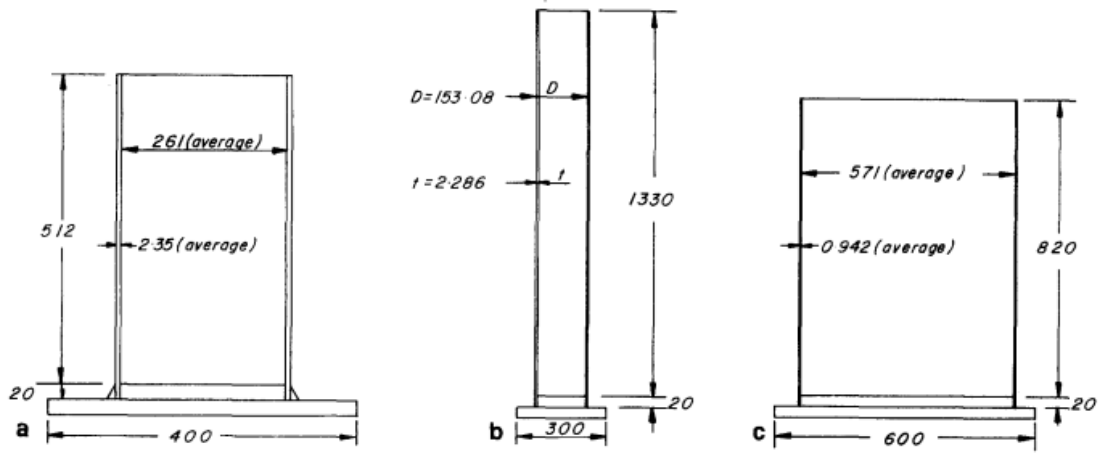
Figure 2.30. Geometry of the tested cylindrical models, adapted from Figure 1 in Maheri and Severn (1992), dimensions in mm

Sinha and Moorthy (1999) conducted tests on perforated tubes representative of submerged structural components in Indian nuclear power plants to evaluate added mass coefficients. The specimens included: 1) a Zircaloy tube of 91 mm outer diameter and 6.57 m length with 1392 perforations of 6 mm diameter at different pitches; 2) a Zircaloy tube of 120 mm outer diameter and 4.98 m length with 1350 perforations of 12 mm diameter, 750 perforations of 10 mm diameter and 720 perforations of 8 mm at different pitches; and 3) an aluminum tube of 12.23 mm diameter and 273 mm length with 14 perforations of 6.11 mm diameter distributed along the length of the tube at an axial and circumferential pitch of 18 mm and 9.6 mm, respectively. The tested specimens are shown in Figure 2.31. The added mass was smaller for the perforated tube than that predicted by theory for a hollow tube. The authors claimed that flow through the perforations reduces the added mass. An empirical formula was proposed to calculate added mass coefficients for perforated tubes. The added mass for a perforated tube, M_f, was expressed as:

$$M_f = (V_{in} + V_{out} - V_h)\rho_f \tag{2.8}$$

where V_{in} is the volume of the fluid inside the tube, V_{out} is the volume of fluid equivalent to outer volume of tube, V_h is the volume of fluid that does not move (due to perforations), and ρ_f is the fluid density. V_h is expressed as:

$$V_h = \sum_{i=1}^{n} A_i L_i \tag{2.9}$$

where A_i is the projected cross-sectional area of the ith perforation on a plane transverse to the vibration direction, L_i is the chord length of the tube at the ith location, and n is the total number of perforations.

Deng *et al.* (2017) presents an experimental and numerical study of fluid-structure interaction of a slender bridge pier, of rectangular cross-section, in water. A drawing of the experimental setup is presented in Figure 2.32. The authors created a numerical model of the pier in ADINA (ADINA 2013) and used modal frequencies and mode shapes as parameters for validation. Experiments and numerical studies for different levels of water and additional mass attached at the tip of the pier are described. An analytical treatment of a similar system is presented in Uściłowska and Kołodziej (1998), where the focus was off-shore structures.
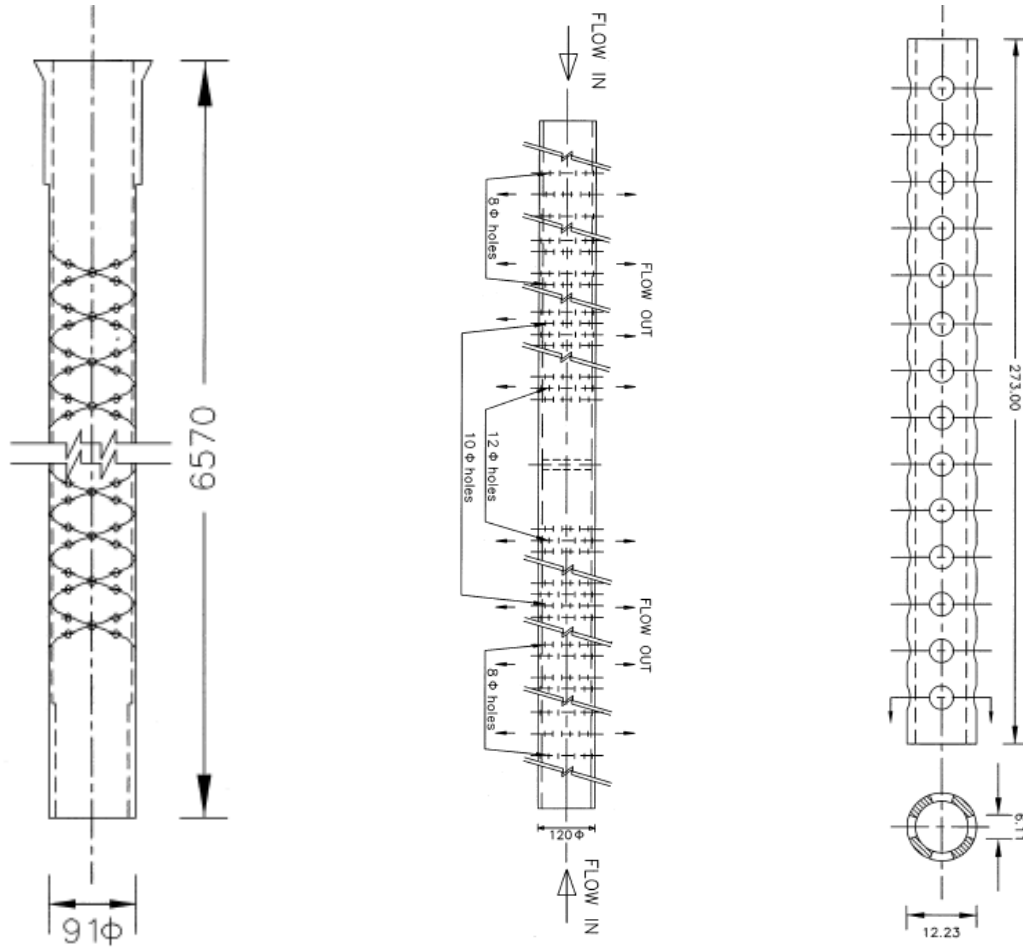
Figure 2.31. Tested perforated tubes, adapted from Fig. 1, 5, and 9 in Sinha and Moorthy (1999)
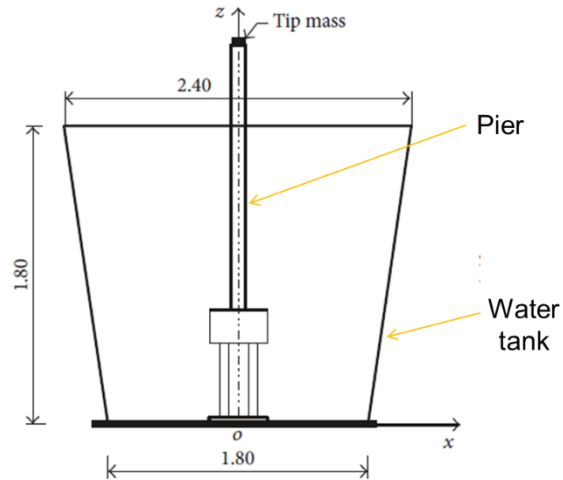
Figure 2.32. Experimental setup, adapted from Figure 2 in Deng *et al.* (2017)

Park *et al.* (2014) describes an experimental and numerical study of the dynamics characteristics of the Korean APR1400 nuclear reactor. A scale model of the reactor vessel including internals was tested and water was used to represent the coolant. Dynamic characteristics were identified for individual components and the integrated model, with and without water. A finite element model of the test specimen was prepared in ANSYS and calibrated using the test results for modal frequencies and mode shapes. Figure 2.33 presents the test specimen and the finite element model. In subsequent studies, Choi *et al.* (2016) and Lee *et al.* (2017) applied model reduction techniques to the ANSYS model to reduce the computational expense for response-history analyses and carried out stress analyses. Je *et al.* (2017) compared results of analysis using the finite element model and explicit modeling of fluid with a simplified model utilizing added masses for the fluid. The authors concluded that the added mass model overestimated material stresses.
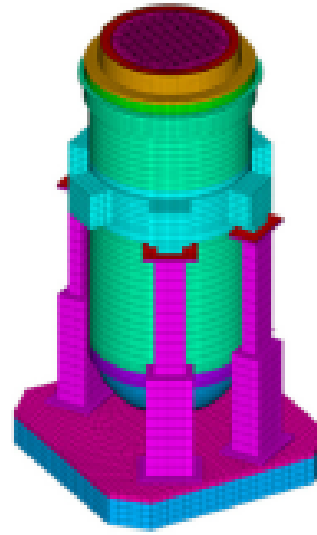
<table>
<tr><td>(a) test specimen</td><td>(b) finite element model in ANSYS</td></tr>
</table>

Figure 2.33. Experimental and numerical study of a scaled model of APR1400 reactor, adapted from
Fig.4 and Fig.7 in Park *et al.* (2014)

2.6   Review of studies on seismic isolation of fluid-filled vessels

The only experimental studies on isolated fluid-filled vessels in the literature are by Chalhoub and Kelly (1988) and Calugaru and Mahin (2009). These were discussed in Section 2.3. Most of the available studies on analysis of seismically isolated fluid-filled containers involve numerical estimation of responses, often utilizing mechanical analogs to represent fluid behavior.

An isolation scheme wherein a fluid containing tank is supported on a large concrete mat which in turn is supported on multiple isolators was proposed by Kelly and Mayes (1989) and numerically analyzed by Tajirian (1993) and Zayas and Low (1995) using rubber bearing and friction pendulum bearings, respectively. Malhotra (1997) proposed an isolation scheme in which the tank wall is disconnected from the base plate of the tank and supported on a ring of horizontally flexible isolators. A flexible membrane between the wall and the base plate is used to prevent leakage of the fluid (see Figure 2.34a). Malhotra performed seismic FSI analysis for this system using a mechanical analog comprising one impulsive and one convective oscillator (to represent fluid behavior per Veletsos (1984)) mounted on a base resting on elastomeric isolators, as shown in Figure 2.34b. Two tanks, one broad and one slender, with a ratio of fluid height-to-radius of 0.6 and 1.85, respectively, were considered and the analogs were analyzed using the code 3D-BASIS-M (Tsopelas *et al.* 2005). Seismic isolation significantly reduced the global tank reactions of base shear and overturning moment. However, because the gravity weight of the fluid was not supported by the bearings, the bearings beneath the slender tank experienced net tension.
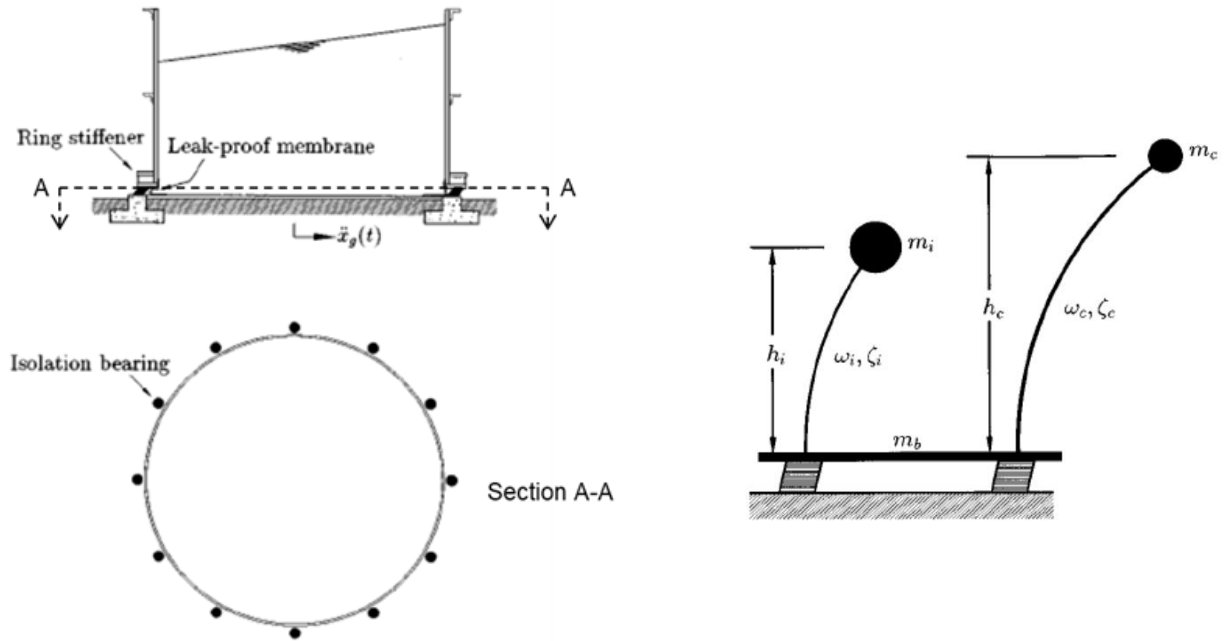
(a) fluid storage tank with a ring of isolators   (b) mechanical analog

Figure 2.34. Isolation scheme proposed by Malhotra (1997), adapted from Figure 1 and Figure 2 in
Malhotra (1997).

Wang *et al.* (2001) analyzed a fluid-filled, rigid tank seismically isolated using friction pendulum bearings. The model comprised multiple oscillators representing the fluid whose properties were derived using an approach similar to that of Veletsos (1984). Figure 2.35 presents the model. The authors described a numerical scheme for evaluating responses of fluid-filled tanks under seismic inputs and present results of a parametric study on a rigid tank with a ratio of fluid height to radius of 2 considering different values of $PGA/\mu g$, where PGA, μ, and g are the peak ground acceleration, the coefficient of sliding friction (of the bearings), and the acceleration due to gravity, respectively. Seismic isolation was found to be effective in reducing the impulsive responses with possible reductions up to 80%. The efficacy of isolation, measured in terms of reductions in responses, increased with increasing $PGA/\mu g$.
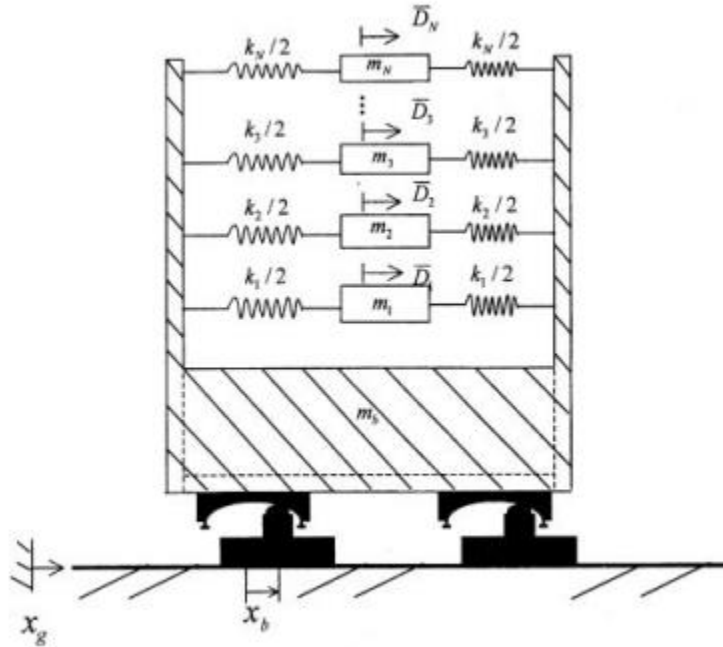
Figure 2.35. Fluid-filled vessel isolated using friction pendulum bearings, adapted from Figure 2 in Wang *et al.* (2001)

Shrimali and Jangid (2002) analyzed the response of fluid-filled tanks with ratio of height-to-radius of 0.6 and 1.85, isolated using sliding bearings. The fluid was represented by a mechanical analog (Housner 1963). Bi-directional (horizontal) inputs were used and the effects of interaction of frictional forces in the two horizontal directions and the velocity dependence of the frictional forces in the two directions were studied. The authors concluded that isolating tanks led to reductions in base reactions. Interaction between frictional forces in the two horizontal directions resulted in greater isolator (sliding) displacements. The dependence of the friction coefficient on sliding velocity had no significant effect on peak system responses.

Gregoriou *et al.* (2006) analyzed the seismic response of base-isolated, liquefied natural gas (LNG) tanks in ANSYS. High damping rubber and lead-rubber bearings were considered for the isolation system, which had a period of 2 seconds. The contained fluid was modeled explicitly. The vertical stiffness of the isolation system was modeled using linear spring elements. The horizontal stiffness of the isolators was modeled using a combination of a non-linear spring and a damper. Figure 2.36 describes the model. The authors reported a 70% (60%) reduction in base shear force (maximum stress in in tank shell) in the base-isolated condition with respect to the fixed base condition. Increased wave heights were predicted for both isolation systems.

40
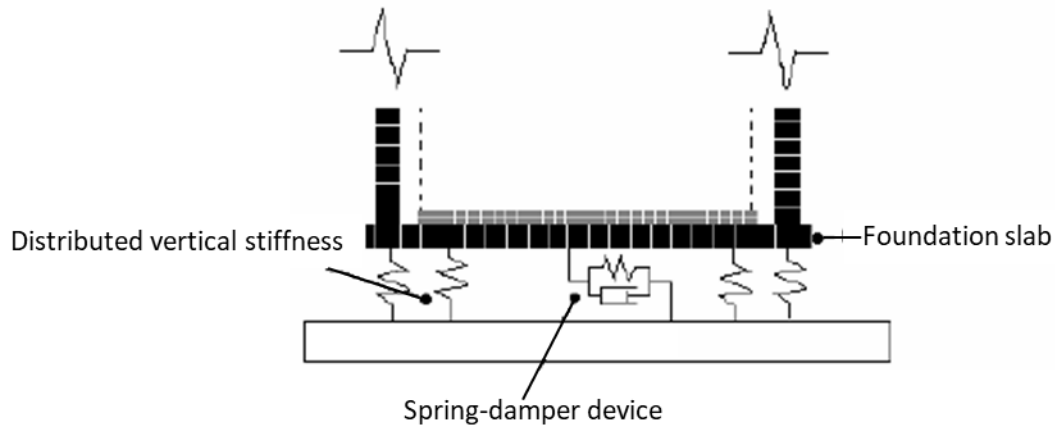
Figure 2.36. Model of the isolation system in an LNG tank, adapted from Figure 2 in Gregoriou *et al.* (2006)

Christovasilis and Whittaker (2008) evaluated the accuracy of the Malhotra mechanical analog for analysis of conventionally founded and seismically isolated LNG tanks by comparing analysis results with a three-dimensional finite element model built in ANSYS. The average percentage differences between results from ANSYS and the mechanical analog for wave height, base shear, and overturning moment were found to be less than 6%. They noted the mechanical analog could be used for the preliminary design of tanks, conventionally founded or seismically isolated. Two isolation systems, with periods of 2 sec and 3 sec, were analyzed. The mean percentage reductions in base shear and overturning moment were 80% and 82%, respectively, for the 2-second isolation system and 85% and 86%, respectively, for the 3-second isolation system. The first convective period of the LNG tank (9+ sec) was remote from the isolated periods and so sloshing responses were not impacted by the introduction of the isolation systems.

Saha *et al.* (2013) analyzed conventionally founded and seismically isolated tanks with ratios of fluid height-to-radius of 0.6 and 1.85. Two mechanical analogs were used to represent the fluid: a two-mode mechanical analog that considered the tank to be rigid (Housner 1963) and a three-mode mechanical analog considering tank wall flexibility (Haroun and Housner 1981b). Two isolation systems, comprising elastomeric and spherical sliding (friction pendulum) bearings, both with an isolated period of 2 sec, were analyzed for bi-directional motions. The authors concluded that the two-mode model underestimated base reactions.

Butenweg *et al.* (2013) present a finite-element model of a base-isolated, fluid-filled tank developed in the finite element package LS-DYNA (LSTC 2017). The lead-rubber base isolation system was idealized using springs and dampers at the base of the tank. The fluid was modeled using the Arbitrary Lagrangian Eulerian

41

(ALE) formulation. An artificially generated seismic excitation, consistent with a Eurocode 8 spectrum, was applied in one horizontal direction at the base of the model. The isolation system was assumed to be rigid in the vertical direction. Results from the finite element analysis, in terms of stresses in the tank wall, were compared with those from a simplified analysis utilizing a two-mass representation, (impulsive component mass and foundation mass), disregarding sloshing, as shown in Figure 2.37, for calculation of seismic demands. (The stress calculations using the simplified model were undertaken per Eurocode 8.) The authors concluded that the results from the two analyses were in good agreement.
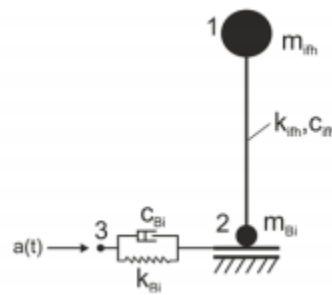
Figure 2.37. Simplified model of the isolated fluid-filled storage tank, adapted from Figure 6 in Butenweg *et al.* (2013)

Castellano and Marcolin (2017) evaluated the effectiveness of an isolation system comprising 121 double concave spherical sliding (friction pendulum) bearings to seismically protect an ammonia tank with a diameter of 29.9 m and a design fluid height of 31 m. Unidirectional, horizontal seismic inputs were used for analysis. The global behavior of the isolation system was represented by a non-linear element and the fluid was represented a two-mode mechanical analog. The horizontal acceleration of the impulsive mass was reduced to less than one half of the peak ground acceleration by the isolation system.

SECTION 3

SEISMIC RESPONSE OF A BASE-SUPPORTED VESSEL: EXPERIMENTAL STUDIES

3.1   Introduction

Seismic responses of liquid-filled advanced reactors are affected by the interaction between the vessel, contained liquid, and internal components, namely fluid-structure interaction (FSI). Seismic FSI analysis of reactors will rely on numerical models, considering complex geometries (see Figure 1.1), multiple components of earthquake shaking, and possible nonlinear fluid responses. Numerical models must be verified and validated. A numerical model can be verified by comparing predictions with analytical solutions and validated using experimental data. This section describes earthquake-simulator experiments on a base-supported vessel that both support validation of FSI numerical models and investigate the efficacy of seismic isolation in reducing hydrodynamic responses.

A base-supported cylindrical vessel was tested using a six-degree-of-freedom earthquake simulator at the University at Buffalo. The vessel was fabricated from carbon steel and filled with water. The dimensions of the vessel were selected based on the capacity of the earthquake simulator and a ratio of height-to-radius that is common to some prototype advanced reactors. A two-phase program of experiments was performed: I) test vessel, and II) test vessel sealed with a head that supported central and off-center internal components immersed in the contained fluid. One-, two-, and three-directional motions with a range of intensities and frequency contents, which generated different hydrodynamic responses, were used as seismic inputs in the Phase I and II tests. This section presents the test setup and results for Phase I, which are used to validate numerical models in Section 4. (Details of the Phase II tests and validation exercises are presented in Section 5 and Section 6.)

Section 3.2 describes the test specimen and the instrumentation. Section 3.3 presents the input motions used for the experiments. Section 3.4 presents experimental results in terms of sloshing frequency, damping ratios in sloshing modes, and hydrodynamic responses (wave height, hydrodynamic pressure, base shear, and base moment), and compares them with available analytical solutions. Section 3.5 studies the impact of seismic isolation on hydrodynamic responses by comparing experimental results for ground-motion inputs and *isolated* inputs that were generated assuming a virtual isolation system. Section 3.6 summarizes the Phase I test program and presents conclusions.

3.2   Test specimen and instrumentation

The test specimen was a base-supported cylindrical vessel with a height of 2 m, a radius of 0.76 m, and a wall thickness of 7.9 mm, as shown in Figure 3.1a. The vessel was supported on a 45 mm thick square base plate with plan dimensions of 2 m × 2 m. A 76.2-mm wide, 25.4-mm thick flange was welded to the top of the vessel. The weight of the specimen (without contained water) was 2.1 tons. Experiments were conducted with the vessel filled to 80% and 100% of its capacity, which added weights of 2.9 tons and 3.6 tons, respectively, to the specimen. The full vessel (100% filled) was enclosed at the top by a 25.4 mm thick square plate with plan dimensions of 1.7 m × 1.7 m and a weight of 0.6 ton. The weight of the 80%-filled specimen was 5 tons (i.e., 2.1+2.9), and that of the 100%-filled specimen, including the top plate, was 6.3 tons (i.e., 2.1+3.6+0.6). The coordinate systems used for the test vessel are presented in Figure 3.1b: a cylindrical coordinate system (r, θ, z) and a Cartesian coordinate system (x, y, z).

(a) specimen on the earthquake simulator (contained water dyed green)

(b) cylindrical (r, θ, z) and Cartesian (x, y, z) coordinate systems used for the test vessel
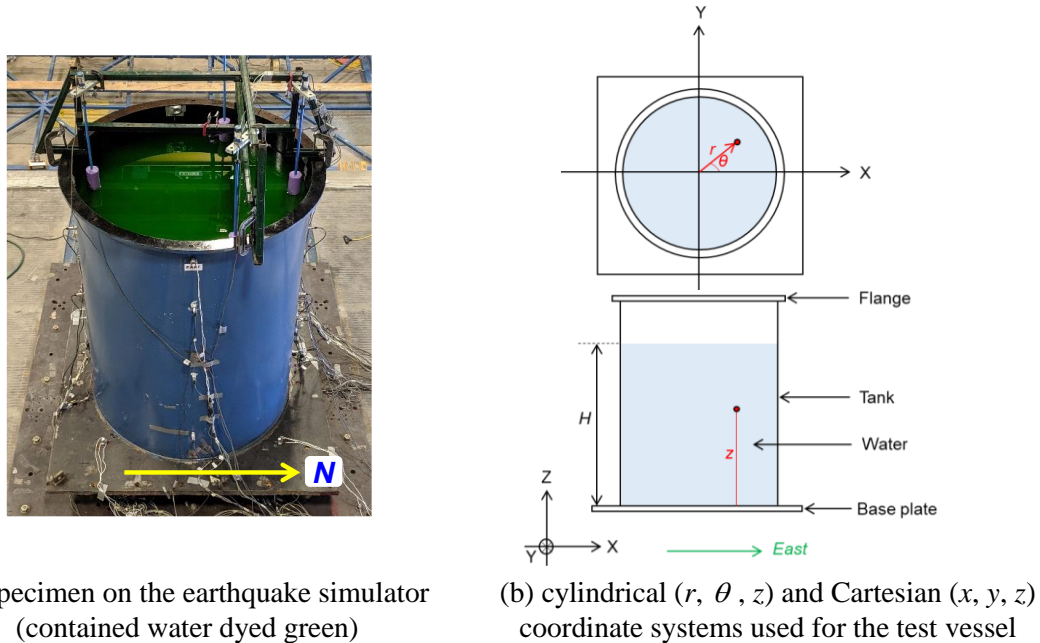
Figure 3.1. Base-supported cylindrical vessel ($H_s = 2$ m, $R = 0.76$ m, $h = 7.92$ mm), 80% fill level ($H = 1.6$ m)

Results from the experiments conducted for the 80% fill level are discussed and analyzed in the following sections (3.4 and 3.5). This choice of fill level was governed by two factors: (1) providing sufficient freeboard to prevent overtopping, and (2) ensuring measurable hydrodynamic responses. The numerical models presented in Sections 4.2 and 4.3 are validated using the measured hydrodynamic responses,

considering both impulsive and convective components[7]. The predicted periods of the first (lateral) impulsive and convective modes, $T_{imp,1}$ and $T_{con,1}$, are 0.01 sec and 1.29 sec, respectively ($f_{imp,1} = 1/T_{imp,1} = 140$ Hz and $f_{con,1} = 1/T_{con,1} = 0.77$ Hz), and are calculated using the following equations (Malhotra *et al.* 2000):

$$T_{imp,1} = C_i \frac{H\sqrt{\rho}}{\sqrt{\dfrac{h}{R}} \times \sqrt{E}} \tag{3.1}$$

$$T_{con,1} = C_c \sqrt{R} \tag{3.2}$$

where H is the water height; R is the vessel radius; h is the thickness of the vessel wall; ρ is the water density; E is the modulus of elasticity of the vessel material; and C_i and C_c are impulsive and convective coefficients, respectively, and vary as functions of H/R. The primary goal of the experiments conducted with a full tank was to generate hydrodynamic responses that precluded the convective component. Experimental results are used in Section 4.4 to investigate the capability of numerical models to accurately predict impulsive responses.

Two test setups (TSs) with different supporting conditions for the vessel were used: 1) TS-1, the base plate of the vessel was directly attached to the extension platform on the earthquake simulator; and 2) TS-2, load cells used to measure base reactions were installed between the base plate and the extension platform. (The extension platform was used to increase the effective working area of the earthquake simulator; see Figure C.1. The trade-off was a higher center-of-gravity of the test specimen with respect to the top of the earthquake simulator and greater rocking motions.) Hydrodynamic pressures on the vessel wall, reactions at the base, and wave actions (heights, frequencies, and damping) generated using TS-2 data are presented in this report. The TS-2 dataset is more comprehensive than the TS-1 dataset and so TS-1 results are not presented.

The instrumentation used for TS-2 is presented in Figure 3.2, including pressure gages, load cells, Temposonic gages, and accelerometers. (The instrumentation for TS-1 was by-and-large identical to that for TS-2 with the exception of the load cells and accelerometers on the base plate.) Twelve pressure gages (make: Omega, model: PXM309-3.5A10V) with silicon-based sensing diaphragms were used to measure hydrodynamic pressures on the vessel wall. The gages were arranged in arrays of four at three different

---

[7] The impulsive response is generated by the part of the fluid accelerating with the vessel, and the convective response is generated by the other part of the fluid assumed not to move with the vessel but to oscillate vertically and induce waves.

45

heights on the vessel wall with the sensors named as shown in Figure 3.2a. The pressure gages on the northern, southern, eastern, and western faces are denoted PN, PS, PE, and PW, respectively, and a number (1, 2, or 3) is appended to the name to identify height. Thus, PE1, PE2, and PE3 denote the lower, middle, and uppermost gages on the eastern face of the vessel.

Base reactions were measured at four anchor points using four 5-degrees-of-freedom load cells, built in-house. Each load cell is capable of measuring axial force, shear forces in two orthogonal directions, and moments about two axes. A NIST (National Institute of Standards and Technology) traceable reference load cell was used to calibrate the load cells in a tension-compression machine (Tinius Olsen Testing Machine Co.) prior to the experiments. Details of the calibration procedures and the associated data are presented in Appendix A. The load cells were tagged LNE, LNW, LSE, and LSW, denoting the locations at the north-eastern, north-western, south-eastern, and south-western corners of the base plate, respectively, as shown in Figure 3.2b.

Wave heights and sloshing periods were measured at four points on the water surface (for the 80% fill), near the vessel wall. Four float-and-Temposonic-based sensors, built in-house at the University at Buffalo were used for this purpose (Mir *et al.* 2019). The design of the wave measurement consisted of a float attached to a lightweight tube that is mounted onto the waveguide of a Temposonic gage. A magnet was attached to the top of the tube. The Temposonic gage recorded the vertical motion of the magnet, which was driven by the motion of the float. These sensors were installed on a Unistrut frame secured to the flange of the vessel, as shown in Figure 3.1a. Appendix B presents different options explored for wave-height measurement, including another in-house design, a commercial capacitive level sensor (make: Loadstar Sensors, model: ilevel-900-A), a wire gage sensor, and cameras supporting image processing for wave actions. The Temposonic-based gage was the most accurate of those considered and was adopted for use in the experiments. Figure 3.2c presents the locations of the sensors adjacent to the northern, southern, eastern, and western faces of the vessel wall, denoted as TN, TS, TE, and TW, respectively. Sensors TN and TS were located at $(r, \theta, z) = (0.67, 0.5\pi, 1.6)$ and $(r, \theta, z) = (0.67, -0.5\pi, 1.6)$, respectively, and TE and TW were located at $(r, \theta, z) = (0.67, 0.1\pi, 1.6)$ and $(r, \theta, z) = (0.67, 0.9\pi, 1.6)$, respectively, where r and z are in units of m.

Three-directional acceleration responses were measured at four locations at the top and near the mid-height of the vessel wall using accelerometers (make: Honeywell; model: JTF; range: ±10g). Each accelerometer measures motion in one direction and so three orthogonal accelerometers were installed at a given location. On the base plate, one accelerometer was installed at its center to measure vertical (z-directional) motion,

and three accelerometers were installed above each load cell to measure tri-directional response. The naming convention and the locations of the accelerometers are shown in Figure 3.2d.

Strain data were collected for the experiments but were not used for the analysis presented in this report. Eight strain rosettes (make: Micro-Measurements; model: CEA-06 250UR-120/P2) were attached on the outer face of the vessel wall, arranged in arrays of four at 50 mm and 1067 mm above the base. Eight waterproof uniaxial gages (make: Texas Measurements Inc.; model: WFLA-3-11-1LDBB) were installed on the inner face of the vessel wall at the same heights as the rosettes on the outer face to capture strain gradients through the wall thickness.

(a) pressure gages   (b) load cells   (c) wave-height sensors

(d) accelerometers
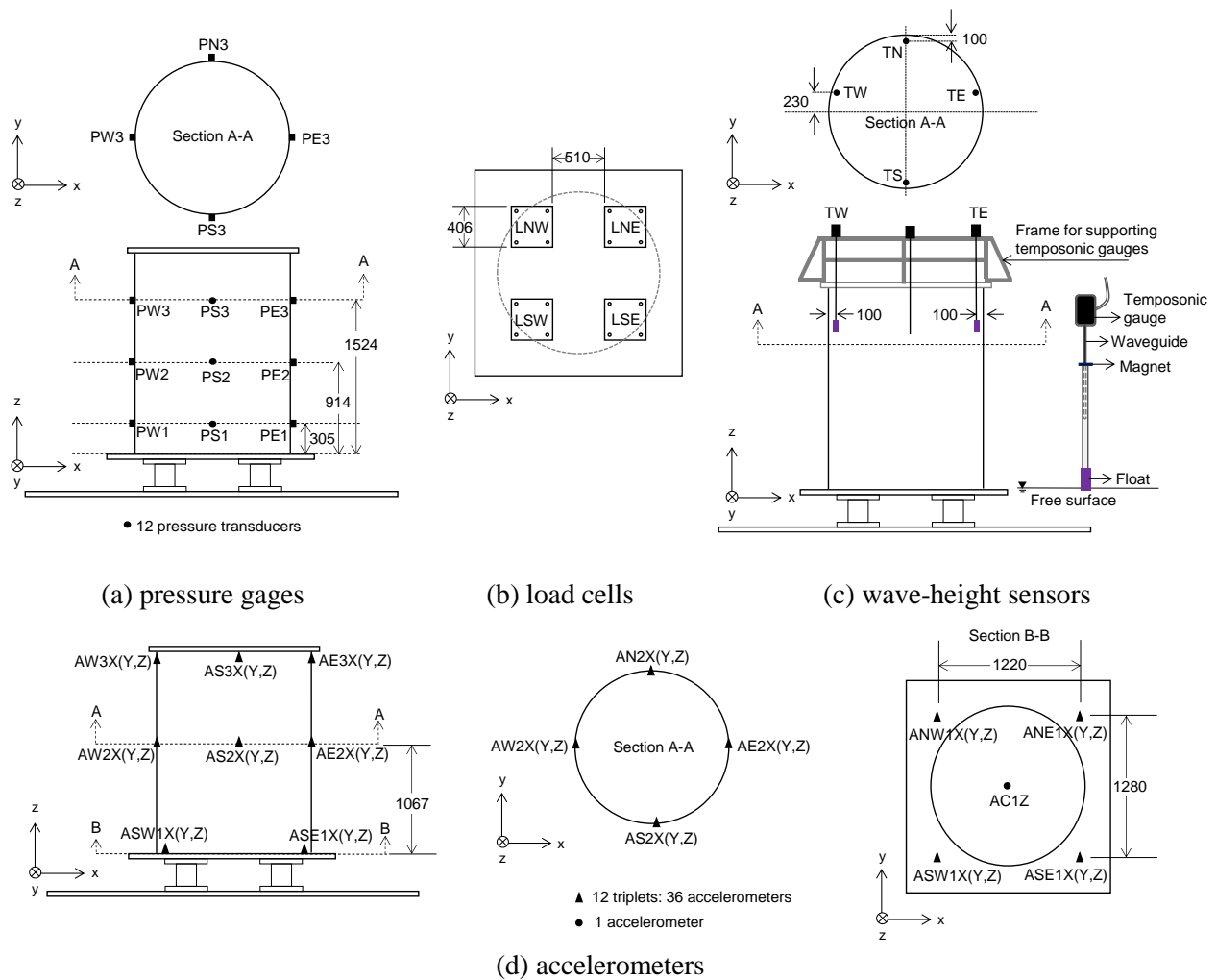
Figure 3.2. Instrumentation for the vessel used in TS-2 and Phase I, unit: mm

3.3　Earthquake-simulator inputs

Phase I of the earthquake-simulator experiments involved 182 sets of input motions, including 68 sets for TS-1 and 114 sets for TS-2. The input motions included white noise, sine waves, earthquake time series extracted from ground motion records, and *isolated* motions (see Section 3.5.1 for details). The input motions for TS-1 and TS-2 are presented in Appendix C. The hydrodynamic responses of the test vessel to motions listed in Table C.3 for TS-2 are presented in this report: (1) results for motions #2, 9 to 11, and 74, 76, 77, 78, 80, 81, 83, 85, and 86 are compared with analytical predictions in Section 3.4; and (2) results for motions #74, 76, 77, 80 to 82, and 85 to 114 are presented in Section 3.5 to study the effect of seismic isolation on the hydrodynamic responses.

Of the inputs utilized in Section 3.4, motions #2, 9, 10, and 11 are unidirectional white noise or sinusoidal used to drive wave actions in the test vessel and identify the frequencies and damping ratios in the convective modes. Motions #74, 76, 77, 78, 80, 81, 83, 85, and 86 are earthquake time series extracted from records of the unidirectional (x), bi-directional (x and y), and tri-directional (x, y, and z) components of the Chi-Chi earthquake (CCE), the El Centro earthquake (ECE), and the Kern County earthquake (KCE). Table 3.1 presents information on these earthquake motions. The time scale of each earthquake motion was compressed per the assumed length scale of the test vessel (see the eighth column of Table 3.1). The peak ground accelerations (PGAs) of the x components of the CCE, ECE, and KCE were initially scaled to 0.1 g, 0.5 g, and 0.4 g, respectively (see the seventh column of Table 3.1). The y and z components of each earthquake set were scaled using the scale factors for the x component. The scaling amplified the ECE and KCE motions, but de-amplified the CCE to prevent sloshing of the contained water and overtopping of the vessel. Figures 3.3 and 3.4 presents their time series and 5%-damped response spectra, respectively, after the time and amplitude (PGA) scaling. Per Figure 3.4, the chosen motions have different frequency contents: the horizontal components of the CCE have a dominant low frequency content (< 10 Hz) whereas those of the ECE and KCE have dominant frequency content around and above 10 Hz.

Table 3.1. Time series[1] used for earthquake-simulator experiments, motions #74, 76, 77, 78, 80, 81, 83, 85, and 86

	Event	Year	Station	Direction	Original PGA (g)	Scaled PGA (g)	Time scale[2]
CCE	Chi-Chi earthquake	1999	TCU052	EW (x)	0.36	0.1	$1/\sqrt{10}$
				NS (y)	0.45	0.12	
				Up (z)	0.19	0.05	
ECE	El Centro earthquake (Imperial Valley-02)	1940	El Centro Array #9	180 (x)	0.28	0.5	$1/\sqrt{10}$
				270 (y)	0.21	0.38	
				Up (z)	0.18	0.31	
KCE	Kern County earthquake	1952	Taft Lincoln School	21 (x)	0.16	0.4	$1/\sqrt{10}$
				111 (y)	0.18	0.44	
				Up (z)	0.11	0.28	

1. Ground motion records extracted from the PEER Ground Motion Database (http://ngawest2.berkeley.edu/, accessed on March 18, 2019)
2. Time scale consistent with the assumed length scale of the test vessel of 1/10

(a) CCE   (b) ECE   (c) KCE
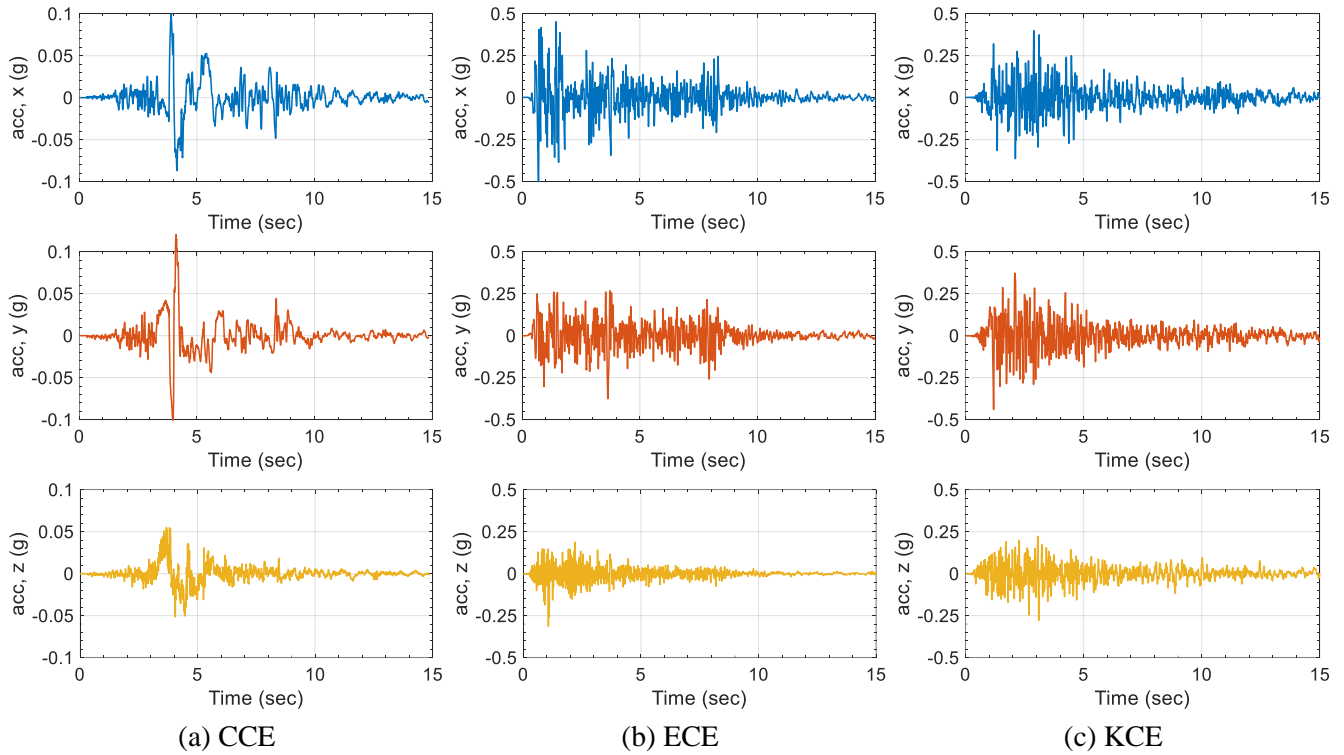
Figure 3.3. Acceleration time series for earthquake-simulator inputs presented in Table 3.1, after time and amplitude scaling

(a) CCE   (b) ECE   (c) KCE
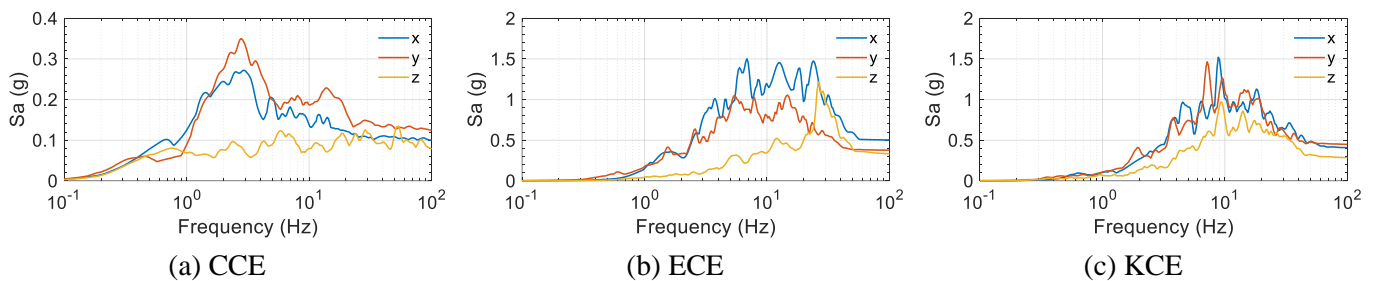
Figure 3.4. Acceleration response spectra of input motions presented in Figure 3.3, damping ratio of 5%

Inputs #74, 76, 77, 80 to 82, and 85 to 87 in Table C.3 are PGA- and time-scaled, unidirectional (*x*), bi-directional (*x* and *y*), and tri-directional (*x*, *y*, and *z*) motions of the CCE, ECE, and KCE. Responses to most of these motions are also presented in Section 3.4 (see Table 3.1), except for those to motions #82 and 87, which are the unidirectional (*x*) components of the ECE and KCE, respectively, with a PGA of 0.8 g. Motions # 88 to 114 are *isolated* motions that simulate CCE, ECE, and KCE (i.e., motions #74, 76, 77, 80 to 82, and 85 to 87) shaking filtered by a seismic isolation system. The *isolated* motions were generated

50

using numerical models of a virtual isolation system. Information on the generation of these *isolated* motions is presented in Section 3.5.1.

3.4 Comparison between experimental results and analytical predictions

Experimental results for the 80%-filled vessel of Figure 3.1a are compared with those calculated using analytical solutions (Case and Parkinson 1957; Mir *et al.* 2021; Veletsos 1984; Veletsos and Tang 1986; Veletsos and Tang 1987)[8] in this section. The analytical solutions used here were developed for rigid, base-supported, cylindrical tanks, filled with ideal fluid (i.e., incompressible and inviscid), and subjected to unidirectional translational or rocking motions. The hydrodynamic response was assumed to be linear and so the analytical solutions are strictly applicable to small amplitude inputs. The hydrodynamic response was parsed into an impulsive and a convective component. The convective component was decoupled into modes.

The first convective frequency and damping ratios in convective modes were identified from measured wave heights generated by white noise and sinusoidal motions. These input motions were small amplitude, unidirectional, and horizontal. The experimental results were compared with analytical predictions per Veletsos (1984) and Case and Parkinson (1957).

Hydrodynamic responses (pressures, base reactions, and wave heights) measured in the experiments for multi-directional motions were compared with analytical results. The amplitudes of the earthquake-simulator input motions were not necessarily small, and so the analytical predictions were not expected to be accurate in these cases. The differences between the measured and analytical results are identified and discussed.

3.4.1 Frequencies of convective mode

Wave height data in the 80%-filled vessel for the white noise input in the *x* direction (motion #2 in Table C.3) were used to identify convective frequencies. Veletsos's solution (1984) for the frequency, $f_{con,i}$, of the i th convective mode is given as:

$$f_{con,i} = \frac{1}{2\pi} \sqrt{\frac{\lambda_i g}{R} \tanh\left(\frac{\lambda_i H}{R}\right)} \qquad (3.3)$$

where H and R denote the liquid height (= 1.62 m) and vessel radius (=0.76 m), respectively; g denotes acceleration due to gravity; and λ_i is a constant depending on the considered mode (=1.841, 5.331, and

---

[8] The solution presented in Mir *et al.* (2021) is discussed in Appendix E.

8.536 for i = 1, 2, and 3, respectively). Per equation (3.3), the first three frequencies are: $f_{con,1} = 0.77$ Hz, $f_{con,2} = 1.32$ Hz , and $f_{con,3} = 1.67$ Hz. Note that $f_{con,1}$ calculated per equation (3.3) is identical to the reciprocal of the period obtained from equation (3.2).

The time series recorded by the wave-height sensor TE is transformed to the frequency domain. Figure 3.5 presents the normalized power spectral density (PSD) plot of the wave-height time series. A prominent peak is observed at the first mode with $f_{con,1} = 0.77$ Hz. The second mode at $f_{con,2} = 1.32$ Hz can be identified in the PSD plot, but the peak is relatively smaller. The PSD plot does not show a significant peak at $f_{con,3}$ = 1.67 Hz, namely, the third mode was not excited by the white noise.
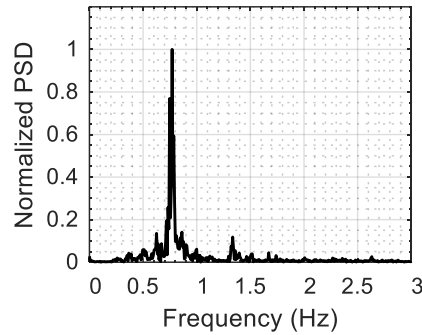
Figure 3.5. Normalized PSD plot for wave height measured by sensor TE, white noise excitation in the x direction

3.4.2 Damping ratios in convective modes

Damping ratios in convective modes were identified using the attenuation of wave heights with the passage of time. As noted in Section 3.4.1, the third and higher convective modes could not be excited significantly by white noise inputs. Consequently, x-directional sinusoidal motions at the first three convective frequencies, 0.77, 1.32, and 1.67 Hz per equation (3.3), were used to excite the test specimen: motions #9, 10, and 11 in Table C.3. Wave-height time series were recorded using the sensor TW. The sensor was moved to a location where the greatest wave amplitude was expected. Per Veletsos (1984) and the modal wave profile of Figure 20 in Yu and Whittaker (2021b), locations for the greatest wave amplitude in the first three convective modes are at $(r,\theta,z) = (0, 180°, H)$, $(0.3R, 180°, H)$, and $(0.2R, 180°, H)$.

Wave-height time series beyond the excitation time were used for analysis, namely, free oscillation of the liquid surface. The wave height in a particular convective mode was extracted from the measured time series by applying a band-pass filter centered at the corresponding modal frequency. Modal wave-height

time series are presented in each panel of Figure 3.6. An exponential function (blue line) was fit to the envelope curve of each response time series to evaluate the damping ratio in the mode. The form of the exponential function, $d_w(t)$, was (Chopra 2012):

$$d_w(t) = A \cdot e^{\zeta \omega t} \tag{3.4}$$

where t is time; ω is the angular frequency ($= 2\pi f_{con,i}$) and ζ is the damping ratio of a convective mode; and A is associated with the amplitude of waves. The damping ratios in the first three convective modes identified using the exponential function and those calculated using the analytical solution of Case and Parkinson (1957) are presented in Table 3.2. A mismatch is evident, more so for the second and third modes. The difference between the experimental and analytical results is likely due to the assumption of the analytical solution of contamination-free fluid and mirror-polished tank surfaces, neither of which were realized in the experiments (or in civil engineering applications, in general): tap water was used for the fluid and the inside of the vessel was painted and not polished to a *mirror-finish*. Similar discrepancies reported elsewhere suggest that damping ratios are extremely sensitive to liquid contamination and vessel surface roughness: small deviations from the idealized conditions result in a large mismatch between theory and experiment (Henderson and Miles 1994).

(a) mode 1 ($f_{con,1} = 0.77$ Hz)

(b) mode 2 ($f_{con,2} = 1.32$ Hz)

(c) mode 3 ($f_{con,3} = 1.67$ Hz)
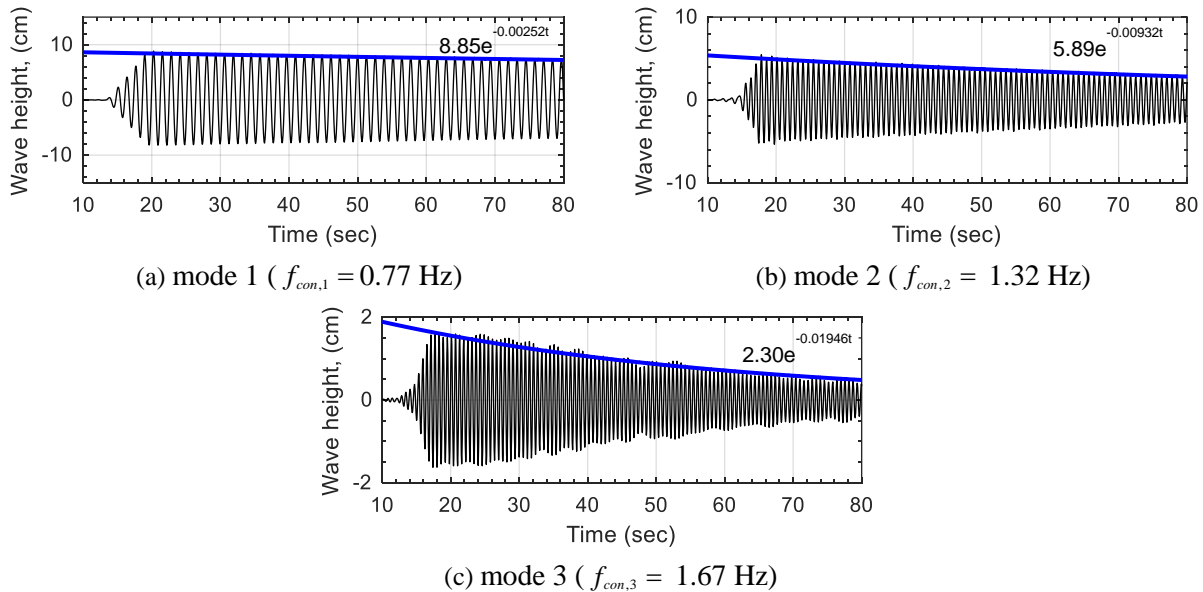
Figure 3.6. Modal wave-height time series and exponential envelope curves $A \cdot e^{\zeta \omega t}$

Table 3.2. Damping ratios in the first three convective modes

	Experiment (herein)	Theory (Case and Parkinson 1957)
Mode 1	0.05%	0.04 %
Mode 2	0.10%	0.02%
Mode 3	0.20%	0.02%

Although the damping ratios from theory and the experiment were similar for the first mode, both values were an order of magnitude smaller than 0.5%, which is routinely assumed for design (Jaiswal *et al.* 2007). Habenberger (2015) notes that there are no experimental or theoretical justifications for the used damping value and that it is "more or less, best guess". It is worth noting that for the practical range of frequency for the first convective mode, which is 0.2 to 1 Hz, the response-spectrum ordinates do not change significantly for damping ratios in the range considered here. To support this observation, response spectra were generated for both horizontal components of the 49 near-field and far-field ground motions[9] in FEMA P695 (ATC 2009). The response-spectrum ordinates of each motion corresponding to damping ratios of 0.5%, 0.2%, and 0.1% were normalized with respect to the ordinate for a damping ratio of 0.05%, in the frequency range of 0.2 to 1 Hz. The normalized values, averaged over the frequency range and for 49 motions are presented in Table 3.3, where SA_r denotes the spectral acceleration for a damping ratio of $r\%$.

Table 3.3. Influence of damping ratios on spectral ordinates for 0.2-1 Hz

Damping ratio, $r\%$	Average $SA_r / SA_{0.05}$
0.5	0.91
0.2	0.96
0.1	0.98

Based on the data presented in Table 3.3, the spectral ordinates for damping ratios of 0.5%, 0.2%, and 0.1% are within 10% of those for 0.05%, in an average sense, for the frequency range of 0.2 to 1 Hz. Although a change in damping ratio from 0.5% to 0.05% may not significantly affect convective responses, the lower

[9]FEMA P695 lists 50 motions. However, the far-field motion with record sequence number (RSN) 829 could not be found on the PEER database.

value is closer to theory, is supported by data from experiments, and should likely replace the widely used value of 0.5%.

3.4.3 Hydrodynamic responses

Hydrodynamic responses, including pressures, base reactions, and wave heights, were measured for the 80%-filled vessel in the experiments. This section reports the hydrodynamic responses for nine sets of earthquake-simulator inputs (#74, 76, 77, 78, 80, 81, 83, 85, and 86 in Table C.3): unidirectional (x; 1D), bi-directional (x and y; 2D) or tri-directional (x, y, and z; 3D) motions of the CCE, ECE, and KCE per Table 3.1. The hydrodynamic responses obtained from the experiments are compared with those calculated using analytical solutions (Mir *et al.* 2021; Veletsos 1984; Veletsos and Tang 1986; Veletsos and Tang 1987). The analytical solutions were developed for a tank supported by a rigid base. To enable a comparison of experimental and analytical results, responses around 37 Hz were removed from all recorded data[10], which was associated with out-of-plane deformation of the base plate and vertical flexibility of the vessel support (i.e., possible gaps between the load cells and their fixtures). A band-stop filter designed for 32 to 42 Hz was used to process experimental data. Accelerations recorded on the base plate in the experiments for earthquake-simulator motions listed in Table 3.1 were used as inputs for the analytical calculations.

The recorded accelerations on the base plate, including translational (x, y, and z) and rocking components, were used for the analytical calculations. The translational motions on the base plate were generated by earthquake-simulator motions in the same directions: x, y, or z. Rocking motions were observed for horizontal excitations due to compliance in the actuators of the earthquake simulator: x (y)-directional earthquake-simulator inputs induced rocking motions on the base plate about the y (x) axis, termed the *ry-* (*rx-*) component. Details on generating the input motions using the recorded data from accelerometers, ANE1X(Y, Z), ANW1X(Y, Z), ASE1X(Y, Z), and ASW1X(Y, Z), on the base plate (see Figure 3.2d) can be found in Yu and Whittaker (2021a) and Yu *et al.* (2021). Figure 3.7 presents acceleration response spectra of each of the translational and rocking components of the recorded accelerations generated by the nine sets of earthquake-simulator motions (i.e., 1D, 2D, or 3D motions and CCE, ECE, and KCE).

---

[10] The empty tank was tested using white noise in the vertical direction, and the vertical motion at the center of the base plate was measured using $AC1Z$ shown in Figure 3.2d. The Fourier amplitude spectrum of the motion shows a peak at $f_z = 58$ Hz, which is associated with out-of-plane deformation of the base plate and vertical flexibility of the tank support. Considering that f_z is proportional to $1/\sqrt{m}$ ($m = 2$ tons, if empty, and 5 tons, if $H = 1.6$ m), the value of f_z for the tank with a water depth of 1.6 m was calculated to be 37 Hz.
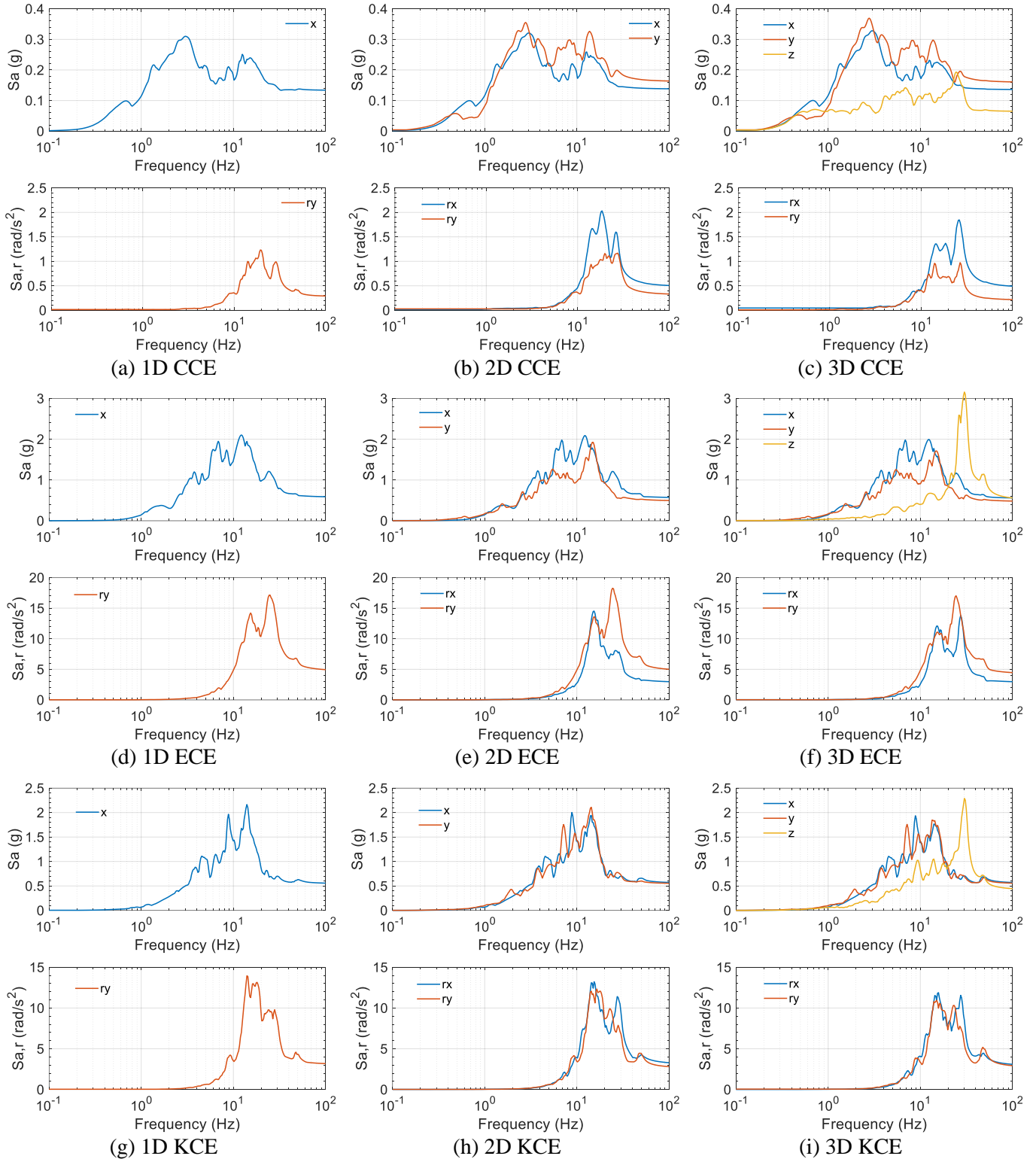
Figure 3.7. Acceleration response spectra of the input motions used for the analytical solutions and the numerical models in Section 4, x, y, z, rx, and ry components, damping ratio of 5%, generated using measured accelerations on the base plate of the specimen

The analytical solutions of Veletsos (1984) were used for the evaluation of hydrodynamic responses to horizontal excitations. The solutions were applied independently in each horizontal direction (x or y). Hydrodynamic responses due to rocking motions (about the x and/or y axes) were evaluated using the analytical solutions proposed by Veletsos and Tang (1987), as modified by Mir *et al.* (2021) (described in Appendix E). Mir *et al.* (2021) considered the change of fluid depth due to rocking motion, which improved the solutions of Veletsos and Tang (1987). The hydrodynamic responses under vertical excitation were evaluated using the approach suggested by Veletsos and Tang (1986), assuming the tank wall and base to be rigid. The inertial force of the vessel was taken into account per Veletsos (1984) and Veletsos and Tang (1987) for lateral and rocking excitations, respectively. The analytical solutions used herein assumed fluid responses to be linear and parsed responses into impulsive and convective components. The analytical solutions of the two components were algebraically summed for comparisons with experimental results. Ten convective modes were considered in the analytical calculations. Responses calculated for excitations along (or about) different directions were superimposed for comparisons with experimental results for multi-directional inputs. For unidirectional inputs along the x direction, the accompanying rocking accelerations about the y axis were also considered. Similarly, for bi-directional and tri-directional inputs, the corresponding rocking accelerations about the x and y axes were considered.

Figure 3.8 presents experimental and analytical time series for the hydrodynamic pressure at the location of PE1, base shear in the x direction, base moment about the y axis, and wave height at the location of TE for the 1D CCE and 3D ECE motions. The earthquake-simulator input for the 1D CCE (3D ECE) was motion #74 (#81) listed in Table C.3, and Figure 3.7a (f) presents the spectra of the input motions used for the analytical calculations. Table 3.4 presents the maximum absolute values of the analytical and experimental results, their percentage differences, and cross-correlation coefficients (R) for the 1D, 2D, and 3D motions of the CCE, ECE, and KCE. The coefficients R between the analytical and experimental results were calculated using 'corr' function in MATLAB (MathWorks 2017). The average differences between the analytical predictions and measured responses are 6%, 4%, 10%, and 12% in the maxima of pressure, base shear, base moment, and wave height, respectively. The average cross-correlation coefficients between the predicted and measured response histories for pressure, base shear, base moment, and wave height are 0.98, 0.99, 0.99, and 0.88, respectively. For the pressures, shear forces, and moments presented in Table 3.4, the differences between the analytical and experimental results for 1D, 2D, and 3D input motions are all less than 15%. For wave heights, the analytical and experimental results are generally not in good agreement (e.g., -18% for the 1D KCE, 49% for the 2D ECE, and 31% for the 3D CCE). These significant differences are in part due to wave breaking, as shown in the snapshot of the free surface for the 3D ECE

motion in Figure 3.9. This nonlinear and chaotic wave action can neither be calculated by theory nor accurately measured in experiments.

On the basis of the data presented here, and for the purpose of preliminary design, hydrodynamic responses due to excitation along (or about) multiple axes can be evaluated independently and superimposed, provided the fluid responses remain linear and chaotic waves do not form.

(a) pressure at the location of PE1

(b) base shear in the *x* direction

(c) base moment about the *y* axis

(d) wave height at the location of TE
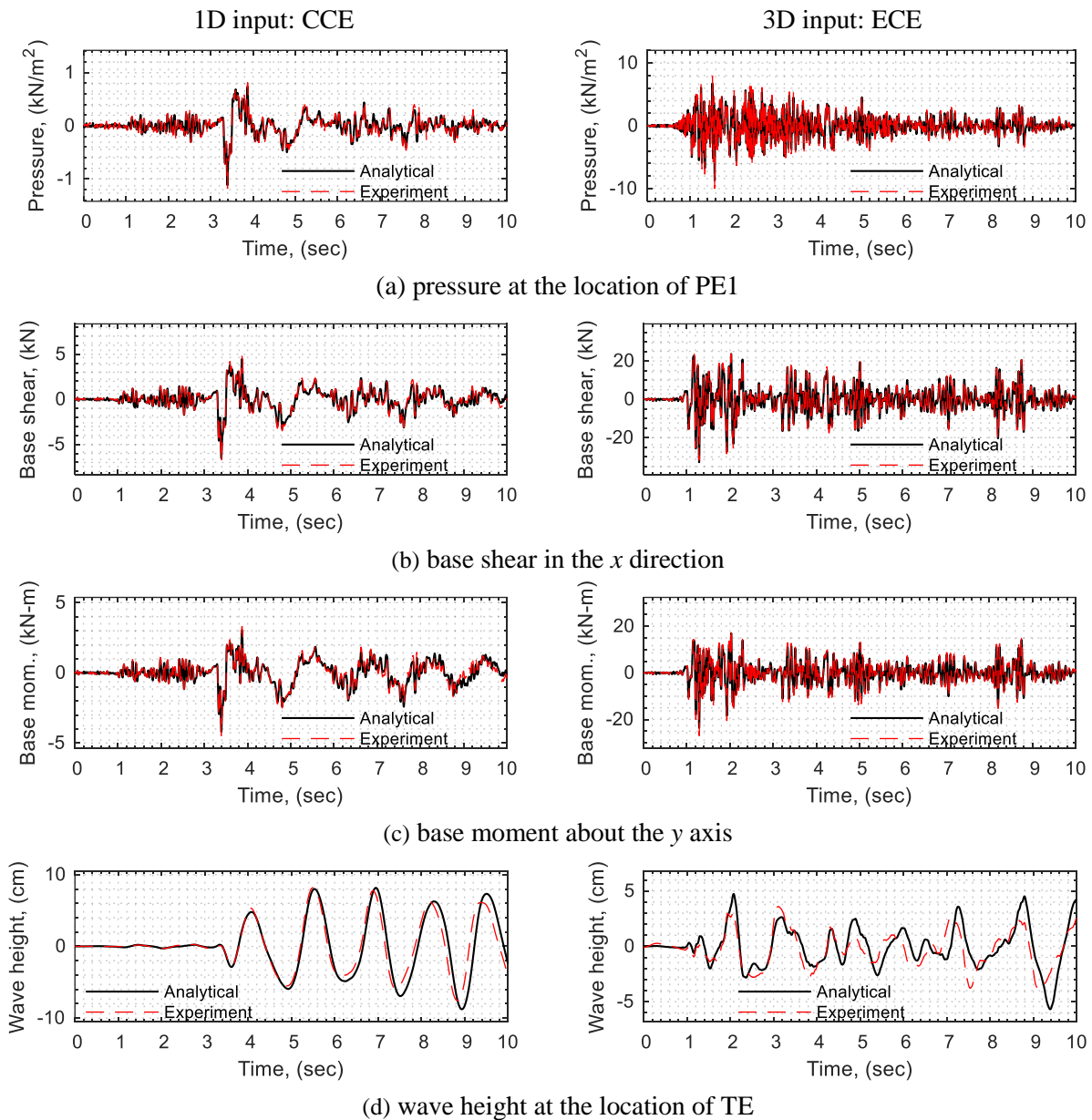
Figure 3.8. Comparison of analytical and experimental response histories

Table 3.4. Maximum absolute hydrodynamic responses of the test vessel, extracted from time series of the experiments and analytical predictions, percentage differences, and cross-correlation coefficients (R)

(a) 1D (x) motions[1]

Response (or location)	CCE			ECE			KCE		
	Theory	Exp.	Diff., % (R)	Theory	Exp.	Diff., % (R)	Theory	Exp.	Diff., % (R)
PE1, kN/m^2	1.1	1.2	-5 (0.98)	5.0	5.4	-8 (0.99)	4.2	4.3	-3 (0.99)
Shear-x, kN	6.5	7.0	-6 (0.99)	35.7	35.2	1 (1.00)	26.8	28.8	-7 (1.00)
Moment-y, kN-m	4.2	4.5	-6 (0.97)	26.0	23.8	9 (1.00)	17.4	19.1	-9 (1.00)
TE, cm	8.8	8.2	7 (0.93)	4.7	4.0	19 (0.86)	3.7	4.6	-18 (0.91)
TW, cm	8.5	8.2	3 (0.93)	4.7	4.5	4 (0.85)	3.4	4.2	-18 (0.88)

(b) 2D (x and y) motions[2]

Response (or location)	CCE			ECE			KCE		
	Theory	Exp.	Diff., % (R)	Theory	Exp.	Diff., % (R)	Theory	Exp.	Diff., % (R)
PE1, kN/m^2	1.1	1.1	0 (0.97)	4.8	5.3	-10 (0.99)	4.3	4.4	-3 (0.99)
PN1, kN/m^2	1.3	1.5	-8 (0.98)	5.0	5.3	-6 (0.99)	4.7	5.0	-6 (0.99)
Shear-x, kN	6.5	6.9	-6 (0.99)	35.1	34.0	3 (1.00)	27.4	28.4	-4 (1.00)
Shear-y, kN	8.2	8.5	-4 (0.99)	29.1	28.4	3 (1.00)	28.7	29.2	-2 (1.00)
Moment-x, kN-m	5.3	6.1	-14 (0.97)	20.1	23.1	-13 (0.99)	18.8	21.1	-11 (0.99)
Moment-y, kN-m	4.1	4.3	-5 (0.97)	25.6	29.1	-12 (1.00)	17.9	19.0	-6 (1.00)
TE, cm	7.5	7.3	3 (0.91)	5.5	3.7	49 (0.79)	3.1	3.0	3 (0.78)
TW, cm	10.1	10.1	0 (0.93)	5.3	5.4	-2 (0.84)	5.1	5.5	-6 (0.90)
TN, cm	5.4	6.0	-10 (0.88)	7.0	6.9	2 (0.83)	5.5	5.1	8 (0.89)
TS, cm	5.4	4.3	26 (0.94)	7.0	6.4	10 (0.85)	5.5	4.7	17 (0.93)

Table 3.4. Maximum absolute hydrodynamic responses of the test vessel, extracted from time series of the experiments and analytical predictions, percentage differences, and cross-correlation coefficients (R) (continued)

(c) 3D (x, y, and z) motions[2]

Response (or location)	CCE			ECE			KCE		
	Theory	Exp.	Diff., % (R)	Theory	Exp.	Diff., % (R)	Theory	Exp.	Diff., % (R)
PE1, kN/m^2	1.3	1.4	-5 (0.98)	8.7	10.0	-13 (0.98)	5.6	5.9	-6 (0.99)
PN1, kN/m^2	1.5	1.5	-2 (0.98)	6.8	7.6	-11 (0.97)	5.1	5.5	-7 (0.99)
Shear-x, kN	6.2	6.6	-6 (0.99)	32.8	31.8	3 (1.00)	27.6	28.4	-3 (1.00)
Shear-y, kN	7.7	8.0	-3 (0.99)	28.4	27.5	4 (1.00)	29.0	29.3	-1 (1.00)
Moment-x, kN-m	4.9	5.8	-14 (0.97)	19.7	22.6	-13 (1.00)	19.2	22.1	-13 (1.00)
Moment-y, kN-m	3.9	4.1	-5 (0.97)	23.6	27.0	-12 (1.00)	18.0	19.2	-6 (1.00)
TE, cm	7.5	7.4	2 (0.92)	5.7	3.9	47 (0.77)	3.4	3.1	11 (0.82)
TW, cm	10.3	10.2	1 (0.93)	5.4	5.2	2 (0.81)	5.1	5.5	-7 (0.90)
TN, cm	5.8	6.1	-4 (0.89)	7.2	7.2	0 (0.81)	5.7	5.0	14 (0.89)
TS, cm	5.8	4.5	31 (0.95)	7.2	6.5	10 (0.84)	5.7	4.7	20 (0.93)

[1]Rocking acceleration about the y axis considered
[2]Rocking accelerations about the x and y axes considered
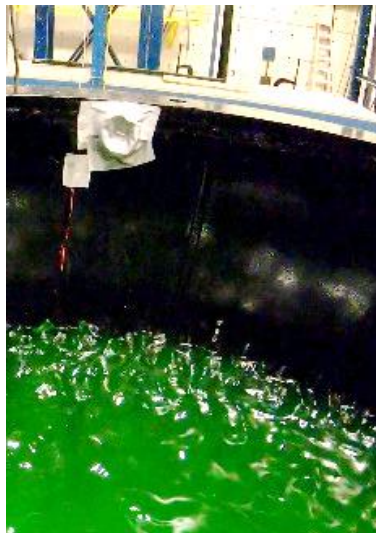
Figure 3.9. Wave breaking for the 3D ECE motion (water dyed green)

3.5   Efficacy of seismic isolation in reducing hydrodynamic responses

This section studies the effects of seismic isolation on hydrodynamic responses of the 80%-filled test vessel. Three friction pendulum (FP) isolation systems were considered. *Isolated* motions that accounted for the three isolation systems were generated using a lumped-mass numerical model. The *isolated* motions were input to the test vessel, and measured hydrodynamic responses were used to identify the benefits of seismic isolation. Rocking motions were not considered.

3.5.1   *Isolated* motions

A lumped-mass model was created in SAP2000 (CSI 2019) to generate *isolated* motions. Figure 3.10 presents the model, including four lumped masses shown using blue solid circles: m_v, m_b, m_i, and m_c, for simulating the vessel, the base plate, the contained water involved in the impulsive mode, and the convective mode, respectively. The model simulated the test vessel supported by a single isolator, which was a two-node link element, shown in red, in Figure 3.10. The black node at the lower end of the link element was fixed to the ground, and the lumped mass of the base plate, m_b, was assigned to the upper node. The lumped mass for the vessel (including the wall and flange), m_v, was supported by a rigid link at the center of the mass: a height h_v above the base plate. For the impulsive and convective modes, the values of the lumped masses, m_i and m_c, their heights above the base plate, h_i and h_c, and the lateral stiffnesses of their supporting springs, k_i and k_c, were calculated per Malhotra *et al.* (2000). The values for the parameters used in the lumped-mass model are noted in Figure 3.10.

The isolator was considered to be a single concave FP bearing, and the link element was assigned '*friction isolator*' material available in SAP2000. Typical sliding periods for a prototype reactor are in the range of 2 to 4 seconds. Consistent with the length scale of the test vessel, the sliding period was compressed: 0.6 to 1.3 seconds. Accordingly, isolation systems with sliding periods of 0.7, 1, and 1.3 seconds were considered in the model of Figure 3.10. The properties used for the three isolation systems (IS#1, IS#2, and IS#3) are listed in Table 3.5. The fast and slow coefficients of friction for the link element were assumed to be 0.06 and 0.03, respectively. The yield displacement and velocity rate parameters were set to 1 mm and 100 sec/m, respectively.

61

Convective mode:
mass, $m_c = 664$ kg
stiffness, $k_c = 15735$ N/m
height, $h_c = 1.255$ m

Vessel:
mass, $m_v = 669$ kg
stiffness, $k_v = \infty$
height, $h_v = 1.132$ m

Impulsive mode:
mass, $m_i = 2300$ kg
stiffness, $k_i = 1.8 \times 10^9$ N/m $\approx \infty$
height, $h_i = 0.803$ m

Base plate mass, $m_b = 1424$ kg
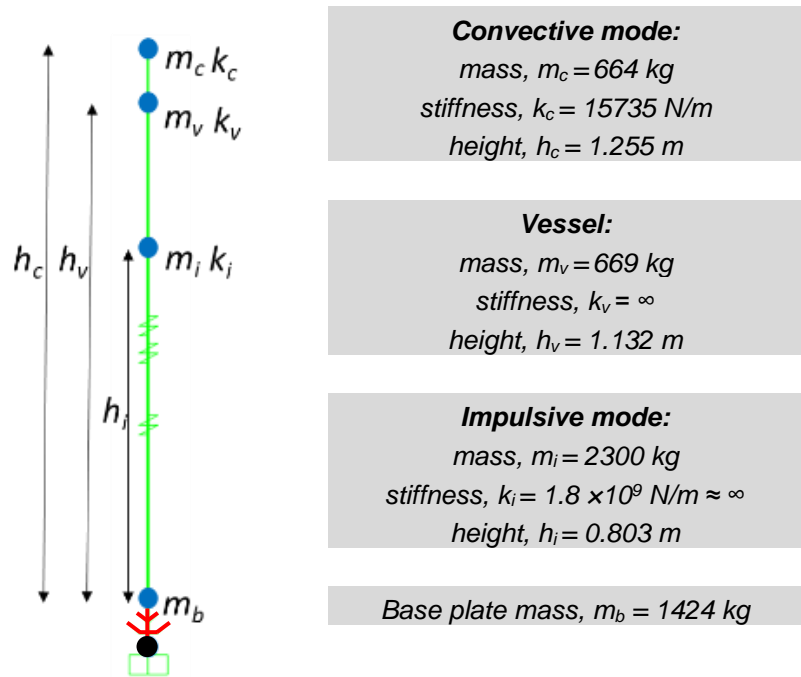
Figure 3.10. Model of the test vessel and seismic isolation system used for the generation of isolated motions, SAP2000

Table 3.5: Isolator properties used for the model of Figure 3.10, SAP2000

System name	IS#1	IS#2	IS#3
Period	0.7 sec	1.0 sec	1.3 sec
Total weight, W	49609 N	49609 N	49609 N
Pendulum radius, R	0.122 m	0.248 m	0.419 m
Friction coefficient (fast), μ_f	0.06	0.06	0.06
Friction coefficient (slow), μ_s	0.03	0.03	0.03
Yield displacement, u_y	1 mm	1 mm	1 mm
Post-elastic stiffness, $K_{pe} = \dfrac{W}{R}$	406631 N/m	200036 N/m	118398 N/m
Elastic stiffness, $K_e = \dfrac{\mu_f W}{u_y}$	2976540 N/m	2976540 N/m	2976540 N/m

Unidirectional (1D), bi-directional (2D), and tri-directional (3D) motions for CCE, ECE, and KCE shaking (#74, 76, 77, 80 to 82, and 85 to 87 in Table C.3) were input to the SAP2000 model at the solid black circular node in Figure 3.10. The acceleration histories at the node immediately above the isolator (i.e., base plate; m_b in Figure 3.10) were extracted, and defined as the *isolated* motions. Figure 3.11 presents the acceleration response spectra of the ground inputs and their *isolated* counterparts. As seen in Figure 3.11, horizontal spectral accelerations (x and y components) in the low-frequency region (0.7 to 2.5 Hz) are amplified by the base isolation, which can lead to increased convective responses, as noted in prior studies (Calugaru and Mahin 2009; Chalhoub and Kelly 1988). The reduction in horizontal spectral accelerations enabled by isolation at frequencies greater than 2.5 Hz is clearly visible in the plots for the ECE and KCE motions: Figures 3.11b, c, e, f, h, and i. For the low amplitude CCE motion (PGAs ≤ 0.12 g per Table C.3), the reduction in horizontal spectral acceleration is insignificant because the isolator displacement is tiny. The base isolation did not affect the vertical components of the 3D motions, shown in Figures 3.11g, h, and i.

The *isolated* motions were then used as earthquake-simulator inputs to the test vessel to simulate the use of different isolation systems. Table C.3 presents the PGA of each component of the *isolated* motions: #88 to 114.
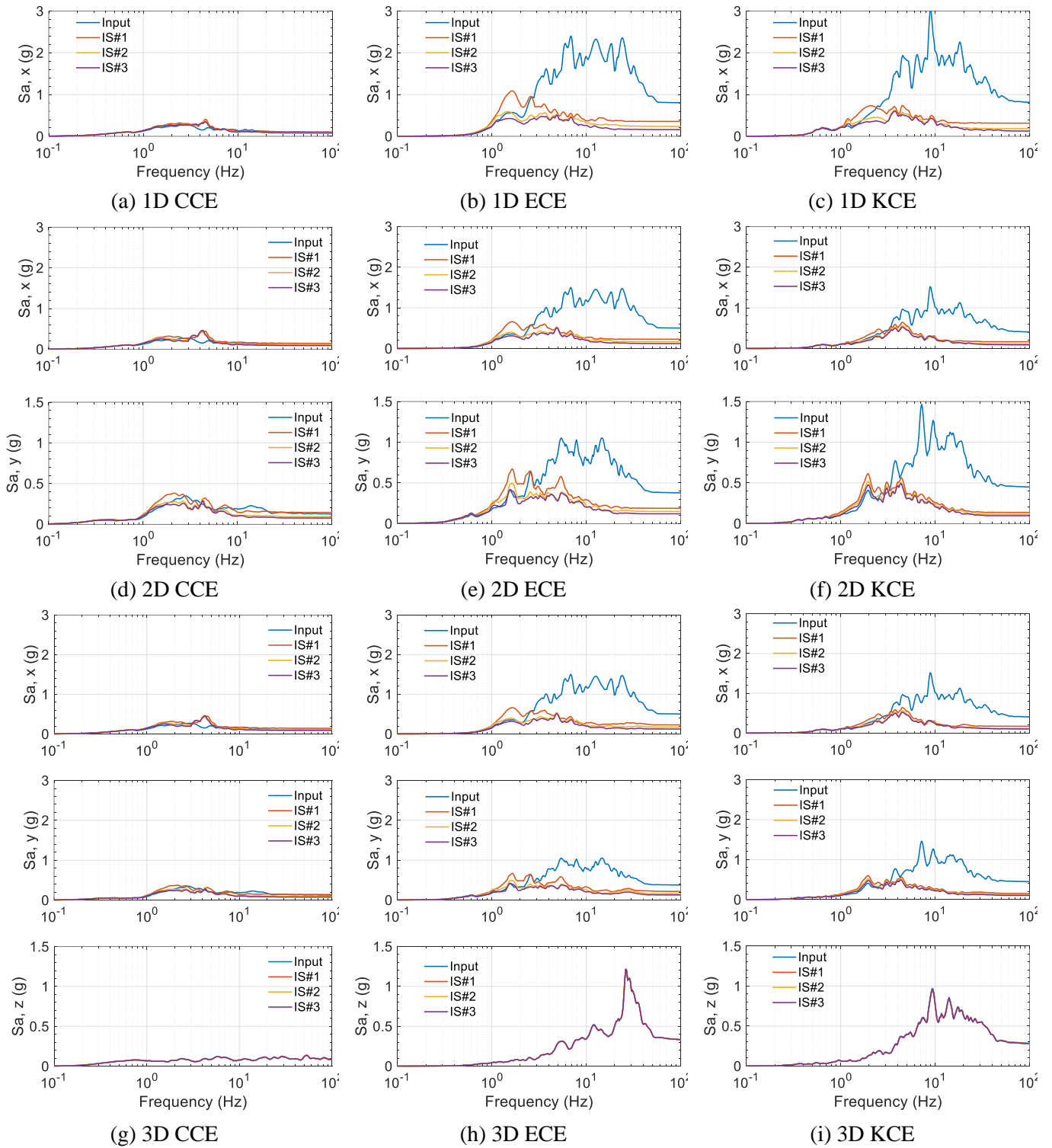
Figure 3.11. Acceleration response spectra of input and isolated motions, damping ratio of 5%, 1D, 2D, and 3D motions of the CCE, ECE, and KCE

3.5.2   Effects of base isolation on hydrodynamic responses

Figure 3.12 enables a comparison of maximum absolute values of responses obtained from experiments for the 1D, 2D, and 3D CCE, ECE, and KCE motions (#74, 76, 77, 80 to 82, and 85 to 87) and their *isolated* counterparts (#88 to 114). The CCE, ECE, and KCE motions are termed hereafter in this section as *non-isolated* motions (3.5.2). The presented responses include hydrodynamic pressures at the location of PE1, base shear in the *x* direction, base moment about the *y* axis, and wave height at the location of TE. The peak response to each *isolated* input is normalized by the corresponding response to the *non-isolated* input. As seen in Figure 3.12, the effect of base isolation for the 1D, 2D, and 3D CCE motions (PGAs ≤ 0.12 g per Table C.3) was not significant: differences in the peak responses between the *isolated* and *non-isolated* cases are less than 25%. For the 1D, 2D, and 3D ECE and KCE motions, for which the amplitudes are relatively large (i.e., 0.3 g $\leq$ PGA ≤ 0.8 g per Table C.3), a reduction of 65% to 85 % is observed in base reactions. The reduction in pressure for these ECE and KCE motions is also significant for the 1D and 2D cases: 60% to 80%. For the 3D ECE and KCE, the reduction in pressure was not as significant because the vertical component of the input motion, which amplifies pressure, was not affected by the horizontal isolation systems considered here, as shown in the vertical spectra of Figures 3.11h and i. The peak wave height, namely, convective response, was generally increased by the three isolation systems for all input motions due to the amplification in the low-frequency region shown in Figure 3.11. The increments in the peak wave height for the 2D and 3D ECE and KCE motions were the most significant, ranging between 45% and 95%.

(a) unidirectional inputs (x)

(b) bi-directional inputs (*x* and *y*)

(c) tri-directional inputs (*x*, *y*, and *z*)
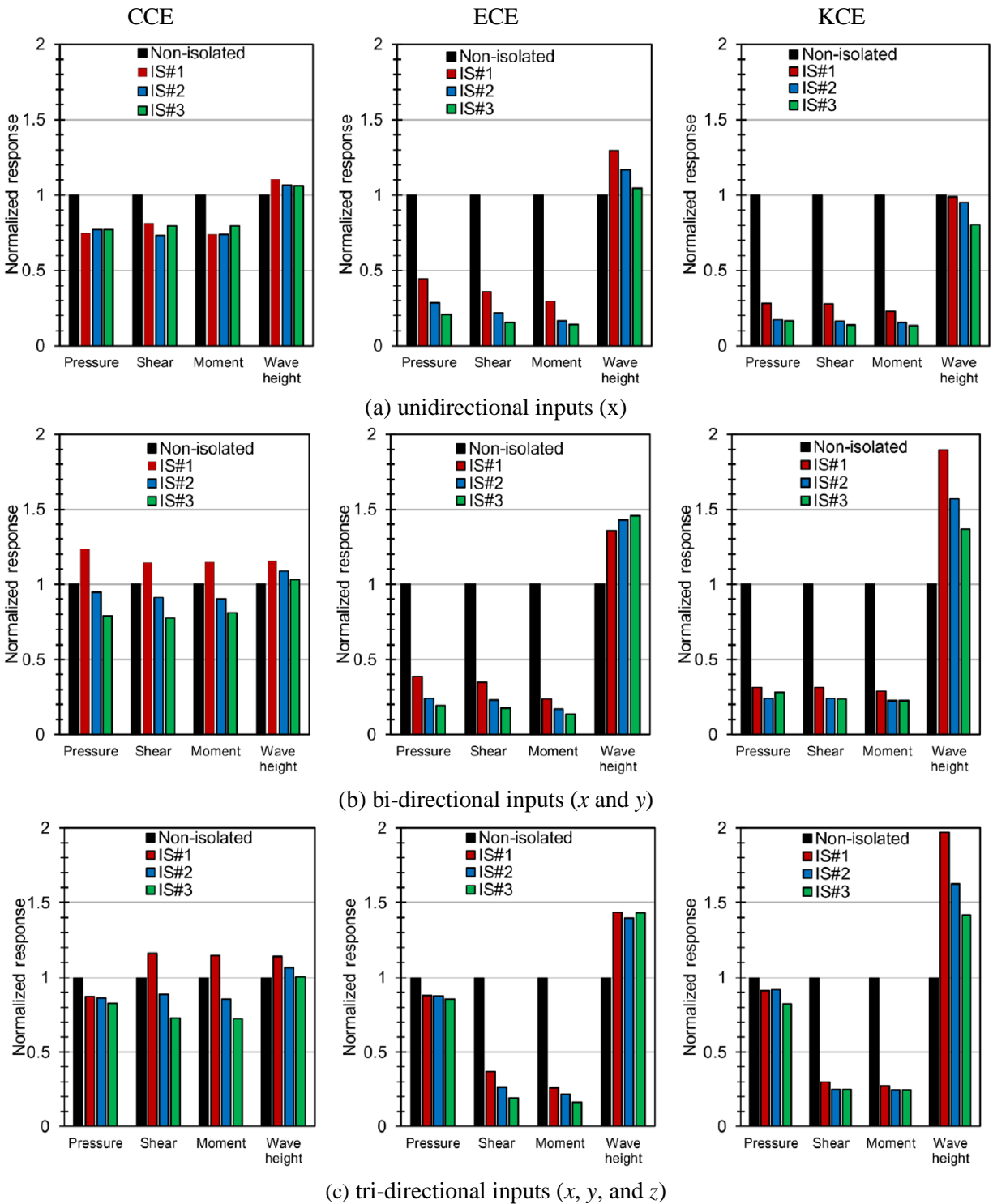
Figure 3.12. Peak responses to the *isolated* motions normalized by those to the *non-isolated* counterparts, three isolation systems (IS#1, IS#2, and IS#3), experimental data for the 80%-filled vessel

3.6 Summary and conclusions

A base-supported cylindrical vessel was tested using a six-degree-of-freedom earthquake simulator at the University at Buffalo. The test vessel was fabricated from carbon steel and filled with water. Data generated from the experiments are compared with analytical predictions, and used to identify the benefits of seismic isolation. (Experimental data are also used for validation of numerical models, as presented in Section 4.)

The measured fundamental convective frequency of the vessel filled to 80% of this capacity is identical to that calculated using the analytical expression of Veletsos (1984). Experimentally measured damping ratios in the first three convective modes are significantly smaller than the value of 0.5% that is routinely used for design of a liquid-filled tank. A value of 0.05% is supported by the experiments and theory.

The hydrodynamic responses, including pressure, base shear, base moment, and wave height, recorded in the experiments and calculated using analytical solutions were compared for lateral, vertical, and rocking accelerations. Responses for multi-directional input were assumed to be algebraic sums of those analytically calculated for one-component motions in different directions. The experimental and analytical results for pressures on the vessel wall, base shears, and base moments were in reasonable agreement. However, errors in predicted maximum values of wave heights were significant. Accordingly, available analytical solutions (e.g., Mir *et al.* (2021); Veletsos (1984); Veletsos and Tang (1986); Veletsos and Tang (1987); Yu and Whittaker (2020)) can be used for preliminary design and sizing of liquid-filled vessels/tanks if the convective responses do not dominate the response.

The implementation of (horizontal) base isolation led to a 65% to 85% reduction in base shear and moment for the high-intensity motions: ECE and KCE. Wave height, associated with the convective modes, increased with the use of the base isolation, for this tank geometry. The reduction in pressure was significant for the unidirectional and bi-directional inputs but smaller for the tri-directional input motions.

SECTION 4

NUMERICAL MODELLING AND VALIDATION FOR A BASE-SUPPORTED VESSEL

4.1   Introduction

This section focuses on numerical modeling of the base supported vessel tested in the experiments described in Section 3. Numerical results calculated using response-history analyses were compared with experimental data. Two numerical approaches were investigated: 1) Arbitrary Lagrangian and Eulerian (ALE), and 2) Lagrangian elastic-fluid. The first approach used the ALE solver, and modeled the fluid using Eulerian elements that do not deform with fluid motion. The Eulerian elements define a fluid domain, and the fluid can flow through each Eulerian element. These elements are not distorted by large deformation of the fluid (e.g., sloshing), and enable the ALE solver to accommodate nonlinear fluid analysis. The second approach, Lagrangian elastic-fluid, is computationally more efficient than the ALE analysis. The fluid was modeled using an elastic material. Numerical models for the ALE solver and the Lagrangian approach were constructed for the test vessel shown in Figure 3.1a: $H_s = 2$ m, $R = 0.76$ m, and $h = 7.92$ mm. The model included the vessel wall, flange at the top, contained water, and base plate. The four load cells, which supported the vessel on the earthquake simulator, were not modeled.

Sections 4.2 and 4.3 describe the models for the ALE solver and the Lagrangian elastic-fluid solver, respectively, and present a comparison between numerical results with data generated from experiments. Section 4.4 discusses the capability of the numerical approaches for computing impulsive responses. Section 4.5 presents a summary and conclusions.

4.2   Arbitrary Lagrangian and Eulerian (ALE) approach

An ALE model was built for the 80%-filled test vessel. Figure 4.1 presents an isometric and a cutaway view of the ALE model, together with the global coordinate (x, y, z) system, consistent with Figure 3.1b. The wall and flange are shown in blue, and the base plate is shown in black, all of which were modeled using three/four-node shell elements. The elements of the wall and flange were assigned an elastic material, and those for the base plate were assigned a rigid material. Material properties consistent with carbon steel were defined for both the elastic and rigid[11] materials: density ρ_s of 7850 kg/m³, elastic modulus E_s of 2×10^{11}

---

[11] The values of the mechanical properties do not affect the responses of the rigid base but must be defined in the LS-DYNA deck (LSTC 2017).

N/m^2, and Poisson's ratio υ_s of 0.27. A damping ratio of 2% was assigned to the elastic shell elements. The fluid domain in the vessel was built using Eulerian, eight-node, solid elements. The fluid domain included the contained water and a void space above the free surface, shown in Figure 4.1b in yellow and light gray, respectively. The effects of atmospheric pressure were not considered. The elements for the fluid domain were assigned properties of water: a density ρ_w of 1000 kg/m^3, a dynamic viscosity μ_w of 10^{-3} N-s/m^2, and a bulk modulus K_w of 2.2 GPa. These water properties were defined in the *MAT (material) and *EOS (equation of state) keywords of the LS-DYNA input file. The Eulerian elements (light grey) above the free surface were assigned *void properties* using the *INITIAL_VOID keyword. Table 4.1 lists the mechanical properties used for the elements of the ALE model. The sizes of the elements as shown in Figure 4.1b were optimized, resulting in smaller elements for the fluid domain adjacent to the vessel wall, and above and below the free surface. Nodes at the interface of the water, void space, and vessel were merged. The gravitational acceleration g of 9.81 m/s^2 was assigned in the negative z direction.

(a) isometric view, void space not shown   (b) cutaway view
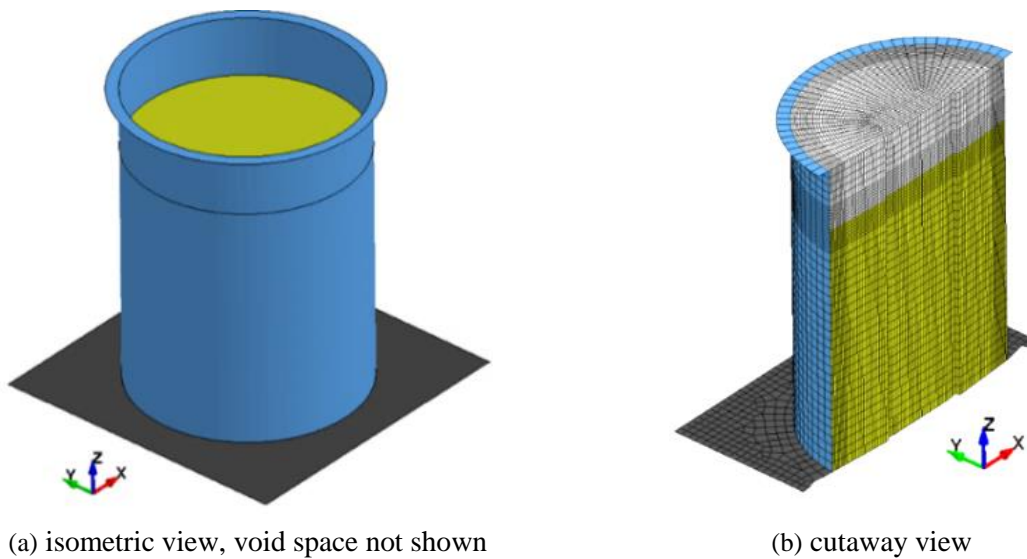
Figure 4.1. ALE model of the test specimen

Table 4.1. Mechanical properties assigned to the elements of the vessel, water, and void space in the models for the ALE and Lagrangian elastic-fluid approaches

		ALE	Lagrangian
Vessel wall, flange, and base	Density, ρ_s	7850 kg/m³	
	Elastic modulus, E_s	2×10^{11} N/m²	
	Poisson's ratio, υ_s	0.27	
Water	Density, ρ_w	1000 kg/m³	
	Dynamic viscosity, μ_w	10^{-3} N/m²-s	--[1]
	Bulk modulus, K_w	2.2 GPa	2.2 GPa
Void space		*INITIAL_VOID	--[2]

1. VC in *MAT_ELASTIC_FLUID was set as 0.1 as suggested (LSTC 2017)

2. Void space not included

Response-history analyses of the ALE model were performed for nine sets of time series: 1D, 2D, and 3D, CCE, ECE, and KCE motions, for which the spectra are shown in Figure 3.7. These motions are accelerations on the base plate measured in the experiments, including translational and rocking components. Details of the input motions are presented in Section 3.4.3. These motions were input at the center of the base plate in the model using *BOUNDARY_PRESCRIBED_MOTION_RIGID keyword. Only the part of an input motion that included 90+% of the Arias intensity (Arias 1970) was used for the response-history analyses to reduce the computational expense. Hydrodynamic pressures on the vessel wall, reactions at the vessel base, and wave heights were extracted from the ALE model. To generate wave-height histories, massless nodes, referred to as tracers, were defined on the free surface of the water using the *DATABASE_TRACER keyword. A number of tracers were assigned around each monitoring location of the four sensors (see TE, TW, TN, and TS in Figure 3.2c) used in the experiments. The tracers are not stationary in plan and move with the fluid velocity. At high fluid velocity, the tracers do not necessarily remain on the free surface (see Section 5 in Yu and Whittaker (2021a) and Yu *et al.* (2021)). The wave height history considered the vertical displacement of the tracer that was both closest to a monitoring location and located on the free surface at each time step.

Figure 4.2 presents time series for hydrodynamic pressures at the location of PE1, base shear in the *x* direction, base moment about the *y* axis, and wave height at the location of TE for the 1D CCE (see Figure 3.7a) and 3D ECE (see Figure 3.7f). Table 4.2 presents the maximum absolute values of the ALE and experimental results, their percentage differences, and cross-correlation coefficients (*R*) for the 1D, 2D, and

3D, CCE, ECE, and KCE motions. The average differences between the numerical predictions and measured responses are 7%, 5%, 5%, and 8% for the maxima of pressure, base shear, base moment, and wave height, respectively. The average coefficients R between the predicted and measured response histories for pressure, base shear, base moment, and wave height are 0.99, 0.99, 0.98, and 0.93, respectively. The percentage differences are within 10% on average, which might be a threshold for commercial grade dedication of software (Doulgerakis *et al.* 2021).
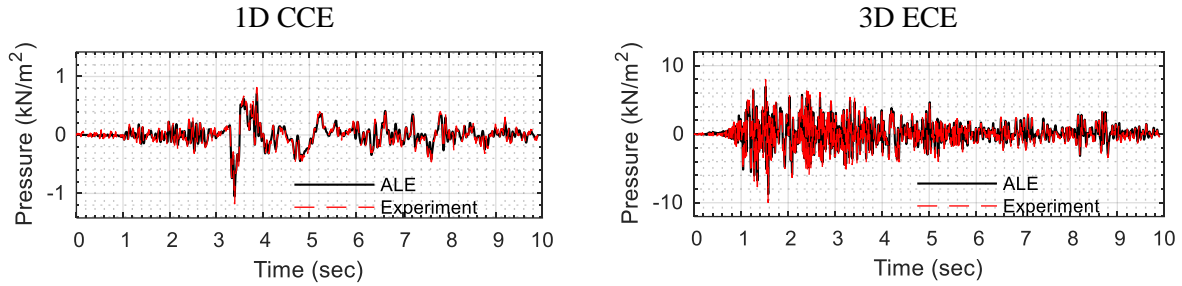
(a) pressure at the location of PE1
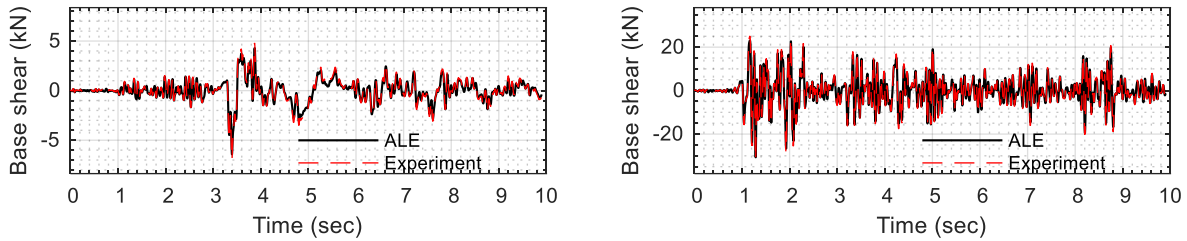
(b) base shear in the x direction
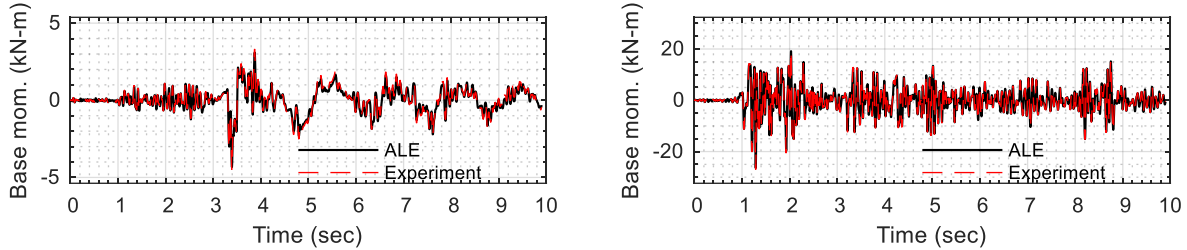
(c) base moment about the y axis
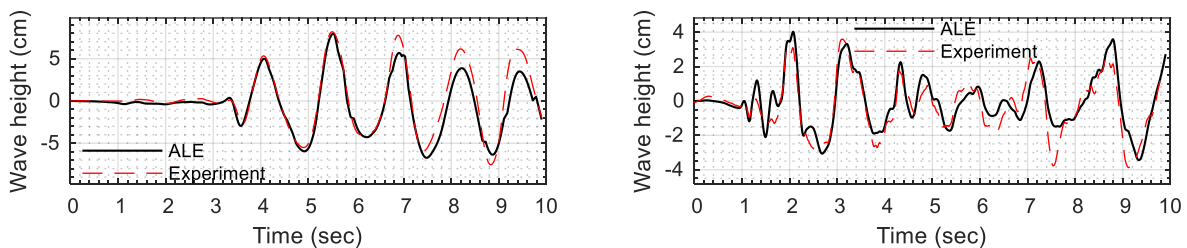
(d) wave height at the location of TE

Figure 4.2. Comparison of ALE and experimental response histories of the 80%-filled test vessel for the 1D CCE and 3D ECE motions

Table 4.2. Maximum absolute responses of the 80%-filled test vessel for the 1D, 2D, and 3D CCE, ECE, and KCE motions, extracted from time series of the experiments and ALE model, percentage differences, and cross-correlation coefficients (R)

(a) 1D (x) motions[1]

Response (or location)	CCE			ECE			KCE		
	Model	Exp.	Diff., % (R)	Model	Exp.	Diff., % (R)	Model	Exp.	Diff., % (R)
PE1, kN/m^2	1.1	1.2	-11 (0.98)	5.7	5.4	4 (0.99)	4.2	4.3	-3 (0.99)
Shear-x, kN	6.4	7.0	-8 (0.99)	33.6	35.2	-5 (0.99)	26.5	28.8	-8 (0.99)
Moment-y, kN-m	4.3	4.5	-3 (0.99)	26.5	23.8	11 (0.98)	18.4	19.1	-4 (0.98)
TE, cm	8.0	8.2	-3 (0.96)	3.9	4.0	-2 (0.93)	4.5	4.6	-2 (0.98)
TW, cm	6.9	8.2	-16 (0.97)	4.2	4.5	-6 (0.92)	4.4	4.2	6 (0.97)

(b) 2D (x and y) motions[2]

Response (or location)	CCE			ECE			KCE		
	Model	Exp.	Diff., % (R)	Model	Exp.	Diff., % (R)	Model	Exp.	Diff., % (R)
PE1, kN/m^2	1.0	1.1	-7 (0.99)	5.6	5.3	5 (0.98)	4.4	4.4	3 (0.98)
PN1, kN/m^2	1.4	1.5	-6 (0.98)	4.5	5.3	-16 (0.98)	4.7	5.0	-9 (0.98)
Shear-x, kN	6.4	6.9	-6 (0.99)	32.9	34.0	-3 (0.99)	27.2	28.4	-5 (0.99)
Shear-y, kN	8.0	8.5	-6 (0.99)	27.8	28.4	-2 (0.99)	28.1	29.2	-3 (0.99)
Moment-x, kN-m	5.5	6.1	-10 (0.98)	22.0	23.1	-5 (0.98)	20.3	21.1	-6 (0.98)
Moment-y, kN-m	4.2	4.3	-3 (0.99)	28.9	29.1	-1 (0.98)	18.3	19.0	-2 (0.99)
TE, cm	8.0	7.3	9 (0.97)	3.8	3.7	2 (0.90)	3.4	3.0	16 (0.94)
TW, cm	8.4	10.1	-17 (0.96)	4.9	5.4	-9 (0.92)	5.4	5.5	-1 (0.96)
TN, cm	6.2	6.0	4 (0.91)	7.2	6.9	4 (0.86)	4.1	5.1	-20 (0.91)
TS, cm	3.6	4.3	-16 (0.92)	6.1	6.4	-5 (0.96)	4.5	4.7	-4 (0.92)

Table 4.2. Maximum absolute responses of the 80%-filled test vessel for the 1D, 2D, and 3D CCE, ECE, and KCE motions, extracted from time series of the experiments and ALE model, percentage differences, and cross-correlation coefficients (R) (continued)

(c) 3D (x, y, and z) motions[2]

Response (or location)	CCE			ECE			KCE		
	Model	Exp.	Diff., % (R)	Model	Exp.	Diff., % (R)	Model	Exp.	Diff., % (R)
PE1, kN/m^2	1.4	1.4	-2 (0.99)	8.8	10.0	-13 (0.99)	5.9	5.9	-1 (1.00)
PN1, kN/m^2	1.5	1.5	-4 (0.99)	6.9	7.6	-10 (0.99)	5.3	5.5	-4 (1.00)
Shear-x, kN	6.2	6.6	-6 (0.99)	30.7	31.8	-4 (0.99)	26.9	28.4	-5 (0.99)
Shear-y, kN	7.5	8.0	-5 (0.99)	27.1	27.5	-1 (0.99)	28.3	29.3	-3 (0.99)
Moment-x, kN-m	5.2	5.8	-10 (0.98)	21.5	22.6	-5 (0.98)	20.8	22.1	-6 (0.98)
Moment-y, kN-m	3.9	4.1	-5 (0.99)	26.4	27.0	-2 (0.98)	18.1	19.2	-6 (0.98)
TE, cm	7.6	7.4	3 (0.91)	3.9	3.9	1 (0.90)	3.3	3.1	7 (0.91)
TW, cm	8.6	10.2	-15 (0.95)	5.3	5.2	1 (0.91)	5.3	5.5	-4 (0.96)
TN, cm	6.8	6.1	13 (0.87)	7.5	7.2	5 (0.87)	4.5	5.0	-11 (0.94)
TS, cm	4.5	4.5	1 (0.82)	6.0	6.5	-8 (0.95)	5.0	4.7	5 (0.92)

[1]Rocking acceleration about the y axis considered
[2]Rocking accelerations about the x and y axes considered

4.3 Lagrangian elastic-fluid approach

Figure 4.3 presents an isometric and a cutaway view of the Lagrangian model of the 80%-filled test vessel, together with the global coordinate (x, y, z) system, consistent with Figure 3.1b. The contained water was modeled using eight/six-node solid elements, shown in yellow. (No void space, such as that used in the ALE model and shown as light grey in Figure 4.1b, was included in the Lagrangian model.) Different from the ALE solver presented in Section 4.2, the Lagrangian model[12] simulated fluid using an elastic material, namely, MAT_ELASTIC_FLUID. The elastic fluid was incompressible. The vessel wall and flange, shown

---

[12] Lagrangian approaches using acoustic elements have been implemented in some finite element packages, for example, Abaqus. The acoustic element formulation in LS-DYNA (LSTC 2017), however, is not suitable for modeling hydrodynamic effects (Huang 2020).

in blue in Figure 4.3, were built using four-node shell elements, similar to those used in the ALE model presented in Section 4.2. The base plate was modeled using eight/six-node solid elements and four/three-node shell elements, shown as dark grey and green, respectively, in Figure 4.3. These shell elements were merged with the bottom nodes of the solid elements of the base plate. The shell elements of the base were assigned to be a massless rigid material. The shell elements of the vessel wall and flange, and the solid elements of the base plate, were assigned to be elastic materials. The mechanical properties used for the vessel and fluid are presented in Table 4.1. A damping ratio of 2% was assigned to the elastic shell and solid elements. The gravitational acceleration g of 9.81 m/s^2 was assigned in the negative z direction. The input motions were applied to the rigid shell elements of the base plate using *BOUNDARY_PRESCRIBED_MOTION_RIGID, as noted in Section 4.2.

(a) isometric view, top   (b) isometric view, bottom
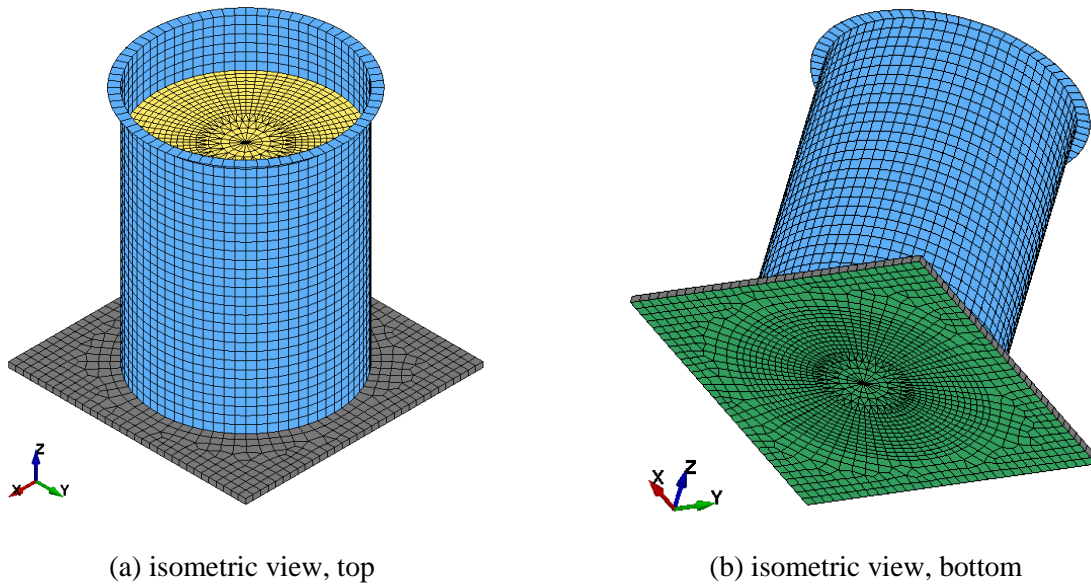
Figure 4.3. Lagrangian-approach model of the test specimen

Two methods for simulating the interaction between the fluid and vessel (the wall and base plate) were evaluated in separate analyses: 1) *CONSTRAINED_NODE_SET, termed *tie constraint*, and 2) *CONTACT_AUTOMATIC_SURFACE_TO_SURFACE, termed *contact*. The tie constraint cannot be assigned to rigid elements. The base plate, including a layer of elastic solid elements that were not needed for the ALE model, enabled the tie constraint to define the interaction between the base and its adjacent fluid. The coincident nodes of the fluid and base were tied in the vertical direction, and the coincident nodes

of the fluid and wall were tied in the horizontal directions. The input file containing the *CONSTRAINED_NODE_SET keyword was generated using a MATLAB script (MathWorks 2017).

To model fluid-structure interaction (FSI) using the contact method, the keyword *CONTACT_AUTOMATIC_SURFACE_TO_SURFACE was assigned at the interfaces between the fluid and the vessel. The static and dynamic friction coefficients were specified to be zero. A contact damping of 20% of critical was specified using the VDC option of the keyword to preclude instabilities due to contact oscillations. Segment-based contact, activated by setting SOFT=2 in the optional input A of the contact keyword, was used.

Response-history analyses of the Lagrangian model with FSI addressed using the two methods (i.e., tie constraint and contact) were performed for the 1D CCE motion (see spectra in Figure 3.7a). Hydrodynamic pressures on the vessel wall, reactions at the vessel base, and wave heights were extracted. Figure 4.4 enables comparisons of results of the Lagrangian analysis and experimental data for hydrodynamic pressures at the location of PE1, base shear in the x direction, base moment about the y axis, and wave height at the location of TE. The numerical results for the tie constraint and contact presented in Figure 4.4 are similar. Table 4.3 presents the maximum absolute values of the numerical and experimental results, their percentage differences, and cross-correlation coefficients (R). The numerical predictions and experimental results are in reasonable agreement for the pressure, base shear, and base moment: the differences presented in Table 4.3 are all less than or equal to 15%. However, results for the wave height are very different: simulations of the tie constraint and contact underestimated the response by 84% and 82%, respectively, compared with the measured data. Accordingly, the Lagrangian model used herein is not suitable for the analysis of vessels whose response is significantly influenced by convective modes. The utility of Lagrangian models to accurately capture impulsive responses in vessels is investigated in Section 4.4.

(a) pressure at the location of PE1

(b) base shear in the x direction

(c) base moment about the y axis

(d) wave height at the location of TE
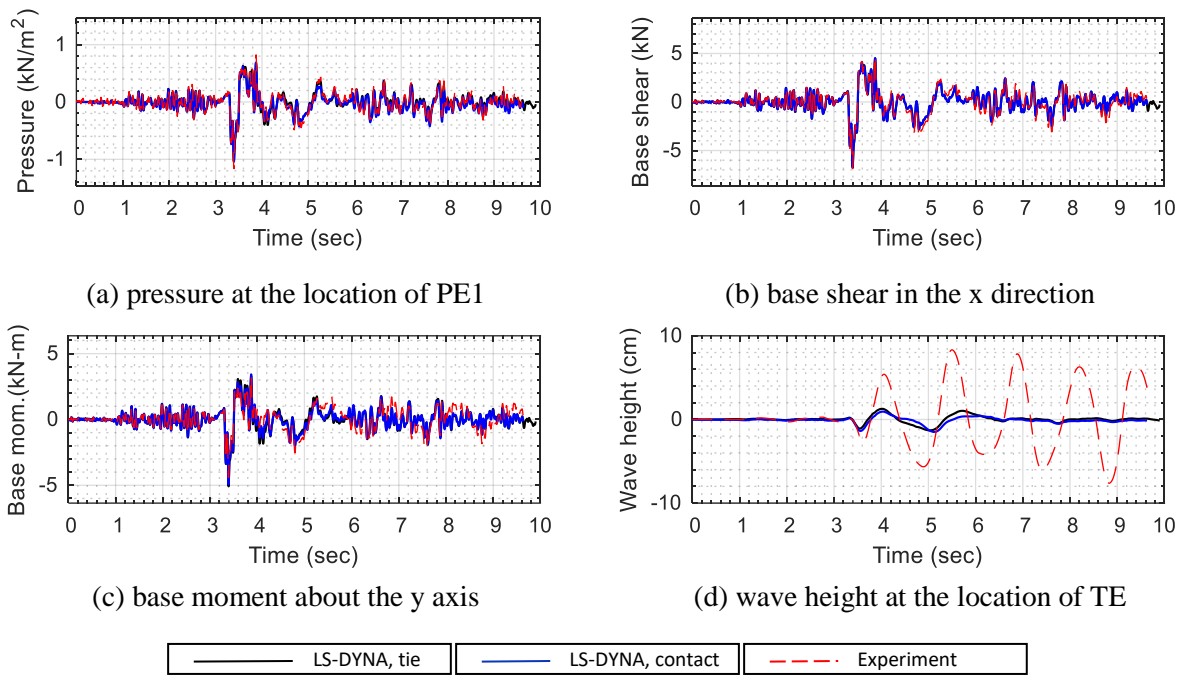
Figure 4.4. Lagrangian and experimental response histories, 80%-filled test vessel, 1D CCE motion

Table 4.3. Maximum absolute responses of the 80%-filled test vessel for the 1D CCE, extracted from the time series of Figure 4.4, Lagrangian model and experiment, percentage differences, and cross-correlation coefficients (*R*)

Response (or location)	Lagrangian model		Experiment	Difference, % (*R*)	
	Tie	Contact		Tie	Contact
PE1, kN/m²	1.0	1.0	1.2	-11 (0.96)	-11 (0.97)
Shear-*x*, kN	6.8	6.7	6.9	-2 (0.95)	-3 (0.95)
Moment-*y*, kN-m	5.1	4.9	4.4	15 (0.81)	11 (0.85)
TE, cm	1.3	1.5	8.3	-84 (0.48)	-82 (0.27)

4.4   Numerical simulation of impulsive responses

As concluded in Section 4.3, the Lagrangian elastic-fluid model cannot simulate wave action (convective mode) correctly. To investigate modeling approaches for the calculation of impulsive responses, results generated using the Lagrangian and ALE solvers were compared with experimental data for a full, enclosed vessel, in which waves cannot form. Because the responses of the Lagrangian models with the tie constraint and contact are essentially identical (see Figure 4.4 and Table 4.3), only results for the tie constraint are presented below.

The ALE and Lagrangian models of the full vessel presented here were modified from those in Sections 4.2 and 4.3, respectively: 1) adding a plate enclosing the vessel at the top, and 2) adding elements for water over the full depth of the vessel. The top plate was modeled using three/four-node shell elements assigned an elastic material with the mechanical properties of carbon steel listed in Table 4.1. The ALE model is presented in Figure 4.5, and the Lagrangian model is presented in Figure 4.6. The top plate for both models is shown in orange. The water is shown in yellow. For the ALE model, a layer of solid elements, shown in light grey in Figure 4.5b, was built for a layer of void space at the top of the tank. The void space had zero pressure and generated a free surface at the top surface of the fluid (yellow elements).

(a) isometric view   (b) cutaway view
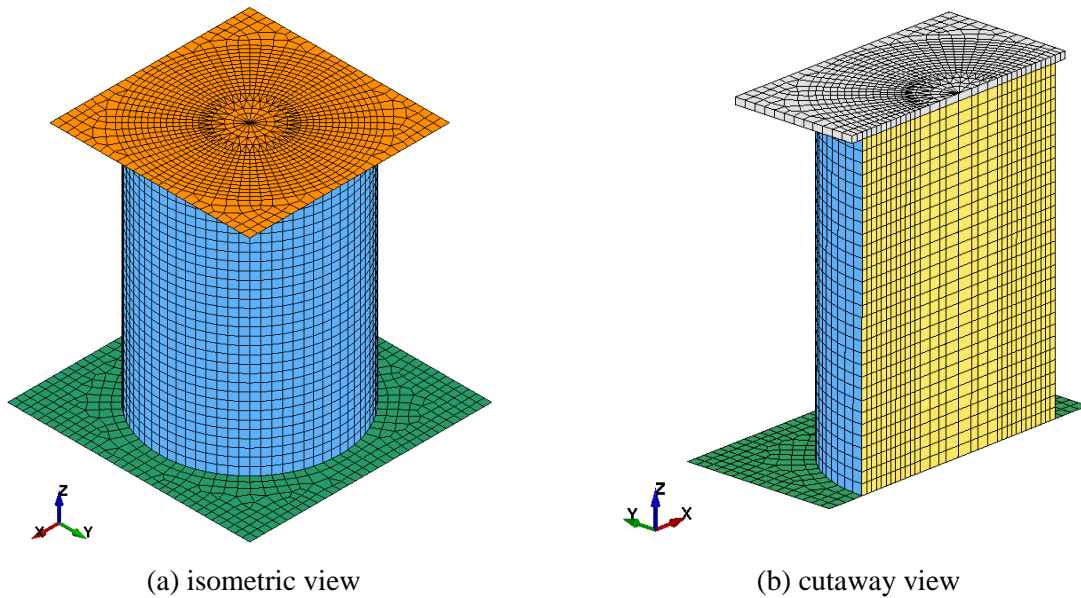
Figure 4.5. ALE model of the test vessel, 100%-filled with water

(a) isometric view   (b) cutaway view
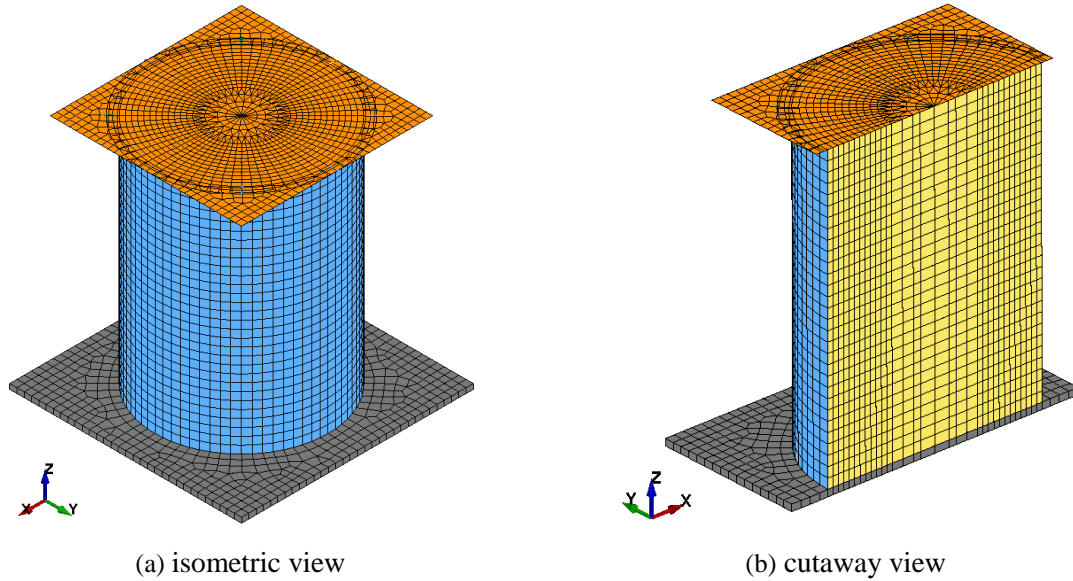
Figure 4.6. Lagrangian model of the test vessel, 100%-filled with water

Figure 4.7 enables a comparison of response histories to the 1D CCE motion obtained from the ALE model, Lagrangian model, and experiment: pressures at two heights (PE1 and PE3), base shear in the x direction, and base moment about the y axis. Table 4.4 presents the maximum absolute values of the numerical and experimental results, their percentage differences, and cross-correlation coefficients (R). Results from analysis of the ALE and Lagrangian models and the experimental data are in reasonable agreement: differences are all less than or equal to 17%. The Lagrangian model, however, is computationally efficient with a run time that was shorter than that of the ALE model by a factor of four.
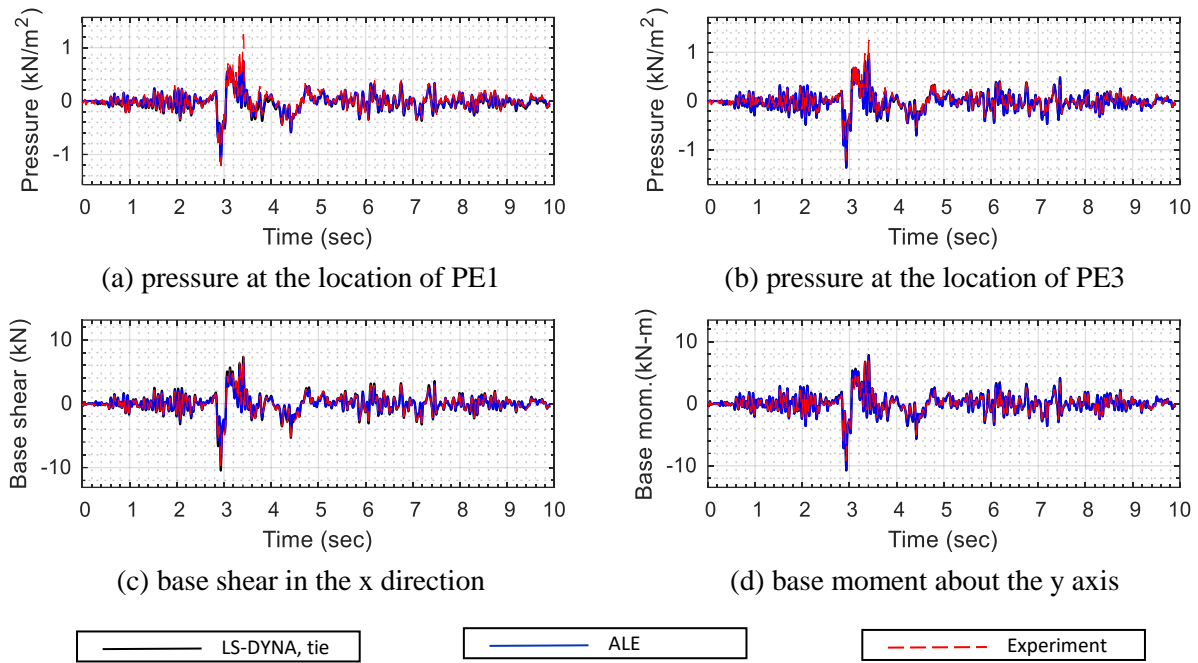
Figure 4.7. ALE, Lagrangian, and experimental response histories of the 100%-filled, enclosed test vessel, 1D CCE motion

Table 4.4. Maximum absolute responses of the fully filled test vessel for the 1D CCE, extracted from the time series of Figure 4.7, ALE, Lagrangian models, and experiments, percentage differences, and cross-correlation coefficients (R)

Response (or location)	Model		Experiment	Difference, % (R)	
	Lagrangian-approach (tie)	ALE		Lagrangian-approach (tie)	ALE
PE1, kN/m^2	1.1	1.1	1.2	-9 (0.95)	-9 (0.96)
PE3, kN/m^2	1.1	1.1	6.9	-16 (0.90)	-14 (0.90)
Shear-x, kN	10.5	8.9	9.8	7 (0.99)	-9 (0.98)
Moment-y, kN-m	10.8	10.6	9.2	17 (0.98)	15 (0.98)

4.5　　Summary and conclusions

Numerical models were built for the base-supported cylindrical vessel used in the experiments presented in Section 3. Two approaches for seismic FSI analysis in LS-DYNA were considered: ALE and Lagrangian elastic-fluid.

The ALE model of the test vessel, filled with water to 80% of its capacity, was validated using 9 sets of multi-directional seismic inputs. For the motions considered in this study, the hydrodynamic responses measured in the experiments and predicted by the ALE model were in good agreement. The average differences in peak responses were less than 10%. The Lagrangian model of the 80%-filled vessel was analyzed for a unidirectional horizontal input motion. Interaction between the fluid and the vessel was defined using two methods, and the analyses were performed separately: tie constraint or contact. The two methods of defining the interaction yielded similar results, but neither calculated wave heights correctly: convective responses cannot be recovered.

The capability of the ALE solver and the Lagrangian approach of analyzing impulsive responses was investigated using the test vessel filled with water fully. Convective responses were suppressed in the full vessel. Analysis results of the 100%-filled vessel calculated using the ALE model and the Lagrangian model with the tie constraint were compared with experimental data. Numerical predations from both models and experimental data were in reasonable agreement. The Lagrangian model was computationally more efficient.

Based on the investigations of the ALE and Lagrangian models, the Lagrangian approach should only be used for analyzing fluid-structure systems for which convective responses are not significant (e.g., full vessels or vessels with a large ratio of fluid height-to-diameter). The ALE approach should be used analysis if convective contributions to the hydrodynamic responses are significant and/or of interest.

SECTION 5

EXPERIMENTAL STUDIES ON SUBMERGED COMPONENTS

5.1   Introduction

This section describes the Phase II tests of a fluid-filled base-supported vessel. (Phase I tests were described in Section 3.) Simplified representations of components submerged in a reactor vessel (described hereafter as internals) were included in the Phase II tests. Unidirectional, bidirectional and three directional seismic motions were input to the specimen and submerged component responses were recorded. The effects of base isolation were studied using ground motions that account for *virtual* base isolation systems, similar to those described in 3.5.1. The tests are grouped into three series: test series 1 through 3.

Section 5.2 describes the test specimens and the objectives of the three test series. 5.3 presents the input motions used for the experiments. Sections 5.4 and 5.5 present results of *in-air* and *in-water* identification tests, respectively. Section 5.6 presents a study on the impact of seismic isolation on hydrodynamic responses by comparing test results for ground-motion inputs and *isolated* inputs that were generated assuming virtual isolation systems. Section 5.7 summarizes the test program and presents conclusions.

5.2   Test series

Submerged internal components were tested in three test series, referred as test series 1, 2, and 3 hereafter. A 25.4 mm thick square steel plate with plan dimensions of 1.67 m $\times$ 1.67 m, referred to as the *head* herein, was attached as a cover to the water-filled (fill level: 80%) base-supported vessel described in Section 3. Internals with different geometries were attached to the head for testing. A description of the specimen and the objectives for each test series are presented in this section. The instrumentation used for each test series is also described.

The layout of accelerometers, load cells, and pressure gages on the vessel was similar to that described in Section 3.2 with a few modifications: pressure gages PN1, PN2, and PN3 were disengaged; uniaxial and biaxial accelerometers (instead of tri-axial accelerometers) were used near the mid-height and top of the vessel, respectively, and a tri-axial accelerometer was placed at the center of the head (AHCX, AHCY, and AHCZ), as shown in Figure 5.1. Four float-and Temposonic based sensors, as shown in Figure 3.2c, were used to record wave heights in all test series. Slots were provided in the head to accommodate these sensors. Stain data on the vessel wall were collected using four rosettes (Make: Micro-Measurements; Model: CEA-06 250UR-120/P2) on the outer face of vessel wall, 50 mm above the base.

83
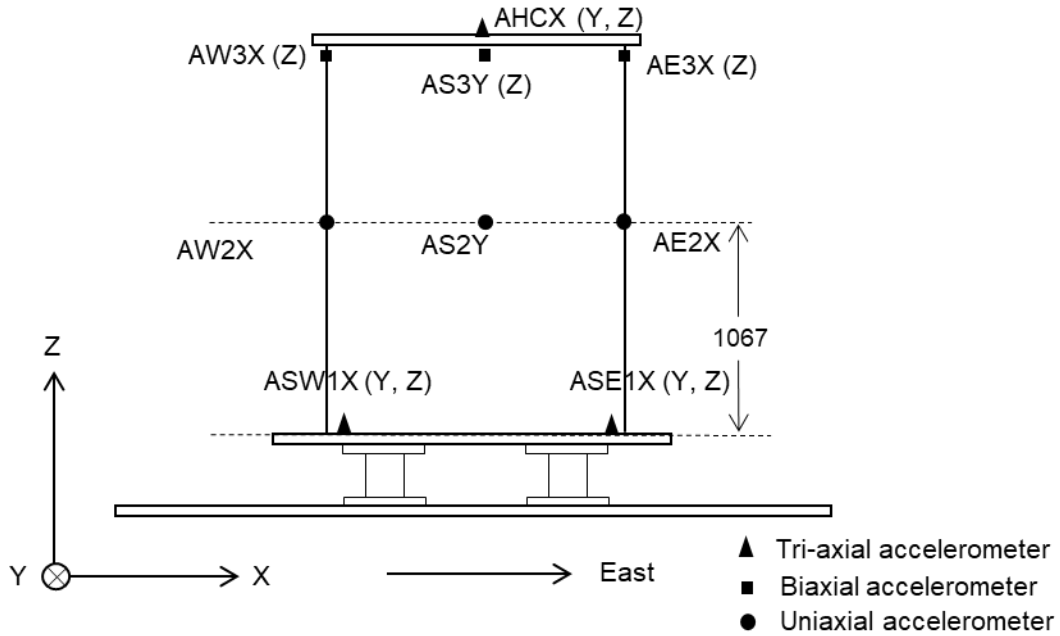
Figure 5.1. Layout of accelerometers used on the vessel wall and base in Phase II tests

5.2.1 Test series 1

Test series 1 involved a steel tube (0.32 m outer diameter, 1.52 m long, and 6.4 mm thick) attached to the head and placed centrally in the water-filled vessel; see Figure 5.2. (The tube is referred to as the *central internal* hereafter.) The primary objective of this test series was to generate acceleration and pressure histories on the wall of the internal for different seismic inputs. The base of the central internal was sealed using a 12.5 mm thick circular disk to prevent the ingress of water. Three pressure gages were installed on the wall of the internal as shown in Figure 5.3. Three directional acceleration response was measured at the end of the internal using a tri-directional Micro-Electro-Mechanical Systems (MEMS) accelerometer (Make: Analog Devices Inc.) waterproofed using an epoxy compound. One such accelerometer is shown in Figure 5.4.

Figure 5.2. Test series 1 specimen, central internal
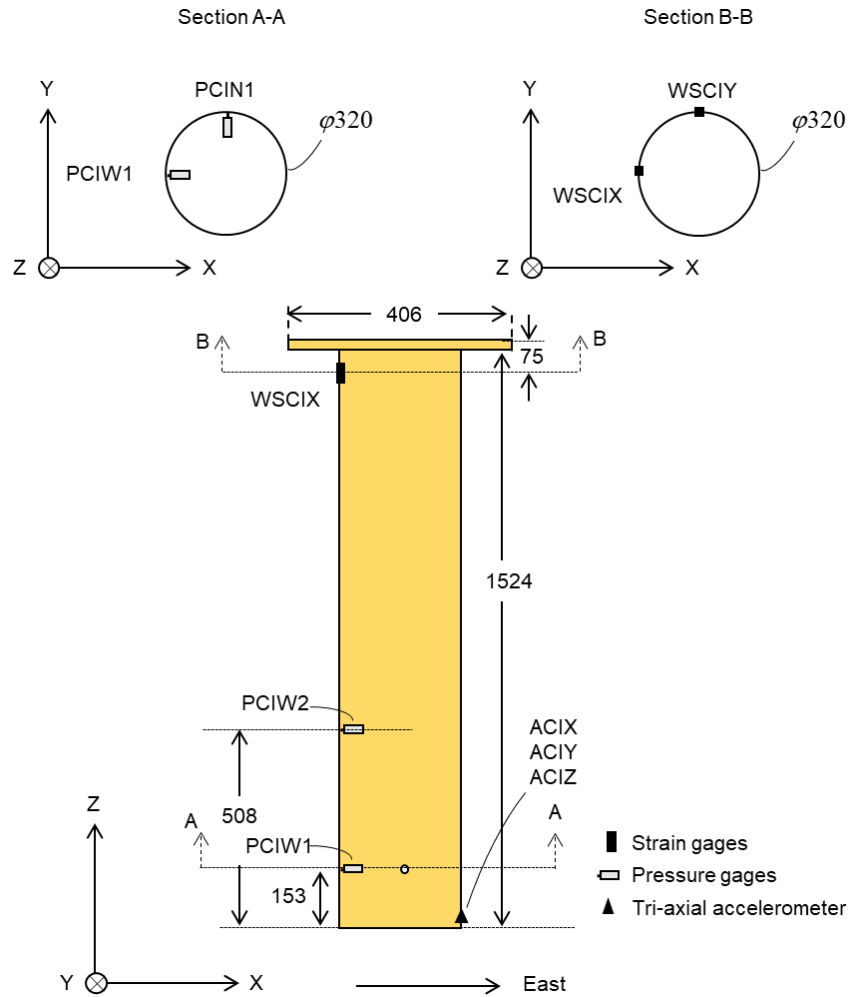
Figure 5.3. Instrumentation for the central internal, dimensions in mm
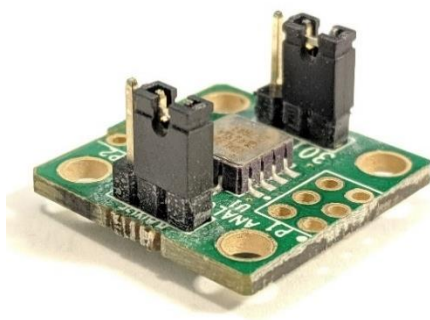
(a) MEMS accelerometer (circuit board)   (b) epoxy encapsulated tri-axial accelerometer
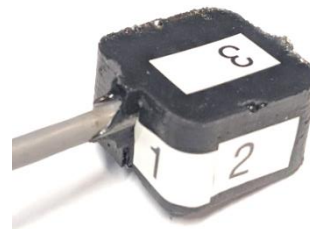
Figure 5.4. Waterproofed accelerometer

5.2.2 Test series 2

Test series 2 involved a 1.83 m long steel plate, 12 mm × 150 mm in cross section (Figure 5.5a), tested at two different distances from the vessel wall, in two test configurations, as shown in Figure 5.5b and Figure 5.5c. (This internal is referred to as the *steel plate internal* hereafter.) The objective of the test series was to study added mass and damping effects for the plate in the two configurations and generate acceleration and strain response histories for the plate with the vessel subjected to different seismic inputs.

(a) steel plate internal attached to vessel head
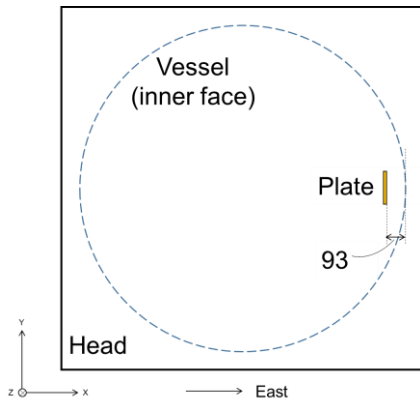
(b) configuration A, plan view
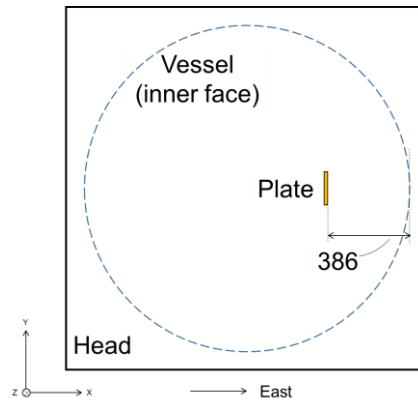
(c) configuration B, plan view

Figure 5.5. Test series 2 specimen, dimensions in mm

Two tri-axial accelerometers were installed at the bottom and mid-height of the plate and two strain gages were installed near the point of attachment to the vessel head, as shown in Figure 5.6.
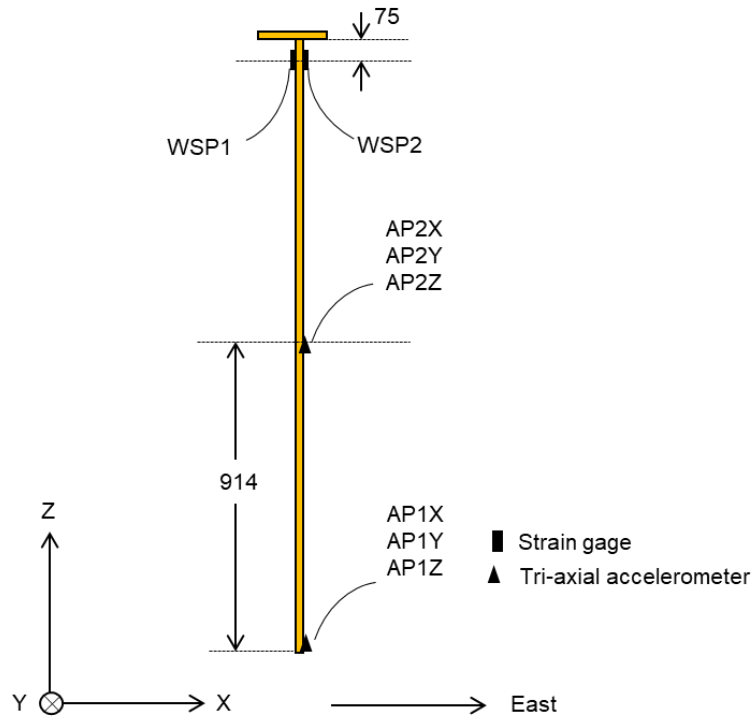
Figure 5.6. Instrumentation for steel plate internal in test series 2, dimensions in mm

5.2.3 Test series 3

Test series 3 involved two 1.83 m long aluminum internals, with diameters of 76 mm and 152 mm, tested in three configurations (A through C). (These internals are referred as the *76 mm diameter internal* and the *152 mm diameter internal* hereafter.) Three specimens were fabricated; see Figure 5.7a. The wall thicknesses for the 76 mm and the 152 mm diameter internals were 1.7 mm and 3.2 mm, respectively. Steel discs weighing 4.82 kg and 9.88 kg, respectively, were attached at their ends (Figure 5.7b) to adjust (reduce) their natural frequencies. (Water could enter the interior of these internals.) The three test configurations are shown in Figure 5.7c. The objective of test series 3 was to study added mass, added damping and coupling effects for the internals and, similar to test series 2, generate acceleration and strain response histories for the internals with the vessel subjected to different seismic inputs.

(a) internals for test series 3

(b) weight attached at the end of an internal
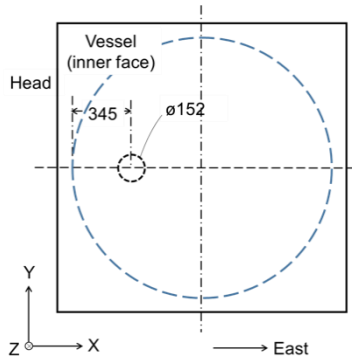
(c) configuration A
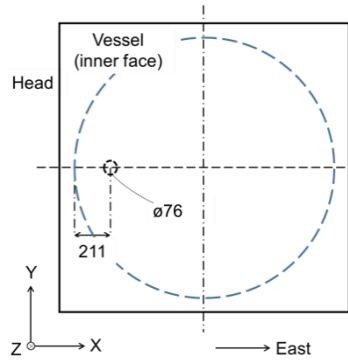
(d) configuration B
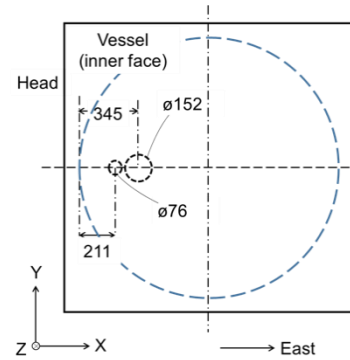
(e) configuration C

Figure 5.7. Specimens and layout for test series 3, plan views, dimensions in mm

Two tri-axial accelerometers and two strain gages were installed on each internal. The instrumentation of the internals in test series 3 is shown in Figure 5.8.
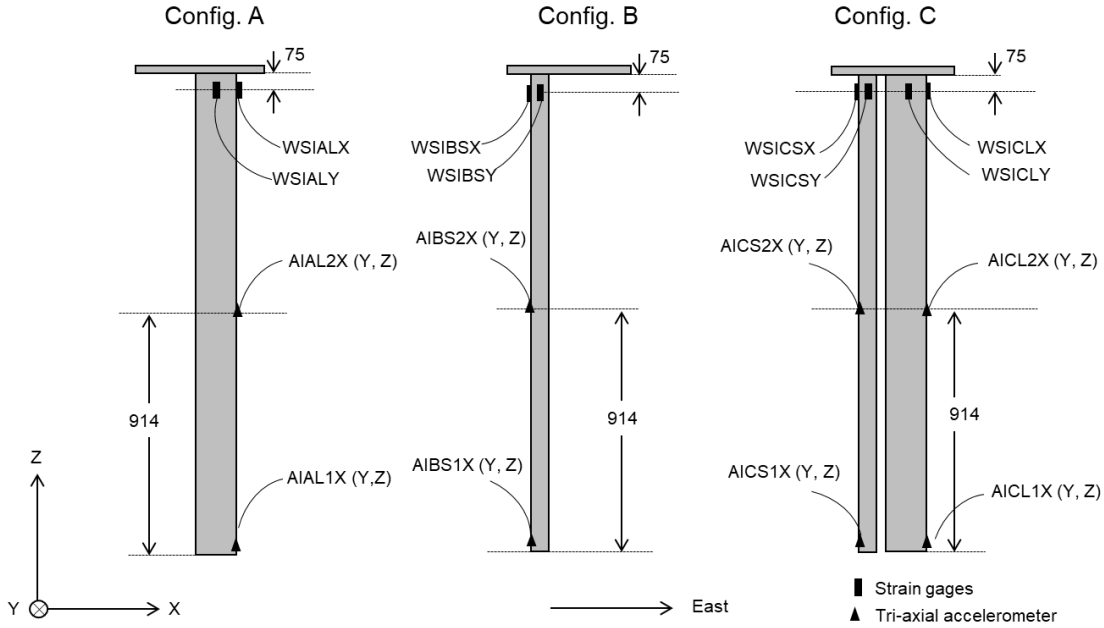
Figure 5.8. Instrumentation for internals in test series 3, dimensions in mm

5.3   Earthquake-simulator inputs and virtual isolation

The earthquake-simulator inputs introduced in Table 3.1 were used for testing, together with white noise and sinusoidal excitations. For test series 1 and test series 3, unidirectional, bidirectional, and tri-directional inputs were used. For test series 2 (steel plate internal), only unidirectional inputs were used. Motions simulating three virtual friction pendulum (FP) isolation systems, as described in Section 3.5, were used for testing. Lists of the input motions used for the tests are presented in Table C.4 through Table C.6 of Appendix C.

The virtually isolated inputs were generated using two lumped-mass models in SAP2000 (CSI 2019): 1) a model representing the test series 1 specimen that included the vessel, contained water, head, and the central internal and 2) a model representing the test series 2 and test series 3 specimens that included the vessel, contained water, and the head. (The mass of the steel plate internal in test series 2 and the aluminum internals in test series 3 was neglected. The two SAP models were similar except for a slight difference in total mass.) The impulsive and the convective modes were characterized identically in the two models (as described in Section 3.5). Figure 3.10 shows the two SAP models, each including four lumped masses shown as blue solid circles: m_v, m_b, m_i, and m_c, for simulating the vessel (including the mass of the head, the flange, and the central internal in SAP model 1), the base plate, and the contained water participating in the impulsive mode and the convective mode, respectively. Friction pendulum isolators were modeled using two-node link elements, shown in red in Figure 3.10. The isolators were assumed to be rigid in the

90

vertical direction. The mass m_b was placed just above the isolator. The mass m_v was placed at the center of mass of the components it represents and the masses m_i and m_c were placed at locations per Malhotra *et al.* (2000). The values of lateral stiffness of the supporting springs, k_i and k_c, were calculated per Malhotra *et al.* (2000). The Malhotra solution is derived for a fluid-filled cylindrical tank without internals. The effect of internals is thus ignored in the calculation of SAP model parameters here.

| (a) SAP Model 1 for test series 1 specimen | (b) SAP Model 2 for test series 2 and 3 specimens |

$m_c = 664\ kg$
$k_c = 15735\ N/m$
$h_c = 1.255\ m$
$m_v = 1316\ kg$
$k_v = \infty$
$h_v = 1.53\ m$
$m_i = 2300\ kg$
$k_i = 1.8 \times 10^9\ N/m \approx \infty$
$h_i = 0.803\ m$
$m_b = 1424\ kg$

$m_c = 664\ kg$
$k_c = 15735\ N/m$
$h_c = 1.255\ m$
$m_v = 1207\ kg$
$k_v = \infty$
$h_v = 1.53\ m$
$m_i = 2300\ kg$
$k_i = 1.8 \times 10^9\ N/m \approx \infty$
$h_i = 0.803\ m$
$m_b = 1424\ kg$
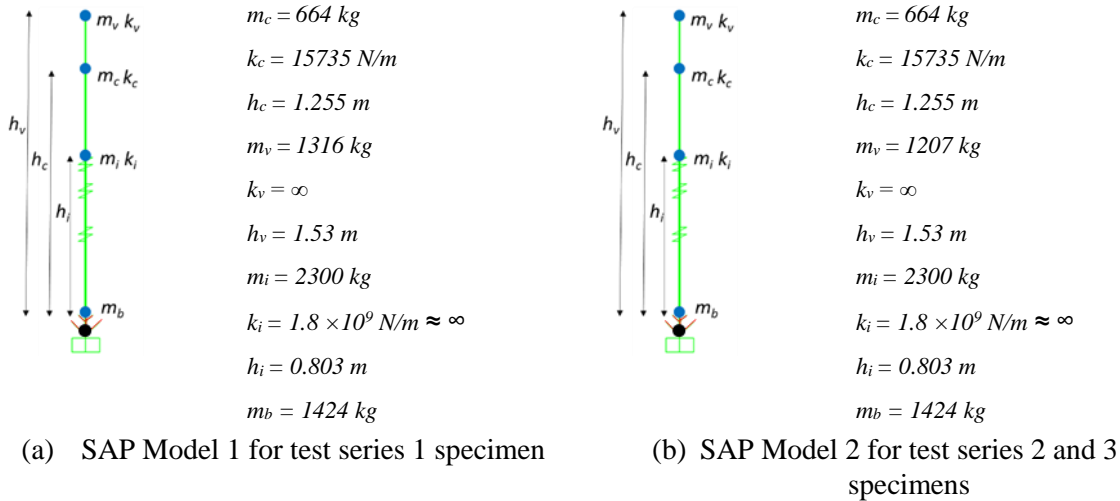
Figure 5.9. SAP models used for generation of *isolated* motions

The properties used for modeling the isolation systems (IS#1, IS#2 and IS#3) with sliding periods of 0.7 sec, 1 sec and 1.3 sec are listed in Table 5.1 and Table 5.2.

Table 5.1 : Isolator properties used for SAP Model 1 (test series 1)

System name	IS#1	IS#2	IS#3
Period	0.7 sec	1.0 sec	1.3 sec
Total weight, W	55956 N	55956 N	55956 N
Pendulum radius, R	0.122 m	0.248 m	0.419 m
Friction coefficient (fast), μ_f	0.06	0.06	0.06
Friction coefficient (slow), μ_s	0.03	0.03	0.03
Yield displacement, u_y	1 mm	1 mm	1 mm
Post-elastic stiffness, $K_{pe} = \dfrac{W}{R}$	458655 N/m	225629 N/m	133546 N/m
Elastic stiffness, $K_e = \dfrac{\mu_f W}{u_y}$	3357360 N/m	3357360 N/m	3357360 N/m

Table 5.2 : Isolator properties used for SAP Model 2 (test series 2 and 3)

System name	IS#1	IS#2	IS#3
Period	0.7 sec	1.0 sec	1.3 sec
Total weight, W	54887 N	54887 N	54887 N
Pendulum radius, R	0.122 m	0.248 m	0.419 m
Friction coefficient (fast), μ_f	0.06	0.06	0.06
Friction coefficient (slow), μ_s	0.03	0.03	0.03
Yield displacement, u_y	1 mm	1 mm	1 mm
Post-elastic stiffness, $K_{pe} = \dfrac{W}{R}$	449893 N/m	221318 N/m	130995 N/m
Elastic stiffness, $K_e = \dfrac{\mu_f W}{u_y}$	3293220 N/m	3293220 N/m	3293220 N/m

Figure 3.11 and Figure 5.11 present the response spectra of the input motions (#4, #12, #17, #6, #10, #15, #7, #11, and #16 in Table C.4 and #4, #12, #17, #6, #10, #15, #7, #11, and #16 in) and their isolated counterparts, obtained using SAP models 1 and 2, respectively. The reduction in horizontal spectral accelerations at frequencies greater than 2.5 Hz (approximately) due to base isolation is significant for the ECE and KCE motions: see Figure 3.11b, c, e, f, h, and i and Figure 5.11b, c, e, f, h, and i. The vertical components of the 3D inputs are unaffected by the used isolation systems (rigid vertically) and so their z-

direction spectra are identical. For the low amplitude CCE motion (PGA < 0.12g), the effects of isolation are insignificant because the isolator displacements are negligible. (A slight amplification in the isolated spectra at low frequencies is observed for the low amplitude CCE motion and is discussed in Section 5.7.)

(a) 1D CCE (b) 1D ECE (c) 1D KCE

(d) 2D CCE (e) 2D ECE (f) 2D KCE

(g) 3D CCE (h) 3D ECE (i) 3D KCE
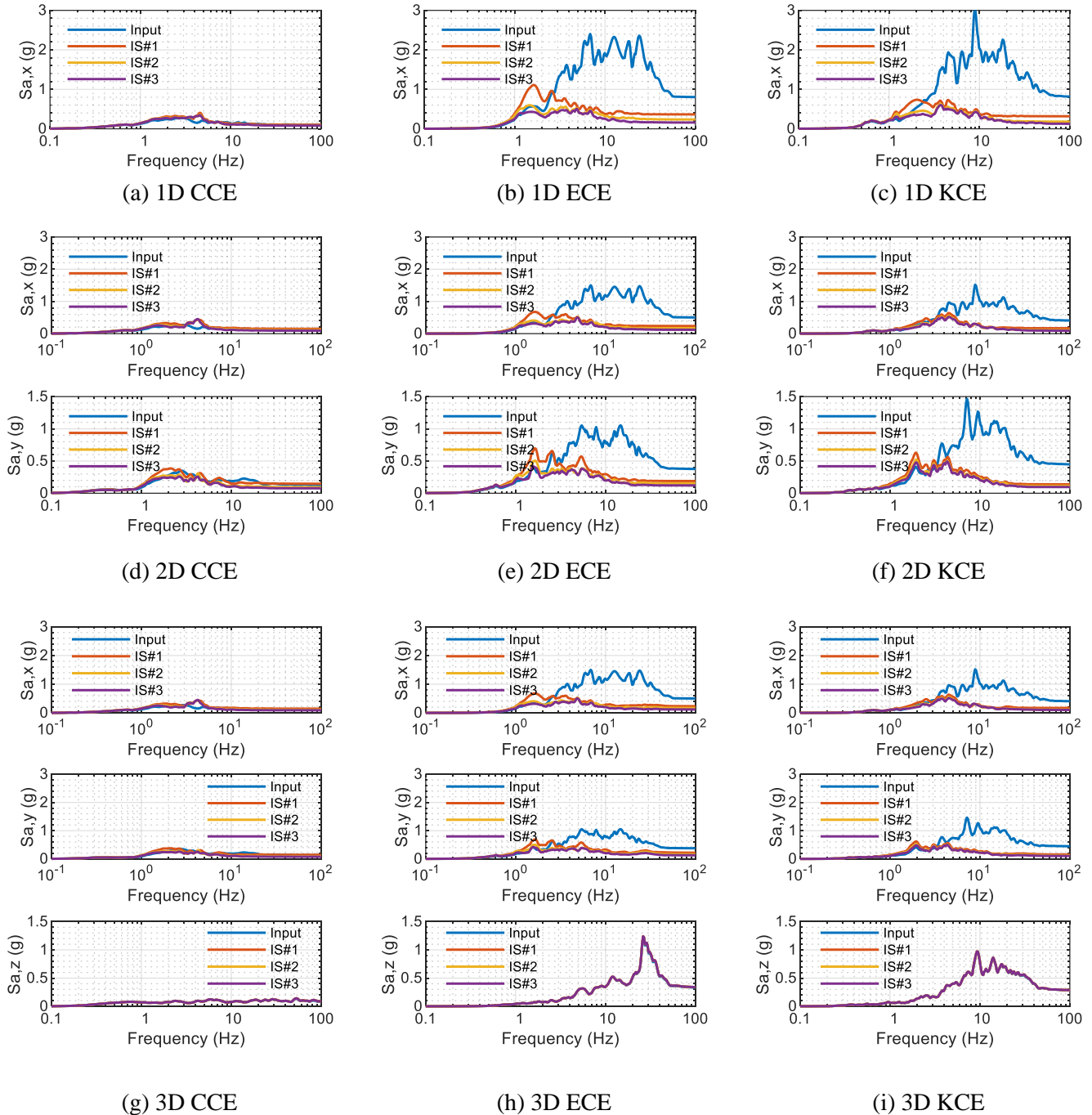
Figure 5.10. Response spectra of input and isolated motions, damping ratio of 5%, 1D, 2D, and 3D motions of CCE, ECE, and KCE, SAP model 1

(a) 1D CCE   (b) 1D ECE   (c) 1D KCE

(d) 2D CCE   (e) 2D ECE   (f) 2D KCE

(g) 3D CCE   (h) 3D ECE   (i) 3D KCE
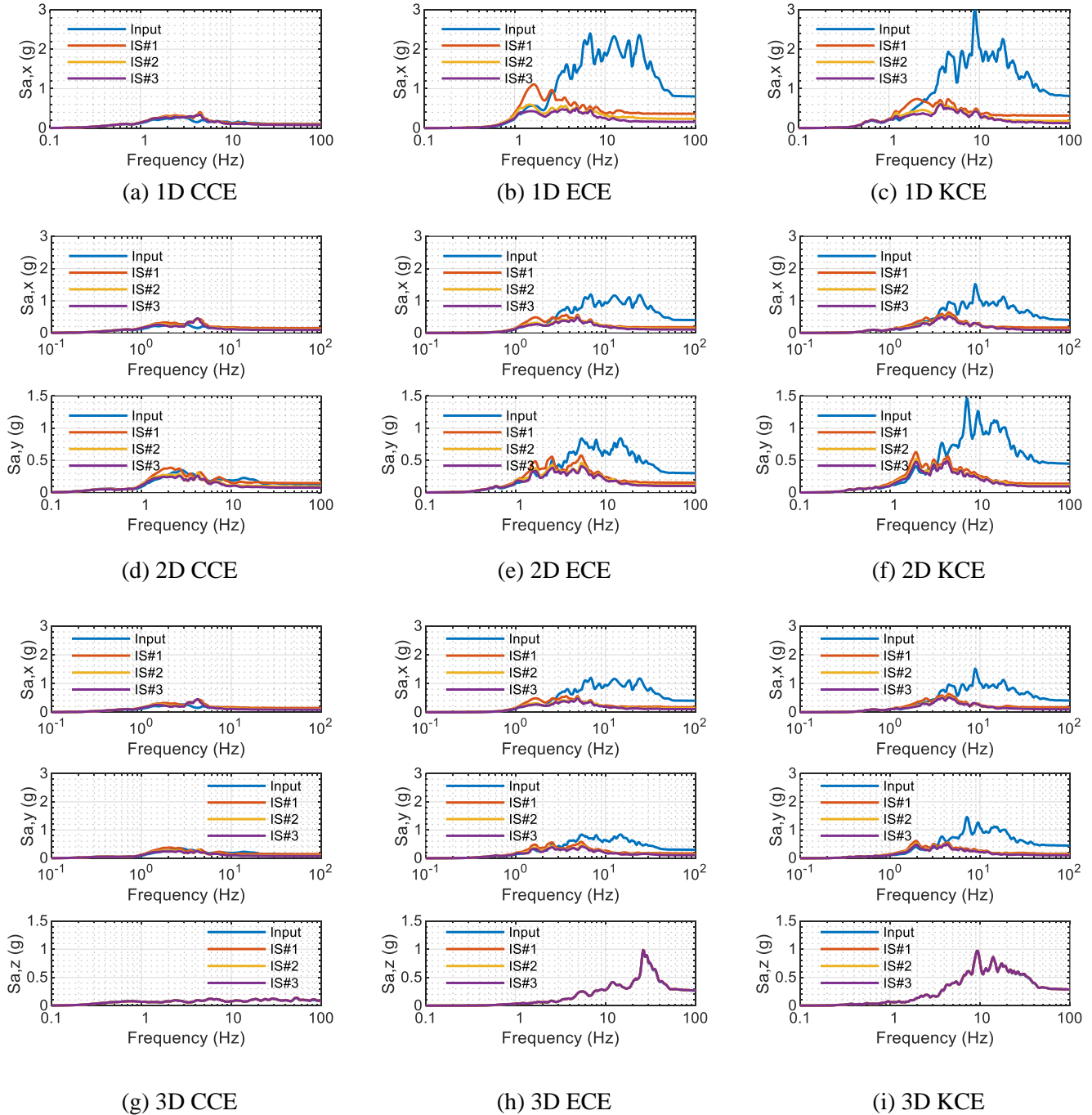
Figure 5.11. Response spectra of input and isolated motions, damping ratio of 5%, 1D, 2D, and 3D motions of CCE, ECE, and KCE, SAP model 2

5.4   *In-air* identification tests

A set of hammer impact tests was carried out to estimate the *in-air* dynamic characteristics (frequency and damping) of the internals. For this purpose, each internal was inverted and attached to the top of head, as shown in Figure 5.12, and hit with an impact hammer. The ensuing acceleration responses were recorded and analyzed. The vessel was empty for these system identification (hammer) tests.

Figure 5.12. Internals attached to the vessel head for hammer impact tests

The responses to hammer impact test were recorded by accelerometers installed at the free ends of the internals. For the central internal of test series 1 and the 76 mm diameter internal of test series 3, the recorded acceleration histories were found to have noticeable beats, as shown in Figure 5.13a and b, indicating excitation of closely spaced vibrational modes (in the two orthogonal directions) due to hammer impact. To evaluate the vibrational characteristics in these two cases, the acceleration response was assumed to be a summation of two modal responses, $R_i(t)$, $(i=1,2)$, with each assumed as:

$$R_i(t) = A_i e^{-\xi_i \omega_i t} \cos(\omega_i \sqrt{1-\xi_i^2} t - \varphi_i) \tag{5.1}$$

where A_i, ξ_i, ω_i, and φ_i are the unknown amplitude, damping, angular frequency, and phase angle for each mode and t denotes time. A non-linear least squares solver in MATLAB (MathWorks 2017) was used to obtain the unknown parameters for the two modes in each case such that the difference between the recorded acceleration and that obtained by superposition of the evaluated modes was minimized in a least squares sense. Figure 5.13c and d show a comparison of the recorded time series and that generated using the obtained parameters for the two internals. The modal frequencies were estimated to be 32.2 Hz and 33.5 Hz for the central internal (average = 32.8 Hz) and 7 Hz and 6.9 Hz for the 76 mm diameter internal (average = 6.95 Hz in the two horizontal directions). The corresponding damping ratios, averaged for the two modes,

were estimated to be 0.45% and 0.03% (of critical)[13] for the central internal and the 76 mm diameter internal, respectively.

(a) beats in acceleration response of the central internal, hammer impact

(b) beats in acceleration response of the 76 mm diameter internal, hammer impact

(c) recorded and fit acceleration series, central internal

(d) recorded and fit acceleration series, 76 mm diameter internal
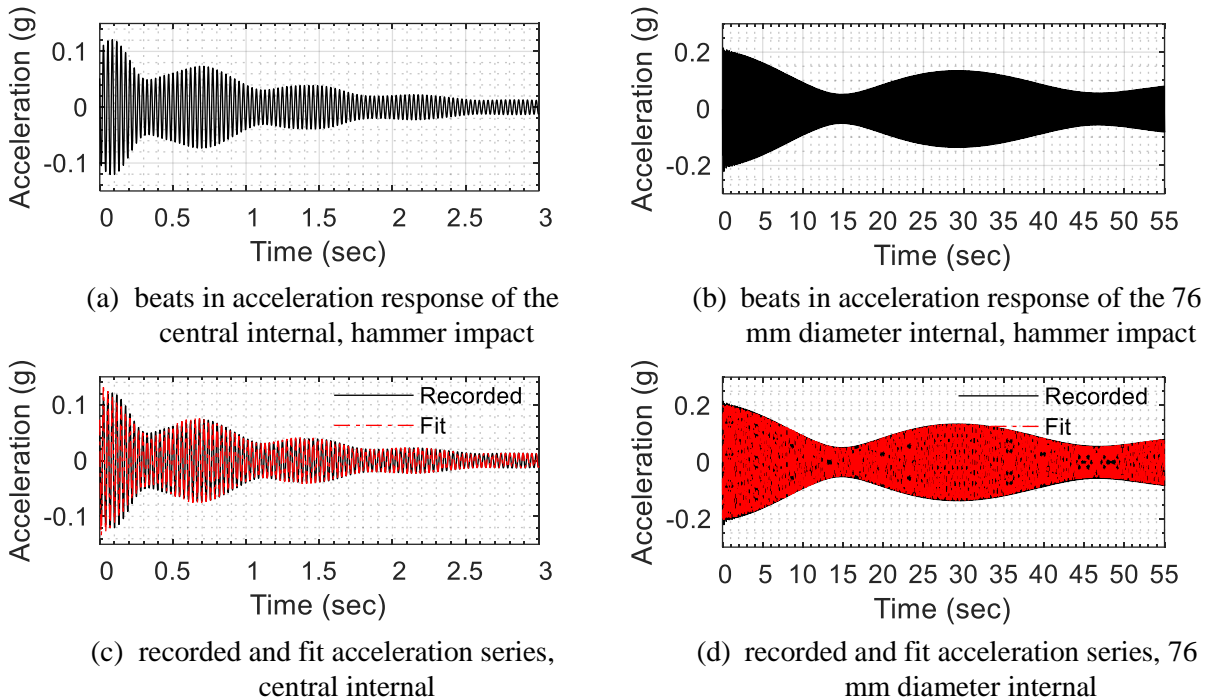
Figure 5.13. Impact hammer test results for the central internal (test series 1) and the 76 mm diameter internal (test series 3)

Figure 5.14a and b present the normalized power spectral density (PSD) plots of the acceleration responses of the steel plate internal of test series 2 and the 152 mm dimeter internal of test series 3, respectively. The first mode frequencies of these two internals were identified as 3.1 Hz and 15.5 Hz, respectively, as indicated in the plots. The damping in the first mode in each case was evaluated by fitting an exponential function (see equation (3.4)) to the modal acceleration history extracted from the measured acceleration time series by applying a band-pass filter centered at the corresponding modal frequency. Figure 5.14c and d present the extracted first mode acceleration time series and the best fit exponential functions for the two internals. The damping was estimated to be 0.04% and 0.06% for the steel plate internal and the 152 mm diameter internal, respectively.

---

[13] The reason for the large damping in the central internal is that unlike other internals, its vibration involves bending of the head. This implies that more connections (8 bolts between head and vessel flange) are 'involved' in the mode - resulting in more damping. This is corroborated by FE analysis presented in the next section.
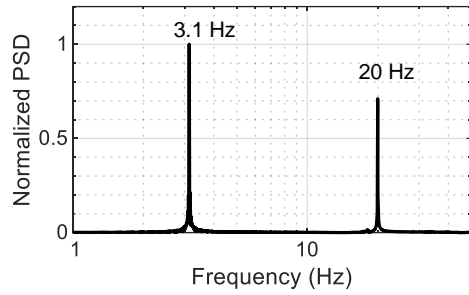
(a) PSD, acceleration response of steel plate internal
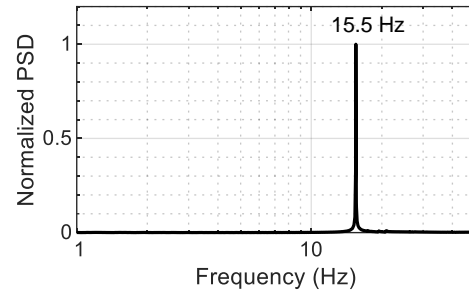
(b) PSD, acceleration response of 152 mm dimeter internal

(c) best fit exponential for first mode response of steel plate internal, t denotes time
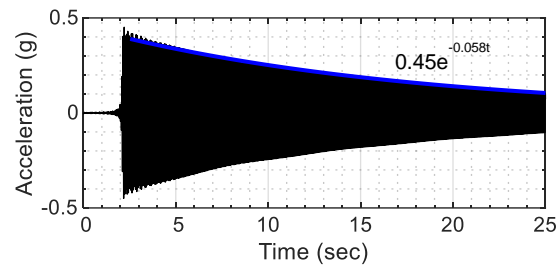
(d) best fit exponential for first mode response of 152 mm diameter internal, t denotes time

Figure 5.14. Impact hammer test results for the steel plate internal (test series 2) and the 152 mm diameter internal (test series 3)

5.5   *In-water* identification tests

Identification tests were also carried out in the submerged state for the internals. For that purpose, and with the exception of the central internal, a string was attached to the lower end of an internal, pulled as indicated in the schematic in Figure 5.15, and then released instantly (i.e., a snap-back test). The ensuing responses were recorded and analyzed.
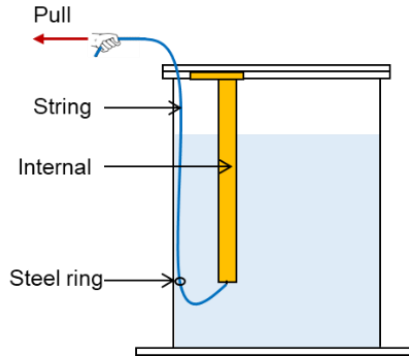
Figure 5.15. Test schematic for *in-water* snap-back tests

Snap-back test results for the submerged steel plate internal in two configurations (test series 2; see Figure 5.5b and c) are presented in Figure 5.16a and b. The first (second) mode frequencies in configurations A and B were 2.07 Hz (13.2 Hz) and 2.25 Hz (13.6 Hz), respectively, indicating a greater added mass in configuration A wherein the plate is located close to the wall of the vessel. The damping ratio in the first mode was estimated by fitting an exponential function to the acceleration response in the first mode as described previously (see Figure 5.16c and d): 1.2% (of critical) for both configurations.

(a) normalized PSD of acceleration response, configuration A

(b) normalized PSD of acceleration response, configuration B

(c) best-fit-exponential for acceleration in first mode, configuration A, *t* denotes time

(d) best-fit-exponential for acceleration in first mode, configuration B, *t* denotes time
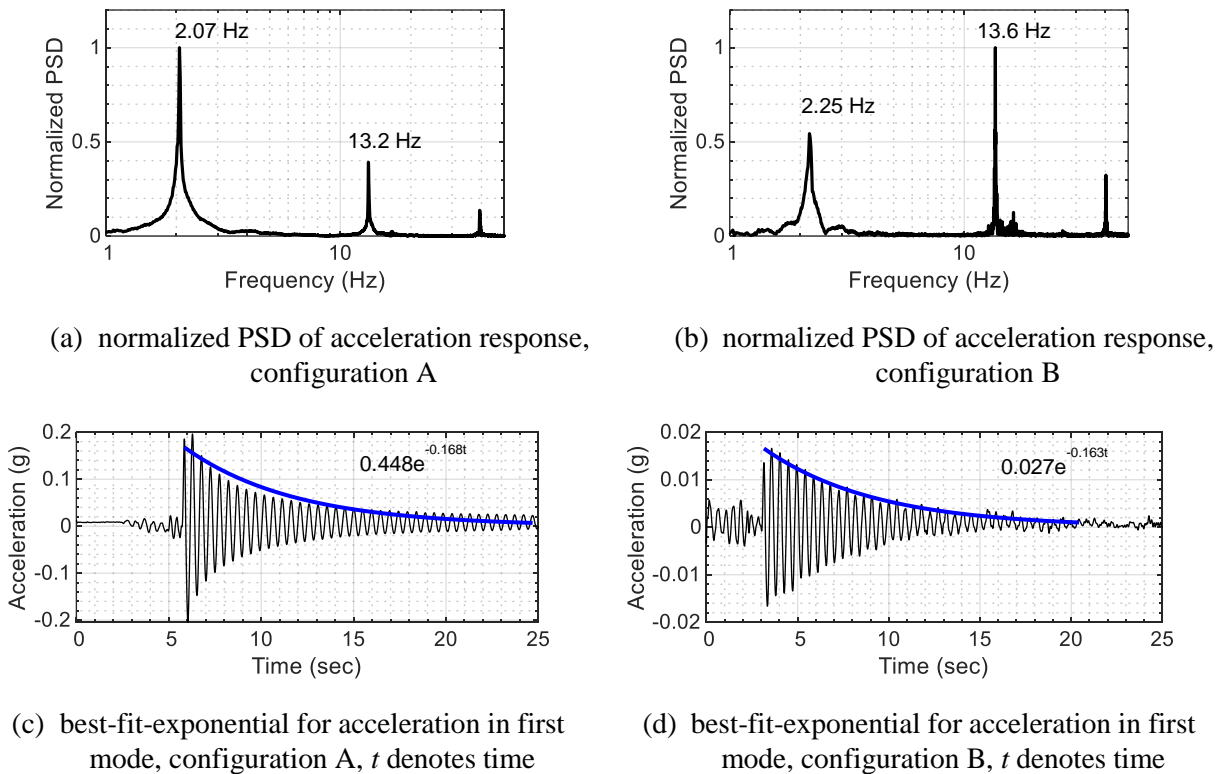
Figure 5.16. Snap-back test results for the submerged steel plate internal in two configurations

98

Snap-back test results for the submerged aluminum tubes in three configurations (test series 3; see Figure 5.7c, d, and c) are presented in Figure 5.17 (normalized PSD plots) and Figure 5.18 (best-fit exponentials for evaluation of first mode damping). The *in-water* frequencies of the 152 mm diameter internal and the 76 mm diameter internal tested separately in configurations A and B of test series 3 were 10.5 Hz and 5.3 Hz, respectively (see Figure 5.17a and b). In the snap-back test results for configuration C (of test series 3), a coupling of responses can be seen in the plot shown in Figure 5.17d, where two peaks are observed in the PSD of the acceleration response of the 76 mm diameter internal, indicating that its response is affected by the vibration of the adjacent 152 mm diameter internal. (For this test, the 152 mm diameter internal was pulled and released.) Damping ratios for first mode were evaluated as described previously (see Figure 5.18) and calculated to be 0.3% for both internals in all (submerged) configurations.
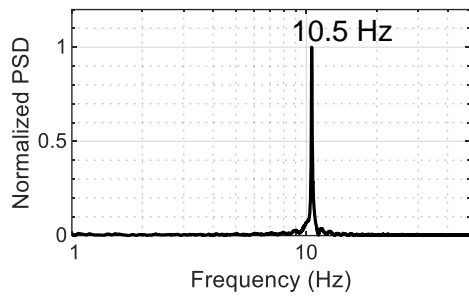
(a) 152 mm diameter internal (test series 3A)
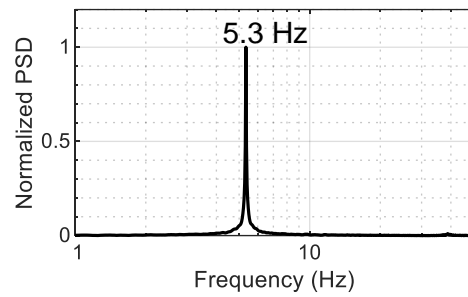
(b) 76 mm diameter internal (test series 3A)
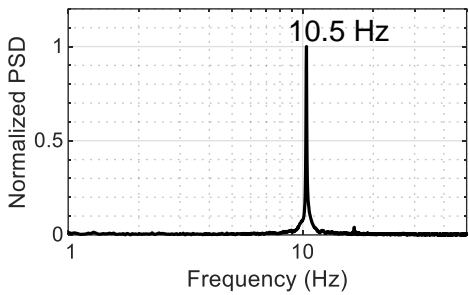
(c) 152 mm diameter internal (test series 3C)
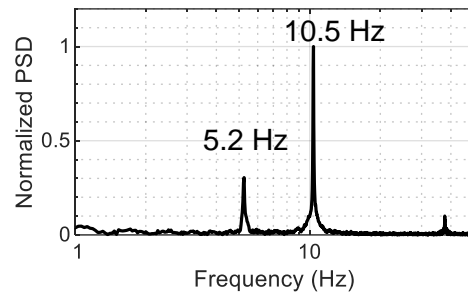
(d) 76 mm diameter internal (test series 3C)

Figure 5.17. Normalized PSD of acceleration responses from snap-back test results of submerged aluminum tubes in test series 3
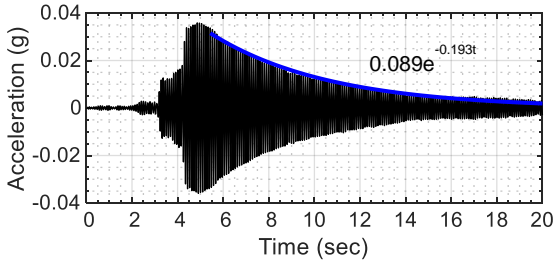
(a) test series 3A (152 mm dia internal)   (b) test series 3B (76 mm dia internal)
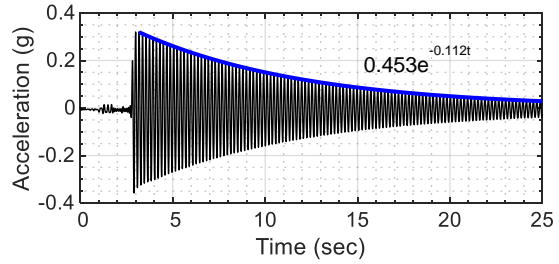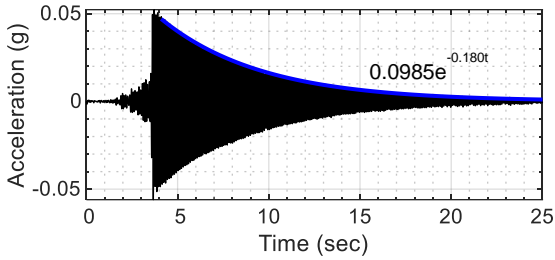
(c) test series 3C (152 mm dia internal)   (d) test series 3C (76 mm dia internal)
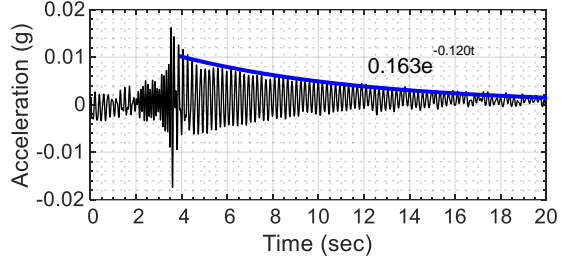
Figure 5.18. Best-fit exponentials for first mode acceleration extracted from snap-back test results of submerged aluminum tubes in test series 3

For the central internal, a snap-back test was not conducted. Instead, its *in-water* frequency was estimated by exciting the vessel with white noise in the horizontal direction and analyzing the acceleration recorded at the free end of the internal. Figure 5.19 presents a normalized PSD plot of the acceleration time series recorded by accelerometer ACIX (see Figure 5.3) when the vessel was subjected to a white noise excitation in a horizontal direction. The *in-water* frequency of the central internal was 21.3 Hz. The i*n-water* damping for the central internal could not be estimated from this test.
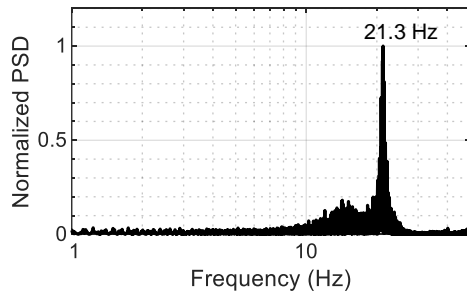
Figure 5.19. Normalized PSD plot of the acceleration recorded by accelerometer ACIX

Table 5.3 presents a summary of the described *in-air* and *in-water* identification tests.

Table 5.3. Summary of identification tests

Internal description		Frequency (Hz)		Damping ratio (%)	
		In-air	*In-water*	*In-air*	*In-water*
Central internal (test series 1)		32.8	21.3	0.45	-
Steel plate internal (test series 2)	Configuration A	3.1	2.07	0.04	1.2
	Configuration B	-	2.25	-	1.2
Aluminum tubes (test series 3)	Configuration A	15.5	10.5	0.06	0.3
	Configuration B	6.95	5.3	0.03	0.3
	Configuration C	-	10.5, 5.2*	-	0.3

*10.5 Hz and 5.2 Hz are the frequencies of the 152 mm diameter internal and the 76 mm diameter internal, respectively.

5.6 Study on seismic isolation using virtually *isolated* inputs

This section describes the effects of seismic isolation on the responses of the submerged components and identifies numerical issues in modeling (friction) isolation systems in SAP2000 for low amplitudes of inputs.

5.6.1 Effect of isolation on responses of internal components

Isolated motions that accounted for the three friction pendulum (FP) isolation systems were generated using numerical models in SAP2000, as described in Section 5.3. The dynamic responses of the submerged internals to the *isolated* motions are used here to identify the benefits of seismic isolation. Rocking motions are not addressed.

Figure 5.20 enables a comparison of peak responses recorded on the central internal for 1D, 2D, and 3D CCE, ECE, and KCE motions (#4, #6, #7, #12, #10, #11, #17, #15 and #16 in Table C.4) and their isolated counterparts (#18 through #44 in Table C.4). Results are presented for pressure recorded by gage PCIW1, denoted as 'Pressure' in Figure 5.20, and accelerations recorded by ACIX, denoted as 'Accel-1' in Figure 5.20 (see Figure 5.3 for the instrumentation layout). The peak response for an input motion is normalized by the maximum peak response recorded for the entire set of inputs considered here. As an example, the peak pressure recorded for input motion #4 per Table C.4 is normalized by the maximum peak pressure recorded for input motions #4, #6, #7, #12, #10, #11, #17, #15 and #16 in Table C.4 and #18 through #44 in Table C.4. The peak pressure at PC1W1 is virtually unaffected by isolation across all motions considered

here. This is because the pressure at the location of this gage is dominated by the convective component, which is not impacted significantly by the isolation systems considered here. (The convective component of hydrodynamic pressure is driven by the low frequency content of an input motion, which is not significantly impacted by isolation; see Figure 3.11 and Figure 5.11. The impulsive component of hydrodynamic pressure, which is affected by isolation, has a maximum magnitude near the walls of the vessel and a minimum magnitude near the center of the vessel and thus does not dominate the pressure response recorded on the internal.) A reduction of more than 60% due to isolation is observed in the peak acceleration recorded by ACIX for the ECE and KCE motions. The reductions for the comparatively low amplitude CCE motion (PGAs ≤ 0.12 per Table C.4) are not significant because the isolator displacements are tiny.
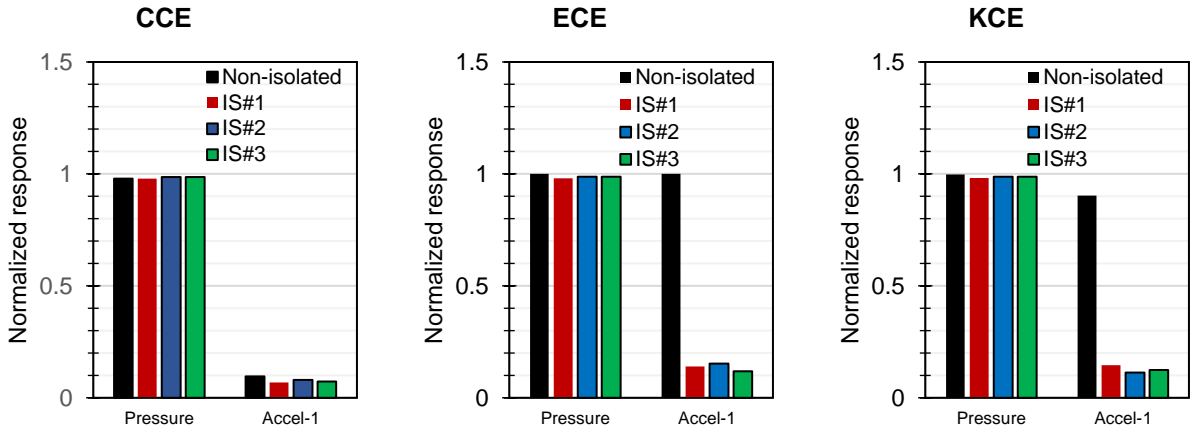
(a) unidirectional inputs (x)
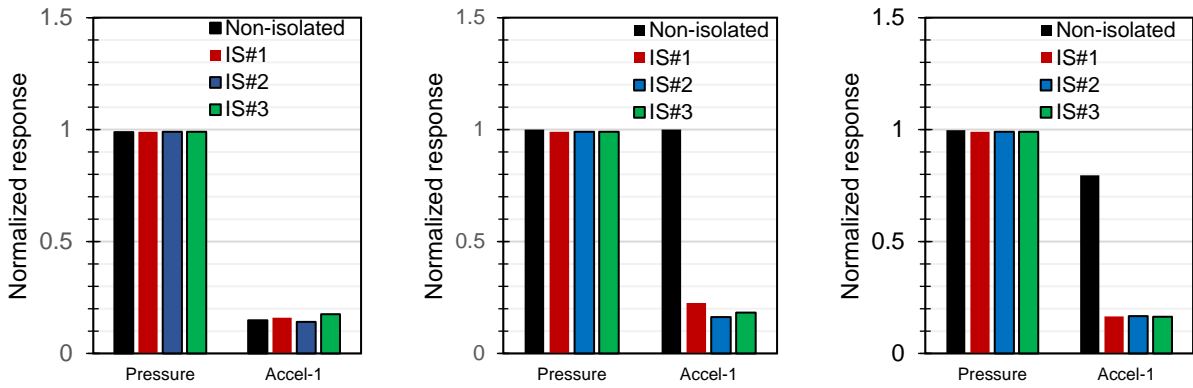
(b) bi-directional inputs (x and y)
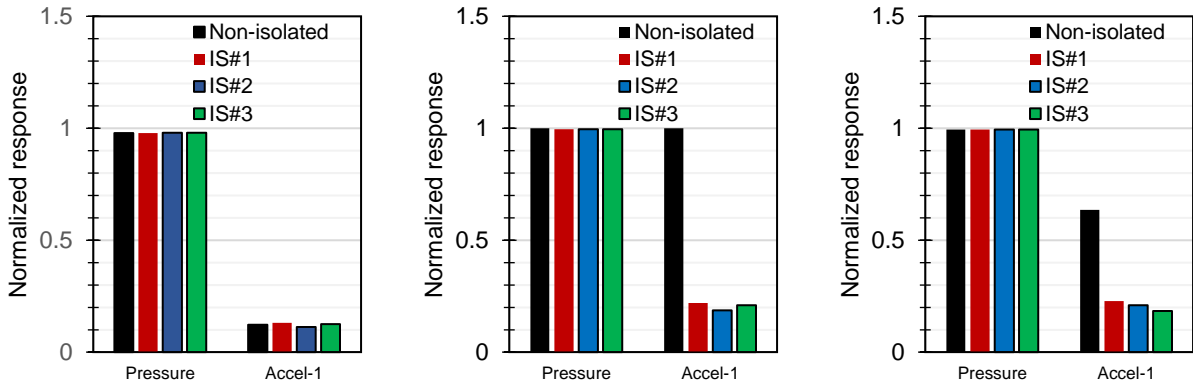
(c) tri-directional inputs (*x, y,* and *z*)

Figure 5.20. Normalized peak responses of the central internal to the non-isolated and *isolated* (IS#1, IS#2, and IS#3) motions

Figure 5.21 enables a comparison of peak responses recorded on the plate internal in configuration B for 1D CCE, ECE, and KCE motions (#4, #6, and #8 in Table C.5) and their isolated counterparts (#9, #11, #13, #14, #16, #18, #19, #21, and #23 in Table C.5). Results are presented for strain recorded by gage WSP1, denoted as 'Strain' in Figure 5.21, and accelerations recorded by AP1X and AP2X, denoted as 'Accel-1' and 'Accel-2', respectively, in Figure 5.20 (see Figure 5.6 for instrumentation layout). The peak response for an input motion is normalized by the maximum peak response recorded for the entire set of inputs considered for comparison here (as explained previously for the case of the central internal). A reduction of at least 40% and 80% is observed in the strain and acceleration responses for the ECE and KCE motions, respectively. The reductions for the low amplitude CCE motion are not significant for the reason given previously. (Slight amplification in responses to the CCE motion is observed due to isolation. This is a numerical artifact and is discussed in Section 5.7.)
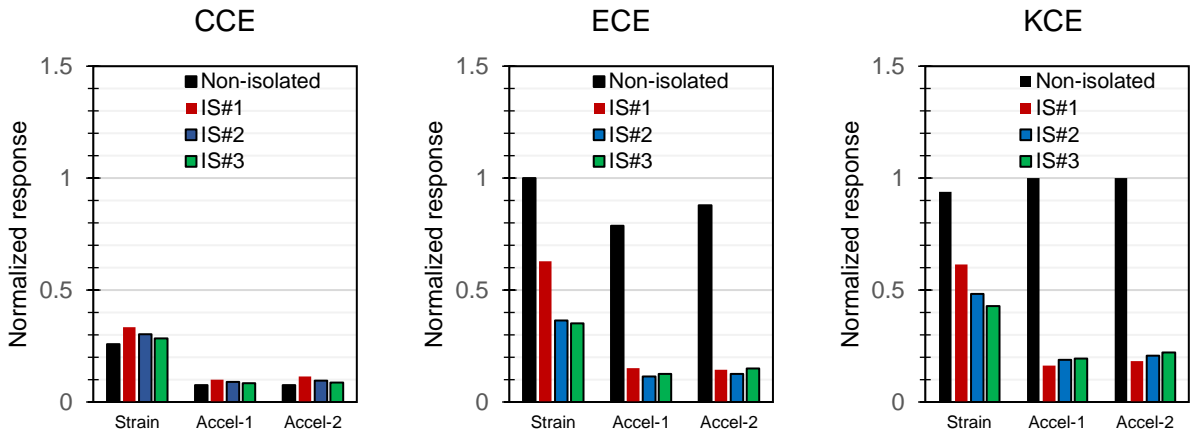
Figure 5.21. Normalized peak responses of the plate internal to the non-isolated and *isolated* (IS#1, IS#2, and IS#3) motions

Figure 5.22 and Figure 5.23 enable a comparison of peak responses recorded on the 152 mm diameter internal and the 76 mm diameter internal in configurations A and B of test series 3, respectively. The 1D, 2D, and 3D CCE, ECE, and KCE motions (#4, #6, #7, #10, #11, #12, #15, #16, and #17 in Table C.6) and their isolated counterparts (#18, #19, #20, #22, #23, #24, #26, #27, #28, #29, #30, #31, #33, #34, #35, #37, #38, #39, #40, #41, #42, #44, #45, #46, #48, #49, and #50 in Table C.6) were used as inputs. Results are presented for strain recorded by gage WSIALX (WSIBSX), denoted as 'Strain' in Figure 5.22 (Figure 5.23), and accelerations recorded by AIAL1X (AIBS1X) and AIAL2X (AIBS2X), denoted as 'Accel-1' and 'Accel-2', respectively, in Figure 5.22 (Figure 5.23); see Figure 5.8 for the instrumentation layout. The

peak response for an input motion is normalized by the maximum peak response recorded for the entire set of inputs considered. A reduction of at least 60% (40%) and 70% (40%) is observed in peak strain and acceleration responses for the ECE and KCE motions in the 152 mm dimeter internal (76 mm dimeter internal). The impacts of seismic isolation for the low amplitude CCE motion are not significant for the reasons presented previously. In some cases (see Figure 5.23) isolation is associated with an increase in response in the CCE motion, which is a numerical artifact, as discussed in Section 5.7.
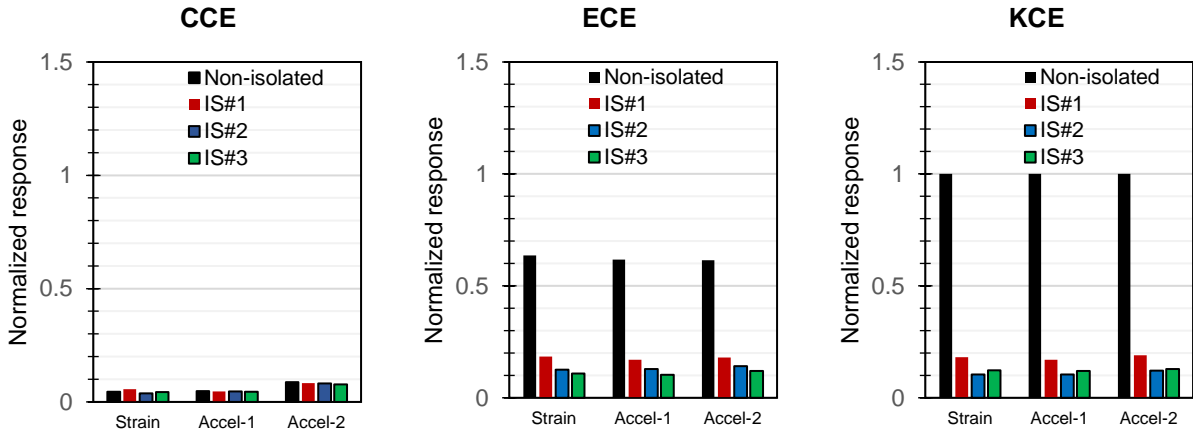
(a) unidirectional inputs (x)
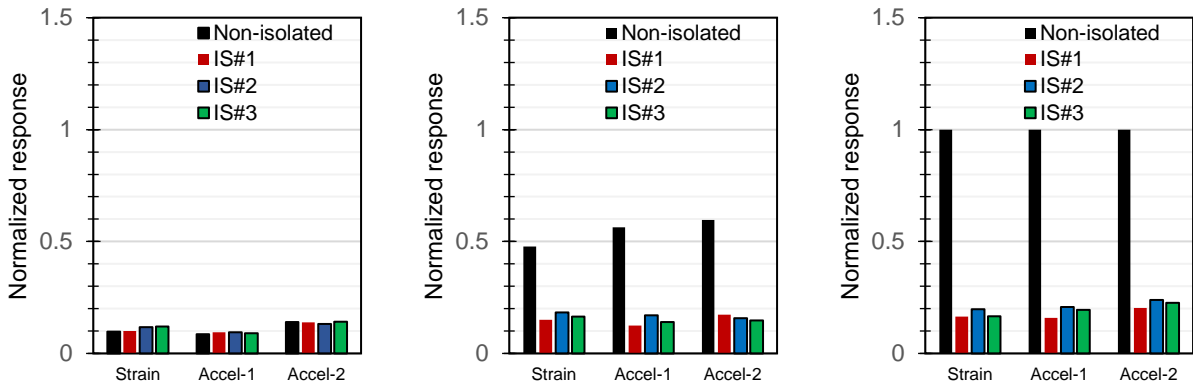
(b) bi-directional inputs (x and y)
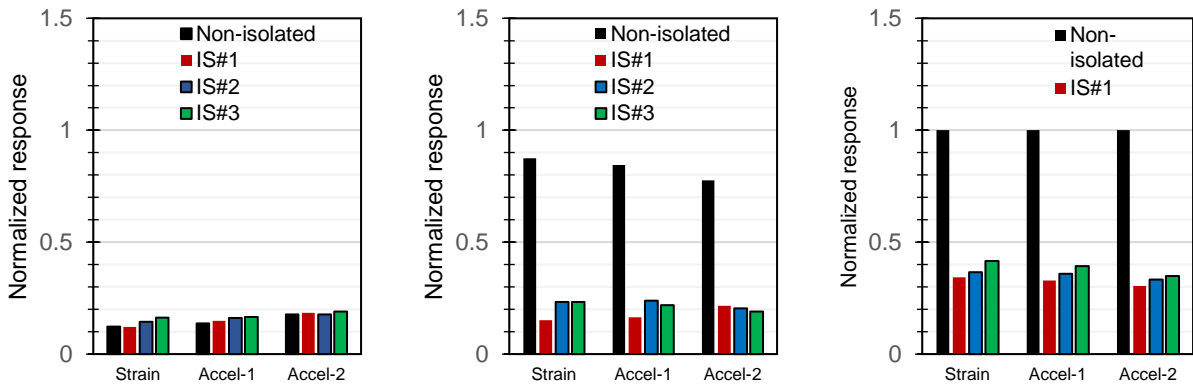
(c) tri-directional inputs (*x*, *y*, and *z*)

Figure 5.22. Normalized peak responses of the 152 mm diameter internal to the non-isolated and *isolated* (IS#1, IS#2, and IS#3) motions
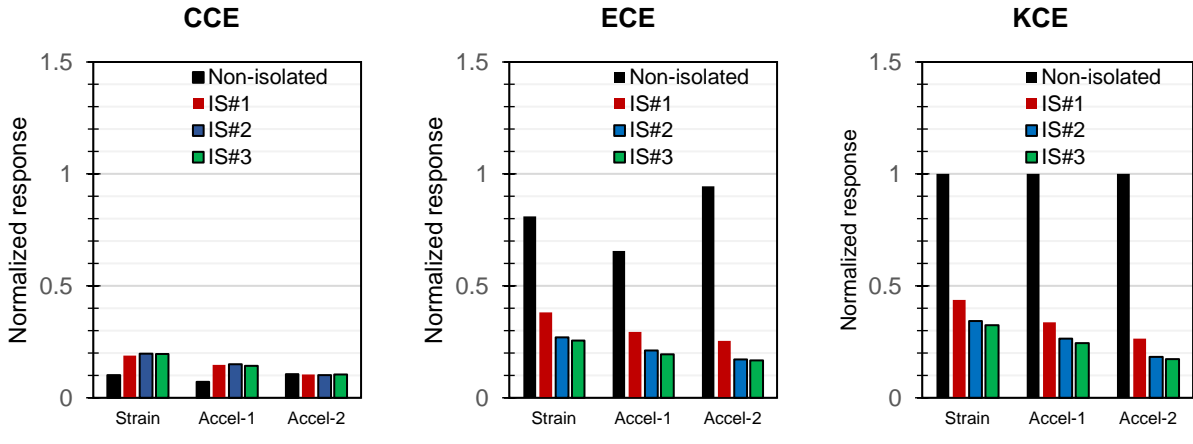
(a) unidirectional inputs (x)
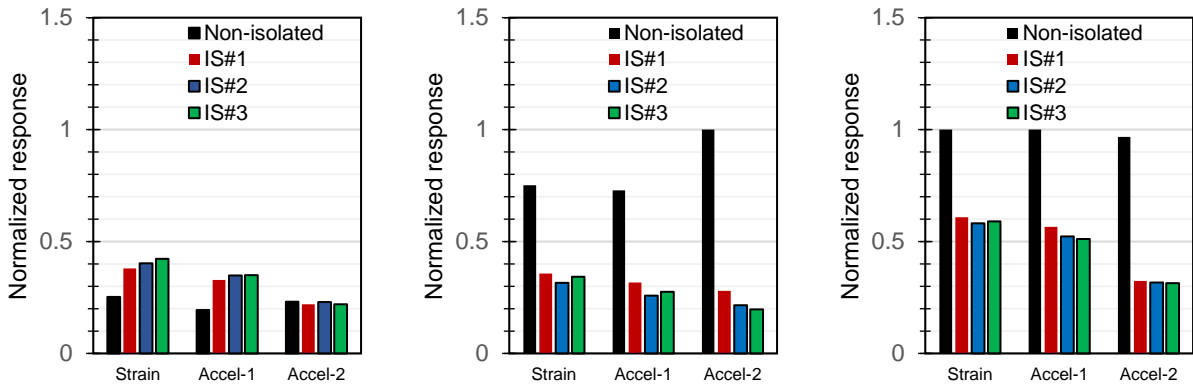
(b) bi-directional inputs (x and y)
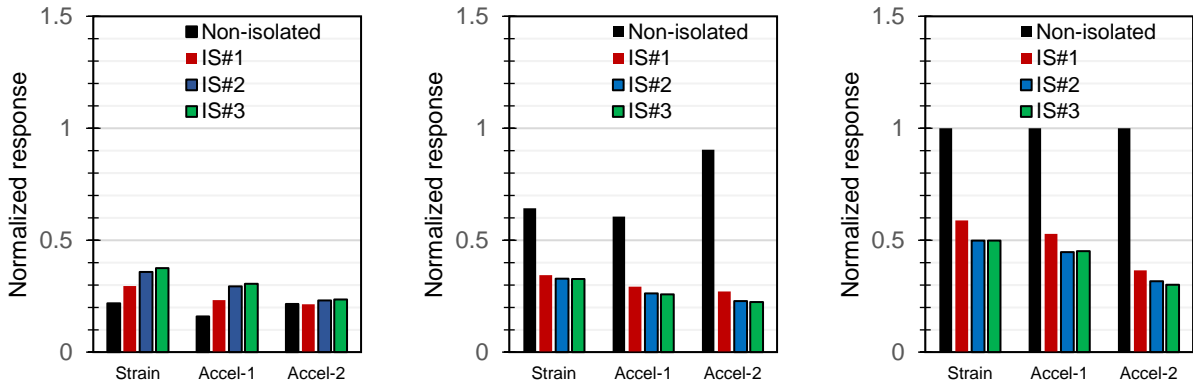
(c) tri-directional inputs (*x*, *y,* and *z*)

Figure 5.23. Normalized peak responses of the 76 mm diameter internal to the non-isolated and *isolated* (IS#1, IS#2, and IS#3) motions

5.7   Numerical amplification in isolated responses for low amplitude inputs

In some cases, the amplification of responses for the CCE input (e.g., Figure 5.23) is a numerical artifact. Figure 5.24a shows the input and isolated (using IS#I) spectra for the CCE motion for SAP model 1 (see Table 5.1 for isolator properties). The corresponding acceleration time series are shown in Figure 5.24b. Amplification in the isolated response is clearly visible from the spectra (at frequencies less than 4.5 Hz) and the time series. For low amplitude inputs, the isolator displacement is dominated by movement in the *elastic* region of the force-displacement loop (see Figure 5.25 and Figure 5.26). For the system under consideration here, this corresponds to an oscillation frequency of 3.9 Hz (i.e., weight of structure = 55956 N, elastic stiffness of isolator = 3357360 N/m). (A similar amplification is observed for the ECE motion if a small input amplitude (= 0.1g) is used, as presented in Figure 5.27.) There is no provision to dampen such oscillations in the elastic region in SAP2000 at this time and as a consequence, the response around the oscillation frequency for low amplitude inputs is amplified.

(a) spectra, damping ratio of 5%

(b) time series
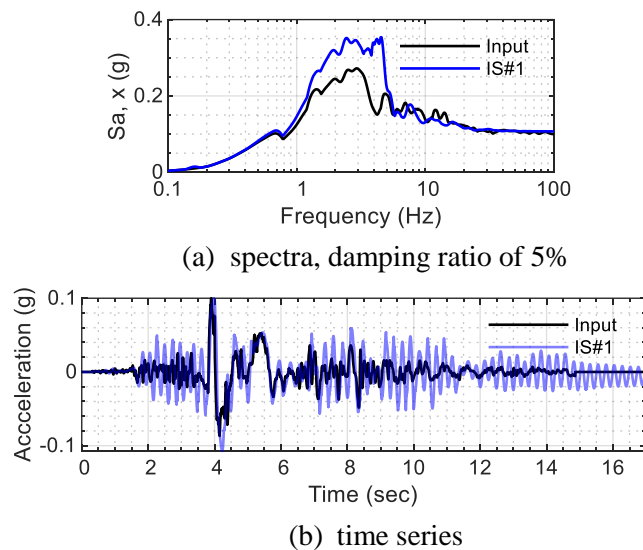
Figure 5.24. Comparison of input and output (isolated) accelerations for CCE input (PGA = 0.1g), IS#1 in SAP model 1
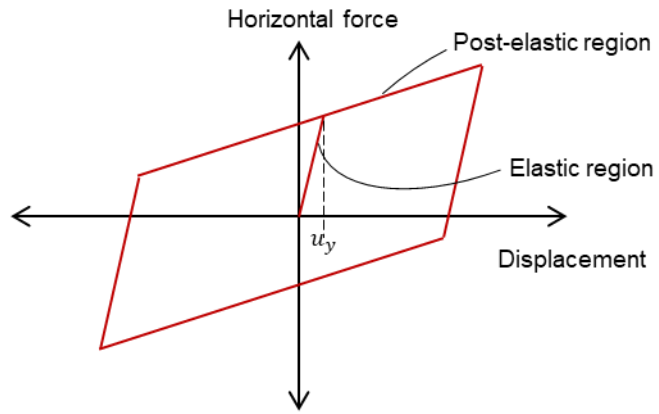
Figure 5.25. Idealized force-displacement loop for a FP isolator
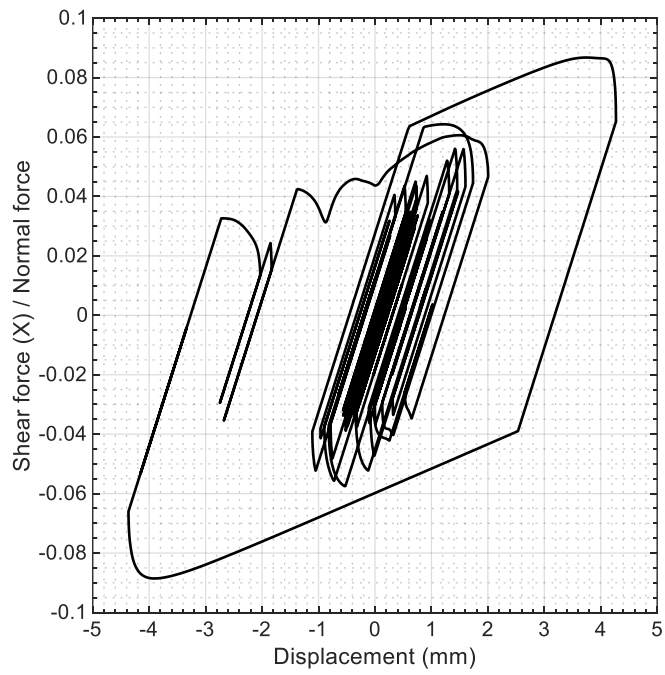
Figure 5.26. Force displacement loop for CCE input, IS#1 in SAP model 1

(a) spectra, damping ratio of 5%

(b) time series
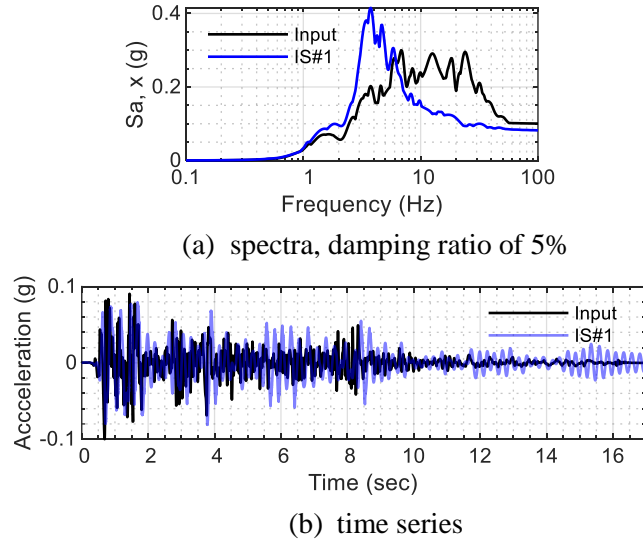
Figure 5.27. Comparison of input and output (isolated) accelerations for low amplitude ECE input (PGA = 0.1g) , IS#1 in SAP model 1

5.8   Conclusions

Multiple internal components submerged in a water filled, base-supported cylindrical vessel were tested using a six-degree-of-freedom earthquake simulator at the University at Buffalo. A centrally placed steel internal, a steel plate internal, and three configurations of aluminum tubes were tested in different test series using a suite of input motions. The data generated from the experiments was used to estimate *in-air* and *in-water* dynamic characteristics (frequency and damping) of the components. The benefits of seismic isolation, in terms of reduction in dynamic responses (pressure, acceleration, and strain) were identified. The implementation of base isolation led to reductions of at least 60%, 80%, 70% and 40% in peak accelerations of the central internal, the plate internal, the 152 mm diameter internal, and the 76 mm diameter internal, respectively, for the relatively large amplitude ECE and KCE motions. For the same motions, reductions in peak strain of at least 40%, 60% and 40% were observed for the plate internal, the 152 mm diameter internal, and the 76 mm diameter internal, respectively. The effect of base isolation on peak pressure recorded on the central internal was insignificant since the hydrodynamic pressure near the center of the vessel is dominated by the convective component. The reductions in dynamic responses for CCE motion were insignificant because of the low amplitude of the motion. The reason for numerical amplification in the *isolated* response spectra at low frequencies for low amplitude inputs was identified.

Data from the tests described in this section are used to validate numerical models, as presented in Section 6.

110

SECTION 6

VALIDATION STUDIES FOR SUBMERGED COMPONENTS

6.1   Introduction

This section focuses on numerical models of internal components (internals) submerged in a base supported vessel, as described in Section 5. Numerical results for dynamic responses of the internals are compared with test data to validate models. The Arbitrary Lagrangian and Eulerian (ALE) approach, as implemented in LS-DYNA, is used for modeling. Numerical models are constructed for the test specimens of the three test-series (1: central internal, 2: steel plate internal, and 3: 76 mm and 156 mm diameter internals) described in Section 5. Challenges in validating the ALE models are identified.

Sections 6.2, 6.3, and 6.4 present the validation studies for the models of the central tubular, steel plate, and off-center aluminum tubular (76 mm and 156 mm diameter internals) internals, respectively. Section 6.5 discusses the use of hourglass control algorithms. Section 6.6 summarizes the numerical studies and provides recommendations for modeling of internals at a prototype scale.

6.2   Validation study of a model of a central tubular internal

This section presents a validation study for pressure response and acceleration response of a numerical model of the central tubular steel internal. A numerical model of the fluid-filled vessel with the central internal attached to the head was developed. The vessel wall, flange, base plate, central internal, and head were modeled using fully-integrated shell elements. The connections between the head and the flange and between the head and the central internal were modeled using fully integrated solid elements. (Under-integrated solid elements have hourglass modes that can be kept in check by using a suitable hourglass control algorithm, but that introduces unwanted *damping* in the system.) Material properties consistent with carbon steel were assigned to the structural components except the base plate, which was modeled using a rigid material with a mass density consistent with carbon steel. The fluid domain was modeled using Eulerian, eight-node, solid elements as described in Section 4. Nodes at the interface of the fluid and solid domains were merged. Water was assigned a density of 1000 kg/m^3, a dynamic viscosity of 10^{-3} Ns/m^2, and a bulk modulus of 2.2 GPa (Yu *et al.* 2021). The effects of atmospheric pressure were not modeled and accordingly, the space above the free surface was assigned void properties using the *INITIAL_VOID keyword in LS-DYNA. Figure 6.1 presents views of the model used for the study together with the coordinate system. (The model is referred as FE model 1 hereafter.) In the figure, the base plate, vessel, and the flange are shown in black, the central internal and the head are shown in orange, water is shown in blue; the elements of the *void* space above the water domain are not shown. A finer mesh was used in the water

domain near the vessel wall and near the internal. Twenty-eight finite elements were used along the circumference of the internal. Instruments on the central internal in the test included three pressure gages (PCIW1, PCIW2, and PCIN1) and a tri-axial accelerometer (*x:* ACIX, *y:* ACIY, and *z:* ACIZ) installed at the locations shown in Figure 5.3. Similar output locations were defined in the numerical model to enable comparison of results. For reference, the pressure history on the wall of the vessel at the location of pressure gage PE1 was also output and compared with experimental results. These output locations in the numerical model are indicated by yellow and red solid circles in Figure 6.1.
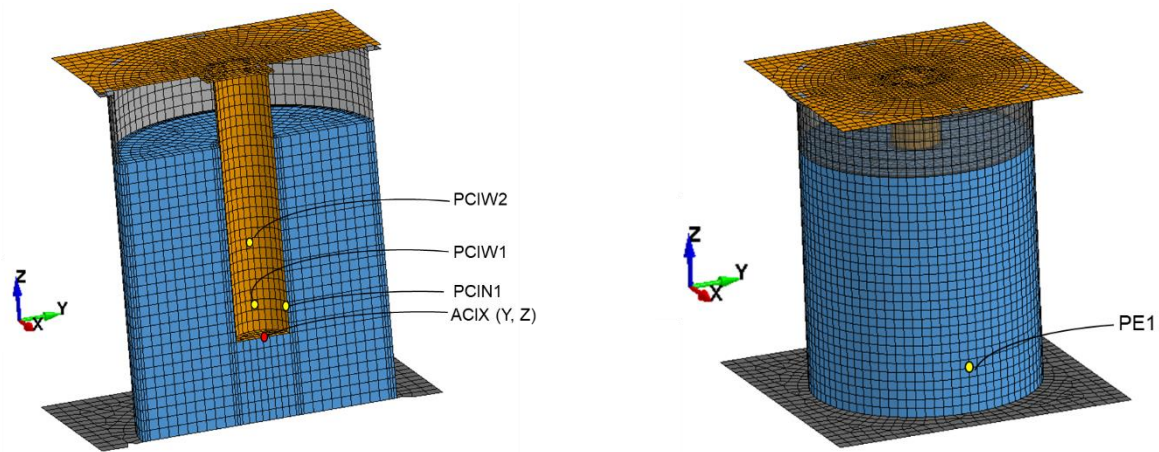
Figure 6.1. FE model 1 in LS-DYNA, output locations indicated by yellow and red solid circles

First, a numerical model without water or the void space was analyzed for eigen values and results were compared with those from system identification tests conducted to obtain the *in-air* frequency of vibration of the internal (see Section 5.4). The *CONTROL_IMPLICIT_EIGENVALUE keyword in LS-DYNA was used for this purpose. The frequency of vibration of the internal in the numerical model was 32 Hz in both horizontal directions, which was essentially identical to the measured 32.8 Hz (see Table 5.3). Figure 6.2 presents the numerically estimated mode shape. The mode shape involves bending of the top plate. In the ALE model for response history analyses, an average damping ratio of 0.45% (of critical) was assigned to the internal in the numerical model per Table 5.3.

112
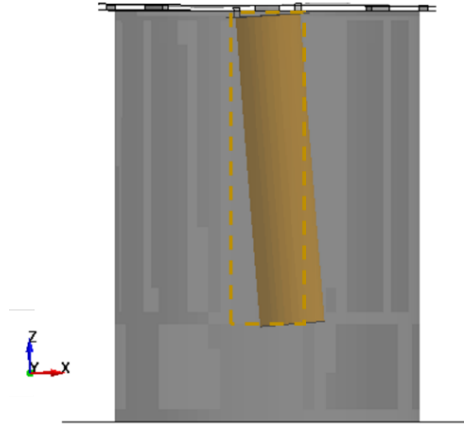
Figure 6.2. Numerically estimated mode shape (without fluid), original position of the central internal shown in dashed yellow line, frequency = 32 Hz

Response-history analyses of the ALE model were performed for nine sets of time series: the 1D, 2D, and 3D CCE, ECE, and KCE motions (#4, #6, #7, #8, #10, #11, #13, #15, and #16 in Table C.4). Details of these input motions were presented in Sections 3.3 and 5.3. Accelerations recorded on the base plate in experiments, including translational and rocking components, were input at the center of the base plate in the ALE model using *BOUNDARY_PRESCRIBED_MOTION_RIGID keyword. Only the part of an input motion that included 90+% of the Arias intensity (Arias 1970) was used for the response-history analyses to reduce the computational expense. For the cases of 1D (x) inputs to the earthquake simulator, vertical (z) accelerations and rocking accelerations (about y) were also recorded at the base plate and input to the numerical model. For 2D (x and y) inputs to the earthquake simulator, vertical (z) accelerations and rocking accelerations about both horizontal axes (x and y) were recorded at the base plate and input to the model together with the recorded x and y translational motions. Similarly, for 3D inputs (x, y, and z), translational accelerations in the three directions and rotational accelerations about the two horizontal directions (x and y) were recorded at the base and input to the numerical model. *Additional* accelerations along/about axes with no specified *command* accelerations are observed due to compliance[14] between the horizontal and vertical actuators of the earthquake simulator. For example, for the 3D CCE input, *command* accelerations were specified along the three translational directions only but *additional* rotational accelerations about the two horizontal axes were also recorded on the earthquake-simulator platform (and base plate). These *additional* accelerations have small peak amplitudes but can affect certain responses as

---

[14]Actuators in a direction with no *commanded* acceleration are active and experience small motions so as to accommodate the displacements of the actuators along directions with *commanded* accelerations.

discussed below. Table 6.1 presents the peak acceleration amplitudes of these *additional* accelerations for all tests considered in this section.

Table 6.1 : Peak additional accelerations recorded on the base plate

Direction	1D inputs			2D inputs			3D inputs		
	CCE	ECE	KCE	CCE	ECE	KCE	CCE	ECE	KCE
z-translation (g)	0.007	0.05	0.03	0.01	0.05	0.08	-	-	-
x-rotation (rad/sec^2)	-	-	-	0.6	3.5	4.3	0.5	3.1	3.7
y-rotation (rad/sec^2)	0.4	5.3	4.0	0.4	5.0	3.8	0.3	4.4	3.1

Figure 6.3 through Figure 6.5 enable a comparison of numerically estimated and experimentally obtained time series for hydrodynamic pressures at locations PCIW1 (internal) and PE1 (vessel wall) for 1D, 2D, and 3D inputs, respectively. Figure 6.6 presents acceleration spectra at the location of ACIX for all the inputs considered. Table 6.2 presents the maximum absolute values of the ALE and experimental results and their percentage differences for the 1D, 2D, and 3D motions of CCE, ECE, and KCE. A *wave-like* profile is present in the pressure history at PCIW1 for the 1D and 2D CCE inputs (see Figure 6.3a and Figure 6.4a) because the hydrodynamic pressure near PCIW1 is dominated by sloshing in the presence of a weak vertical input, as is the case for 1D and 2D CCE (peak vertical acceleration ≤ 0.01g per Table 6.1). For 3D inputs or 1D and 2D inputs with significant *additional* vertical acceleration, the pressure history has a significant contribution from the vertical component of the motion and the *wave-like* profile is not evident. At the wall (PE1), the pressure is dominated by the impulsive response and the pressure response to vertical accelerations. Simulating sloshing response accurately is challenging as discussed in Section 4. Thus, the errors in peak pressure on the internal are expected to be high. The entries in Table 6.2 show a similar trend: an average absolute error of 13% for pressure responses on the internal as opposed to 7% on the wall.

A good match was observed between the response spectra of the accelerations from the model and the experiment (see Figure 6.6). An average absolute error of 11% is observed in peak acceleration responses of the internal in the three directions (for all inputs considered here). A consistent peak at 22 Hz was observed in the spectra of lateral accelerations (from both model and experiment). This peak corresponds to the 32 Hz (approximately) frequency of vibration in air considering an added mass (Dong 1978) of 88 kg for the internal for the used immersed depth of 1.1 m. (mass of internal = 76 kg).
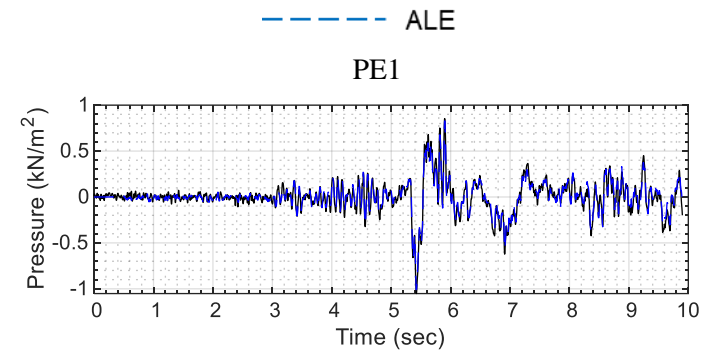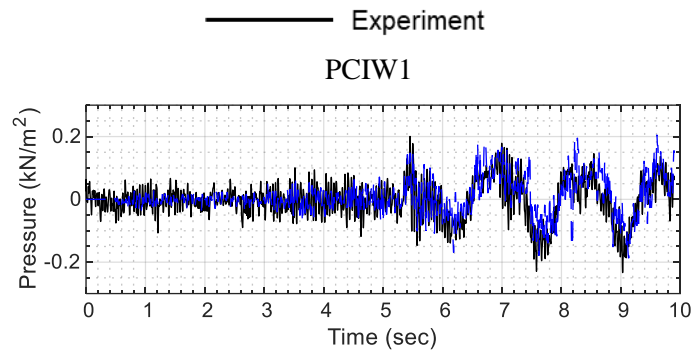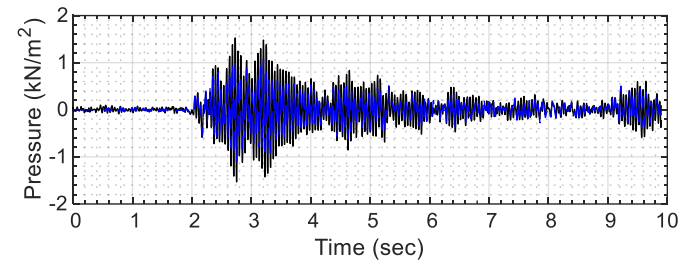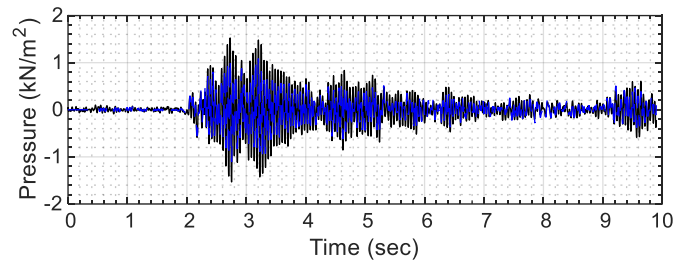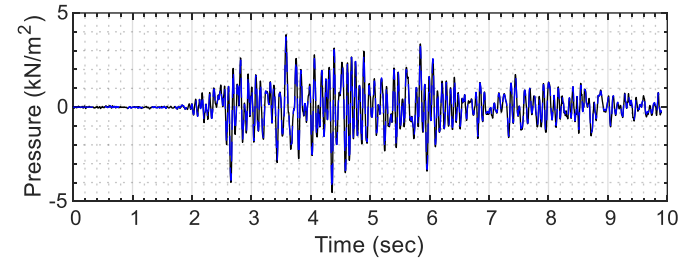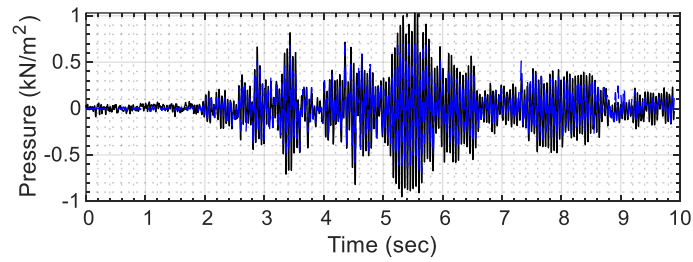
Figure 6.3. Numerical and experimental results, hydrodynamic pressure at PCIW1 and PE1, 1D inputs
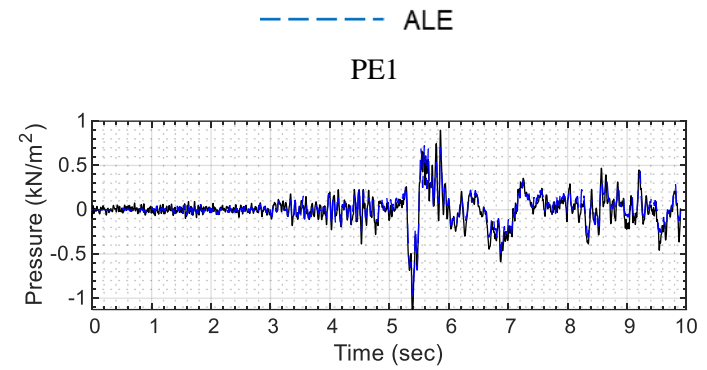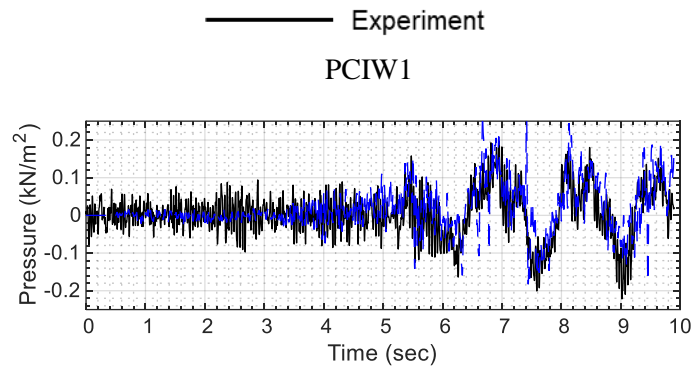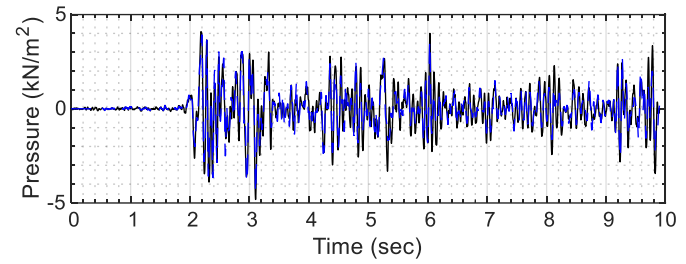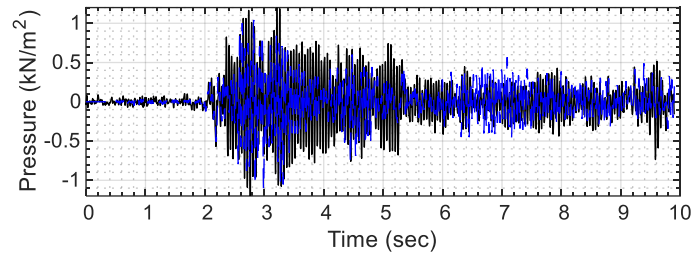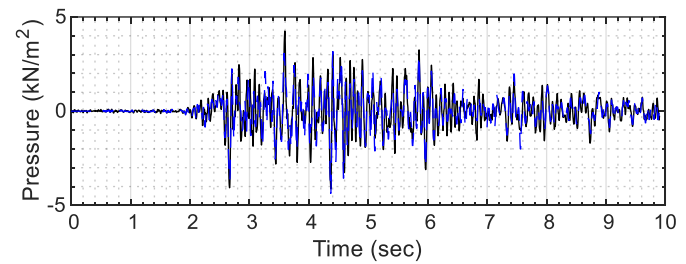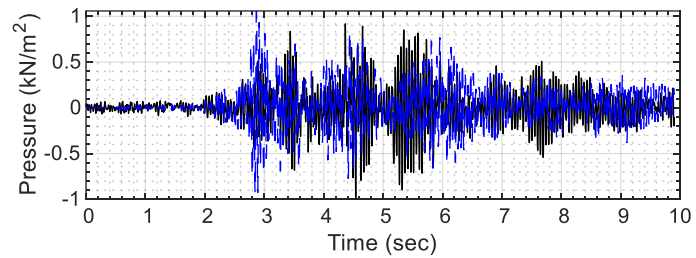
Figure 6.4. Numerical and experimental results, hydrodynamic pressure at PCIW1 and PE1, 2D inputs
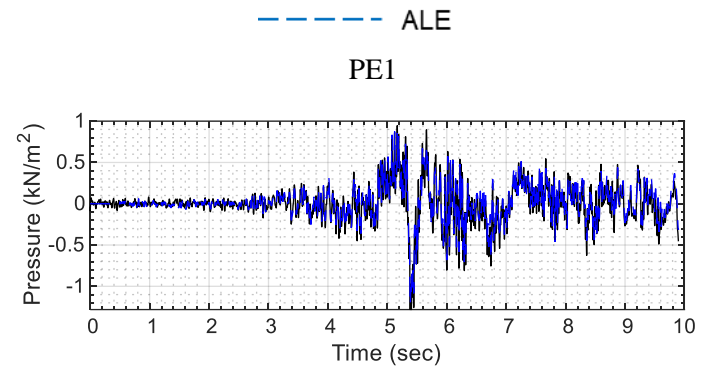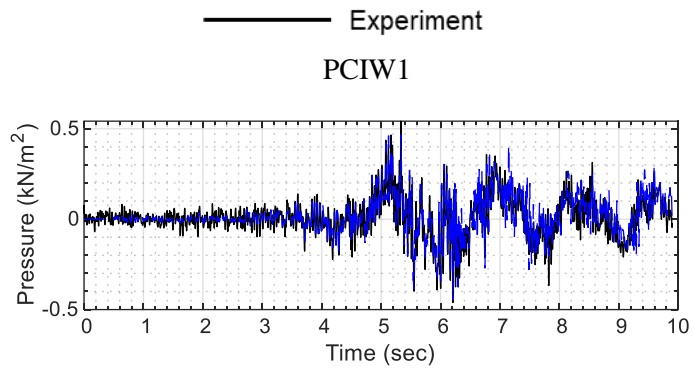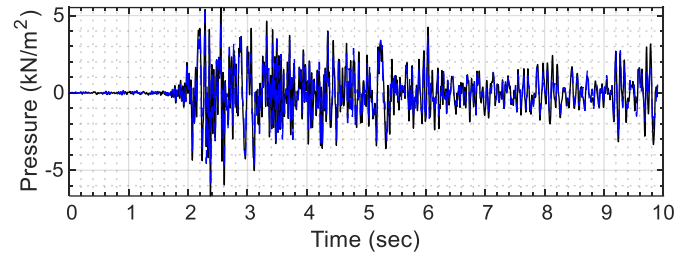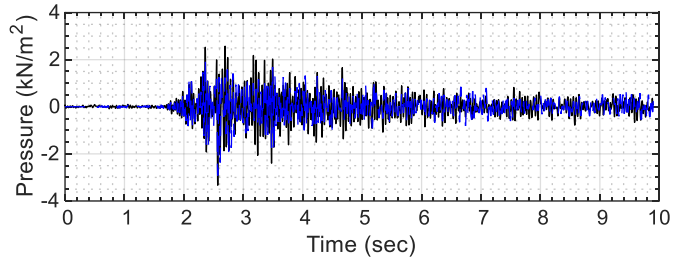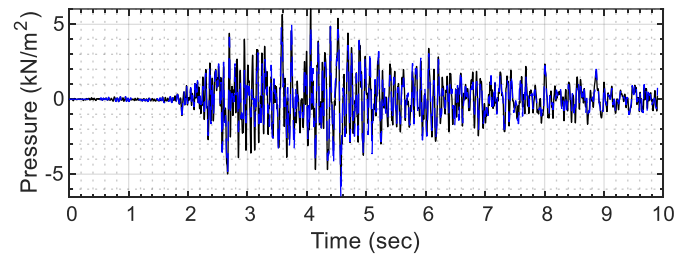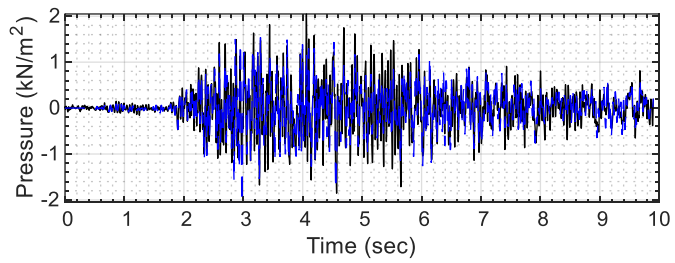
Figure 6.5. Numerical and experimental results, hydrodynamic pressure at PCIW1 and PE1, 3D inputs
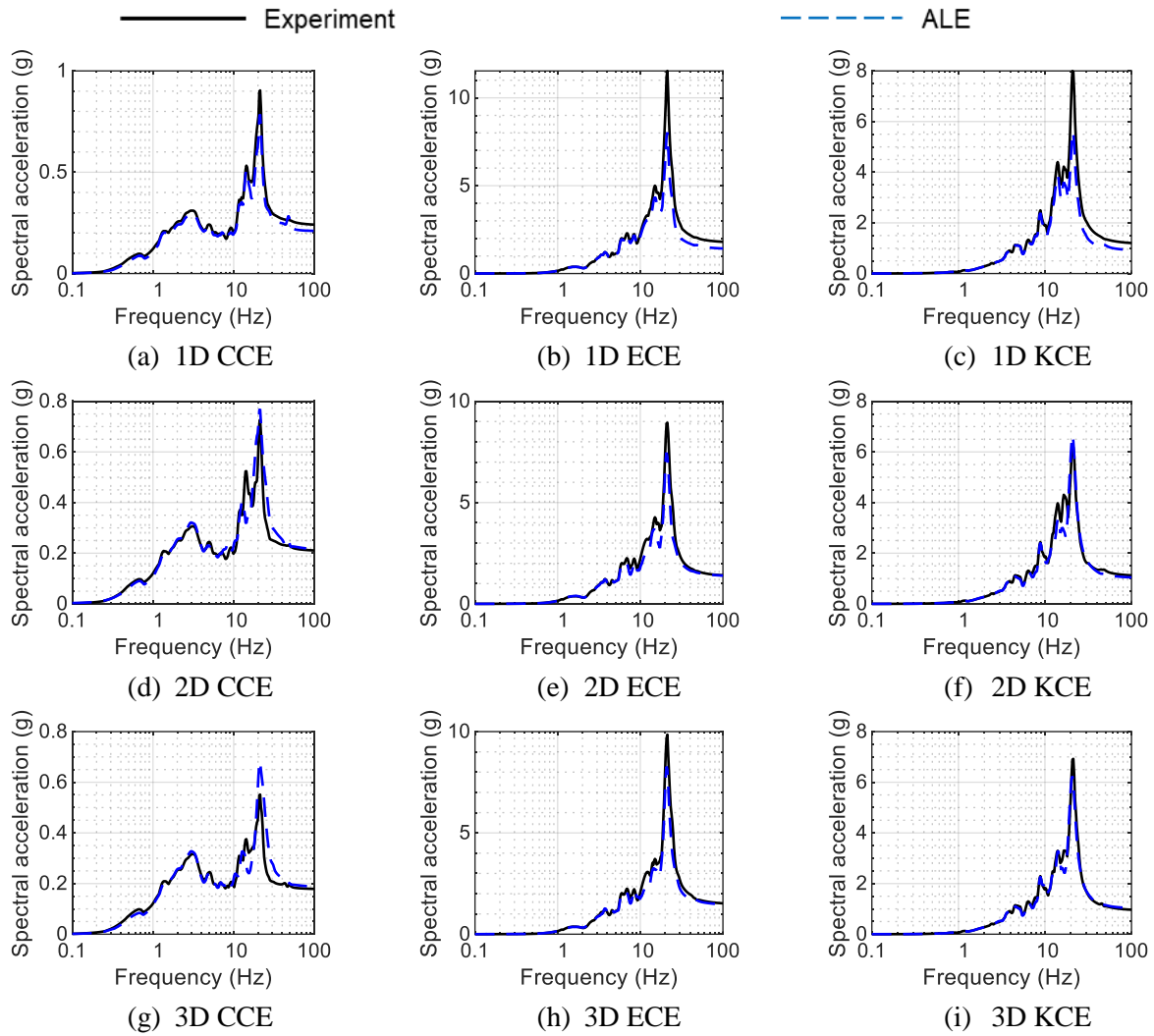
Figure 6.6. Numerical and experimental results, acceleration response spectra at ACIX

118

Table 6.2 : Maximum absolute FSI responses of test specimen 1 (central internal) for 1D, 2D, and 3D CCE, ECE, and KCE motions, extracted from time series of the tests and ALE model, percentage differences

(a) 1D (x) motions									
Response	CCE			ECE			KCE		
(or location)	Model	Exp.	Diff. %	Model	Exp.	Diff. %	Model	Exp.	Diff. %
PCIW1, KN/m^2	0.21	0.23	-12	1.11	1.53	-28	0.70	1.03	-32
PCIW2, KN/m^2	0.31	0.26	18	1.45	1.90	-24	1.14	1.20	-5
PE1, KN/m^2	1.01	1.05	-4	4.55	4.68	-3	4.39	4.53	-3
ACIX, g	0.21	0.24	-12	1.39	1.75	-21	0.90	1.16	-22
(b) 2D (x and y) motions									
Response	CCE			ECE			KCE		
(or location)	Model	Exp.	Diff. %	Model	Exp.	Diff. %	Model	Exp.	Diff. %
PCIW1, KN/m^2	0.28	0.22	28	1.11	1.43	-22	1.06	0.99	7
PCIW2, KN/m^2	0.27	0.21	26	1.45	1.71	-15	1.37	1.43	-4
PCIN1, KN/m^2	0.27	0.29	-5	1.56	1.54	1	1.32	1.41	-7
PE1, KN/m^2	0.96	1.13	-15	4.43	4.82	-8	4.37	4.25	3
ACIX, g	0.21	0.21	2	1.35	1.37	-2	1.02	1.09	-6
ACIY, g	0.19	0.27	-27	1.38	1.38	0	1.04	1.12	-8
(c) 3D (x, y, and z) motions									
Response	CCE			ECE			KCE		
(or location)	Model	Exp.	Diff. %	Model	Exp.	Diff. %	Model	Exp.	Diff. %
PCIW1, KN/m^2	0.47	0.54	-14	2.92	3.33	-12	2.05	2.05	0
PCIW2, KN/m^2	0.75	0.81	-8	4.57	5.06	-10	3.07	2.93	5
PCIN1, KN/m^2	0.65	0.77	-16	4.16	4.16	0	2.94	2.90	1
PE1, KN/m^2	1.23	1.28	-4	5.82	6.66	-13	6.55	6.03	9
ACIX, g	0.18	0.18	4	1.43	1.47	-3	1.01	0.93	8
ACIY, g	0.18	0.26	-31	1.41	1.47	-4	0.99	1.18	-17
ACIZ, g	0.26	0.21	26	0.73	0.73	0	0.72	0.69	5

6.3 Validation study of a model of a steel plate internal

This section presents a numerical model for estimating the dynamic responses (acceleration and strain) of the steel plate internal (test specimen 2) described in Section 5. A finite element model of the steel plate internal in configuration B[15] was constructed in LS-DYNA using a modelling approach similar to that described in Section 4 and Section 6.2. (The numerical model is referred as FE model 2B hereafter.) The steel plate internal was modelled using fully-integrated shell elements with material properties of carbon steel. Figure 6.7 presents a cutaway view of the numerical model and a plan view of the fluid domain mesh. Six fluid elements, nearly square in plan, were used along the width of the internal as indicated in Figure 6.7b. Monitoring locations for acceleration and strain, defined corresponding to the instrumentation layout described in Section 5.2.2, are indicated in Figure 6.7a.

(a) cutaway view, monitoring locations   (b) fluid mesh, plan view
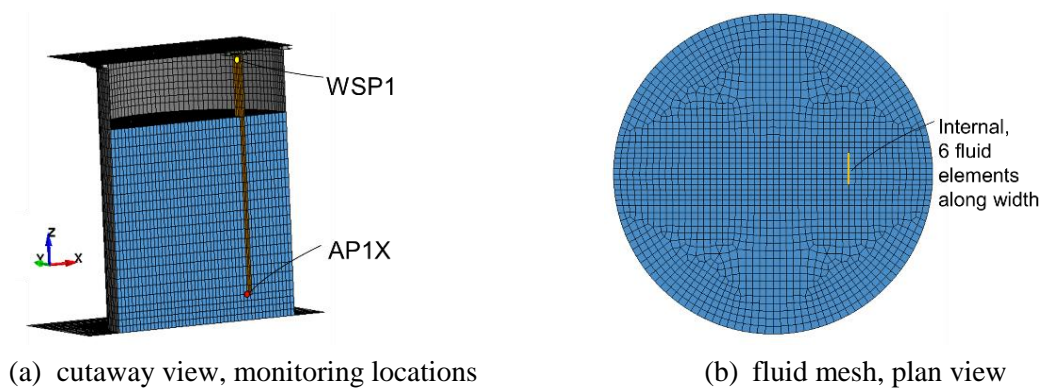
Figure 6.7. Numerical model of steel plate internal in LS-DYNA

An eigen value analysis of the numerical model without the fluid domain was carried out first to evaluate the numerical *in-air* frequency of the internal. The *in-air*, first-mode frequency of the internal was estimated to be 3.1 Hz, which is equal to the test value per Table 5.3. Per Table 5.3, the internal was assigned a damping of 0.04% for response-history analyses.

Response-history analyses of the model were carried out for two motions: 1D ECE motion and 1D KCE motion (#5 and #7 in Table C.5). Accelerations recorded at the base of the vessel in tests were input to the

---

[15]The experimental *in-water* frequencies of the steel plate internal in configurations A and B are 2.07 Hz and 2.25 Hz, respectively (implying more added mass in configuration A where the plate is close to the wall). However, this difference in frequencies is small and is unlikely to be resolved in the ALE approach using a reasonable mesh size. A *coarse* mesh, *reasonable* in terms of analysis time, results in a greater added mass when using the ALE method, as explained later. Hence, only configuration B was modeled for numerical analyses.

base of the model as explained in the previous section. Figure 6.8 presents experimental and numerical responses of the internal. Table 6.3 presents the maximum absolute values of the numerical and experimental results and their percentage differences.

From the acceleration spectra in Figure 6.8, it is clear that: a) the second mode of vibration of the internal is dominant for both input motions, and b) the numerically predicted first mode or second mode frequencies are less than corresponding experimental values. The numerical, *in-water*, first mode frequency was 1.7 Hz, and lower than the experimentally measured value of 2.2 Hz (see the inset plot in Figure 6.8b). Similarly, the numerical, *in-water*, second mode frequency was 11.1 Hz, and lower than the experimentally measured value of 13.7 Hz. The reason for the smaller numerical values of *in-water*, frequencies is a greater added mass due to the use of a *coarsely* meshed fluid domain around the internal. Using a *very fine* (computationally expensive) mesh around the internal will reduce the differences between the numerical and experimental predictions of *in-water* frequency. This is demonstrated for the internals of test series 3, discussed in Section 6.4.

The peak values of strain and acceleration differ significantly with average absolute errors in peak values of strain and acceleration greater than 40% (see Table 6.3). Possible reasons for these large differences are:

a) frequency mismatch due to more *added mass* in the numerical model, as explained above.

b) there is additional *non-physical* damping in the numerical model due to the use of an hourglass control algorithm (see Section 6.5 for details).

The numerical model of the steel plate internal can be considered validated for estimating *in-water* frequency (differences < 23%) but not for estimating acceleration and strain responses of the internal. To improve the strain and acceleration response estimates, a mesh refinement that precludes the need of using an hourglass control algorithm is needed, but such analyses are impractical, in terms of computational time, at the time of this writing. (The simulations described here were executed on a computer with AMD EPYC 7763 (2.45 GHz) processor and 128 GB RAM.)

(a) strain at WSP1, 1D ECE

(b) acceleration spectra at AP1X, 1D ECE

(c) strain at WSP1, 1D KCE

(d) acceleration spectra at AP1X, 1D KCE
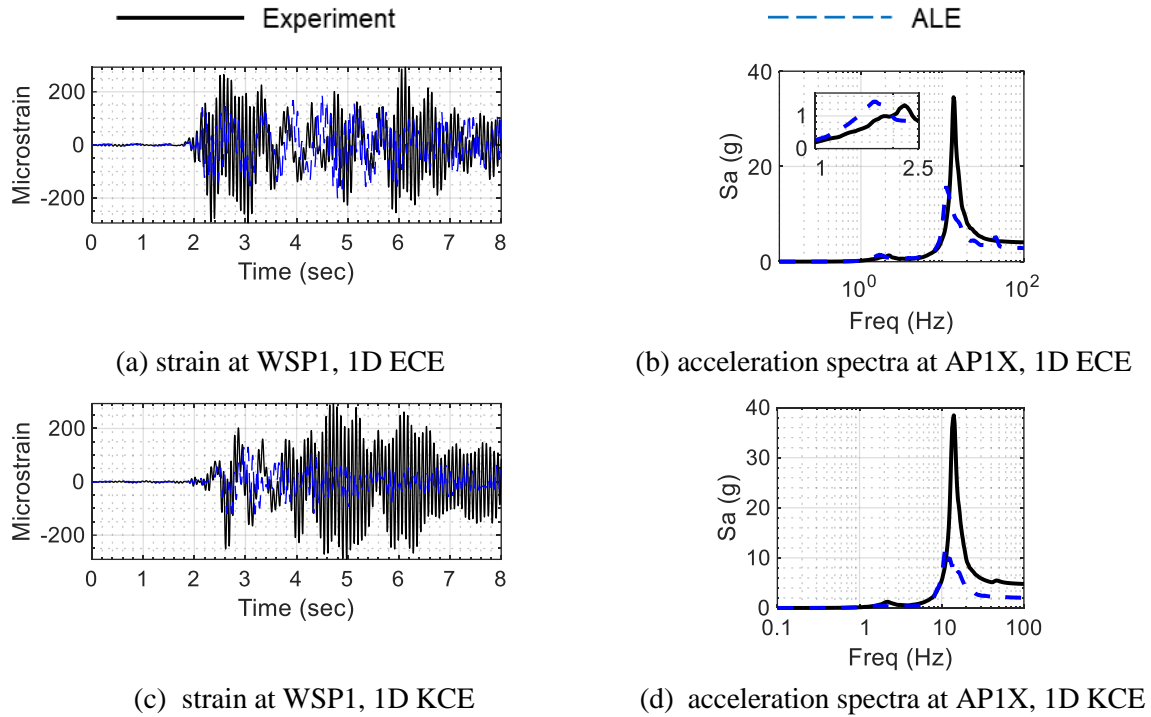
Figure 6.8. Numerical and experimental responses for the steel plate internal, acceleration spectra for damping ratio of 5%

Table 6.3 : Maximum absolute FSI responses of test specimen 2 (steel plate internal), extracted from time series of the tests and ALE model, percentage differences

Response (or location)	1D ECE			1D KCE		
	Model	Exp.	Diff. %	Model	Exp.	Diff. %
AP1X, g	2.9	4.1	-30	2.0	4.8	-57
WSP1, microstrain	203	294	-31	130	293	-56

6.4   Validation study of a model of off-center aluminum tube internals

This section deals with numerical modelling of the aluminum internals of test series 3 described in Section 5.2.3. Finite element models of the submerged aluminum tubes in the three configurations (A through C) were constructed using an approach similar to that described in Section 6.2. (The three models are referred as FE model 3A, FE model 3B, and FE model 3C hereafter.) The internals were modeled using fully-integrated shell elements with material properties consistent with 6061 aluminum alloy, namely, Young's modulus of 68 GPa, mass density of 2700 kg/m^3, and Poisson's ratio of 0.33 (BSI (2007) and Summers *et al.* (2015)). Figure 6.9 presents cutaway views of the numerical models and a plan view of the fluid domain mesh used for modeling the specimens of test series 3. Response-output locations, defined corresponding to the instrumentation layout described in Section 5.2.3, are indicated in Figure 6.9a through Figure 6.9c. These include accelerometers and strain gages on the internals. In each numerical model, a fine mesh was used in the fluid domain around the internals. The circumference of the 152 mm and 76 mm diameter internals was meshed using 48 elements and 24 elements, respectively, as shown in Figure 6.9d. The masses of the steel discs attached at the ends of the internals were lumped as nodal masses using the *ELEMENT_MASS_NODE_SET keyword and are indicated in light blue in the figure. The bolts connecting the head to the flange and the end-plate of the internals to the head were represented by fully-integrated solid elements.

(a) cutaway view, FE model 3A (152 mm diameter internal seperately)

(b) cutaway view, FE model 3A (76 mm diameter internal seperately)

(c) cutaway view, FE model 3C (152 mm and 76 mm diameter internals together)

(d) fluid-domain mesh, plan view
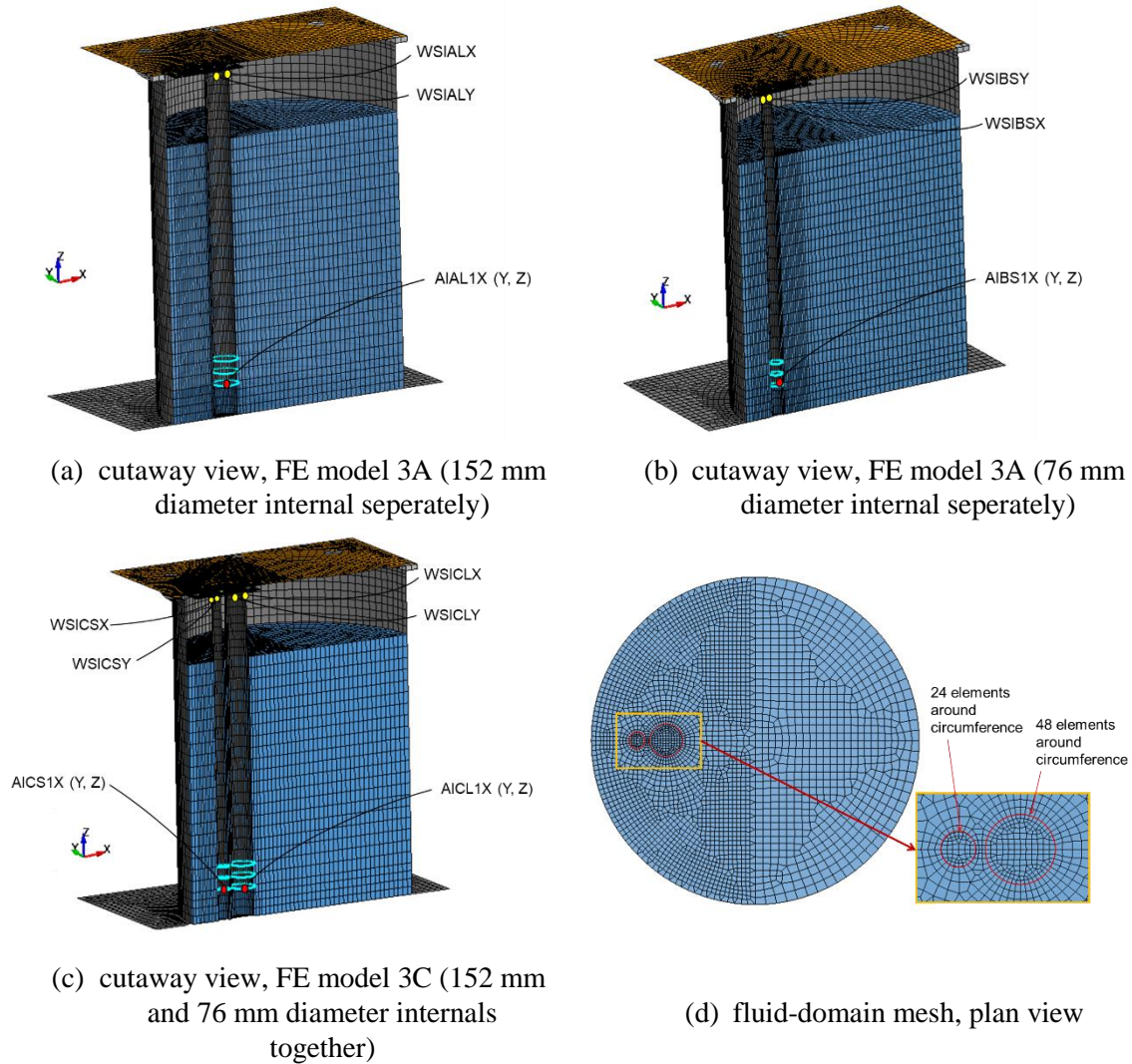
Figure 6.9. Finite element models of test series 3 specimens and response output locations, void space not shown

Numerical estimates of the *in-air* natural frequencies of the two internals were first estimated by eigen value analysis of the models without the fluid domains. The first-mode frequency of the 152 mm diameter internal was 15.7 Hz and essentially identical to the test result of 15.5 Hz, and that of the 76 mm diameter internal was 7.0 Hz, which was equal to the test result of 7 Hz (see Table 5.3). Figure 6.10 presents the numerically estimated mode shapes (without fluid) of the two internals. The two internals in the numerical models were assigned damping ratios per Table 5.3, namely, 0.06% for the 152 mm diameter internal and 0.03% for the 76 mm diameter internal.

(a) FE model 3A (without fluid), frequency = 15.7 Hz

(b) FE model 3B (without fluid), frequency = 7.0 Hz

Figure 6.10. Numerically evaluated mode shapes (without fluid) of internals of test series 3, original positions of internals shown in dashed yellow lines

Each of the three ALE models (of the three test specimens) was analyzed for the 1D CCE motion and the 3D ECE motion. (#4 and #11 per Table C.6). The seismic inputs recorded in experiments were input at the base of the model using the *BOUNDARY_PRESCRIBED_MOTION_RIGID keyword as explained in Section 4 and Section 6.2.

To enable a comparison of numerically-estimated, *in-water* frequencies of the internals with corresponding test results, response spectra of accelerations at the ends of the internals, obtained from response-history analysis of FE models 3A and 3B, are compared with corresponding test results for the 1D CCE input in Figure 6.11.
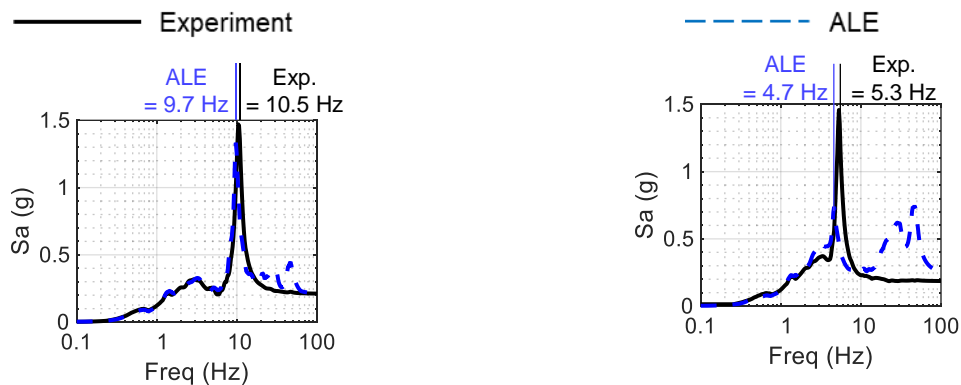
(a) FE model 3A, response location of accelerometer AIAL1X

(b) FE model 3B, response location of accelerometer AIBS1X

Figure 6.11. Acceleration spectra, *x*-direction, 1D CCE input, damping ratio of 5%

The ALE model (FE model 3A) predicted an *in-water* frequency of 9.7 Hz for the 152 mm diameter internal that was 8% lower than the experimentally measured value of 10.5 Hz. For the 72 mm diameter internal, the numerical model (FE model 3B) predicted an *in-water* frequency of 4.7 Hz, which was 11% lower than the experimental value of 5.3 Hz. The reason for the smaller obtained values of numerical predictions is that the mesh used here for analyses is *coarse* and leads to an artificially greater *added mass*.

A finer mesh was also considered for analyses. The circumference of the 152 mm diameter and the 76 mm diameter internals was meshed using 36 and 72 finite elements, respectively, in this model, as shown in Figure 6.12. (Models of the three specimens utilizing the finer mesh are referred as FE model 3A$_{finer}$, FE model 3B$_{finer}$, and FE model 3C$_{finer}$ hereafter.) Response-history analyses for the 1D CCE input were repeated using FE model 3A$_{finer}$ and FE model 3B$_{finer}$ and acceleration spectra at the ends of the internals for the 1D CCE input are presented in Figure 6.13. The models with finer mesh captured the *in-water* frequencies exactly but were computationally expensive. (Response-history analysis of FE model 3A$_{finer}$ for an eight-second earthquake input took 96 hours on a computer with AMD EPYC 7763 (2.45 GHz) processor and 128 GB RAM, and much longer than the 19.5 hours for a similar analysis of FE model 3A.) Analyses described below were therefore run with FE models 3A, 3B, and 3C.
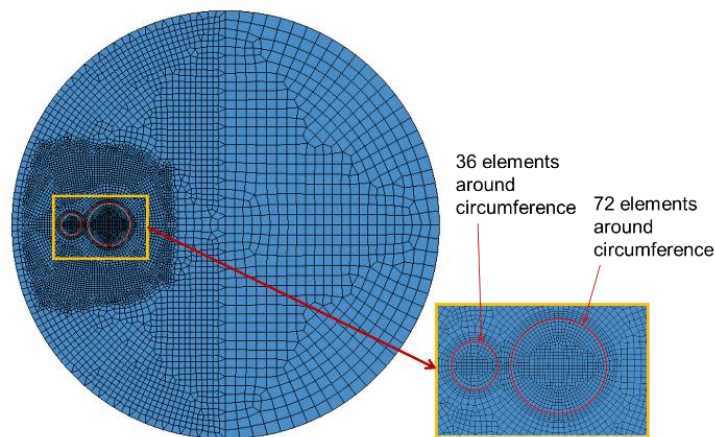
Figure 6.12. Finer mesh in fluid domain
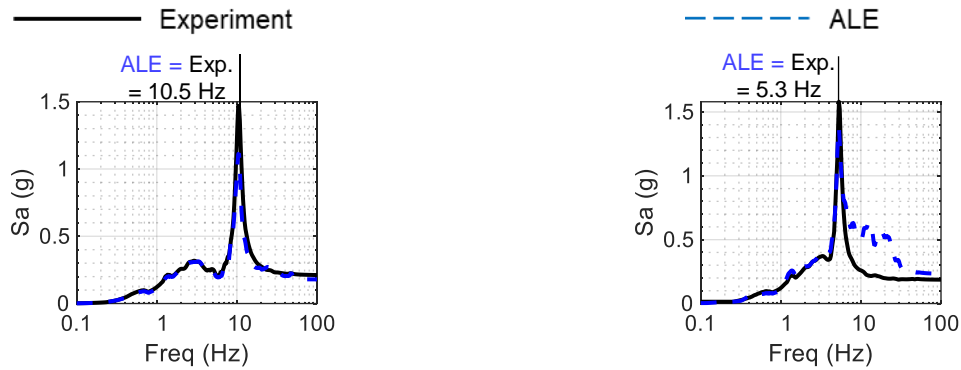
(a) FE model 3A$_{finer}$, response location of accelerometer AIAL1X

(b) FE model 3B$_{finer}$, response location of accelerometer AIBS1X

Figure 6.13. Acceleration spectra, *x*-direction, finer mesh in fluid domain, 1D CCE input, damping ratio of 5%

Figure 6.14 through Figure 6.19 enable comparisons of results from experiments and numerical simulations of FE model 3A, FE model 3B, and FE model 3C, for the 1D CCE and 3D ECE inputs. Strain histories near the points of attachment of the internals and acceleration histories near the ends of internals are presented. Monitoring locations are identified in the figure captions. Table 6.4 presents the maximum absolute values of the ALE and experimental results and the percentage differences for the three models.

The frequencies of the submerged components were captured well by the ALE model. Strain responses were generally not captured well (average absolute error in peak strain amplitudes = 43% per Table 6.4). The experimentally measured values of strain were generally greater than corresponding numerical predictions. Possible reasons for mismatch in strain histories are:

a) Strains measured in the tests were small making accurate recording challenging.

b) The internals have low damping and the *in-water* damping of the internals was not captured reasonably well by the ALE model (as explained below).

The shape of the response spectra of accelerations of the internals was captured reasonably well by the numerical models although there were differences in peak accelerations (average absolute error in peak acceleration amplitudes = 20% per Table 6.4). These differences are attributed to mismatches in numerical and experimental *in-water* damping. The major sources of damping in the physical system are fluid viscosity and damping of the structural components (internals, connections). The former was simulated in the numerical model by specifying dynamic viscosity of water using the *MAT_NULL keyword in LS-DYNA and the latter, estimated by hammer impact tests described in Section 5.4, was simulated using the

127

*DAMPING_FREQUENCY_RANGE_DEFORM keyword. However, additional *non-physical* damping was introduced in the numerical model by the use of an hourglass control algorithm, as discussed in Section 6.5.

(a) strain at WSIALX

(b) acceleration spectra at AIAL1X
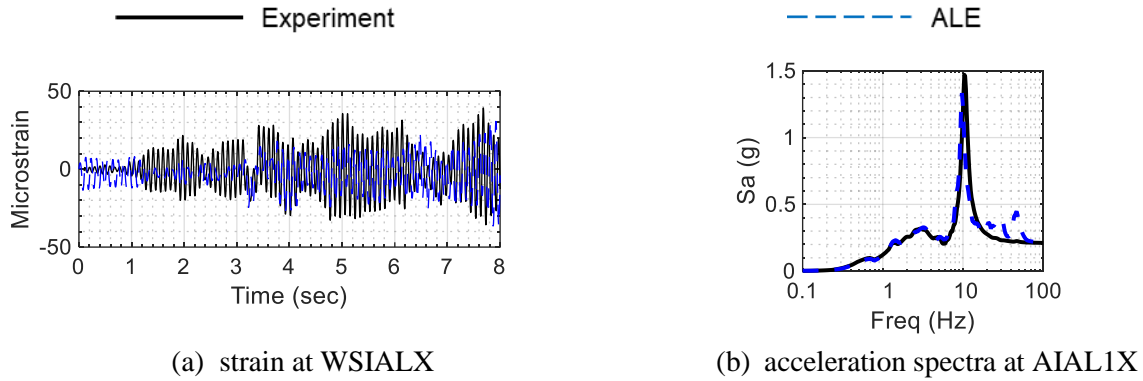
Figure 6.14. Numerical and experimental responses of the 152 mm diameter internal, FE model 3A, 1D CCE input, acceleration spectra are for 5% damping

(a) strain at WSIALX

(b) strain at WSIALY

(c) acceleration spectra at AIAL1X

(d) acceleration spectra at AIAL1Y

(e) acceleration spectra at AIAL1Z
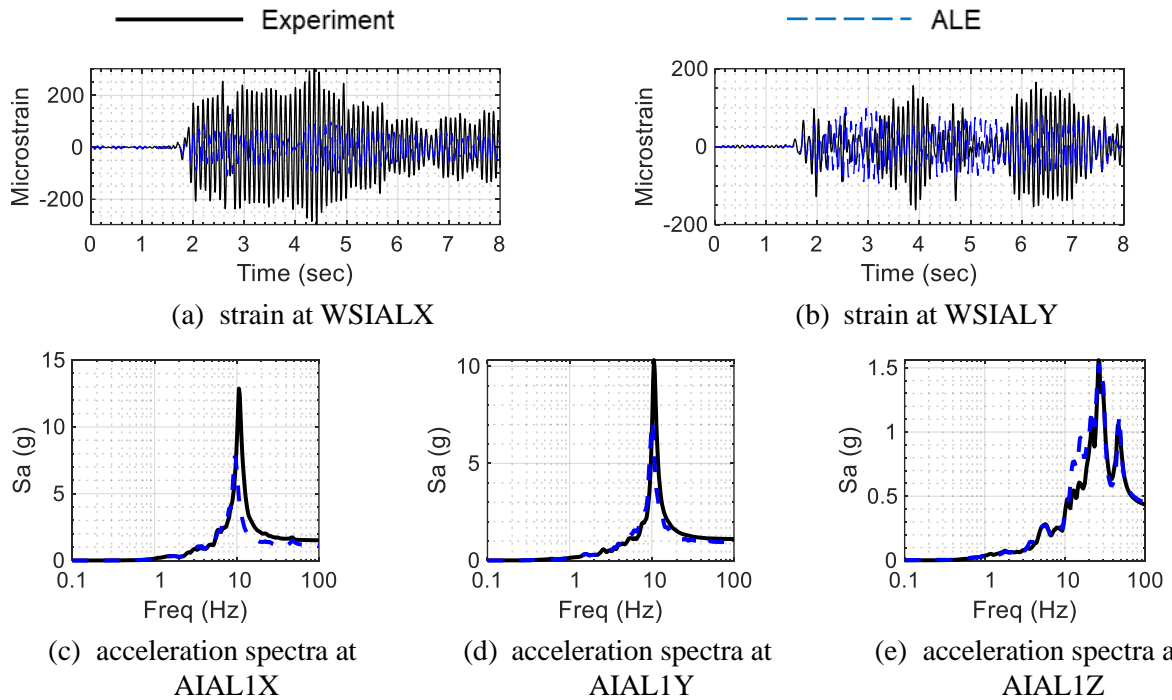
Figure 6.15. Numerical and experimental responses of the 152 mm diameter internal, FE model 3A, 3D ECE input, acceleration spectra are for 5% damping

(a) strain at WSIBSX

(b) acceleration spectra at AIBS1X, 5% damping
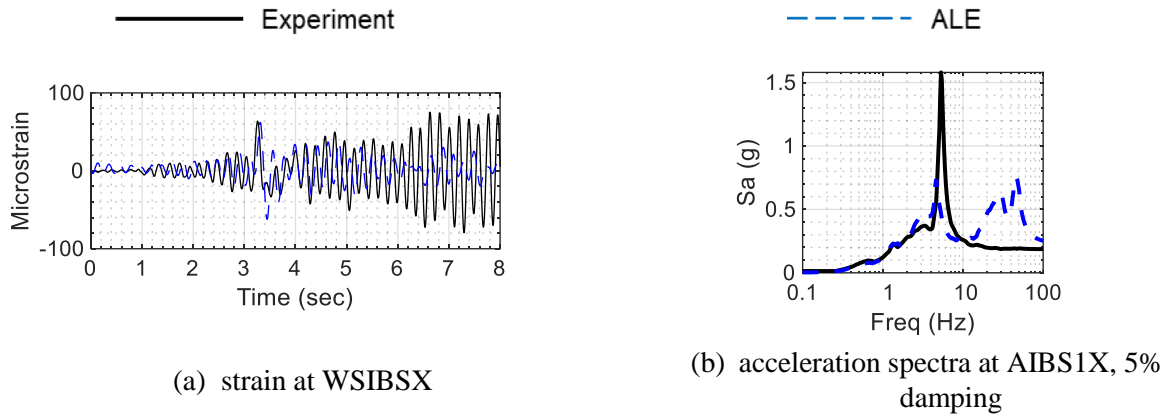
Figure 6.16. Numerical and experimental responses of the 76 mm diameter internal, FE model 3B, 1D CCE input

(a) strain at WSIBSX

(b) strain at WSIBSY

(c) acceleration spectra at AIBS1X

(d) acceleration spectra at AIBS1Y

(e) acceleration spectra at AIBS1Z
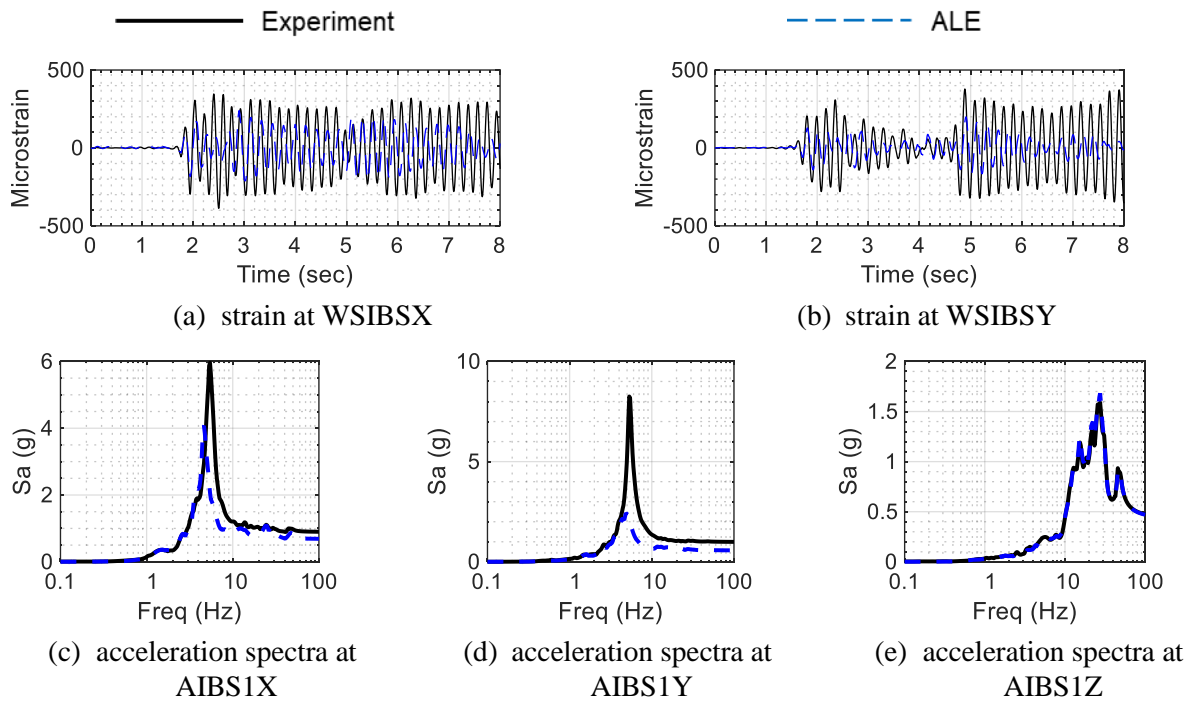
Figure 6.17. Numerical and experimental responses of the 76 mm diameter internal, FE model 3B, 3D ECE input, acceleration spectra are for 5% damping

.
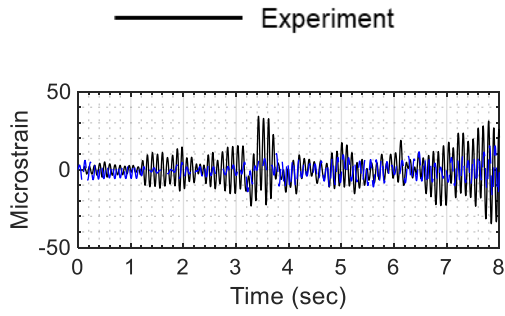
(a) strain at WSICLX
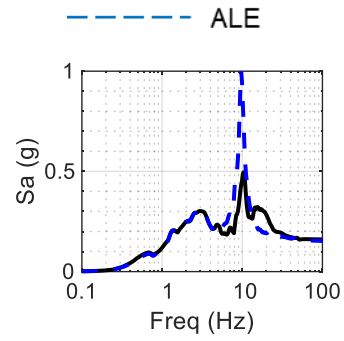
(b) acceleration spectra at AICL1X, 5% damping
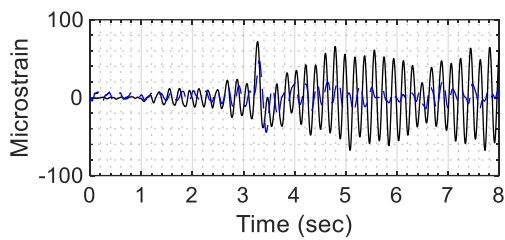
(c) strain at WSICSX
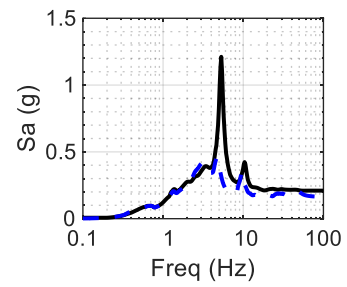
(d) acceleration spectra at AICS1X, 5% damping

Figure 6.18. Numerical and experimental responses of the 152 mm and 72 mm diameter internals, FE model 3C, 1D CCE input

130
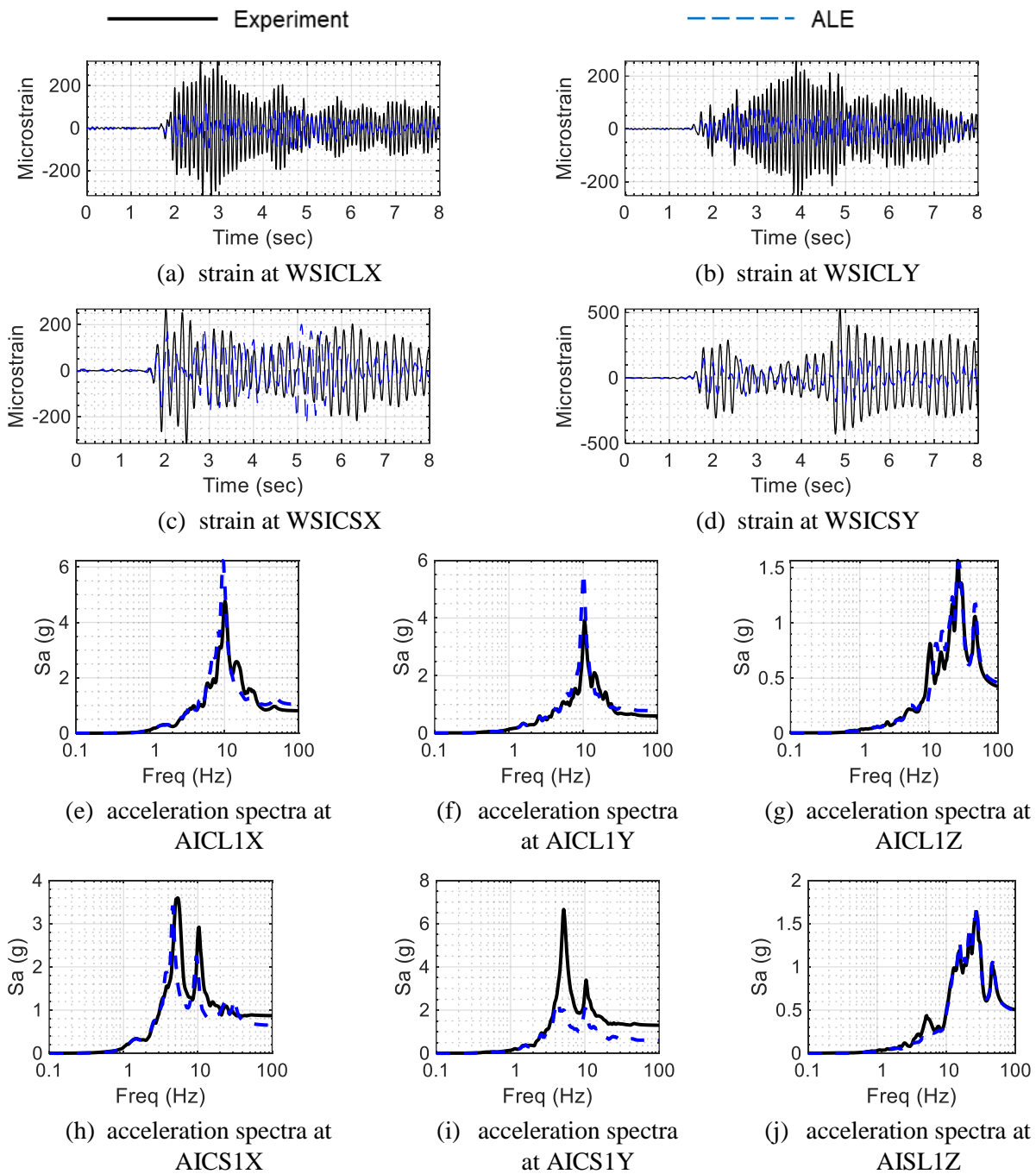
Figure 6.19. Numerical and experimental responses of the 152 mm and 72 mm diameter internals, FE model 3C, 3D ECE input, acceleration spectra are for 5% damping

Table 6.4 : Maximum absolute FSI responses of test series 3 internals for 1D CCE and 3D ECE motions, extracted from time series of the ALE model and tests, percentage differences

(a) FE model 3A						
Response (or location)	1D CCE			3D ECE		
	Model	Exp.	Diff. %	Model	Exp.	Diff. %
AIAL1X, g	0.2	0.2	1	1.1	1.5	-25
AIAL1Y, g	-	-	-	0.9	0.8	16
AIAL1Z, g	-	-	-	0.5	0.4	4
WSIALX, microstrain	37	39	-7	127	303	-58
WSIALY, microstrain	-	-	-	101	166	-39
(b) FE model 3B						
Response (or location)	1D CCE			3D ECE		
	Model	Exp.	Diff. %	Model	Exp.	Diff. %
AIBS1X, g	0.3	0.2	35	0.7	0.9	-23
AIBS1Y, g	-	-	-	0.6	0.9	-36
AIBS1Z, g	-	-	-	0.5	0.5	-1
WSIBSX, microstrain	62	80	-22	240	388	-38
WSIBSY, microstrain	-	-	-	199	378	-47
(c) FE model 3B						
Response (or location)	1D CCE			3D ECE		
	Model	Exp.	Diff. %	Model	Exp.	Diff. %
AICL1X, g	0.2	0.2	-5	1.0	0.8	27
AICL1Y, g	-	-	-	0.8	0.6	31
AICL1Z, g	-	-	-	0.5	0.4	8
AICS1X, g	0.2	0.2	-22	0.7	0.9	-25
AICS1Y, g	-	-	-	0.6	1.3	-53
AICS1Z, g	-	-	-	0.5	0.5	-2
WSICLX, microstrain	18	35	-50	116	317	-63
WSICLY, microstrain	-	-	-	85	256	-67
WSICSX, microstrain	47	72	-34	231	316	-27
WSICSY, microstrain	-	-	-	211	527	-60

6.5 Effect of using hourglass control

The fluid domain elements used in the described ALE simulations use single-point integration (ELFORM = 12 in *SECTION_SOLID keyword). Such elements are susceptible to non-physical modes of deformation, referred to as hourglass modes. These spurious modes can be mitigated by using a suitable hourglass control algorithm that creates internal nodal forces to resist such modes. For fluid elements, the recommended control algorithm is the standard LS-DYNA viscous form (IHQ=1 in *HOURGLASS keyword) with an hourglass coefficient equal to 10^{-3} or less (that is, QM $\leq 10^{-3}$ in *HOURGLASS keyword). This algorithm generates hourglass controlling forces that are proportional to the components of nodal velocity contributing to the hourglass modes. In essence, the control algorithm adds a *non-physical viscous damping* to the system. Using refined meshes helps avoid hourglass modes, but they are computationally expensive. Also, in many cases, the geometry of the model inevitably requires *irregular-shaped* elements in certain regions of the finite element mesh (for example, around the 76 mm internal in numerical models described in the previous section). The use of an hourglass control algorithm is unavoidable in such cases. Care should be taken when choosing parameters of a particular hourglass algorithm because they can affect the obtained response quantities. As an example, acceleration spectra at the ends of the two aluminum internals in FE model $3C_{finer}$ obtained from analysis considering three values of QM are presented in Figure 6.20. The analyses are for the 1D CCE input. The experimental results are also plotted for reference.

(a) spectra at AICL1X (152 mm diameter internal)

(b) spectra at AICS1X (76 mm diameter internal)
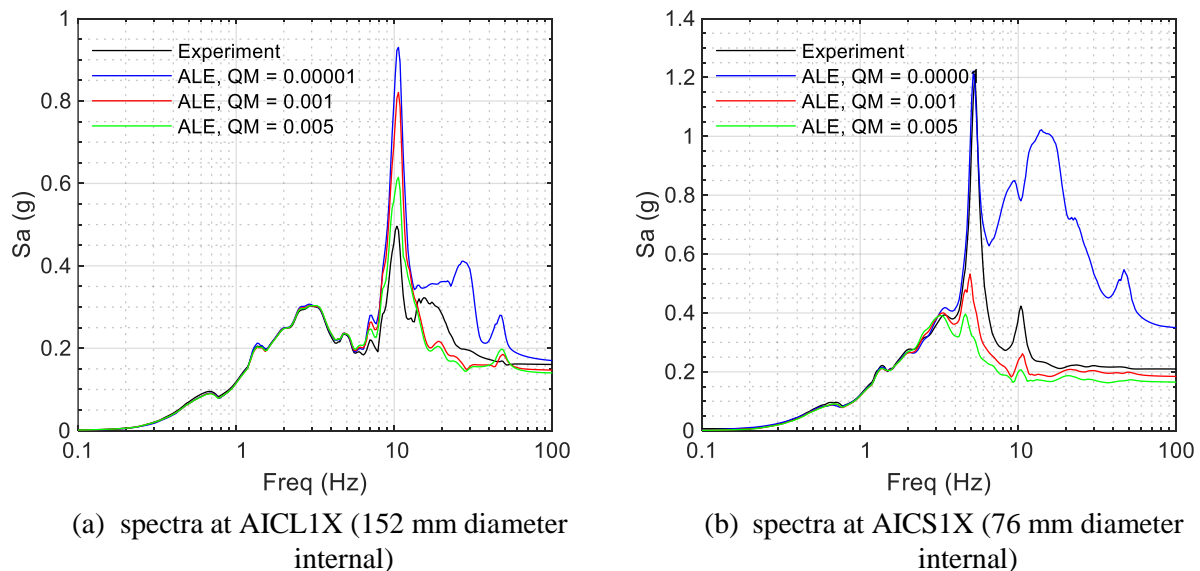
Figure 6.20. Effect of using different hourglass coefficients on accelerations, 1D CCE input, FE model $3C_{finer,}$ acceleration spectra are for 5% damping

The differences in spectral shapes and peak accelerations for different hourglass coefficients are evident in the presented plots. This presents a challenge in finite element analysis of a fluid-structure system for which no experimental data is available and the modelling of which requires the use of an hourglass control algorithm. If mesh refinement is not an option, a solution is to begin with a low value of hourglass coefficient (say 10^{-5}) and increase it, if needed for a stable simulation. However, this will not address the lack of confidence associated with response estimates generated using a particular *stabilizing* hourglass coefficient. A parametric analysis using a range of hourglass coefficients (say between 0.00001 and 0.001) may be useful in such a case.

Table 6.5 presents the values of hourglass coefficients used in the analyses of different models presented in this section. A very small value of this coefficient (10^{-5}) was used for the analysis of FE model 1 and FE model 3A. Higher values ($\geq 10^{-4}$) were required for analysis of other models.

Table 6.5: Hourglass coefficients used in analysis
of numerical models

FE model 1	10^{-5}
FE model 2B	10^{-4}
FE model 3A	10^{-5}
FE model 3B	3×10^{-4}
FE model 3C	3×10^{-4}

6.6   Summary and conclusions

Numerical models of internal components submerged in water in a base supported cylindrical vessel, described in Section 5, were built in LS-DYNA. The internal components included a central steel internal, a steel plate internal, a 76 mm diameter aluminum internal, and a 152 mm diameter aluminum internal with *in-air* frequencies of 32.8 Hz, 3.1 Hz, 15.5 Hz, and 7 Hz, respectively. The ALE solver of LS-DYNA was used for the response-history analyses.

Table 6.6 presents a summary of differences between numerical predictions and experimental results for different response parameters of the internals. The average of absolute percentage differences between peak numerical and experimental responses is used in cases where time series are compared, as done previously.

The specification of an error threshold for validating models is problem- and analyst-specific and could change depending on the complexity of the problem at hand. A fluid-filled vessel with submerged

components is more complex than a fluid-filled vessel without submerged components (such as that presented in Sections 3 and 4). Consequently, a higher threshold error percentage, say 25%, could be used. Based on this threshold and the values presented in Table 6.6, the numerical models presented in this section can be considered to be validated for estimating *in-water* frequencies of the components. The numerical model of the central internal can be considered validated for estimation of pressure response on the central internal. All models, except the one for the steel plate internal, can be considered validated for estimating acceleration responses. Numerical estimates of strain responses, in general, were not in good agreement with experimental results and thus, none of the models here is considered validated for estimating strains.

Table 6.6: Summary of differences between ALE and experimental results

Internal component	Response quantity	Difference between ALE and experimental results
Central internal	*In-water* frequency	0%
	Pressure on internal	13%
	Acceleration response of internal	11%
Steel plate internal	*In-water* frequency	23% (first mode), 19% (second mode)
	Strain response near point of attachment	**44%**
	Acceleration response of internal	**44%**
152 mm diameter aluminum internal	*In-water* frequency	8%*
	Strain response near point of attachment	**47%**
	Acceleration response of internal	15%
76 mm diameter aluminum internal	*In-water* frequency	11%*
	Strain response near point of attachment	**38%**
	Acceleration response of internal	25%

*This difference was reduced to 0% when a finer mesh was used

135

Better estimates of *in-water* frequency can be obtained if fine meshes are used around the submerged components. In the absence of experimental data on frequency in the submerged state, (for example, for the internal components of a prototype reactor) a mesh convergence study should be performed before selecting a mesh size for response-history analyses. In such cases, and depending on available computational resources, an analyst may compromise on the achieved accuracy of the frequency estimates and choose to not select the *finest* (most accurate) mesh for response-history analyses.

The *damping* effect of using an hourglass control algorithm was investigated. In the absence of experimental data or in cases where mesh refinement is not possible for reasons related to computational resources, a small value of hourglass coefficient should be used, if needed.

SECTION 7

EXPERIMENTAL AND NUMERICAL STUDIES ON A SEISMICALLY ISOLATED VESSEL

7.1 Introduction

This section focuses on earthquake-simulator experiments and numerical modelling of a fluid-filled, base-supported vessel seismically isolated using four single concave friction pendulum bearings (SFP bearings or isolators). Numerical studies wherein the vessel is modelled using the Arbitrary Lagrangian and Eulerian (ALE) approach (as described in Section 4) and the bearings are modeled using the MAT_SEISMIC_ISOLATOR property in LS-DYNA (LSTC 2017) are presented. Isolator behavior and fluid responses from the numerical model are compared with experimental results for validation.

The fluid-filled vessel described in Section 3 was used for the experiments described in this section. The base of the vessel and the instrumentation were modified as described in Section 7.2. Section 7.3 presents the mechanical properties of the SFP bearings, Section 7.4 describes the seismic inputs used for testing and the observed behavior of the isolation system in the earthquake-simulator tests. The numerical modeling approaches used for the seismically isolated vessel and results of the validation study are discussed in Section 7.5. Section 7.6 summarizes the study.

7.2 Test specimen and instrumentation

The cylindrical vessel described in Section 3 (height of 2 m, radius of 0.76 m, and wall thickness of 7.9 mm) was used for the tests presented in this section. The thickness of the 2 m $\times$ 2 m base of the vessel was increased from 45 mm to 95 mm and the points of attachment of the base plate to load cells were also modified to increase the distance between them from 0.61 m to 1.12 m. (This distance is marked as d_{lc} in Figure 7.1b.) These changes were made to increase the frequencies of the vertical and rocking modes of the base-isolated specimen. The cartesian and cylindrical coordinate systems adopted for the study are shown in the figure. A fill level of 80% was used for testing.

(a) elevation   (b) section A-A
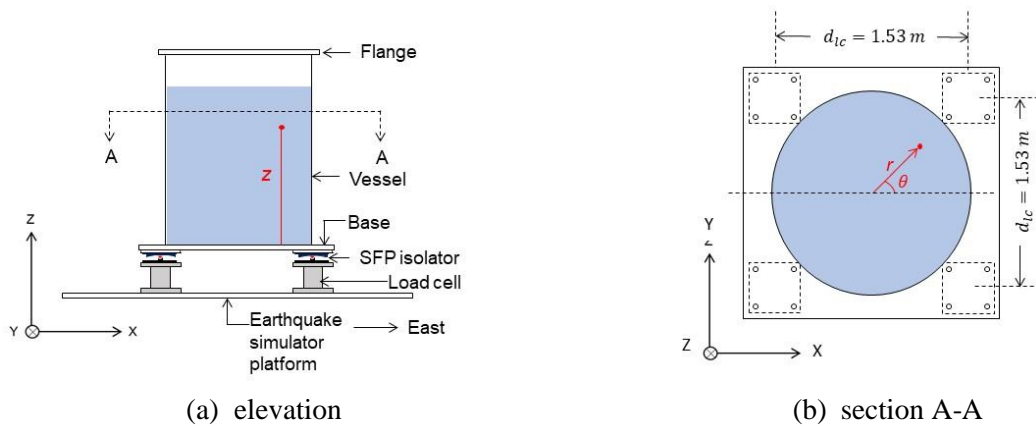
Figure 7.1. Test specimen

The vessel was instrumented with twelve pressure gages for recording hydrodynamic pressure on its wall. These gages were located at locations shown in Figure 3.2a except the bottom array of four gages (PE1, PW1, PN1, and PS1) was located 150 mm above the base of the vessel. Three-directional acceleration responses were measured at four locations near the top of the vessel, above the four SFP bearings (on the base plate of the vessel), and above the four load cells. Three-directional accelerations were also recorded at the center of the earthquake-simulator platform. The locations of the tri-axial accelerometers are indicated by green solid triangles in Figure 7.2. Four vertically-oriented accelerometers were installed on the earthquake-simulator platform as shown in Figure 7.2e for the purpose of recording rocking accelerations of the simulator about the two horizontal axes. A similar arrangement of four accelerometers was also installed on the base of the vessel (in addition to the accelerometers above the SFP bearings; see Figure 7.2c). The locations of these vertically-oriented accelerometers are marked by solid blue triangles in Figure 7.2. Horizontal displacements of the isolators were measured using eight string potentiometers: four installed above the load cells and four above the bearings. The locations of the string potentiometers are indicated by solid yellow circles in the figure.

(a) elevation

(b) section B-B, top of the vessel

(c) section C-C, base plate

(d) section D-D, load cells

(e) section E-E, earthquake simulator, dimensions in mm
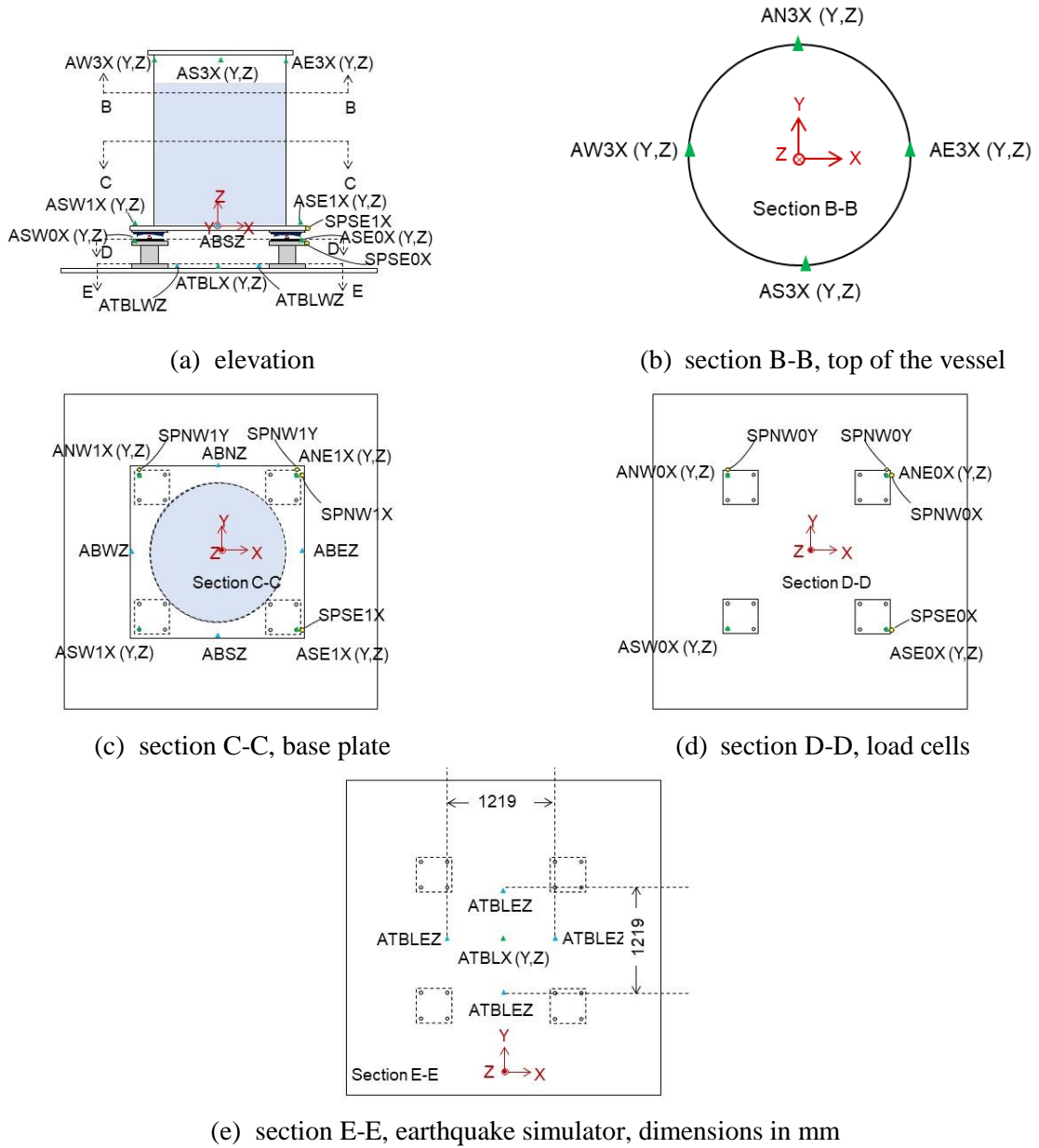
Figure 7.2. Location of accelerometers and string potentiometers, accelerometer names begin with 'A' and string potentiometers names begin with 'SP'

Wave heights were measured at two points on the water surface near the eastern and western ends of the vessel wall using float-and-Temposonic-based sensors (described in Section 3). These are identified as TE and TW, and were located at $(r,\theta,z)=(0.67,0,1.6)$ and $(r,\theta,z)=(0.67,\pi,1.6)$, respectively.

7.3   SFP isolators

Four single concave friction pendulum bearings were used for testing. These are identified as SFP1, SFP2, SFP3, and SFP4. Each bearing consists of a sliding surface (concave plate), a housing plate, and a slider that is coated with a PTFE-type composite, as shown in Figure 7.3. Figure 7.4 shows the fabrication drawings of the bearings, as provided by the manufacturer, Earthquake Protection Systems.

Figure 7.3. Components of an SFP isolator (Lal *et al.* 2021)
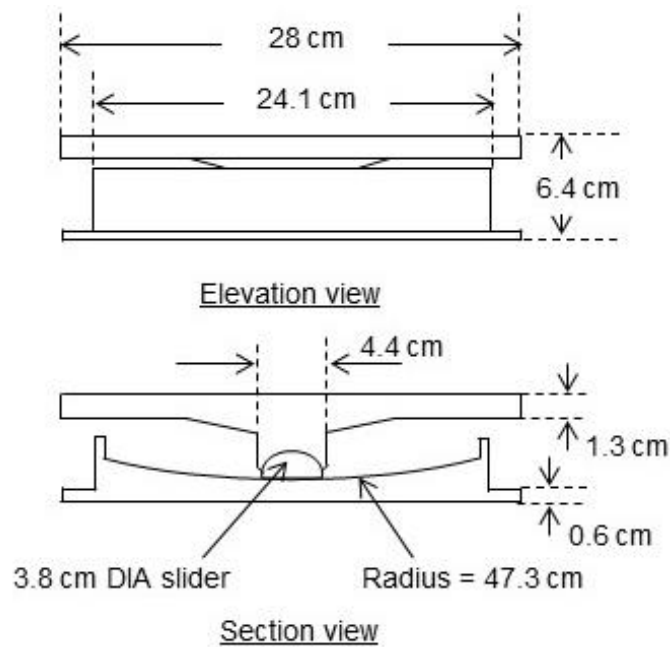
Figure 7.4. Fabrication drawings of SFP isolators (provided by Earthquake Protection Systems)

The idealized force-displacement behavior of an SFP isolator in the horizontal directions is characterized by the radius of curvature of the sliding surface (R) and the coefficient of friction (μ) at the sliding surface. The coefficient of friction is a function of axial load on the bearing, sliding velocity, and temperature of the sliding surface. An increase in axial load leads to a reduction in the coefficient of friction. The coefficient of friction at near zero sliding velocity is referred to as the breakaway friction. As the sliding velocity increases, the coefficient of friction drops to a minimum value (μ_{min}) before attaining a maximum value (μ_{max}) at high velocity. In general, for a fixed value of axial load, the relationship between the coefficient of friction and the sliding velocity (V) can be described by (Constantinou *et al.* 2007):

$$\mu = \mu_{max} - (\mu_{max} - \mu_{min})e^{-aV} \qquad (7.1)$$

where a is a rate parameter. The coefficient of friction reduces with an increase in temperature of the sliding surface.

The behavior of the SFP bearing in the vertical direction is characterized by stiffness under a specified (compressive) axial load (the stiffness in tension is zero). Figure 7.5 shows a representative axial force-axial displacement behavior of an SFP bearing. The axial stiffness is small at low axial load and increases with axial load.
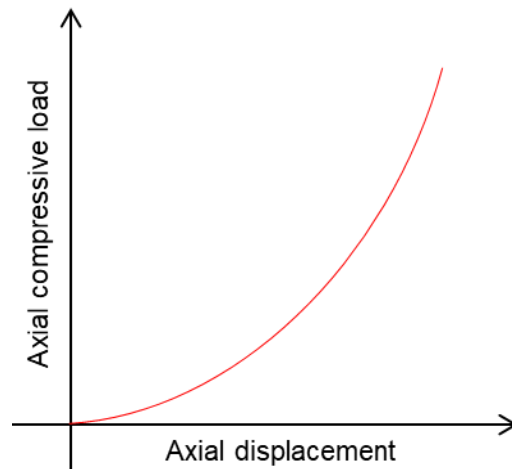
Figure 7.5. Representative behavior of an SFP isolator in compression

The radius of curvature of the sliding surface is a known geometric property (equal to 47.3 cm here). (This corresponds to a sliding period of 1.38 seconds or a frequency of 0.72 Hz). The friction coefficient and stiffness in compression were determined from characterization tests described in detail in Appendix D.

The characterization tests described in Appendix D were carried out for an axial load of 20 kN (4.5 kips), which is slightly greater than the axial load per bearing in the earthquake-simulator tests described in this section (=17.2 kN or 3.9 kips). Table 7.1 summarizes the results of the characterization tests.

Table 7.1. Summary of characterization tests, axial load = 20 kN

Bearing	Friction coefficient, slow (%)	Friction coefficient, fast (%)	Rate parameter (sec/cm)	Axial stiffness ($\times 10^5$ kN/m)
SFP1	3.7	12.5	0.39	1.08
SFP2	2.3	7.5	0.67	0.96
SFP3	2.6	10.5	0.35	1.07
SFP4	2.4	10.1	0.35	1.20
Average	2.8	10.2	0.44	1.07

7.4   Seismic inputs and isolation-system behavior

The earthquake-simulator inputs CCE, ECE, and KCE, introduced in Table 3.1, were used for testing. Table 7.2 lists the motions and the corresponding peak accelerations in the three orthogonal directions. Motion #1 is a large amplitude (peak amplitude = 0.8g), uni-directional input; motion #2 is a small amplitude (peak amplitude < 0.12g), three-directional input; and motions 3 and 4 are large amplitude, three-directional inputs.

Table 7.2. Earthquake-simulator inputs used for testing

Number	Motion	x-direction PGA (g)	y-direction PGA (g)	z-direction PGA (g)
1	ECE	0.8	-	-
2	CCE	0.1	0.12	0.05
3	ECE	0.8	0.6	0.5
4	KCE	0.8	0.88	0.56

Response spectra for the acceleration time series recorded above and below the bearings in the tests are presented in Figure 7.6 through Figure 7.9 (All of the time-series data presented in this section are filtered

using a 0.05 Hz – 50 Hz *bandpass* filter). Rocking accelerations of the earthquake-simulator platform (about the two horizontal axes) are observed in addition to translational accelerations due to compliance in the horizontal and vertical actuators of the earthquake simulator. A reduction in spectral acceleration above the isolation interface is observed in the case of horizontal components of the high amplitude motions (#1, #3, and #4 in Table 7.2) for frequencies less than 30 Hz: see Figure 7.6a, Figure 7.8a, b, and Figure 7.9a, b. For motion #3, the horizontal spectra are amplified near 30 Hz (see Figure 7.8a, b) due to the vertical flexibility of the bearings and the vertical component of the motion. Spectral accelerations in the vertical direction above the isolation interface are amplified around 30 Hz. Rocking accelerations above the isolation interface are also amplified around this frequency.
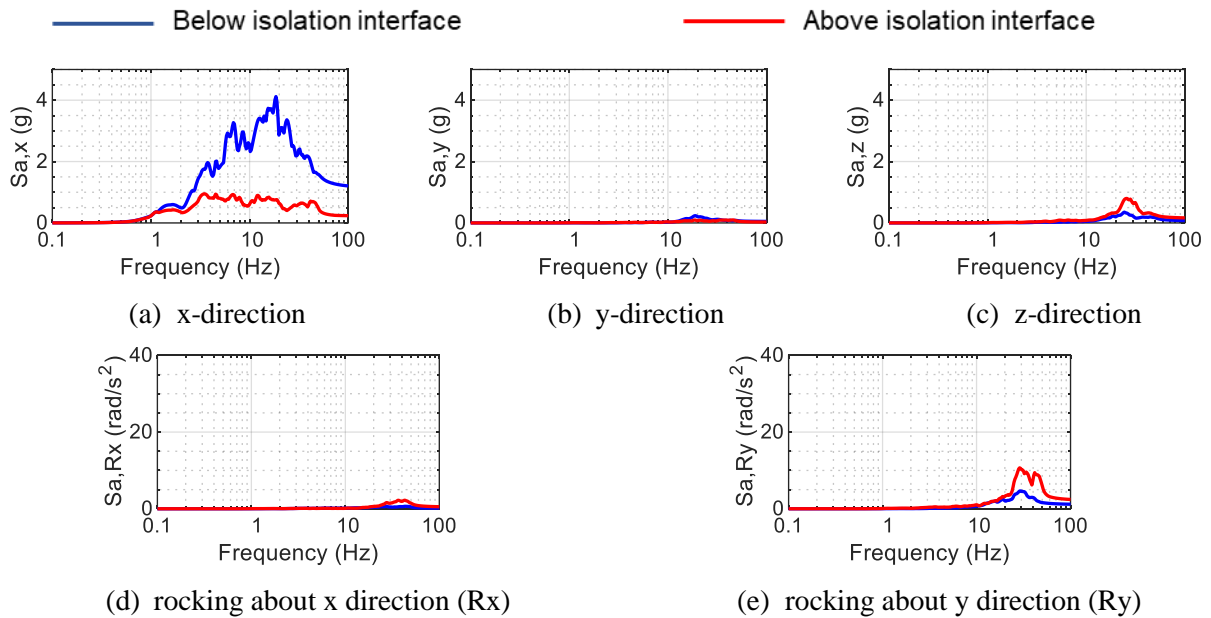
Figure 7.6. Acceleration spectra below and above the isolation interface, motion #1 in Table 7.2

(a) x-direction   (b) y-direction   (c) z-direction

(d) rocking about x direction (Rx)   (e) rocking about y direction (Ry)
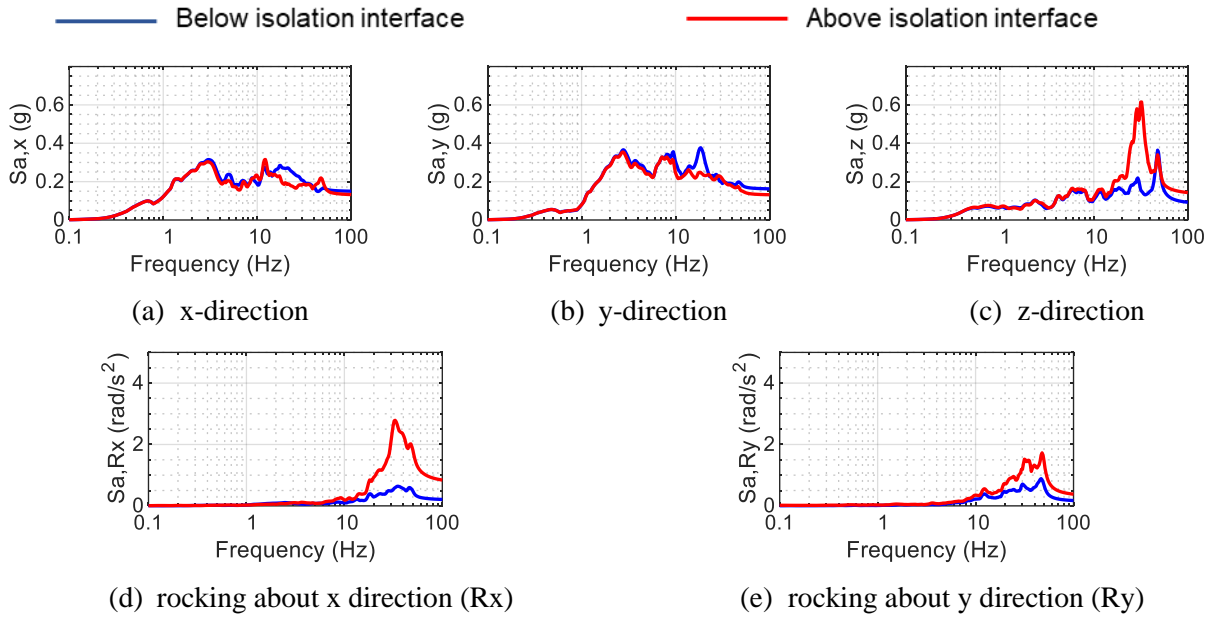
Figure 7.7. Acceleration spectra below and above the isolation interface, motion #2 in Table 7.2

(a) x-direction   (b) y-direction   (c) z-direction

(d) rocking about x direction (Rx)   (e) rocking about y direction (Ry)
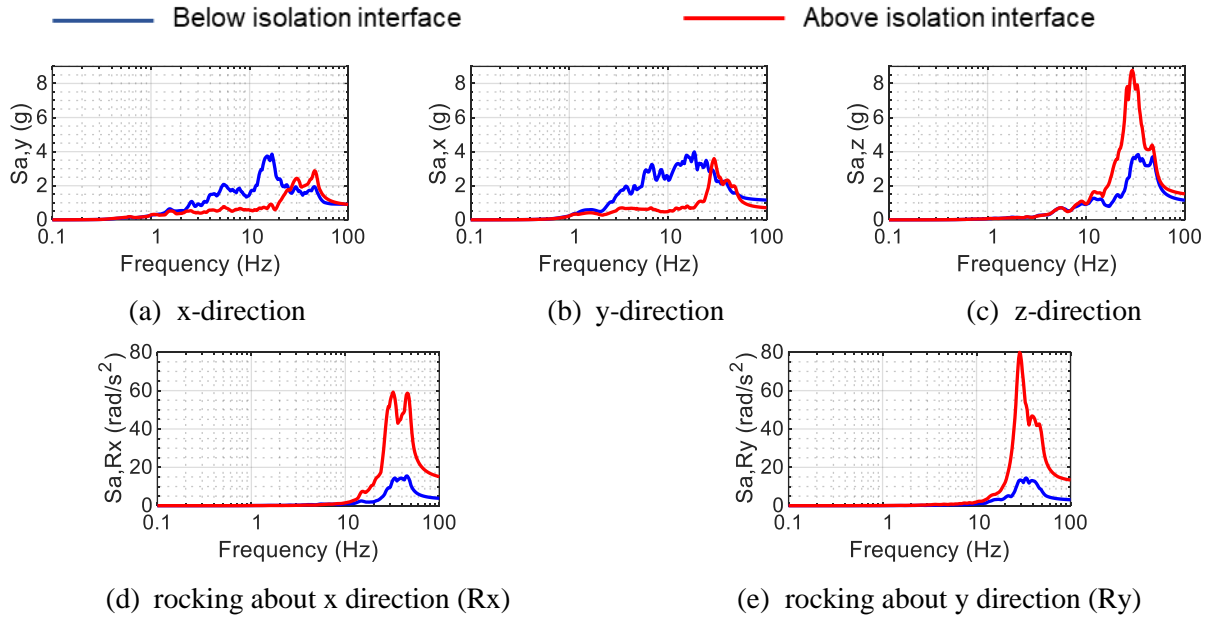
Figure 7.8. Acceleration spectra below and above the isolation interface, motion #3 in Table 7.2

144

(a) x-direction   (b) y-direction   (c) z-direction

(d) rocking about x direction (Rx)   (e) rocking about y direction (Ry)
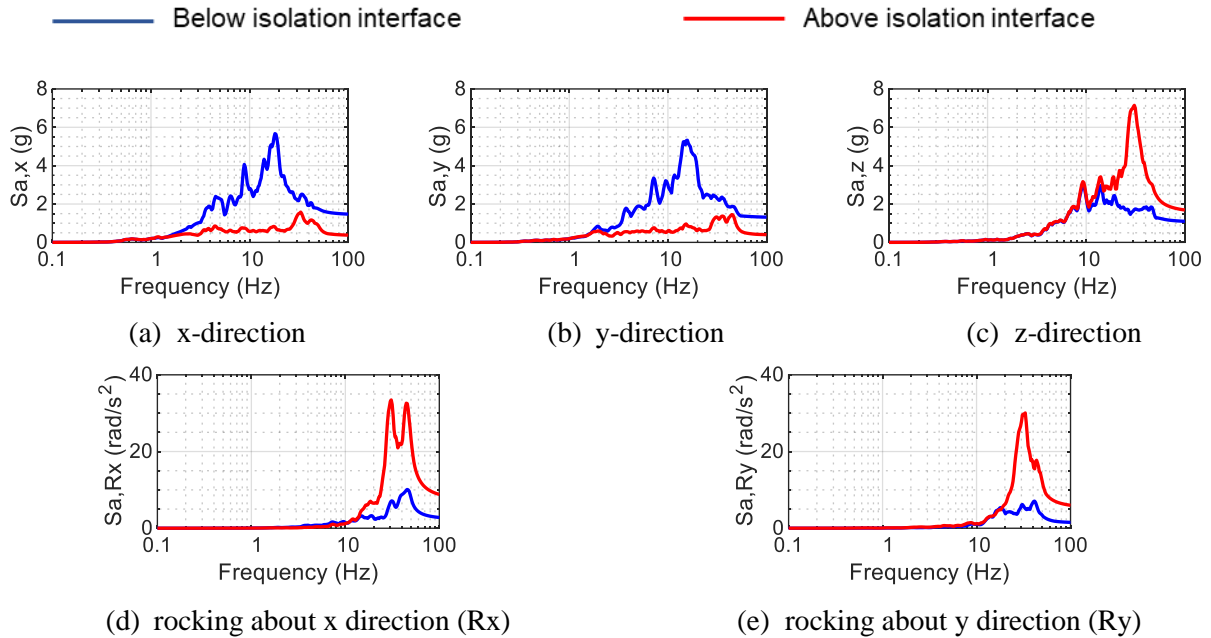
Figure 7.9. Acceleration spectra below and above the isolation interface, motion #4 in Table 7.2

The average axial stiffness of the SFP bearings at an axial load of 20 kN (4.5 kips) is 1.07×10^5 kN/m (see Table 7.1). As noted previously, the axial load per bearing in the tests described here is less than 20 kN: 17.2 kN. Since axial stiffness is dependent on axial load, a vertical stiffness of 0.9×10^5 kN/m was used instead of the test value of 1.07×10^5 N/m at 20 kN (16% reduction) for the numerical analyses presented later in this section.[16]

A normalized force-displacement loop from the test with a unidirectional earthquake-simulator input (motion #1 in Table 7.2) is presented in Figure 7.10. The normalized force is computed as the total shear force along the *x*-direction normalized by the total instantaneous axial load. An idealized force-displacement loop considering a maximum displacement equal to that observed in the test is also plotted to enable a comparison. A high velocity friction value of 12% is used for constructing the idealized loop and in the numerical analyses presented later in this section. This value is greater than the average value of 10.2% reported in Table 7.1 above. One of the reasons for the greater obtained value of friction is that these

---

[16] A numerical model of the isolated vessel was constructed in SAP2000 (CSI 2019) with the mass of the fluid lumped on the wall and base of the vessel. An axial stiffness of 0.9×10^5 kN/m in the bearings resulted in a vertical mode at 32.5 Hz and rocking modes (about *x* and *y* axes) at 31.5 Hz. These frequencies are similar to those observed in the earthquake-simulator experiments.

tests were conducted after another set of experiments involving more than 30 earthquake motions (using the same bearings), which led to wear in the slider surface and more uniform bearing (i.e., greater contact area) of the slider on the concave plate. A larger contact area implies a reduction in contact pressure. The axial load in the tests described here is 13% lower than the load at which the friction values were characterized, again implying a reduction in contact pressure. An increase in the coefficient of friction with a reduction in contact pressure is well-documented (Constantinou *et al.* 2007).
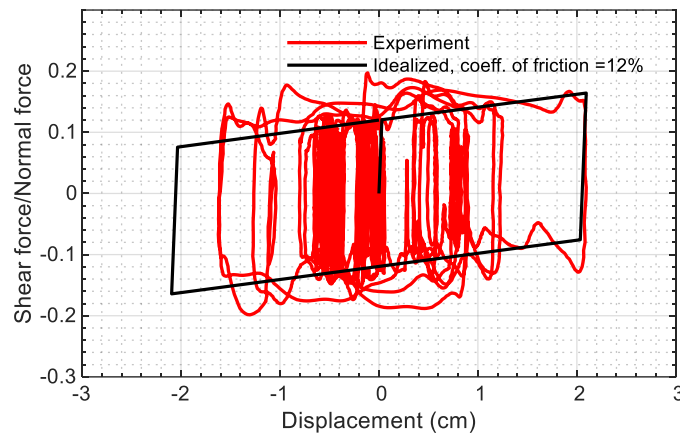
Figure 7.10. Normalized force-displacement loop, motion #1 in Table 7.2

The force-displacement loop in Figure 7.10 shows spikes in normalized force (or friction coefficient), which is a departure from the idealized behavior. A possible reason for this behavior is that the base of the tank (which has concave plates attached to it) rotates with respect to the horizontal plane in which the housing plates lie. Fenz and Constantinou (2008) presents a detailed discussion on the effect such rotations have on the force-displacement behavior of an SFP bearing (see section 2.5.5 in Fenz and Constantinou (2008)). A rotational displacement of τ radians leads to an upward or downward shift (depending on the sign of τ) of τ in the normalized force-displacement loop. Accordingly, a rotational displacement of 1° can lead to a vertical shift of 0.02 in the normalized force-displacement loop.

7.5   Numerical modelling

This section focuses on numerical modeling of the isolated, fluid-filled vessel. Key inputs used to model the base-isolated vessel are described. Numerical results for responses of the isolation system and fluid in the vessel are calculated using response-history analyses and compared with experimental data.

7.5.1   ALE model with SFP bearings

The Arbitrary Lagrangian and Eulerian (ALE) solver in LS-DYNA is used for numerical analyses. A description of the ALE model for a fluid-filled vessel was provided in Section 4.2. A similar approach was used here to model the vessel and the contained fluid. The base of the vessel was modeled using shell elements and an elastic material having properties consistent with carbon steel (unlike in Section 4.2 where the base of the vessel was modeled using a rigid material). The four SFP bearings were modeled using two-noded beam elements oriented vertically. The lower ends of the four isolators were connected to a rigid plate representing the plane in which the upper ends of the load cells (see Figure 7.1a) lie. The rigid plate was assigned a negligible mass (0.2 kg). Accelerations recorded at the tops of the load cells (below the bearings) in the experiment were input to this rigid plate using the *BOUNDARY_PRESCRIBED_MOTION_RIGID keyword. Translational accelerations along the three orthogonal axes and rocking accelerations about the two horizontal axes recorded in experiments were used as inputs to the model. Figure 7.11 presents the numerical model in LS-DYNA. The rigid plate used to input accelerations is shown in light brown; the isolators are shown in red; the vessel wall, flange, and base are shown in grey; and the water is shown in blue. The *void* space modeled above the water domain, to accommodate sloshing motion, is not shown in the figure. In the experiments, the concave plates of the SFP isolators were connected to the 95 mm thick base of the vessel via 0.41 m × 0.41 m × 0.025 m adapter plates made of carbon steel. The locations of these adaptor plates are indicated in green in Figure 7.11b. The area of the vessel base in contact with the adapter plates was assigned a rigid material property and the mass density of carbon steel.

(a) elevation   (b) isometric view
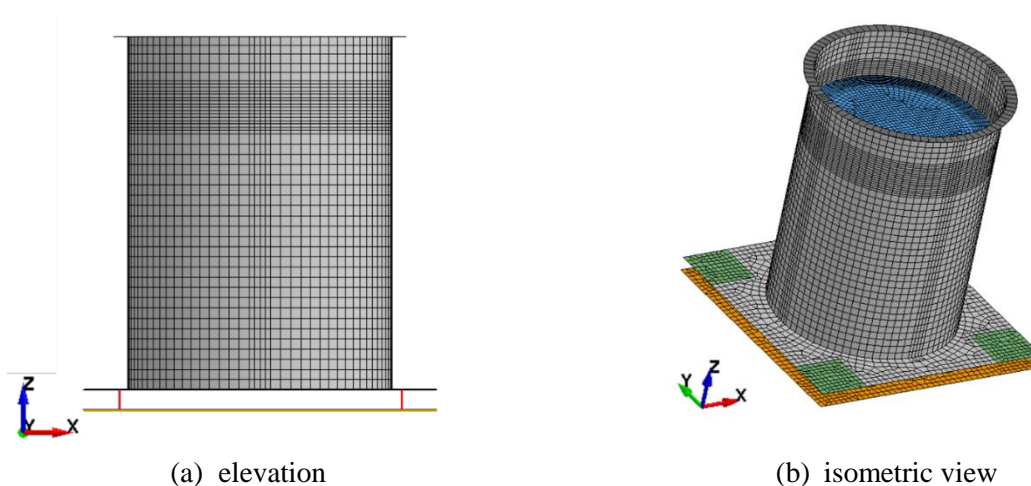
Figure 7.11. Numerical model in LS-DYNA

The bearings were modelled using two-noded beam elements with *MAT_SEISMIC_ISOLATOR property assigned to them. Beam element formulation 6 (ELFORM = 6 in *SECTION_BEAM) suitable for modeling discrete beams was used. The volume of the discrete beam was defined in *SECTION_BEAM keyword. The volume specified here is used for calculation of mass of the discrete beam per the density defined in *MAT_SEISMIC_ISOLATOR keyword (discussed below). The total mass of the beam is distributed equally to the two nodes of the beam. A definition of a reasonable value of mass for the discrete beam is important to avoid unnecessarily small calculation time steps (large run times) in explicit analysis. A total *beam mass* of 80 kg was defined for analysis here such that 40 kg is lumped on the top node of each beam element representing a bearing. (This mass approximately represents one adapter plate and one concave plate.) The *SECTION_BEAM keyword also has an input field for definition of the mass moment of inertia of the discrete beam (INER in *SECTION_BEAM keyword). Since the isolator element has no rotational stiffness, this input has no effect on the solution. However, some LS-DYNA solvers (for example R 12.0, which was used for this study) require definition of a non-zero INER value to maintain reasonably large analysis time steps. A value of 0.4 kg-m^2 was used here. (Higher values can also be used. In the LS-DYNA model being described here, the analysis time step was not governed by the isolator element for INER=0.4 kg-m^2). Key inputs required for definition of *MAT_SEISMIC_ISOLATOR property are listed in Table 7.3.

An acceleration of 9.81 m/sec^2 (gravity) was applied in the negative *z*-direction in the model. This acceleration was applied as a ramp from 0 to 9.81 m/sec^2 in the initial 0.05 sec of analysis (followed by a constant gravitational acceleration of 9.81 m/sec^2 thereafter). Acceleration inputs to the model were applied after the initial 0.1 sec of analysis. This ensured proper initialization of hydrostatic pressure and isolator axial load in the model before the application of acceleration inputs.

Table 7.3. Key inputs for definition of *MAT_SEISMIC_ISOLATOR for SFP bearings in LS-DYNA

Input field	Description
RO	Mass density used with the volume input in *SECTION_BEAM to calculate the mass of the discrete beam. A volume of 80 m^3 was specified in *SECTION_BEAM and RO here was assigned a value of 1 kg/m^3 resulting in a net mass of 80 kg.
DISPY	*Yield displacement* of the seismic isolator. A value of 0.3 mm was used here based on the slope of the *elastic region* of the (experimental) force-displacement loop for motion #1. For simulations involving large isolator displacements, a higher value of 1 mm is reasonable.
STIFFV	Vertical stiffness of the isolator. For the sliding bearings, the behavior in compression is linear elastic[17] and no tensile force can be resisted. A value of 0.9×10^5 kN/m was used here per the discussion in Section 7.4.
ITYPE	Equal to 0 for sliding bearings (=1 for elastomeric bearings).
PRELOAD	Vertical pre-load on the bearings. A zero pre-load was assigned to the bearings. Gravity was applied before application of seismic inputs as discussed in Section 7.5.1.
FMAX	Maximum coefficient of friction; set to 0.12 per Section 7.4.
DELF	Difference between the maximum and static coefficients of friction. A value of 0.087 was used consistent with FMAX above and the ratio of fast and slow friction coefficients per Table 7.1.
AFRIC	Rate parameter used to characterize the velocity dependence of the friction coefficient. A value of 44 sec/m was used per Table 7.1.
DAMP	Fraction of critical damping for free vertical vibration of the isolator, based on the mass of the isolator (including any attached masses) and its vertical stiffness. A parametric study of this input parameter revealed that leaving this value as default (= 0) leads to a stable response in the vertical direction. (DAMP = 0 does not mean that that there is no damping in the vertical direction. Instead, it activates the default algorithm that may occasionally increase DAMP if vertical oscillations become significant and affect numerical stability. Specification of a value, for example DAMP = 0.05, was found to cause instabilities.)
RADX, RADY	Radii of the sliding surface in the two directions. A value of 47.3 cm was used for both directions, per the fabrication drawings of Figure 7.4.
RADB, STIFFL, DFAIL	Radius of the bearings' retaining ring, stiffness (for lateral contact) against the retaining ring, and the lateral displacement at which the isolator fails. Large values were assigned to these input fields since these values are of no significance for the analyses described here.

---

[17] The use of a linear spring in the axial direction (active only in compression) for numerical analyses is an approximation because at low axial loads (as is the case here), the axial stiffness changes appreciably with a change in axial load due to vertical acceleration inputs.

Experimental and numerical isolator responses (acceleration spectra above the isolation plane, isolator displacements, and shear forces) for the four motions are presented in Figure 7.12 to Figure 7.15. For motion #2 (CCE 3D), the isolator displacements are negligible (< 3 mm). In motions #3 and #4, peak vertical accelerations greater than $1g$ above the isolation system are observed, which leads to zero axial force at multiple instants (see Figure 7.16). A normalized force-displacement loop is thus only shown for motion #1 (ECE 1D). Experimental and numerical fluid responses (hydrodynamic pressure at PE1 and PN1 and wave heights at TE and TW) for the four motions are compared in Figure 7.17 to Figure 7.20. There is an excellent agreement between numerical predictions and experimental results. Table 7.4 presents the maximum absolute values of key numerical and experimental results and their percentage differences for the four motions. An average absolute error of 7%, 6%, and 7% is observed in maximum absolute isolator displacements, shear forces in the two horizontal directions, and normal forces, respectively. Average absolute errors in pressure and wave height responses are 11% and 12%, respectively. The relatively high errors in wave height responses are expected, as explained in Section 4. High errors in pressure responses in some motions are primarily due to slight mismatches in the simulated and experimental vertical accelerations (above the isolation system).

(a) acceleration spectra, *x*-direction

(b) acceleration spectra, rocking about *y*-axis

(c) acceleration spectra, *z*-direction

(d) isolator displacement, *x*-direction

(e) shear force, *x*-direction

(f) normalized force-displacement loop, *x*-direction
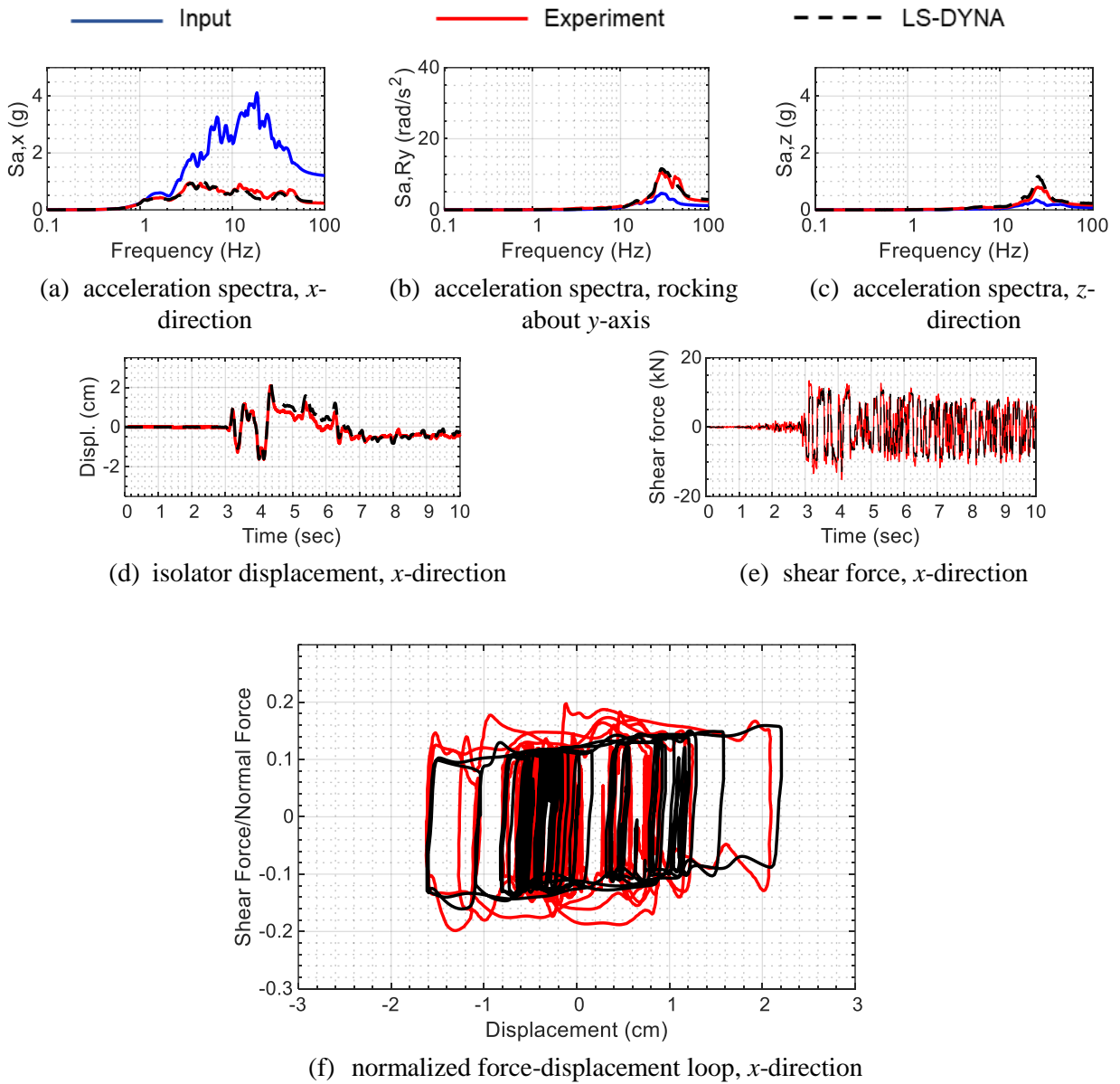
Figure 7.12. Comparison of numerical and experimental results, isolation system response, motion #1 in Table 7.2, acceleration spectra for 5% damping

(a) acceleration spectra, *x*-direction

(b) acceleration spectra, *y*-direction

(c) acceleration spectra, *z*-direction

(d) acceleration spectra, rocking about *x*-axis

(e) acceleration spectra, rocking about *y*-axis

(f) isolator displacement, *x*-direction

(g) isolator displacement, *y*-direction

(h) shear force, *x*-direction

(i) shear force, *y*-direction
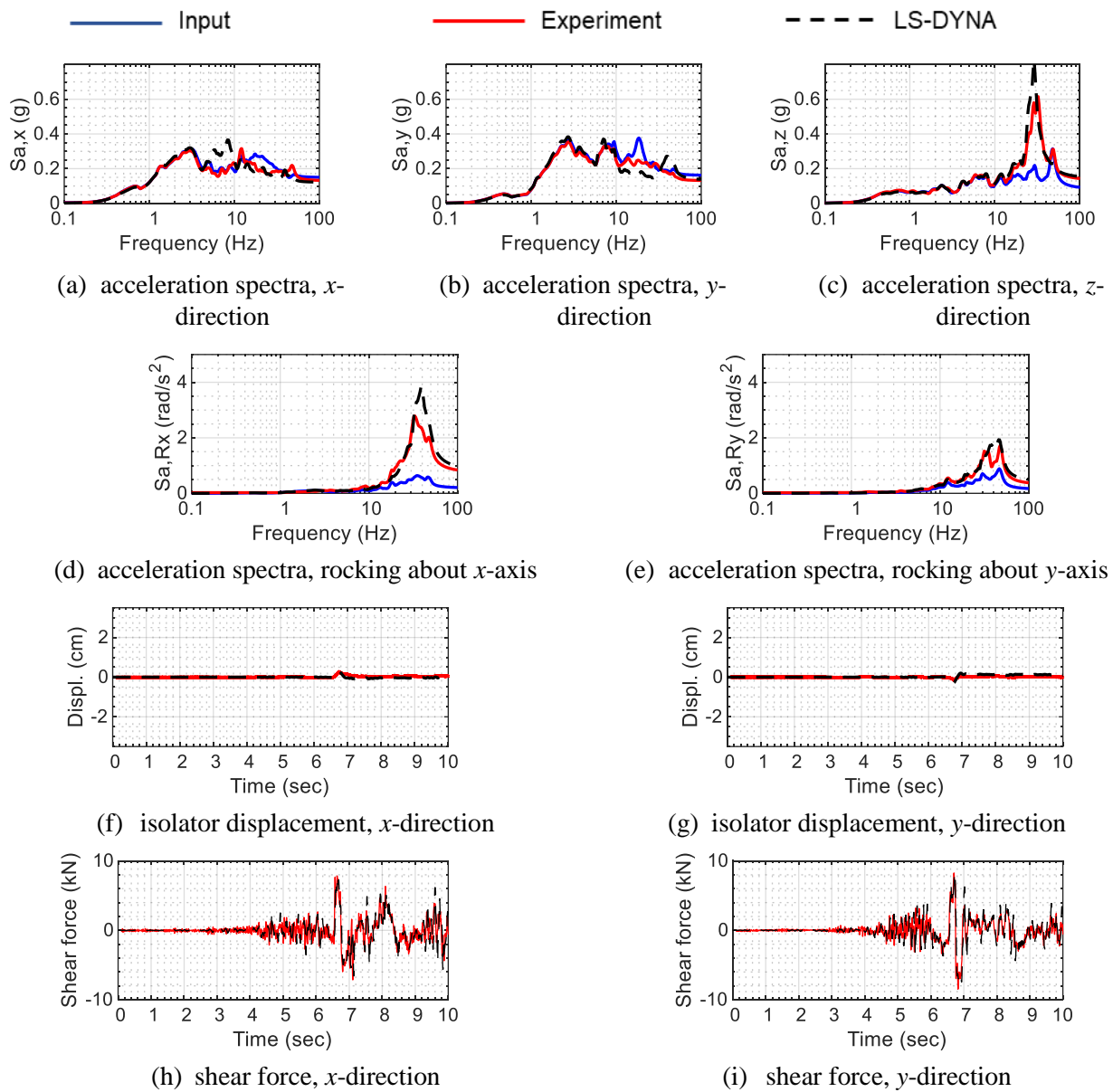
Figure 7.13. Comparison of numerical and experimental results, isolation system response, motion #2 in Table 7.2, acceleration spectra for 5% damping

152
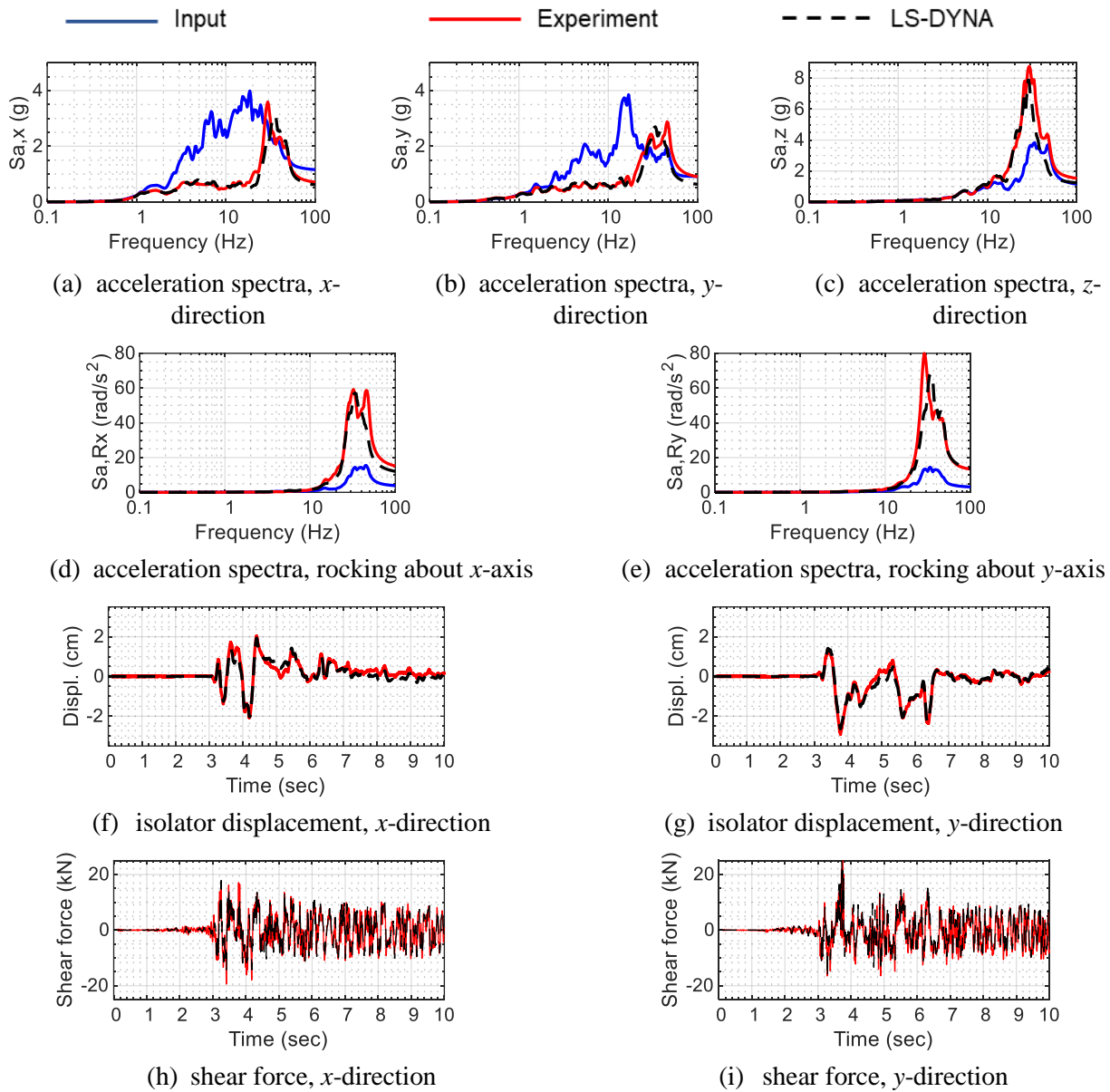
Figure 7.14. Comparison of numerical and experimental results, isolation system response, motion #3 in Table 7.2, acceleration spectra for 5% damping
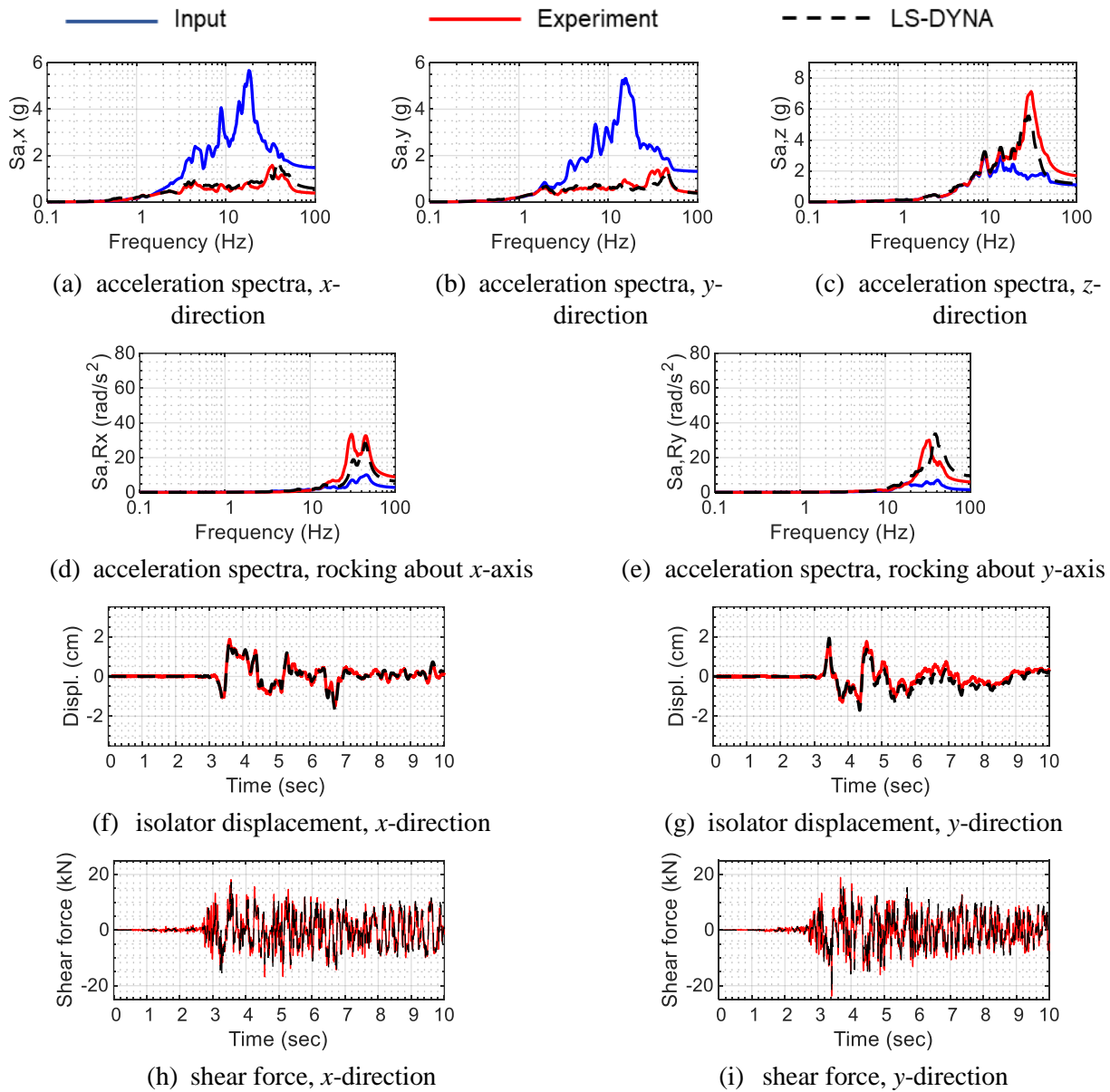
Figure 7.15. Comparison of numerical and experimental results, isolation system response, motion #4 in Table 7.2, acceleration spectra for 5% damping

154

(a) motion #3 (ECE 3D)   (b) motion #4 (KCE 3D)
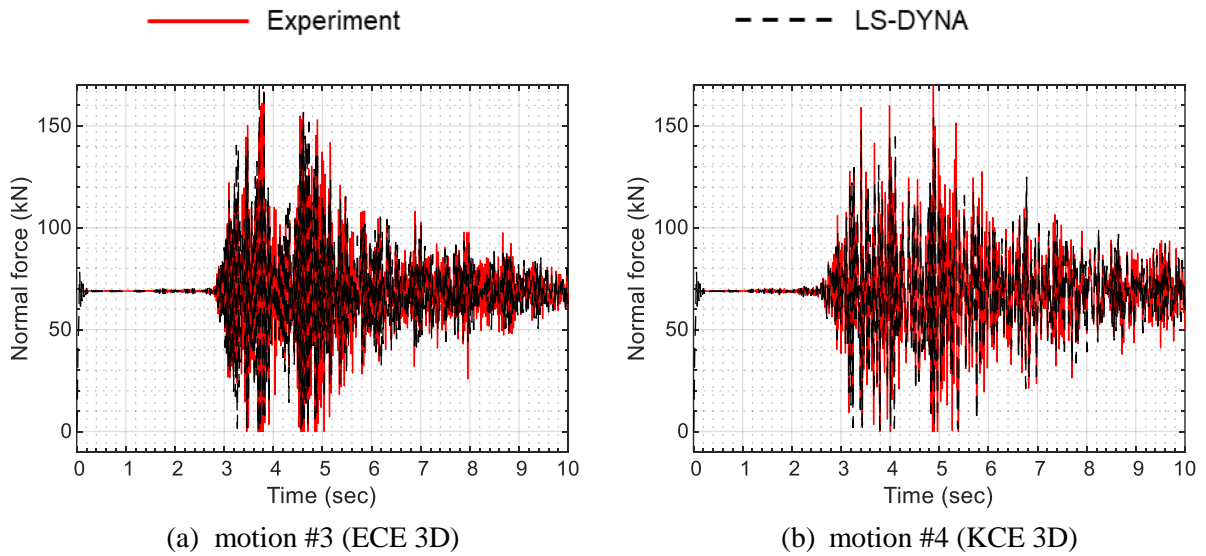
Figure 7.16. Numerical and experimental axial (normal) force histories, compression is positive

(a) hydrodynamic pressure at location of PE1

(b) wave height at location of TE   (c) wave height at location of TW
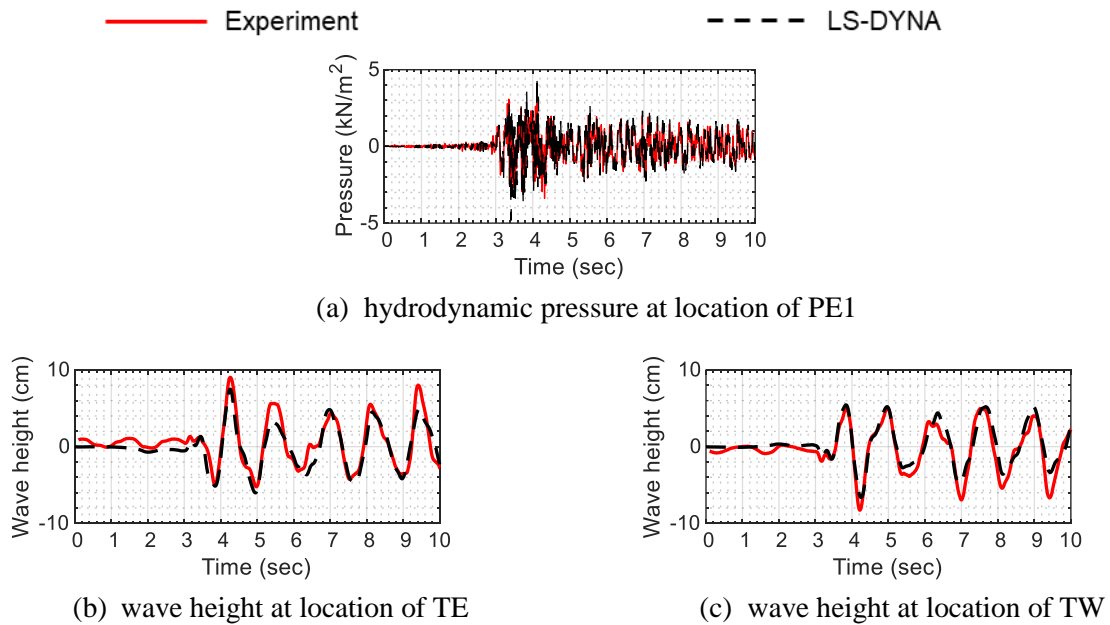
Figure 7.17. Comparison of numerical and experimental fluid responses, motion #1 in Table 7.2

155

(a) hydrodynamic pressure at location of PE1

(b) hydrodynamic pressure at location of PN1

(c) wave height at location of TE

(d) wave height at location of TW
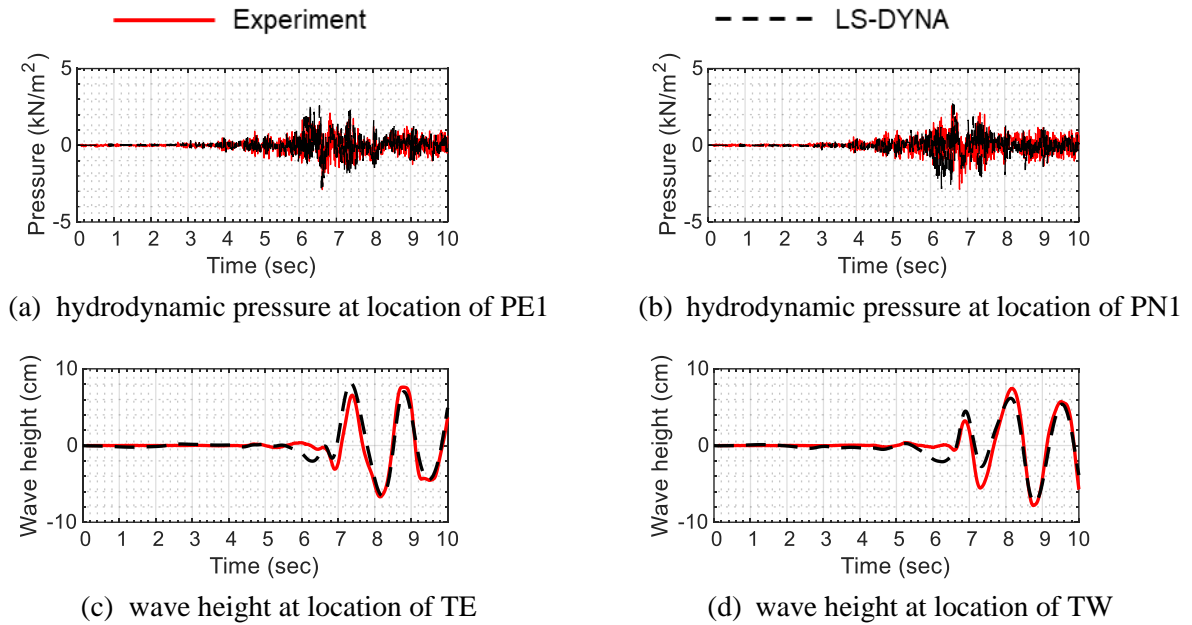
Figure 7.18. Comparison of numerical and experimental fluid responses, motion #2 in Table 7.2

(a) hydrodynamic pressure at location of PE1

(b) hydrodynamic pressure at location of PN1

(c) wave height at location of TE

(d) wave height at location of TW
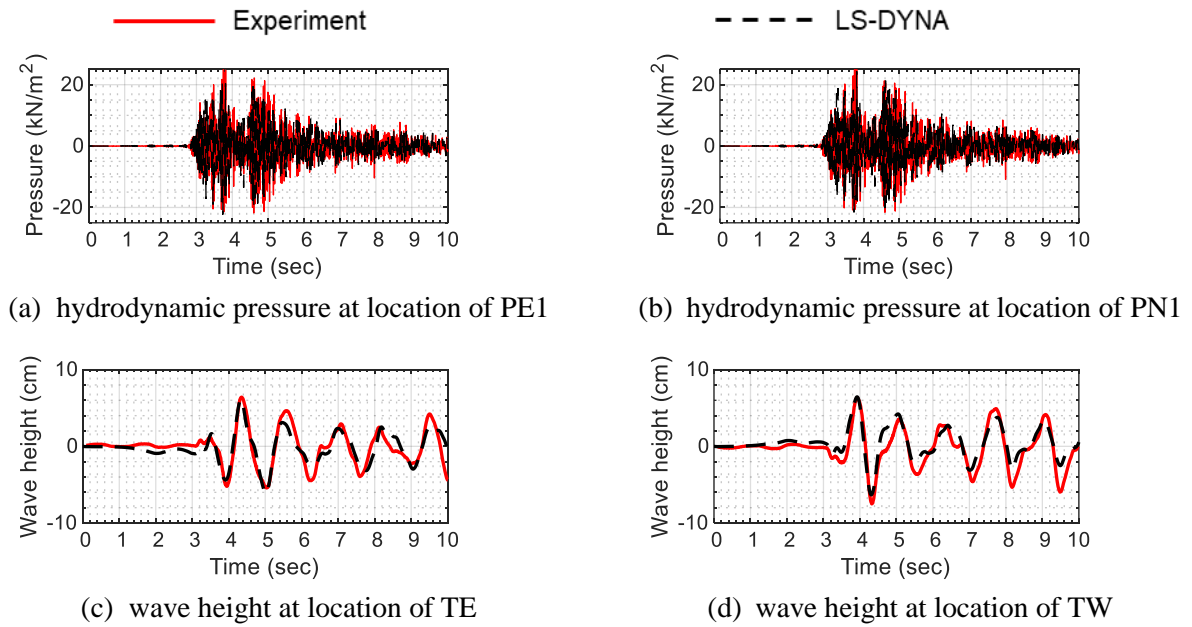
Figure 7.19. Comparison of numerical and experimental fluid responses, motion #3 in Table 7.2
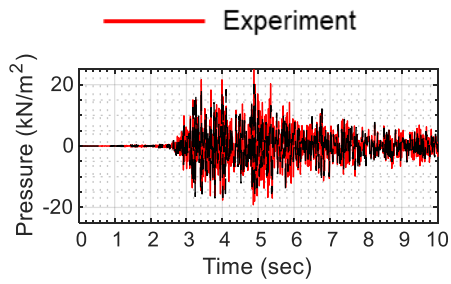
(a) hydrodynamic pressure at location of PE1
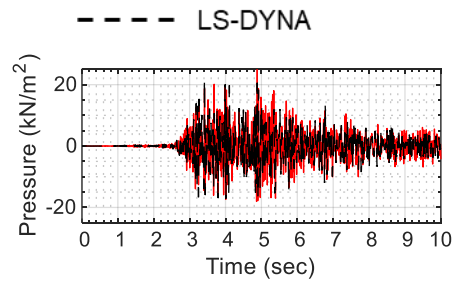
(b) hydrodynamic pressure at location of PN1
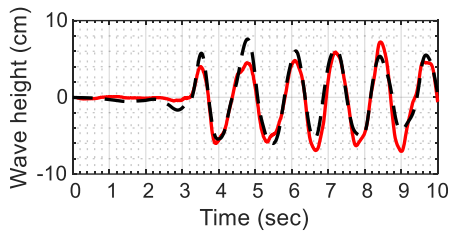
(c) wave height at location of TE
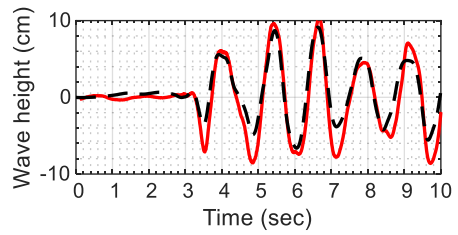
(d) wave height at location of TW

Figure 7.20. Comparison of numerical and experimental fluid responses, motion #4 in Table 7.2

Table 7.4. Maximum absolute isolation system responses and fluid responses (rounded to one decimal digit) and percentage differences

Response (or location)	Motion #1 (ECE 1D)			Motion #2 (CCE 3D)			Motion #3 (ECE 3D)			Motion #4 (KCE 3D)		
	Model	Exp.	Diff., %	Model	Exp.	Diff., %	Model	Exp.	Diff., %	Model	Exp.	Diff., %
Isolator displ. – x, cm	2.2	2.1	5	0	0	-	2.0	2.1	-3	1.8	1.9	-3
Isolator displ. – y, cm	-	-	-	0	0	-	2.6	2.9	-10	1.9	1.8	10
Shear force– x, kN	12.9	15.2	-15	7.8	7.8	-1	17.9	19.4	-8	17.2	18.2	-5
Shear force– y, kN	-	-	-	8.3	8.5	-3	25.3	27.6	-8	22.4	23.8	-6
Normal force, kN	82.9	80.0	4	80.3	76.9	4	171.0	166.6	3	154.0	181.9	-15
PE1, kN/m^2	4.8	4.0	21	2.8	2.9	-2	22.3	25.5	-12	20.2	23.8	-15
PN1, kN/m^2	-	-	-	2.8	2.9	-1	24.4	28.0	-13	21.8	25.7	-15
TE, cm	7.5	9.0	-17	8.2	7.6	7	6.1	6.4	-5	7.6	7.2	5
TW, cm	6.6	8.3	-20	7.4	8.8	-16	6.4	7.5	-14	9.1	10.4	-12

7.5.2   Scaling issue in pressure output

The simulations described in this section were run using Massively Parallel Processing (MPP) type of computing available for LS-DYNA that uses multiple CPUs (central processing units) running in parallel to execute a single analysis. The run time for the ALE models (for an analysis time of 10 sec) is about 6 hours using 28 cores on a computer with AMD EPYC 7763 (2.45 GHz) processor and 128 GB RAM.

In LS-DYNA, two sets of model outputs are generally generated. One is based on the generated D3PLOT files and contains plotting information that allows visualization of results over the three-dimensional geometry of the model and the other set (which is based on ASCII or BINOUT output files) is used to plot specific pre-requested results (for example, nodal acceleration histories of specified nodes). In general, a large output time interval is used for the former to keep the size of the output files small. Results (time series) at small output time intervals are requested using the latter.

The MPP-DYNA runs do not write ASCII output files directly but instead write the requested data to BINOUT files. The pressure output using the BINOUT files (in R 12.0 solver) must be processed. Figure 7.21 shows the total pressure (hydrostatic plus hydrodynamic) histories for a fluid domain element (near the location of pressure gage PE1) for motion #1 generated using outputs from the D3PLOT and BINOUT files at respective time steps of 0.1 sec and 0.002 sec. The element is located at a depth of 1.48 m from the free surface and thus the calculated hydrostatic pressure is 14.52 kN/m^2, which is what is observed in the output from the D3PLOT file (see Figure 7.21a). However, the pressure output using the BINOUT file is consistently scaled up by a factor or 22000 as can be evaluated by considering a ratio of the hydrostatic pressure (total pressure around 1 sec, when the input acceleration magnitude is negligible) read from the two plots. The hydrodynamic pressure histories presented earlier in Figure 7.17 to Figure 7.20 were obtained from the BINOUT files after scaling down the total pressure history by a factor of 22000.[18]

---

[18] This issue of scaling is not encountered with ASCII output files that are written if Symmetric Multi-Processing (SMP) solvers in LS-DYNA are used.
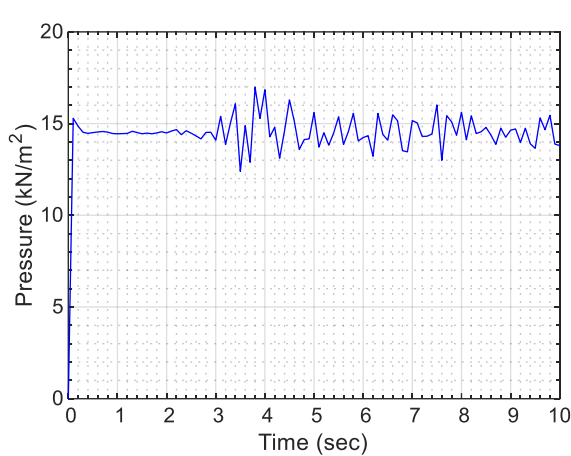
(a) using D3PLOT file, output time step = 0.1 sec
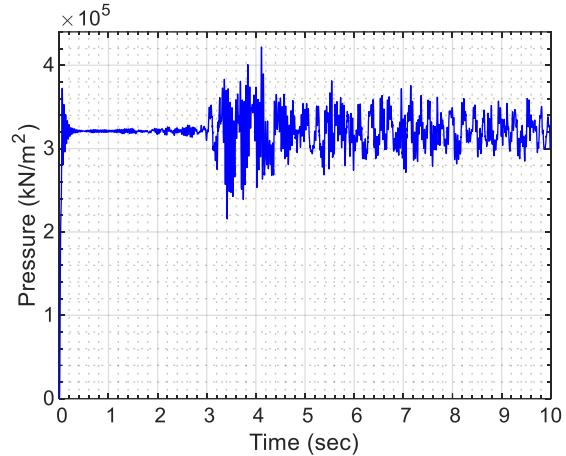
(b) using BINOUT file, output time step = 0.002 sec

Figure 7.21. Total pressure output for a fluid element located at a depth of 1.48 m near pressure gage PE1, motion #1 in Table 7.2

7.6   Summary

Earthquake-simulator experiments on a fluid-filled, base-supported vessel seismically isolated using four single concave friction pendulum bearings (SFP isolators) were described in this section. The base-supported vessel represents a prototype vessel at approximately 1/10th length scale. The SFP isolators have a sliding radius of 0.473 m, which corresponds to a sliding period of 1.38 sec, and a fast friction coefficient of 12%. The use of seismic isolation significantly reduced horizontal accelerations above the isolation interface except around a frequency of 30 Hz, which is the frequency of the vertical mode of the isolation system. Vertical and rocking accelerations were also amplified around 30 Hz.

A numerical study was presented wherein the fluid-filled vessel is modelled using the Arbitrary Lagrangian and Eulerian (ALE) approach and the SFP isolators are modeled using two-noded beam elements with MAT_SEISMIC_ISOLATOR property in LS-DYNA. Numerical predictions of isolation-system responses and fluid responses were found to be in excellent agreement with experimental results. The average differences in peak values of isolation-system responses (isolator displacements and shear forces) were less than 7%. Average differences in peak values of fluid responses (pressure and wave height) were less than 12%. Based on outcomes presented in this section, it can be concluded that the discussed numerical modeling approach can be used to obtain robust seismic response estimates for systems involving fluids and isolators.

SECTION 8

SUMMARY

8.1   Introduction

The construction of safe and economically-competitive next generation nuclear reactors, referred to as advanced or Generation IV (Gen IV) reactors, is critical for limiting greenhouse gas emissions and achieving long-term climate goals. An international cooperation framework, the Generation IV International Forum (https://www.gen-4.org/gif/), has identified six promising reactor technologies that could be deployed in the near term (GIF 2002). Some of these advanced reactor technologies (i.e., lead-cooled fast reactor, molten slat reactor, and sodium-cooled fast reactor) use liquid coolants that operate at near atmospheric pressure. Such reactors provide an opportunity to use thin-walled reactor vessels and internal equipment, and simpler core designs. However, the seismic capacity of a thin-walled vessel is substantially smaller than its thick-walled counterpart and so fluid-structure interaction (FSI) effects will be more pronounced in terms of impact on design. Verified and validated numerical models for analyzing the interaction of a liquid coolant with submerged or enclosing structural components are required because other approaches of analysis have limited application; namely, available analytical solutions for seismic FSI cannot be used for complex geometries and multi-directional, high-amplitude seismic inputs; and physical testing of advanced reactor components is impractical and cost-prohibitive. Detailed discussions on verification of numerical models for seismic FSI analyses of advanced reactors are presented in Yu and Whittaker (2021a).

The smaller seismic capacity of thin-walled vessels and components, with all other details including geometry remaining the same, can be offset by the use of seismic isolation. For all advanced reactors, seismic isolation can help significantly reduce the associated overnight capital cost by reducing seismic demands on components, and enable deployment of standardized designs at sites of varying seismicity (Lal *et al.* 2022; Parsi *et al.* 2022). The design of base-isolated advanced reactors will also require robust numerical models capable of predicting isolation-system and fluid-structure responses for high intensity, multi-directional seismic inputs. Validation of numerical models of advanced reactors, base-isolated and conventionally founded, with a focus on fluid-structure interaction, was addressed in this report.

To support validation of numerical models for seismic FSI analysis of advanced reactors, this report: 1) described earthquake-simulator experiments conducted on a fluid-filled vessel with and without submerged components, and with and without physical isolators installed, and 2) used the data generated from these experiments to validate numerical models using the Arbitrary Lagrangian-Eulerian (ALE) solver in LS-

DYNA. The benefits of seismic isolation in terms of reduced demands on components were characterized by using *virtual* seismic inputs simulating a range of isolation-system properties.

Section 1.4 identified the three broad objectives of this report. Objective 1, the generation of experimental datasets for seismic responses of a fluid-filled vessel and submerged components, is addressed in Section 3 and Section 5. The generation of an experimental dataset for hydrodynamic responses and isolation-system responses in a base-isolated, fluid-filled vessel, objective 2, is described in Section 7. Objective 3, the validation of numerical models, is met in Section 4, Section 6, and Section 7.

Section 8.2 summarizes the work presented in Section 2 to Section 7. Section 8.3 discusses how the work products presented in this report can be used to model and analyze prototype reactors. Although the motivation behind the work described in this report is to support the deployment of advanced nuclear reactors, the products are broadly applicable to other construction sectors that utilize fluid-filled vessels such as oil, gas, and water storage.

8.2   Summary

Section 2 presented a review of the literature on analytical and experimental studies addressing fluid-filled containers, submerged components, and seismically isolated fluid-filled containers. Analytical and experimental studies on the dynamic (seismic) responses of fluid-filled containers began in the 1930s and were later included in design guidelines for fluid-filled tanks and reactor vessels. Dynamic responses of submerged components were studied first in the late 19th century and a significant body of work on such responses in nuclear reactors was completed at the Argonne National Lab in the 1970s. Most of the studies on base-isolated, fluid-filled vessels involve numerical estimation of responses. The experimental studies on base-isolated vessels by Chalhoub and Kelly (1988) and Calugaru and Mahin (2009) were described.

Section 3 presented details of experiments on a base-supported cylindrical vessel tested using a six-degree-of-freedom earthquake simulator. Details of the test setup, instrumentation, and seismic inputs were described and discussed. Experimental results in terms of sloshing frequency, damping ratios in sloshing modes, and hydrodynamic responses (wave height, hydrodynamic pressure, base shear, and base moment) were presented and compared with predictions from available analytical solutions. The impact of seismic isolation on hydrodynamic responses of the fluid-filled container was studied by using *isolated* inputs generated assuming a virtual isolation system. The analytical prediction of convective mode frequency was in excellent agreement with the experimental results. Hydrodynamic responses for multi-directional inputs, calculated by superposition of responses due to the different components of the input, were found to be in reasonable agreement with experimental results for hydrodynamic pressure, base shear, and base moment. However, the errors in maximum values of wave height, predicted using this approach, were significant.

The implementation of (horizontal) base isolation led to significant reductions in base shear and moment for high-intensity motions but wave height, associated with the convective modes, increased with the use of base isolation for the selected tank geometry and isolation-system properties.

Section 4 focused on validating numerical models of the base-supported vessel tested in the experiments described in Section 3. Two numerical approaches, the Arbitrary Lagrangian and Eulerian (ALE) and Lagrangian elastic-fluid, were investigated. Numerical predictions were compared with experimental results to support validation. The ALE approach models the fluid using Eulerian elements that do not deform with fluid motion. Such elements can accommodate large deformations and nonlinear fluid responses (e.g., large amplitude sloshing). The Lagrangian elastic-fluid approach models the fluid using elastic properties and is limited in terms of its ability to accommodate large deformations. The ALE model of the fluid-filled vessel was validated using experimental results from nine sets of multi-directional seismic inputs. The Lagrangian model, analyzed for a unidirectional horizontal input motion with interactions between the fluid and the vessel defined using tie constraints or contact, did not simulate convective responses accurately, but was computationally more efficient.

Section 5 described experiments on components submerged in the fluid-filled, base-supported vessel described in Section 3. A centrally placed tubular steel internal, a steel plate internal, and three configurations of aluminum tubes were tested in three different test series. Details of the tested specimen, instrumentation used, *in-air* and *in-water* identification tests, and the earthquake-simulator inputs were presented. The effects of base isolation on submerged-component responses were studied using inputs generated using a *virtual* isolation system. The benefits of seismic isolation, in terms of reduction in dynamic responses (pressure, acceleration, and strain), were identified.

Section 6 focused on numerical modelling of the submerged internal components described in Section 5. Numerically estimated dynamic responses of the submerged internals, generated using the Arbitrary Lagrangian and Eulerian (ALE) algorithm in LS-DYNA, were compared with experimental results to support validation of the models. All numerical models (of the different specimens) were validated for estimation of *in-water* frequencies of the internal components. The numerical model of the central tubular steel internal was validated for estimation of pressure response on the wall of the internal, and all models, except for that of the steel plate internal, were validated for estimation of acceleration responses. Strain responses, in general, were not validated. The effect of using fine meshes, in terms of improved accuracy of *in-water* frequency estimates, and the effect of using hourglass control algorithms, in terms of added *non-physical* damping, were discussed.

Section 7 presented details of earthquake-simulator experiments and subsequent numerical modelling of a fluid-filled, base-supported vessel seismically isolated using four single concave friction pendulum bearings. The test specimen and instrumentation, friction pendulum bearings, and seismic inputs were introduced, followed by a discussion on numerical modelling of the base-isolated vessel. The ALE algorithm was used to model the fluid-filled vessel (as in Section 4) and the isolators were modelled using the MAT_SEISMIC_ISOLATOR property in LS-DYNA. Numerical predictions of isolation-system responses and fluid responses were compared with experimental results and the agreement was excellent.

8.3   Recommendations for validation of prototype reactor models

The experiments described in this report were conducted on specimen geometries that are simpler than prototype reactor vessels and internal geometries. However, these experiments provide a first-of-a-kind curated dataset that could be used to characterize a solver's capabilities and limitations when constructing numerical models of a prototype reactor in a finite element package. An analyst may choose to construct numerical models similar to those described in Sections 4, 6, and 7 of this report (for a fluid-filled vessel, submerged components, and a base-isolated vessel, respectively) and validate the models in a particular solver before modifying the geometry, boundary conditions, and mechanical properties to represent a prototype reactor. This would help understand the effect of various input parameters (e.g., the effects of specifying damping, hourglass control algorithms, using fully integrated elements versus reduced integration elements) in the solver.

The error thresholds for judging whether a numerical model is validated are specific to the problem and analyst. Thresholds of 10%, 25%, and 12% were used in Section 4, Section 6, and Section 7, respectively. These values reflect the complexity of the models studied and the thresholds may be relaxed or made more stringent depending on how the numerical results from the prototype model will be used for decision making.

SECTION 9

REFERENCES

ADINA. (2013). "ADINA Theory and Modeling Guide." ADINA R & D Inc, MA.

Alemberti, A., Smirnov, V., Smith, C. F., and Takahashi, M. (2014). "Overview of lead-cooled fast reactor activities." *Progress in Nuclear Energy*, 77, 300-307.

American Society of Civil Engineers (ASCE). (2017). "Seismic analysis of safety related nuclear structures." *ASCE/SEI Standard 4-16*, American Society of Civil Engineers, Reston, VA.

ANSYS. (2017). "ANSYS theory reference." Ansys Inc, Canonsburg, PA.

Applied Technology Council (ATC). (2009). "Quantification of building seismic performance factors." *FEMA-P695*, Applied Technology Council for the Federal Emergency Management Agency, Washington, D.C.

Arias, A. (1970). "A measure of earthquake intensity." *Seismic Design for Nuclear Power Plants*, Massachusetts Institute of Technology, Cambridge, MA.

Aslam, M., Godden, W. G., and Scalise, D. T. (1978). "Earthquake sloshing in annular and cylindrical tanks." *LBL-7525*, Lawrence Berkeley National Laboratory, Berkeley, CA.

Au-Yang, M. (1976). "Free vibration of fluid-coupled coaxial cylindrical shells of different lengths." *Journal of Applied Mechanics*, 33, 480-484.

Benson, M., Rudland, D., and Kirk, M. (2012). "Thermomechanical analysis of pressure vessels." *Proceedings, Pressure Vessels and Piping Conference (ASME),*Toronto, Ontario, Canada, 853-860.

British Standards Institution (BSI). (2007). "Eurocode 9 - Design of aluminum structures, Part 1-2: structural fire design." British Standards Institution (BSI), London, UK.

Butenweg, C., Rosin, J., and Kubalski, T. (2013). "Seismic response of conventional and base-isolated liquid storage tanks." *Proceedings, 50SE-EEE 1963-2013 International Conference on Earthquake Engineering,* Skopje, Macedonia.

Calugaru, V., and Mahin, S. A. (2009). "Experimental and analytical studies of fixed base and seismically isolated liquid storage tanks." *Proceedings, International Conference on Advances in Experimental Structural Engineering,* San Francisco, CA.

Case, K., and Parkinson, W. (1957). "Damping of surface waves in an incompressible liquid." *Journal of Fluid Mechanics*, 2(2), 172-184.

Castellano, M., and Marcolin, L. (2017). "Seismic isolation of an ammonia tank in Turkey through pendulum isolators." *Proceedings, 16th World Conference on Earthquake Engineering (16WCEE 2017),* Santiago, Chile.

CEN. (2008). "Eurocode 8: Design of structures for earthquake resistance, Part 4: Silos, tanks and pipelines." European Committee for Standardization (CEN), Brussels, Belgium.

Chalhoub, M. S., and Kelly, J. M. (1988). "Theoretical and experimental studies of cylindrical water tanks in base isolated structures." *UCB/EERC-88/07*, Earthquake Engineering Research Center, University of California at Berkeley, Berkeley, CA.

Chen, S.-S. (1975a). "Vibrations of a row of circular cylinders in a liquid." *ANL-CT-75-34*, Argonne National Laboratory, Lemont, IL.

Chen, S. (1975b). "Vibration of fuel bundles." *ANL-CT-75-42*, Argonne National Laboratory, Lemont, IL.

Chen, S., and Rosenberg, S. (1975). "Dynamics of a coupled shell-fluid system." *ANL-CT-76-13*, Argonne National Laboratory, Lemont, IL.

Chen, S., Wambsganss, M., and Jendrzejczyk, J. (1976). "Added mass and damping of a vibrating rod in confined viscous fluids." *Journal of Applied Mechanics*, 43(2), 325-329.

Chen, S. S. (1975c). "Dynamic responses of two parallel circular cylinders in a liquid." *Journal of Pressure Vessel Technology*, 97(2), 77-83.

Chen, S. S., Jendrzejczyk, J., and Wambsganss, M. (1977). "Experiments on fluidelastic vibrations of tube arrays." *ANL-CT-77-16*, Argonne National Laboratory, Lemont, IL.

Chilukuri, R. (1987). "Added mass and damping for cylinder vibrations within a confined fluid using deforming finite elements." *Journal of Fluids Engineering*, 109(3), 283-288.

Choi, Y., Park, J.-B., Lee, S.-J., Park, N.-C., Park, Y.-P., Kim, J.-S., and Roh, W.-J. (2016). "Seismic analysis of the APR 1400 reactor vessel internals using the model reduction method." *Journal of Nuclear Science and Technology*, 53(11), 1701-1714.

Chopra, A. K. (2012). *Dynamics of structures: theory and applications to earthquake engineering*, Prentice Hall, Upper Saddle River, NJ.

Christovasilis, I. P., and Whittaker, A. S. (2008). "Seismic analysis of conventional and isolated LNG tanks using mechanical analogs." *Earthquake Spectra*, 24(3), 599-616.

Chung, H., and Chen, S.-s. (1977). "Vibration of a group of circular cylinders in a confined fluid." *Journal of Applied Mechanics*, 44(2), 213-217.

Clough, R. W. (1960). "Effects of earthquakes on underwater structures." *Proceedings, 2nd World Conference on Earthquake Engineering,* Tokyo, Japan.

Compagnoni, M. E., and Curadelli, O. (2018). "Experimental and numerical study of the response of cylindrical steel tanks under seismic excitation." *International Journal of Civil Engineering*, 16(7), 793-805.

Computers and Structures (CSI). (2019). "CSI analysis reference manual." Computer and Structures, Inc., Berkeley, CA, USA.

Constantinou, M. C., Whittaker, A. S., Kalpakidis, Y., Fenz, D. M., and Warn, G. P. (2007). "Performance of seismic isolation hardware under service and seismic loading." *Report MCEER-07-0012*, The State University of New York at Buffalo, Buffalo, NY.

Deng, Y., Guo, Q., and Xu, L. (2017). "Experimental and numerical study on modal dynamic response of water-surrounded slender bridge pier with pile foundation." *Shock and Vibration*, 2017, 1-20.

Dong, R. G. (1978). "Effective mass and damping of submerged structures." *UCRL-52342*, Lawrence Livermore National Labortary, Livermore, CA.

Doulgerakis, N., Tehrani, P. K., Talebinejad, I., Kosbab, B., Cohen, M., and Whittaker, A. S. (2021). "Software verification and validation guidance for nonlinear seismic analysis." *Report developed under DOE grant number DE-NE0008857*, United States Department of Energy, Washington, DC.

Edwards, N. W. (1969). "A procedure for the dynamic analysis of thin walled cylindrical liquid storage tanks subjected to lateral ground motions." Dissertation, presented to University of Michigan, Ann Arbor, Michigan, in partial fulfillment of the requirements for the degree of Doctor of Philosophy.

Energy Information Administration (EIA). (2020). "How much carbon dioxide is produced per kilowatthour of U.S. electricity generation?", <https://www.eia.gov/tools/faqs/>. (March 15, 2021).

Fenz, D. M., and Constantinou, M. C. (2008). "Mechanical behavior of multi-spherical sliding bearings." *Report MCEER-08-0007*, The State University of New York at Buffalo, Buffalo, NY.

Frano, R. L., and Forasassi, G. (2009). "Conceptual evaluation of fluid–structure interaction effects coupled to a seismic event in an innovative liquid metal nuclear reactor." *Nuclear Engineering and Design*, 239(11), 2333-2342.

Fritz, R. (1972). "The effect of liquids on the dynamic motions of immersed solids." *Journal of Engineering for Industry*, 94(1), 167-173.

Fujita, K., Ito, T., and Okada, K. (1986). "Seismic response of liquid sloshing in the annular region formed by coaxial circular cylinders." *Bulletin of JSME*, 29(258), 4318-4325.

Generation IV International Forum (GIF). (2002). "A technology roadmap for Generation IV nuclear energy systems." *GIF-002-00*, Generation IV International Forum (GIF) and U.S. Department of Energy, Washington D.C.

GIF. (2020). "Sodium-cooled fast reactor (SFR)." <https://www.gen-4.org/gif/jcms/c_42152/sodium-cooled-fast-reactor-sfr>. (March 15, 2021).

Goudarzi, M. A., and Sabbagh-Yazdi, S. R. (2012). "Investigation of nonlinear sloshing effects in seismically excited tanks." *Soil Dynamics and Earthquake Engineering*, 43, 355-365.

Graham, E. W., and Rodriquez, A. M. (1951). "The characteristics of fuel motion which affect airplane dynamics." *SM-14212*, Douglas Aircraft Company, Santa Monica, CA.

Gregoriou, V. P., Tsinopoulos, S. V., and Karabalis, D. L. (2006). "Base isolated LNG tanks: seismic analyses and comparison studies." *Proceedings, First European Conference on Earthquake Engineering and Seismology,* Geneva, Switzerland.

Habenberger, J. (2015). "Fluid damping of cylindrical liquid storage tanks." *SpringerPlus*, 4(1), 1-11.

Haroun, M., and Housner, G. (1981a). "Earthquake response of deformable liquid storage tanks." *Journal of Applied Mechanics*, 48, 411-418.

Haroun, M. A. (1983). "Vibration studies and tests of liquid storage tanks." *Earthquake Engineering and Structural Dynamics*, 11(2), 179-206.

Haroun, M. A., and Housner, G. W. (1981b). "Seismic design of liquid storage tanks." *Journal of the Technical Councils of ASCE*, 107(1), 191-207.

Henderson, D. M., and Miles, J. (1994). "Surface-wave damping in a circular cylinder with a fixed contact line." *Journal of Fluid Mechanics*, 275, 285-299.

Hoskins, L. M., and Jacobsen, L. S. (1934). "Water pressure in a tank caused by a simulated earthquake." *Bulletin of the Seismological Society of America*, 24(1), 1-32.

Housner, G. W. (1954). "Earthquake pressures on fluid containers." *NR-081-095*, Office of Naval Research, Arlington, VA.

Housner, G. W. (1957). "Dynamic pressures on accelerated fluid containers." *Bulletin of the Seismological Society of America*, 47(1), 15-35.

Housner, G. W. (1963). "The dynamic behavior of water tanks." *Bulletin of the Seismological Society of America*, 53(2), 381-387.

Jacobsen, L. S. (1949). "Impulsive hydrodynamics of fluid inside a cylindrical tank and of fluid surrounding a cylindrical pier." *Bulletin of the Seismological Society of America*, 39(3), 189-204.

Jacobsen, L. S., and Ayre, R. S. (1951). "Hydrodynamic experiments with rigid cylindrical tanks subjected to transient motions." *Bulletin of the Seismological Society of America*, 41(4), 313-346.

Jaiswal, O., Rai, D. C., and Jain, S. K. (2007). "Review of seismic codes on liquid-containing tanks." *Earthquake Spectra*, 23(1), 239-260.

Je, S. Y., Chang, Y.-S., and Kang, S.-S. (2017). "Dynamic characteristics assessment of reactor vessel internals with fluid-structure interaction." *Nuclear Engineering and Technology*, 49(7), 1513-1523.

Jhung, M. J. (1996). "Hydrodynamic effects on dynamic response of reactor vessel internals." *International Journal of Pressure Vessels and Piping*, 69(1), 65-74.

Kammerer, A., Whittaker, A. S., and Constantinou, M. C. (2019). "Technical considerations for seismic isolation of nuclear facilities." *NUREG/CR-7253*, United States Nuclear Regulatory Commission, Washington, D.C.

Keane, J. A. (1963). "On the elastic vibration of a circular cantilever tube in a Newtonian fluid." Dissertation, presented to Carnegie Institute of Technology,Pittsburgh, PA, in partial fulfillment of the requirements for the degree of Doctor of Philosophy.

Kelly, T. E., and Mayes, R. L. (1989). "Seismic isolation of storage tanks." *Proceedings, Structures Congress,* NY, USA.

Kusić, M. S., Radnić, J., Grgić, N., and Harapin, A. (2019). "Fluid structure interaction analysis of liquid tanks by the coupled SPH-FEM method with experimental verification." *Defect and Diffusion Forum*, 391, 152-173.

Lal, K. M., Constantinou, M. C., and Whittaker, A. S. (2021). "Seismic isolation of safety-class equipment in nuclear power plants." *Proceedings, 17th World Conference on Earthquake Engineering (17WCEE),* Sendai, Japan.

Lal, K. M., Parsi, S. S., Kosbab, B. D., Ingersoll, E. D., Charkas, H.,, and Whittaker, A. S. (2022). "Towards standardized nuclear reactors: seismic isolation and the cost impact of the earthquake load case." *Nuclear Engineering and Design*, 386, 111487.

Lamb, H. (1932). *Hydrodynamics*, Cambridge University Press, Cambridge, UK.

Lee, S.-J., Park, J.-B., Park, N., Kim, J., and Choi, Y. (2017). "Seismic analysis of the nuclear reactor vessel and internals with using model reduction method." *Proceedings, 24th International Conference on Structural Mechanics in Reactor Technology (SMiRT-24),* Busan, Korea.

Lindholm, U. S., Kana, D. D., Chu, W.-H., and Abramson, H. N. (1965). "Elastic vibration characteristics of cantilever plates in water." *Journal of Ship Research*, 9(02), 11-36.

Livermore Software Technology Corporation (LSTC). (2017). "LS-DYNA user's manual – Version R 11.0." Livermore Software Technology Corporation, Livermore, CA, USA.

Maheri, M., and Severn, R. (1992). "Experimental added-mass in modal vibration of cylindrical structures." *Engineering Structures*, 14(3), 163-175.

Malhotra, P. K. (1997). "New method for seismic isolation of liquid‐storage tanks." *Earthquake Engineering & Structural Dynamics*, 26(8), 839-847.

Malhotra, P. K., Wenk, T., and Wieland, M. (2000). "Simple procedure for seismic analysis of liquid-storage tanks." *Structural Engineering International*, 10(3), 197-201.

MathWorks. (2017). "MATLAB user guide." MathWorks, Inc., Natick, MA.

Mir, F. U. H., Yu, C.-C., Cohen, M., Bardet, P., Coleman, J. L., and Whittaker, A. S. (2019). "Dataset generation for validation of fluid-structure interaction models." *25th International Conference on Structural Mechanics in Reactor Technology (SMiRT-25)*Charlotte, NC.

Mir, F. U. H., Yu, C.-C., and Whittaker, A. S. (2021). "Rocking response of liquid-filled cylindrical tanks." *Earthquake Spectra*, 1-12.

Mitra, S., and Sinhamahapatra, K. (2007). "Slosh dynamics of liquid-filled containers with submerged components using pressure-based finite element method." *Journal of Sound and Vibration*, 304(1-2), 361-381.

Moretti, P. M., and Lowery, R. L. (1976). "Hydrodynamic inertia coefficients for a tube surrounded by rigid tubes." *ASME Journal of Pressure Vessel Technology*, 120, 190-193.

Morris, B. T. (1938). "A laboratory model study of the behavior of liquid filled cylindrical tanks in earthquakes." Dissertation, presented to Stanford University, Stanford, CA, in partial fulfilment of the requirements for the Degree of Engineer.

Mulcahy, T. (1980). "Fluid forces on rods vibrating in finite length annular regions." *ASME Journal of Applied Mechanics*, 47, 234-240.

Naidin, M., Pioro, I., Duffey, R., Mokry, S., Grande, L., Villamere, B., Allison, L., Rodriguez-Prado, A., Mikhael, S., and Chophla, K. (2009). "Super critical water-cooled nuclear reactors (SCWRs) thermodynamic cycle options and thermal aspects of pressure-channel design." *Proceedings, International Conference on Opportunities and Challenges for Water Cooled Reactors in the 21st Century,* Vienna, Austria.

Pacific Earthquake Engineering Research (PEER). "PEER ground motion database." <http://peer.berkeley.edu/peer_ground_motion_database>. (Jan. 12, 2019).

Pal, N., Bhattacharyya, S., and Sinha, P. (2001). "Experimental investigation of slosh dynamics of liquid-filled containers." *Experimental Mechanics*, 41(1), 63-69.

Park, J.-B., Choi, Y., Lee, S.-J., Park, N.-C., Park, K.-S., Park, Y.-P., and Park, C.-I. (2014). "Modal characteristic analysis of the APR1400 nuclear reactor internals for seismic analysis." *Nuclear Engineering and Technology*, 46(5), 689-698.

Park, J. H., Bae, D., and Oh, C. K. (2016). "Experimental study on the dynamic behavior of a cylindrical liquid storage tank subjected to seismic excitation." *International Journal of Steel Structures*, 16(3), 935-945.

Park, J. Y. (2017). "SiCf/SiC composites as core materials for Generation IV nuclear reactors." *Structural Materials for Generation IV Nuclear Reactors*, Woodhead, United Kindom, 441-470.

Parsi, S. S., Lal, K. M., Kosbab, B. D., Ingersoll, E. D., Shirvan, K., and Whittaker, A. S. (2022). "Seismic isolation: a pathway to standardized advanced nuclear reactors." *Nuclear Engineering and Design*, 387, 111445.

Pioro, I., and Duffey, R. (2019). "Current and future nuclear power reactors and plants." *Managing Global Warming*, Academic Press, Cambridge, MA, 117-197.

Radnić, J., Grgić, N., Kusić, M. S., and Harapin, A. (2018). "Shake table testing of an open rectangular water tank with water sloshing." *Journal of Fluids and Structures*, 81, 97-115.

Saha, S. K., Matsagar, V. A., and Jain, A. K. (2013). "Comparison of base-isolated liquid storage tank models under bi-directional earthquakes." *Natural Science*, 5(8), 27-37.

Sangsari, M. K., and Hosseinzadeh, N. (2014). "Shake table study of impulsive and convective damping coefficients for steel cylindrical tanks and comparison with API 650." *Journal of Seismology and Earthquake Engineering*, 16(2), 129-137.

Sato, H., Suzuki, K., Kamata, T., Taira, T., Niwa, H., and Nakajima, M. (1989). "Test results on seismic proving test of BWR core internals." *Proceedings, 10th International Conference on Structural Mechanics in Reactor Technology (SMiRT-10),* Anaheim, CA.

Shrimali, M., and Jangid, R. (2002). "Seismic response of liquid storage tanks isolated by sliding bearings." *Engineering Structures*, 24(7), 909-921.

Sinha, J. K., and Moorthy, R. (1999). "Added mass of submerged perforated tubes." *Nuclear Engineering and Design*, 193(1-2), 23-31.

Summers, P. T., Chen, Y., Rippe, C. M., Allen, B., Mouritz, A. P., Case, S. W., and Lattimer, B. Y. (2015). "Overview of aluminum alloy mechanical properties during and after fires." *Fire Science Reviews*, 4(1), 1-36.

Tajirian, F. E. (1993). "Seismic isolation of critical components and tanks." *Proceedings, Seminar on Seismic Isolation, Passive Energy Dissipation and Active Control,* San Francisco, CA.

Tang, Y., Grandy, C., and Seidensticker, R. (2010). "Seismic response of annular cylindrical tanks." *Nuclear Engineering and Design*, 240(10), 2614-2625.

Thomas, T., Yasui, G., Graham, R., Williamson, R., Lowe, R., and Hoak, W. (1963). "Nuclear reactors and earthquakes." *TID-7024*, Division of Reactor Development, United States Atomic Energy Commission, Washington, D. C.

Tsopelas, P. C., Roussis, P. C., Constantinou, M. C., Buchanan, R., and Reinhorn, A. M. (2005). "3D-BASIS-ME-MB: Computer program for nonlinear dynamic analysis of seismically isolated structures." *MCEER-05-0009*, University at Buffalo, Buffalo, NY.

Uściłowska, A., and Kołodziej, J. (1998). "Free vibration of immersed column carrying a tip mass." *Journal of Sound and Vibration*, 216(1), 147-157.

Veletsos, A. (1974). "Seismic effects in flexible liquid storage tanks." *Proceedings, 5th World Conference on Earthquake Engineering (5WCEE),* Rome, Italy.

Veletsos, A. S. (1984). "Seismic response and design of liquid storage tanks." *Guidelines for the seismic design of oil and gas pipeline systems*, Committee on Gas and Liquid Fuel Lifelines, American Society of Civil Engineers (ASCE), Reston, VA, 255-370.

Veletsos, A. S., and Tang, Y. (1986). "Dynamics of vertically excited liquid storage tanks." *Journal of Structural Engineering*, 112(6), 1228-1246.

Veletsos, A. S., and Tang, Y. (1987). "Rocking response of liquid storage tanks." *Journal of Engineering Mechanics*, 113(11), 1774-1792.

Veletsos, A. S., and Yang, J. Y. (1977). "Earthquake response of liquid storage tanks-advances in civil engineering through mechanics." *Proceedings, ASCE Second Engineering Mechanics Specially Conference,* Raleigh, NC.

Wang, Y. P., Teng, M. C., and Chung, K. W. (2001). "Seismic isolation of rigid cylindrical tanks using friction pendulum bearings." *Earthquake Engineering & Structural Dynamics*, 30(7), 1083-1099.

Watabe, M., Shibata, H., Sato, H., Kawakami, S., Ohno, T., Ichiki, T., and Sasaki, Y. (1989). "Preliminary study on seismic proving test of BWR core internals." *Proceedings, 10th International Conference on Structural Mechanics in Reactor Technology (SMiRT-10),* Anaheim, CA.

Westergaard, H. M. (1933). "Water pressures on dams during earthquakes." *Transactions of American Society of Civil Engineers (ASCE)*, 95, 418-433.

Williams, A. N. (1986). "Earthquake response of submerged circular cylinder." *Ocean Engineering*, 13(6), 569-585.

World Nuclear Association (WNA). (2011). "Comparison of lifecycle greenhouse gas emissions of various electricity generation sources." World Nuclear Association, London, UK.

World Nuclear Association (WNA). (2020). "Molten Salt Reactors." <https://www.world-nuclear.org/information-library/current-and-future-generation/molten-salt-reactors.aspx>. (March 27, 2021).

Yamada, T., Yoshimura, S., Koide, Y., Onitsuka, S., and Iijima, T. (2018). "Verification and validation of dynamic response simulation codes for BWR fuel assemblies under seismic loading." *International Journal of Pressure Vessels and Piping*, 167, 25-31.

Yu, C.-C., Mir, F. U. H., Cohen, M., Coleman, J., Bardet, P., and Whittaker, A. (2019). "Verification of numerical models for seismic fluid-structure-interaction analysis of advanced reactors." *Proceedings, 25th International Conference on Structural Mechanics in Reactor Technology (SMiRT-25),* Charlotte, NC.

Yu, C.-C., Mir, F. U. H., and Whittaker, A. S. (2021). "Validation of numerical models for seismic fluid-structure-interaction analysis of nuclear, safety-related equipment." *Nuclear Engineering and Design*, 379, 111179.

Yu, C.-C., and Whittaker, A. S. (2020). "Analytical solutions for seismic fluid-structure interaction of head-supported cylindrical tanks." *Journal of Engineering Mechanics*, 146(10).

Yu, C.-C., and Whittaker, A. S. (2021a). "Analytical and numerical studies of fluid-structure interaction in liquid-filled vessels - revision 1." *Report MCEER-20-0003*, The State University of New York at Buffalo, Buffalo, NY.

Yu, C.-C., and Whittaker, A. S. (2021b). "Review of analytical studies on seismic fluid-structure interaction of base-supported cylindrical tanks." *Engineering Structures*, 233, 111589.

Zayas, V. A., and Low, S. S. (1995). "Application of seismic isolation to industrial tanks." *Proceedings, Joint ASME/JSME Pressure Vessels and Piping Conference,* Honolulu, HI.

Zhang, D. (2016). "Generation IV concepts: China." *Handbook of Generation IV Nuclear Reactors*, Woodhead Publishing, Cambridge, United Kingdom, 373-411.

APPENDIX A

CALIBRATION OF FIVE-CHANNEL LOAD CELLS

A.1 Introduction

This appendix documents the process used to calibrate the four five-channel load cells (LCs) that were used to measure reaction forces in the earthquake-simulator experiments described in this report. The load cells were originally designed and fabricated for the Structural Engineering and Earthquake Simulation Laboratory (SEESL) in the Department of Civil, Structural and Environmental Engineering at the University at Buffalo. A copy of the original design sheet is presented in Figure A.1. The LCs were last calibrated systematically in 2006 (Warn and Whittaker 2006). For the calibration exercise described here, LC 1 was re-machined and re-gaged, and the other three LCs were re-gaged. The next section presents a discussion on the construction and wiring of the LCs. The following section presents the calibration procedure, results, and compares calibration data with that reported by Warn and Whittaker.

Department of Civil, Structural, and Environmental Engineering

212 Ketter Hall, North Campus, Buffalo, NY 14260-4300
http://www.civil.buffalo.edu/

Fax: (716) 645-3733 Tel: (716) 645 2114, x 2419
Andrei M. Reinhorn, P.E., Ph.D.   e-mail: reinhorn@buffalo.edu
Professor of Structural Engineering

26-Mar-92

_____FIVE AXES LOAD CELL USING TUBE STRUCTURE_____
Designed by Prof. Andrei M. Reinhorn, Assisted by Prof. Joe Bracci (Texas A&M University)

Height of load cell total	HH	13.00	in					
Size of top plate (square)	BB	16.00	in					
		Capacity			SI		Max Output	
Axial Load Capacity	N	50.00	Kips		222.7 kN		10.0 V	
Moment Capacity	M	200.00	Kips-in		22.6 kN-m		10.0 V	
Shear Capacity	S	20.00	Kips		89.1 kN		10.0 V	
		Design data						
Outside Diameter	Do	8.00	in					
Outside Diameter Gap	Dg	5.00	in	Seamless Alloy Steel 4140 Heat Treated			HFHT4140	
Inside diameter	d	4.00	in					
Height of gap	hg	3.00	in	<---------- This dimension should be equal or bigger than d !!|				
Height of pipe section	H	9.00	in					
Thickness of top plate	t	2.00	in					
Cross section area	A	7.07	in^2		37.7 in^2			
Moment of inertia	I	18.11	in^4		188.5 in^4			
Modulus of section	W	7.25	in^3		75.4 in^3			
		Performance						
Axial Strain	en	235.8	µSt	2	2.9	mV	4241	2200
Moment strain	em	920.1	µSt	4	18.4	mV	679	800
Shear strain	es	122.6	µSt	4	4.9	mV	2549	2800
Gage factor	-	2.0	-				Ampl.Fact= 1.25	
Excitation Voltage	Vo	10.0	V	Nr of arms	Max Output		Amplification for full scale	
		Total Strains						
Modulus of elasticity	E	30000.0	ksi	30.0 Msi				
Steel yield stress	fy	36.0	ksi					
Allowable yield strain	ey	1200.0	µSt					
Total principal strain	et	1168.8	µSt					
		Natural Freq.						
Horizontal Stiffness	Kh	5.37E+03	kips/in					
Vertical Stiffness	Kv	2.36E+04	kips/in					
Horizontal Frequency	fx	51	Hz					
Vertical Frequency	fy	68	Hz					
		Bolts						
Number of bolts	nnb	8		High Strength (Tens=180 ksi)				
Bolt diameter	db	0.625	in	(Shear=162 ksi)				
Bolt circle diameter	Db	6.00	in					
Distance between bolts	s	1.73	in					
Bolts tension Capacity	Nb	441.8	Kips	Single bolt:	55 Kips			
Bolts shear capacity	Sb	397.6	Kips	Single bolt:	50 Kips			

Colored data can be adjusted
NOTE: OUTPUT=10V*GF=2*uSt*#GAGES/4 = 10*2*463*2.6(MU=0.3)/4
NOTE: OUTPUT=10V*GF=2*uSt*#GAGES/4 = 10*2*728*4/4

Figure A.1. Original design sheet, adapted from Warn and Whittaker (2006)

A.2   Description

Each of the four LCs comprises a cylindrical tube and two square end plates, as shown in Figure A.2. A protective cover, not shown in the figure, is placed around the cylindrical tube.
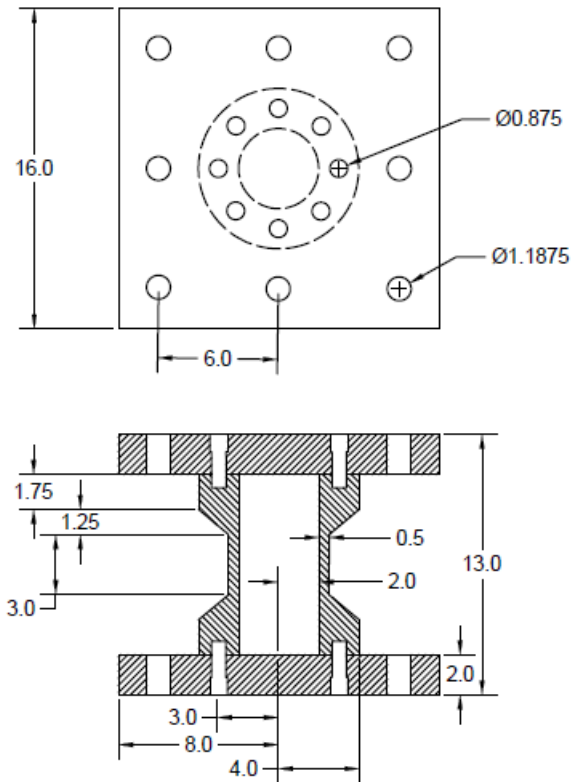
Figure A.2. Plan and elevation of a five-channel load cell, dimensions in inches

The instrumentation on each load cell comprises four strain rosettes and twelve uniaxial strain gages placed around the circumference of the cylindrical steel tube. The gages are clustered in four groups, A, B, C, and D around the circumference as shown in Figure A.3a with each group consisting of a strain rosette and three uniaxial gages. The orientation of the gages in a particular group is shown in Figure A.3b wherein gage numbers 1, 2, and 3 correspond to the strain rosette and 4, 5 and 6 correspond to uniaxial gages.
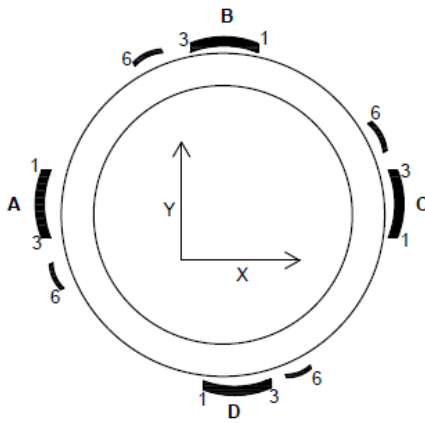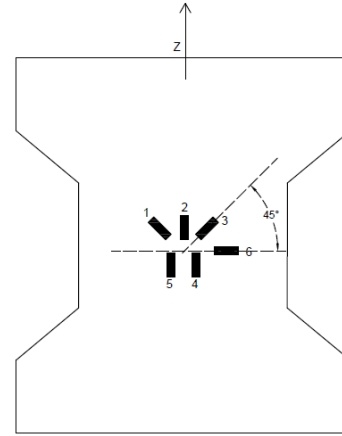
(a) location in plan   (b) location in elevation and numbers

Figure A.3. Strain gages, adapted from Bracci *et al.* (1992)

The gages are oriented and connected in a manner that enables measurement of applied normal force (N) along the axis of the cylindrical tube (*z*-axis in Figure A.3), applied shear forces (Sx and Sy) and applied moments (Mx and My) along the other two orthogonal directions. Specific gages around the circumference are connected to form Wheatstone bridge circuits, with each circuit measuring a particular action. The five circuits employed for measuring N, Sx, Sy, Mx, and My are shown in Figure A.4 wherein the involved strain gages are denoted by an alpha numeric sequence denoting the gage group and number. As an example, the shear force along *x* direction (Sx) is measured utilizing the actions of strain gages B1, B3, D1 and D3. Similarly, the normal-force-measuring circuit comprises normal strain measuring gages A2, B2, C2, D2 and gages A6, B6, C6, and D6 oriented perpendicular to the normal strain for thermal compensation. The shear and moment circuits are so designed that the need for thermal compensation gages is eliminated.
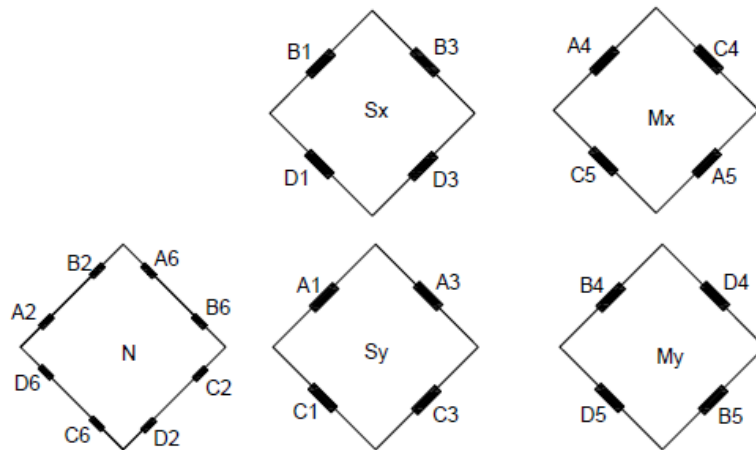
Figure A.4. Wheatstone bridge circuitry, adapted from Bracci *et al.* (1992)

A.3   Calibration procedure

A NIST (National Institute of Standards and Technology) traceable reference load cell was used for calibrating the load cells in a tension-compression machine (Tinius Olsen Testing Machine Co.). A Pacific Instruments 6000 Acquisition and Control system was used for data acquisition. Two configurations were used to calibrate all five channels of each load cell. The normal force channels of the all the load cells were calibrated simultaneously by stacking the load cells along with the reference load cell as shown in Figure A.5 and compressing them using the Tinius Olsen machine.
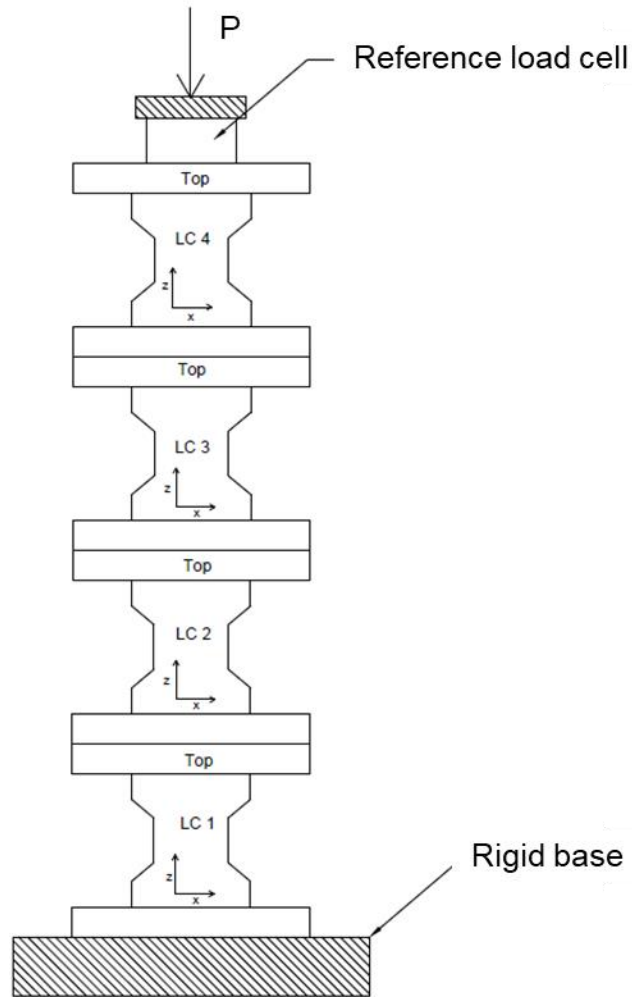
Figure A.5. Calibration setup for normal force channels

The shear and moment channels were calibrated using the two-point loading arrangement shown in Figure A.6. A "two-point" loading beam with tack-welded steel rods was used to simulate point loading. The end plates of the load cells have grooves along the periphery at their mid-depth. The loading beam was placed in a manner such that the tack-welded steel rods were placed in the grooves of the inner end plate of the outer two load cells (LC 1 and LC 4, as shown in Figure A.6). The steel rods supporting the LCs were placed in the grooves of the outer end plates of the outer load cells (LC 1 and LC 4, as shown in Figure A.6). Using this scheme, a shear channel of the two outer load cells (LC 1 and LC 4 as shown in Figure A.6) and a moment channel of the two inner load cells (LC 2 and LC 3 in Figure A.6) were calibrated. The other channels were calibrated after rotating or rearranging the assembly.
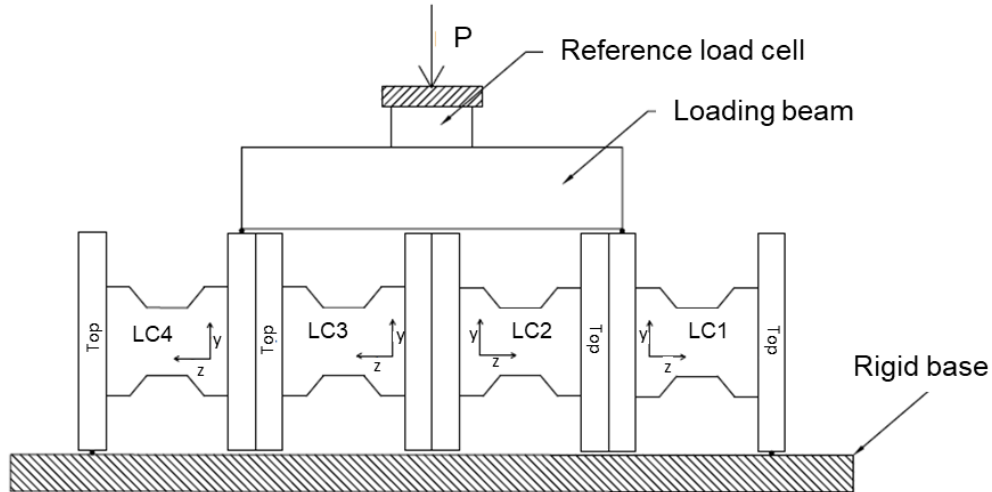
Figure A.6. Calibration setup for shear force (LC 1 and LC 4) and moment (LC 2 and LC 3) channels

The following step-by-step procedure was used to calibrate each channel (Warn and Whittaker 2006):

1. Balance all circuits (bridge balance)

2. Ensure that the reference load cell and the active channels read zero (tare removal)

3. Apply load using the Tinius Olsen machine

4. Initiate a two-point engineering unit (EU) calibration

5. Enter first EU calibration point at full-scale using the reading from the reference load cell

6. Unload

7. Enter second EU calibration point at zero load

8. Note the obtained EU slope for the channel being calibrated

9. Balance all circuits (bridge balance)

10. Ensure that the reference load cell reads zero

11. Initiate calibration dataset

12. Load till full scale EU value

13. Terminate calibration dataset

Table A.1 summarizes the calibration information. A gain of 1000 and a full-scale unamplified output of 10 mV was used for all channels during the calibration process. The EU slope (engineering units per volt)

179

obtained from the two-point calibration is noted for each channel. The 'full-scale EU' is obtained by multiplying the 'EU slope' by the 'amplified full-scale output' and the 'amplified output per EU' is obtained by dividing the 'amplified full-scale output' by the 'full-scale EU'.

For information, Table A.2 presents the average EU slopes obtained for the shear, moment and axial channels and the values reported in Warn and Whittaker (2006). The range (difference between maximum and minimum values) of the obtained slopes is also noted in parentheses.

Table A.1. Calibration data

LC No.	Channel	Eng. unit (EU)	Gain	Unamplified full-scale output (mV)	Amplified full-scale output (V)	EU slope (EU/V)	Full-scale EU	Amplified output per EU (V/EU)
1	Sx	kN	1000	10	10	28.6	286.0	0.0350
1	Sy	kN	1000	10	10	27.0	270.0	0.0370
1	Mx	kN-m	1000	10	10	2.4	23.7	0.4221
1	My	kN-m	1000	10	10	2.4	24.0	0.4159
1	N	kN	1000	10	10	93.8	938.1	0.0107
2	Sx	kN	1000	10	10	30.2	302.0	0.0331
2	Sy	kN	1000	10	10	29.5	294.9	0.0339
2	Mx	kN-m	1000	10	10	2.4	24.4	0.4101
2	My	kN-m	1000	10	10	2.4	23.6	0.4235
2	N	kN	1000	10	10	90.6	906.1	0.0110
3	Sx	kN	1000	10	10	30.6	305.6	0.0327
3	Sy	kN	1000	10	10	30.2	302.0	0.0331
3	Mx	kN-m	1000	10	10	2.4	23.6	0.4237
3	My	kN-m	1000	10	10	2.4	23.6	0.4237
3	N	kN	1000	10	10	92.6	925.7	0.0108
4	Sx	kN	1000	10	10	27.9	279.3	0.0358
4	Sy	kN	1000	10	10	27.7	277.1	0.0361
4	Mx	kN-m	1000	10	10	2.4	23.7	0.4221
4	My	kN-m	1000	10	10	2.5	25.3	0.3946
4	N	kN	1000	10	10	90.7	907.0	0.0110

Table A.2. Averaged obtained EU slopes

	Warn and Whittaker (2006)	Obtained results	% change
Shear force channels	26.7 (4.3)[*]	28.9 (3.6)[*]	8
Moment channels	2.1 (0.3)[*]	2.4 (0.1)[*]	14
Axial force channels	93.8 (1.8)[*]	91.9 (3.2)[*]	-2

[*]Values in parentheses identify the range

Figure A.7 through Figure A.10 present calibration curves for the four load cells. The plots are for data sets that were recorded after calibration of all the LC channels. Each plot presents the output from all five channels of a LC as a function of the reference signal. The sub-caption identifies the force channel under consideration. For example, the sub-caption My indicates that the plots are from a configuration in which the load cell is placed like LC 3 or LC 2 in Figure A.6. The moment values in all of the plots are normalized by the moment arm, which is 0.28 m (11 inches).

As seen in the last panel of Figure A.7 through Figure A.10, there is negligible cross talk under axial load (N). However, under shear or moment loading, the axial channels read non-zero values. For example, in Figure A.7a, LC 1 is loaded in shear along the *x*-direction. At the peak reference load of 180 kN, the normal (N) channel reads approximately 9 kN. Similarly, under moment loading (see plots for Mx or My in Figure A.7 through Figure A.10), the shear channels read non-zero values at full scale. For example, in Figure A.9c, LC 3 is subjected to a moment along the *x*-direction. At full scale, the Sx channel reads approximately 6.5 kN. This is negligible.

In some plots, the signal is seen to cut-off near the full-scale value (see, for example Figure A.7c). This is due to the fact that post calibration, the unamplified circuit output exceeded the unamplified full-scale range set in the data acquisition system for such channels. This outcome does not affect the calibration results.
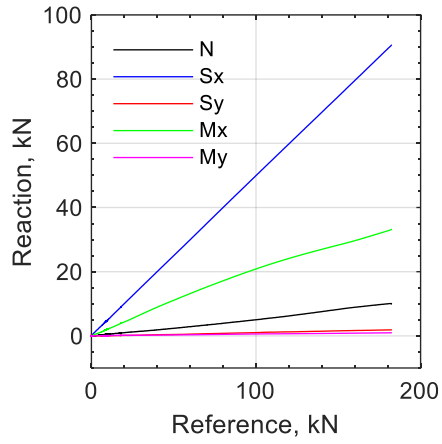
(a) channel: Sx
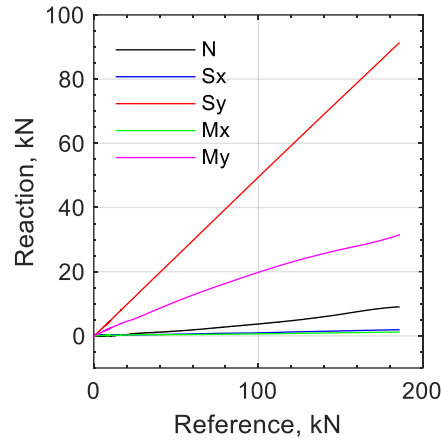
(b) channel: Sy
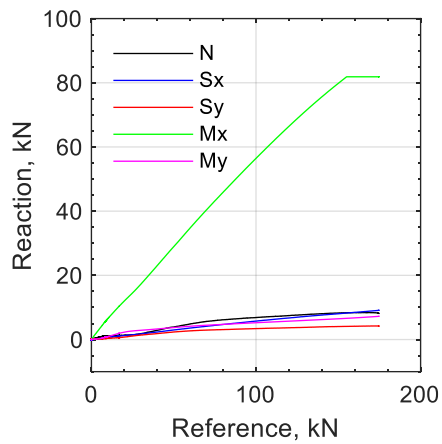
(c) channel: Mx, moment arm = 0.28m
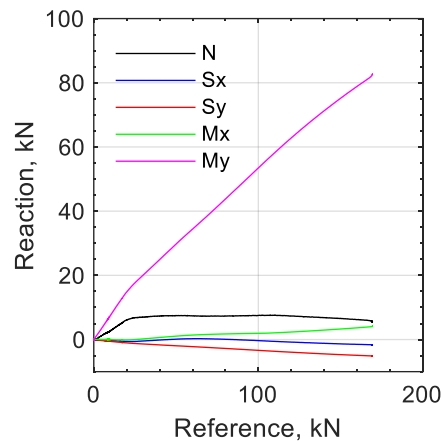
(d) channel: My, moment arm = 0.28m
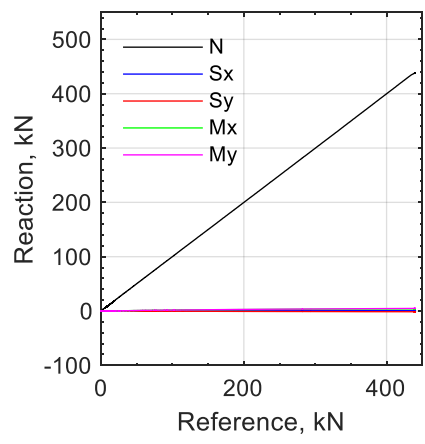
(e) channel: N

Figure A.7. Calibration results for LC1
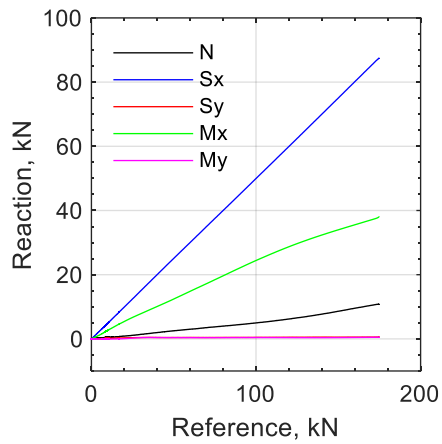
(a) channel: Sx
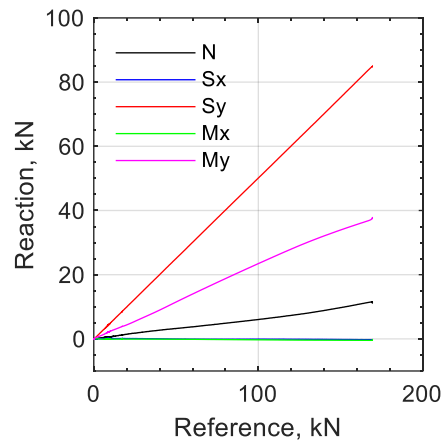
(b) channel: Sy
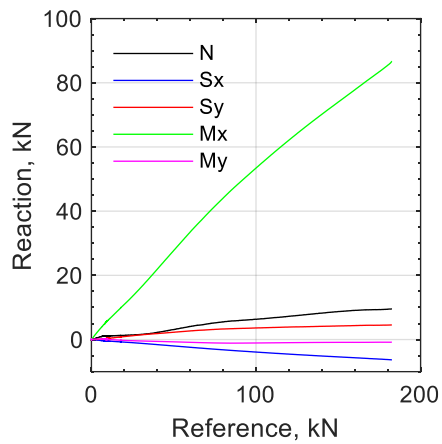
(c) channel: Mx, moment arm = 0.28m
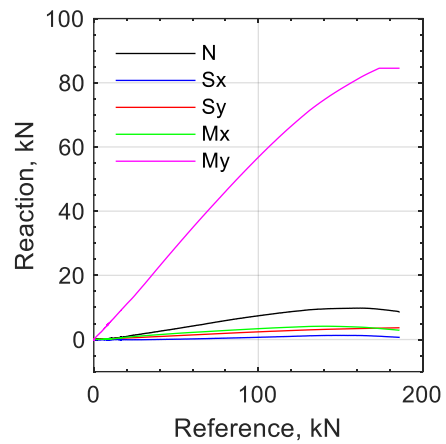
(d) channel: My, moment arm = 0.28m
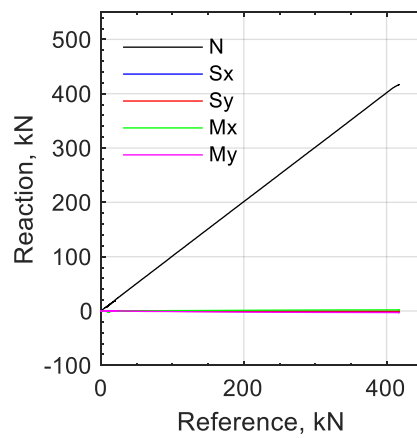
(e) channel: N

Figure A.8. Calibration results for LC2
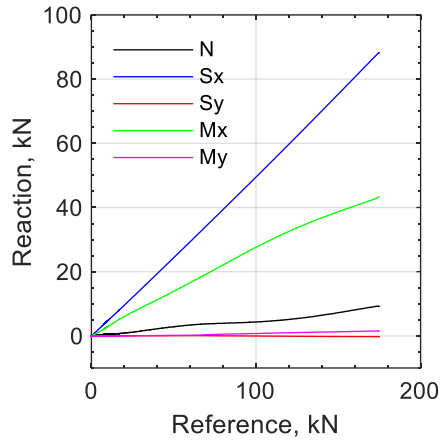
183
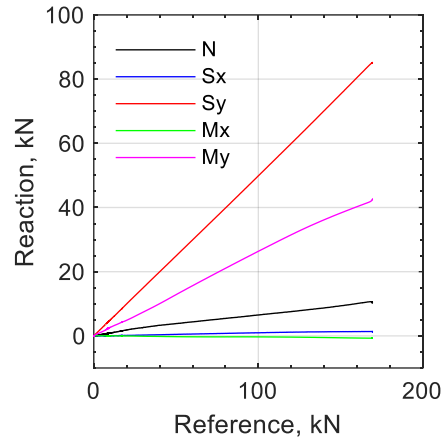
(a) channel: Sx
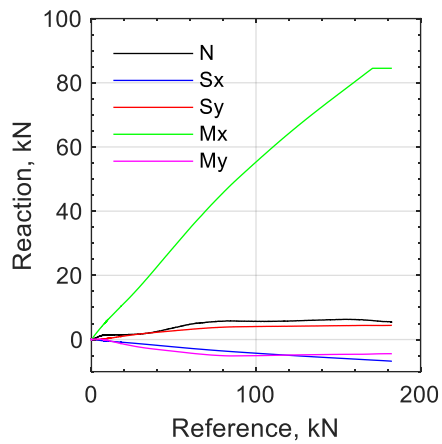
(b) channel: Sy

(c) channel: Mx, moment arm = 0.28m
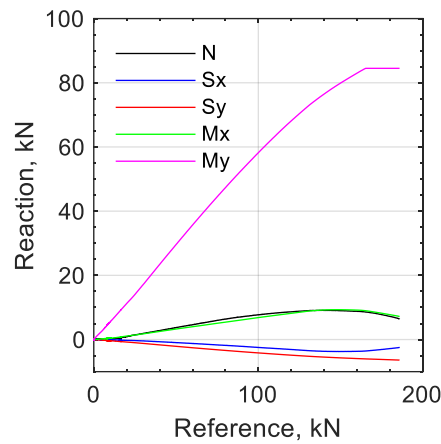
(d) channel: My, moment arm = 0.28m
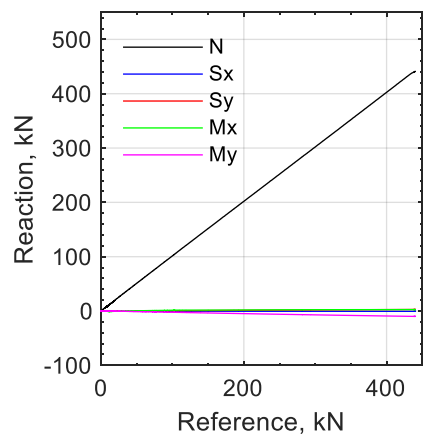
(e) channel: N

Figure A.9. Calibration results for LC3
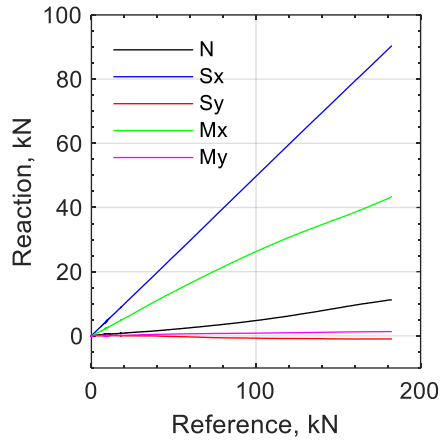
184
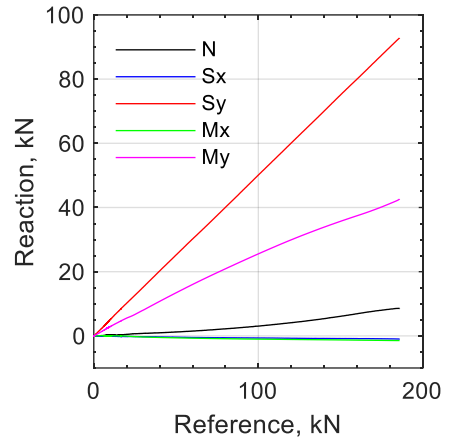
(a) channel: Sx

(b) channel: Sy
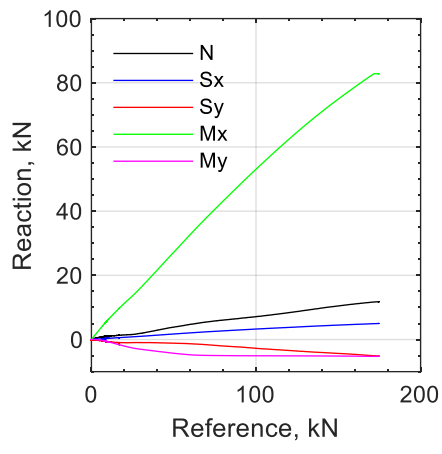
(c) channel: Mx, moment arm = 0.28m
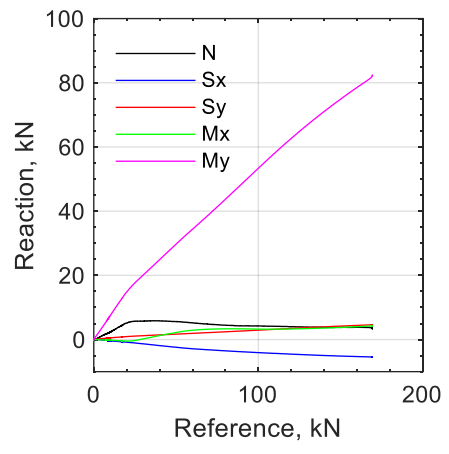
(d) channel: My, moment arm = 0.28m
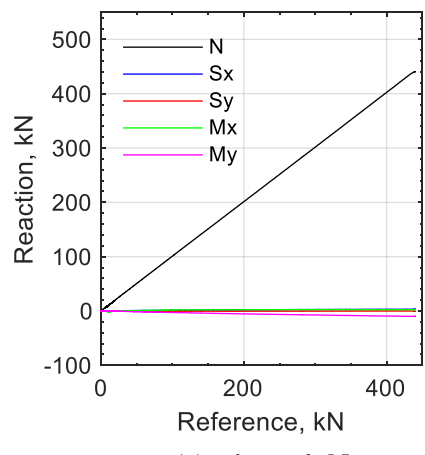
(e) channel: N

Figure A.10. Calibration results for LC4

185

A.4   Summary

Four five channel load cells were calibrated per the procedure outlined in Warn and Whittaker (2006). A description of the load cells and the calibration procedure was presented in this appendix along with results from the calibration exercise. The load cells were used under the base of the vessel, as described in Section 3 and Section 5, for recording reactions in earthquake-simulator experiments.

A.5   References

Bracci, J. M., Reinhorn, A. M., and Mander, J. B. (1992). "Seismic resistance of reinforced concrete frame structures designed only for gravity loads: part I - design and properties of a one-third scale model structure." *Report NCEER-92-0027*, The State University of New York at Buffalo, Buffalo, NY.

Warn, G. P., and Whittaker, A. S. (2006). "A study of the coupled horizontal-vertical behavior of elastomeric and lead-rubber seismic isolation bearings." *Report MCEER-06-0011*, The State University of New York at Buffalo, Buffalo, NY.

APPENDIX B
WAVE HEIGHT MEASUREMENT

B.1   Introduction

This appendix describes five strategies for measuring wave height that were explored as part of instrumentation design for the earthquake-simulator experiments described in Section 3 of this report. These five strategies are discussed in Section B.2 through Section B.6 below. Results from preliminary tests utilizing the different strategies are presented and challenges with practical implementation, if any, are identified. The preliminary tests were conducted using the cylindrical, fluid-filled vessel described in Section 3 or a smaller test tank having a diameter of 0.57 m. The viability of a particular strategy was assessed based on comparison of recorded wave height histories with those predicted analytically per Veletsos (1984).

B.2   Camera-based approach

The first strategy that was explored involved a camera that was used to track the movement of the free surface of water near the wall of the vessel. For this purpose, the vessel wall was painted black on the inside and water was dyed green to provide a contrast. The camera was oriented in a manner that it could capture the movement of green-dyed water against the black background (see Figure B.1a). The relative proportions of black and green in the field of view of the camera, captured as areas defined by lengths $L \tan \theta_1$ and $L \tan \theta_2$ (see Figure B.1a) on a frame of specified width, is related to the height of water at the vessel wall. Sixteen pictures at sixteen known water heights over a range of ±0.2 m around the initial water level were taken and used to calibrate a model relating the proportion of *green* in a captured frame with the height. This was done by writing an image-processing algorithm in MATLAB (MathWorks 2017). Figure B.1b shows a typical frame used for calibration and the defined 'region of interest' (ROI) considered for analysis. Pixel values corresponding to the green channel[19] were averaged over the width of the ROI and the variation of the average values was analyzed. The demarcation between the green region, representing water, and the black region, representing the tank wall, is marked by a steep increase in the *green-channel pixel value* (intensity) as shown in Figure B.1c. The created model relating the proportion of green in the frame to height was used to analyze frames extracted from a video taken during a test to give the wave height history. This method of tracking wave height at the tank wall works for *well-behaved* sloshing as seen in the

---

[19] Each pixel in an image is composed of a specific *intensity* of the three primary colors: red, green, and blue. The terminology of three *channels* for each pixel is used here to refer to these three colors.

fundamental mode (see Figure B.2a) because the wave profile in such a case permits equal proportions of color in a frame taken with a horizontal water surface at height H (as shown in Figure B.1a) and in a frame taken at an instant when the wave height at the wall is H. This is not true for the wave profiles seen in the higher convective modes, as illustrated in Figure B.2b. The calibration method discussed earlier would not be applicable for such a case. Similarly, the method will perform poorly in those cases where waves break in the tank as shown in Figure B.2c wherein the response of the water surface to a sinusoidal excitation of frequency 10 Hz is shown (the vessel described in Section 3 was used here). It is pertinent to add here that the convective response under low amplitude recorded earthquake motions is *well-behaved* in general, with a dominant first-mode response, and thus the method performs well, as indicated in Figure B.3 wherein wave histories evaluated using the method described here are compared with analytical predictions for two seismic inputs. The major challenges in implementing this method are: 1) the need to eliminate reflections from the water surface due to nearby lights or reflecting objects, and 2) the need to repeat the calibration exercise each time the orientation of the camera is changed. Another (minor) challenge with this method is syncing the camera recording with other data recorded using a conventional data acquisition system.
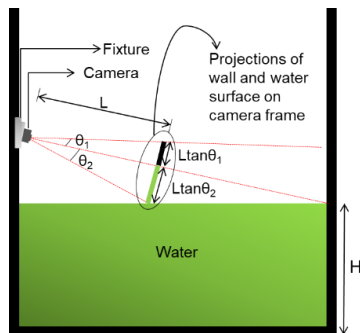
(a) camera placement and water surface profile during calibration
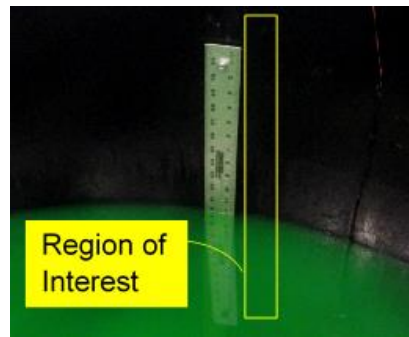
(b) selecting the ROI in a frame
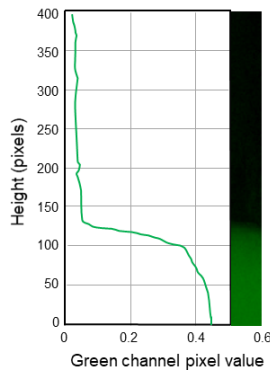
(c) analyzing green-channel pixel values for ROI

Figure B.1. Implementation of camera-based method for wave height tracking near the tank wall

(a) first convective mode   (b) higher convective mode
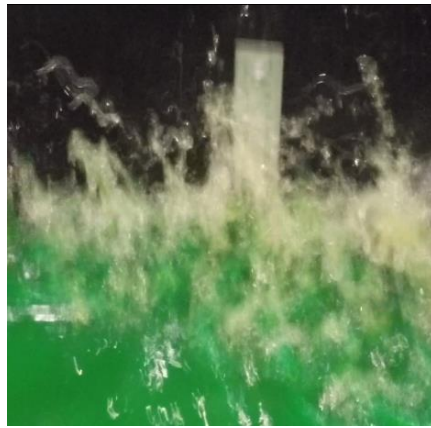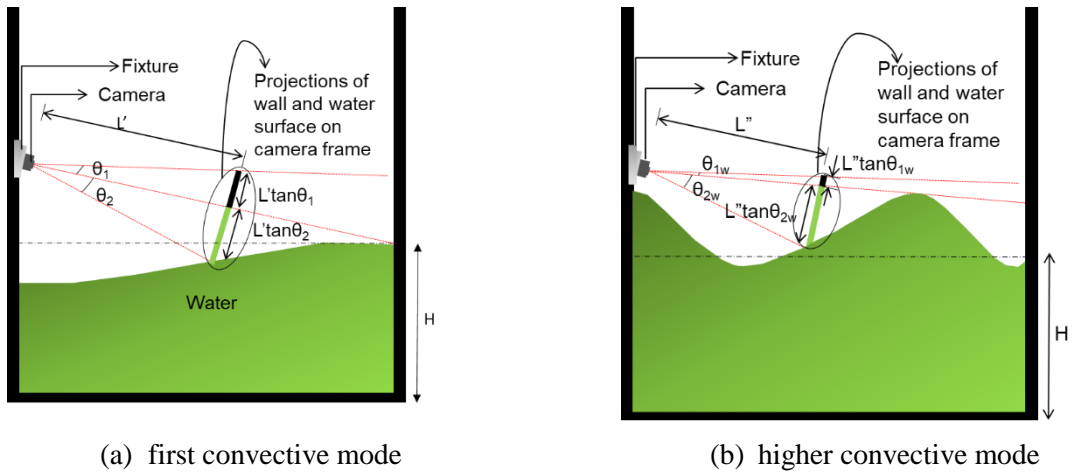
(c) wave breaking for sinusoidal base acceleration input with a frequency of 10 Hz

Figure B.2. Applicability of the camera-based method for first and higher convective modes
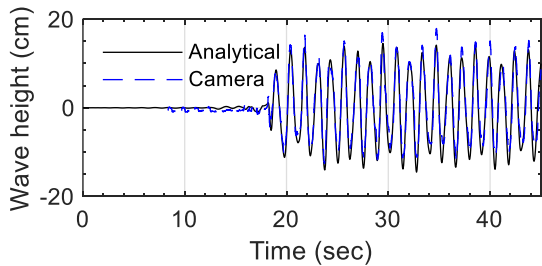
(a) CCE motion, peak acceleration = 0.1g   (b) ECE motion, peak acceleration = 0.4g
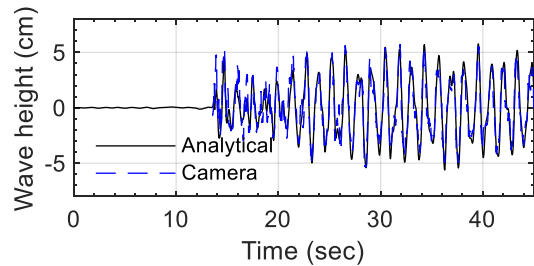
Figure B.3. Wave height histories from the camera-based method and from analytical solution, unidirectional motions (see Table 3.1), test vessel and fluid height per Section 3[20]

---

[20]The time series obtained from the camera-based method were manually shifted in time such that the first *major* peak in the time series coincided with the first *major* peak in the analytically evaluated time series.

B.3   Capacitive level sensor

A capacitive level sensor comprises two concentric tubes, seperated by a small annulus, that function as a capacitor. A change in water level in the annulus causes a change in capacitance of the assembly that can be calibrated to measure water height. The feasibility of using a capacitive level sensor (Make: Loadstar Sensors, Model: ilevel-900-A) for wave height measurements in earthquake-simulator tests was evaluated using a cylindrical test tank of 0.57 m diameter and a fluid height of 0.48 m. The tank was secured to the earthquake-simulator platform and the capacitive level sensor was installed 38 mm from the wall of tank along the direction of shaking. The setup is shown in Figure B.4. Two sinusoidal inputs with different acceleration amplitudes and a frequency of 0.5 Hz were used for testing. Test results and analytical predictions are shown in Figure B.5. The sensor was not able to capture the peak wave amplitudes predicted by the analytical solution, although the profile of the recorded response matched that of the analytical prediction. The design of the sensor, wherein four holes are provided at the lower end of the sensor for the fluid to move in and out of the tubing, is not suitable for applications where large-amplitude dynamic motions of fluids are involved.

(a) tank on earthquake simulator   (b) sensor arrangement
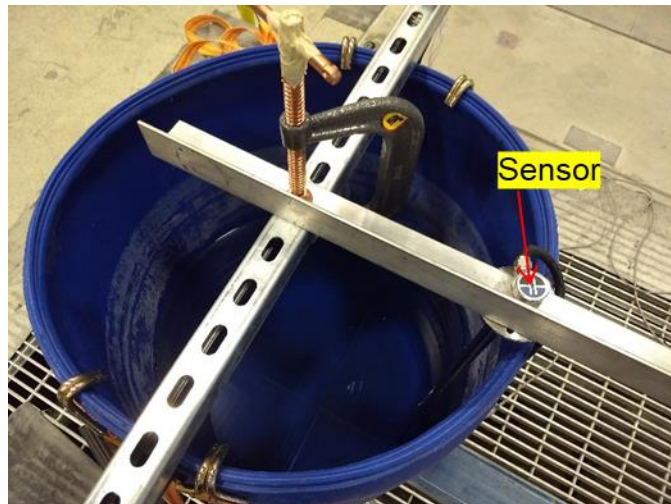
Figure B.4. Test setup for capacitive level sensor

(a) input amplitude = 0.1g　　　　　　　　(b) input amplitude = 0.15g
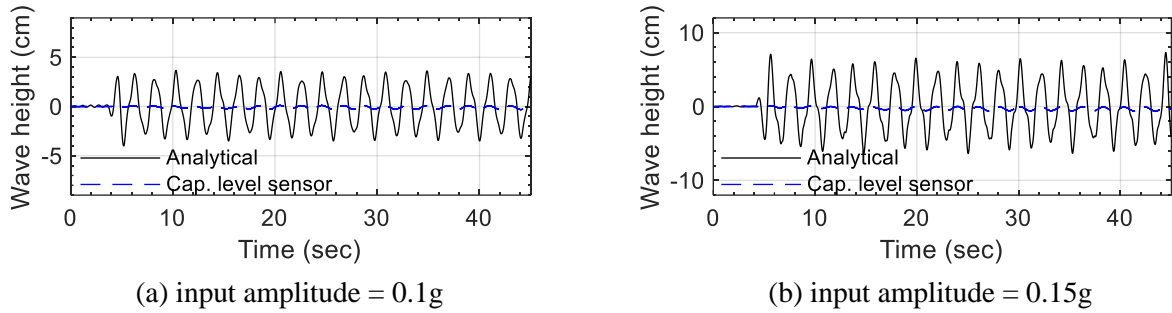
Figure B.5. Wave height histories from the capacitive level sensor and the analytical solution, unidirectional sinusoidal input motions, frequency =0.5 Hz, test vessel of 0.57 m diameter, water height of 0.48 m

B.4　　Resistance wire gage sensor

The resistance wire gage sensor works similarly to a full-bridge strain gage. Figure B.6 shows a schematic of the sensor, comprising a Wheatstone bridge, one resistor of which is immersed in water. The immersed resistor is composed of two parallel wires. Fluctuations in water level alter the resistance of the immersed wires and the magnitude of the change can be calibrated to record the fluctuations in water level. This setup was used by Calugaru and Mahin (2009) to record wave height in their earthquake-simulator experiments[21]. A resistance wire gage set up comprising two parallel brass wires was tested in the vessel described in Section 3. Figure B.7 shows a comparison of the wave height recorded by the resistance wire gage with the analytically predicted time series for a unidirectional earthquake input[22].

---

[21]Calugaru and Mahin (2009) used this wave gage in earthquake simulator experiments. However, details on the working of the gage, materials used for fabricating the gage, and signal conditioning systems used are not provided in the study.

[22]The earthquake input used here was derived from the TCU084 station recording of the 1999 Chi-Chi earthquake, available in the PEER Ground Motion Database (http://ngawest2.berkeley.edu). The *east* component was amplitude scaled to 0.1g and time-scaled by compressing the time scale by 1.58, consistent with the length scale (2.5) of another set of experiments executed on the earthquake simulator at SEESL, University at Buffalo.
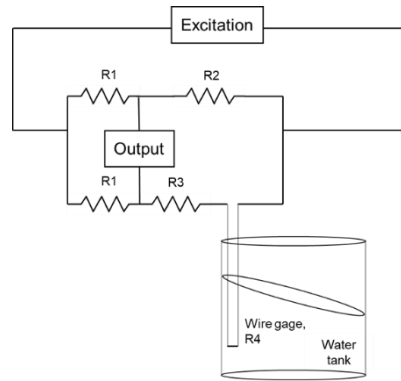
Figure B.6. Schematic representation of a resistance wire gage for measuring wave height
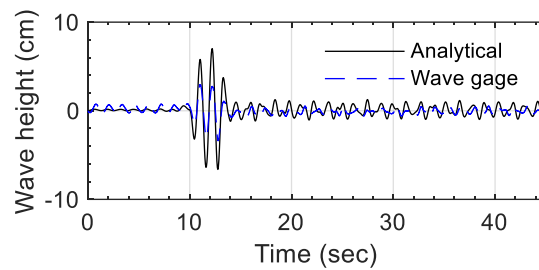
Figure B.7. Wave height histories from the resistance wire gage and from analytical solution, unidirectional sinusoidal input motions, test vessel and fluid height per Section 3

The wave gage recording has a similar profile as the analytical prediction but does not recover the peaks in the time series. The major challenges faced in the implementation of this system were: 1) non-linearities in the calibration curve of the gage, 2) corrosion of the brass rods when used for a prolonged period of time (few hours), and 3) erratic gage behavior due to dissolved impurities in water.

B.5   Float-and-stringpot-based sensor

A float-based sensor combining a string potentiometer (stringpot) and a float was tested using the 0.57 m diameter tank described in Section B.3. The sensor comprised a hinged float and a string potentiometer that was calibrated to measure the vertical displacements of the float. A schematic of the sensor is presented in Figure B.8a and the actual set up is shown in Figure B.8b. The performance of the sensor was found to be unsatisfactory as can be seen in Figure B.9 where the wave height recording from the sensor is plotted against the analytical predictions for a sinusoidal base input motion of 0.7 Hz frequency and 0.3 g amplitude. The (small) restoring force in the cable of the string potentiometer complicates the behavior of the sensor.
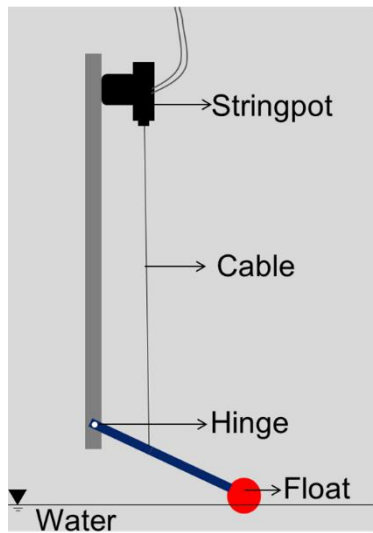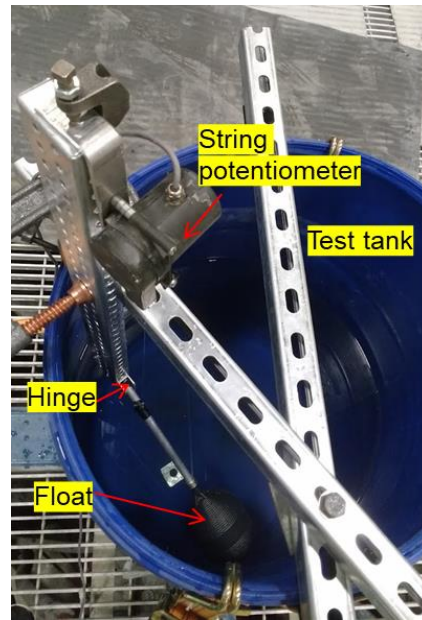
(a) schematic   (b) setup for preliminary testing

Figure B.8. Float-and-stringpot based sensor for measuring wave height
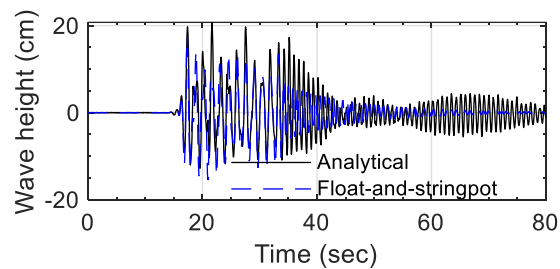
Figure B.9. Wave height histories from the float-and-stringpot sensor and from analytical solution, unidirectional sinusoidal input motions, frequency =0.7 Hz, peak amplitude =0.3g, test vessel of 0.57 m diameter, water height of 0.48 m

B.6 Float-and-Temposonic-based sensor

Another float-based design, consisting of a float attached to a lightweight tube mounted on to the waveguide of a Temposonic, was tested. The waveguide and the inner surface of the tube were lubricated with a silicone spray. A magnet was attached to the top of the tube as shown in Figure B.10a. The Temposonic recorded the vertical motion of the magnet, which was driven by the motion of the float. This design was found to perform satisfactorily and was used in the tests. A comparison of the recording of this sensor with the analytically predicted results is presented in Figure B.10b and c for two earthquake inputs.
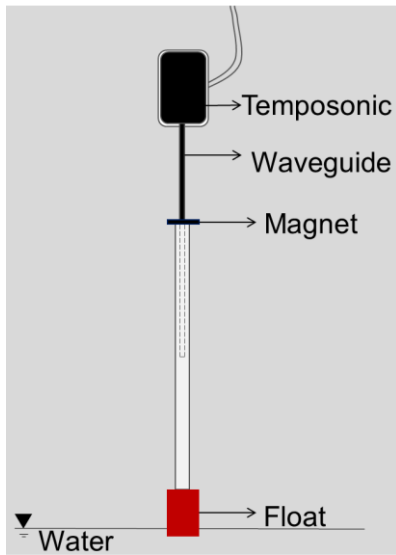
(a) sensor arrangement
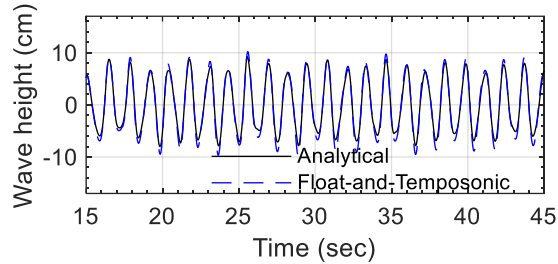
(b) comparison for unidirectional CCE motion (see Table 3.1), peak acceleration = 0.1g
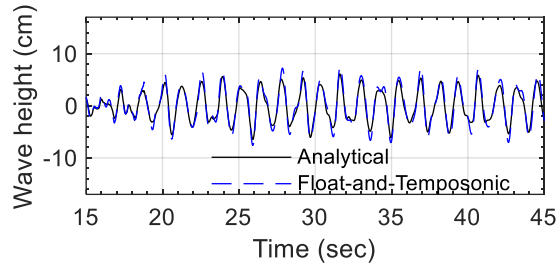
(c) comparison for unidirectional ECE motion (see Table 3.1), peak acceleration = 0.5g

Figure B.10. Float-and-Temposonic-based sensor, arrangement and performance, test vessel and fluid height per Section 3

B.7   Summary

Five strategies for recording wave heights in earthquake-simulator experiments were explored: a camera-based method, a capacitance level sensor, a resistance wire gage, and two float-based approaches utilizing a string potentiometer or a Temposonic. The camera-based method and the float-and-Temposonic-based method were found to perform best. However, implementation of the camera-based method involved the challenges listed in Section B.2. Accordingly, the float-and-Temposonic-based method was used in the earthquake-simulator experiments.

B.8   References

Calugaru, V., and Mahin, S. A. (2009). "Experimental and analytical studies of fixed base and seismically isolated liquid storage tanks." *Proceedings, International Conference on Advances in Experimental Structural Engineering,* San Francisco, CA.

MathWorks. (2017). "MATLAB user guide." MathWorks, Inc., Natick, MA.

Veletsos, A. S. (1984). "Seismic response and design of liquid storage tanks." *Guidelines for the seismic design of oil and gas pipeline systems*, Committee on Gas and Liquid Fuel Lifelines, American Society of Civil Engineers (ASCE), Reston, VA, 255-370.

APPENDIX C

SEISMIC MOTIONS FOR EARTHQUAKE-SIMULATOR EXPERIMENTS

C.1   Introduction

A base-supported cylindrical vessel was tested using a six-degree-of-freedom earthquake simulator at the University at Buffalo. The simulator, with an extension platform (blue framing with grey infill grating) to expand the working area, is shown in Figure C.1. (The extension framing obscures the earthquake simulator below.) A two-phase program of experiments was performed to support validation of numerical models and demonstrate the merits of seismic isolation. Phase I involved the vessel only. Phase II involved the vessel sealed with a head, supporting central and off-center internal components immersed in the contained fluid. Two test setups (TSs) with different supporting conditions were used: 1) TS-1: the base plate of the vessel was bolted to the extension platform; and 2) TS-2: load cells used to measure base reactions were installed between the base plate and the extension platform. Phase II involved three test series described in Section 5. The Phase I tests involved 182 sets of motions, 68 sets for TS-1 and 114 sets for TS-2. Information on the input motions used in the two phases of testing is provided in the next section. Details on the specimen design, test setups, instrumentation, and use of experimental data can be found in Section 3 and Section 5 of this report and Mir et al. (2019; 2020; 2021).
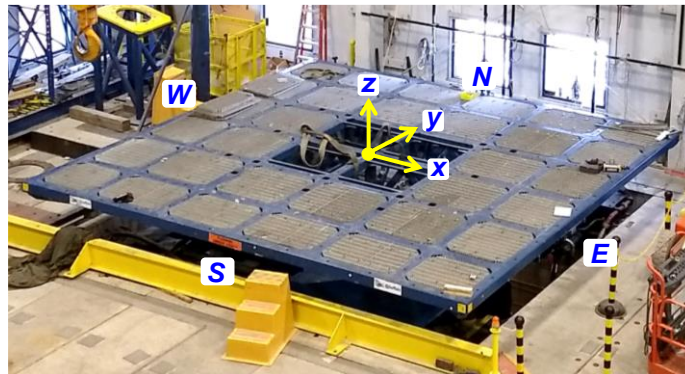
Figure C.1. Extension platform on earthquake simulator and coordinate system (x, y, z)

C.1   Seismic inputs and experiment sequence

White noise, sine waves, earthquake records, and *isolated* motions (see Section 3.5.1) were used as inputs to the earthquake simulator in the tests. Information on the earthquake records is presented in Table C.1, including the earthquake events, the components used for the experiments, and the peak ground acceleration

(PGAs). The time scale of each earthquake motion was compressed to be consistent with the length scale of the test vessel. Figure C.2 presents 5%-damped acceleration response spectra of the earthquake motions, with time compression. In these spectra, the peak acceleration of the x-component of each earthquake is amplitude scaled to 1 g. The y- and z-components of the earthquake are amplitude scaled using the factor for the x-component. The five-second input motions were extracted from the earthquake records, after compressing the time scale, and each includes the strong motion.

Table C.1. Input motion time series[1] used for earthquake-simulator experiments

Event	Year	Station	Direction[2]	Original PGA (g)	Scaled PGA[3] (g)	Time scale[3]
El Centro earthquake (Imperial Valley-02)	1940	El Centro Array #9	180 (x)	0.28	1	$1/\sqrt{10}$
			270 (y)	0.21	0.56	
			Up (z)	0.18	0.42	
Hualien earthquake	2018	HWA019	EW (x)	0.39	1	$1/\sqrt{10}$
			NS (y)	0.37	0.88	
			Up (z)	0.23	0.81	
Chi-Chi earthquake	1999	TCU052	EW (x)	0.36	1	$1/\sqrt{10}$
			NS (y)	0.45	1.25	
			Up (z)	0.19	0.55	
Tohoku earthquake (a)	2011	AKT014	EW (x)	0.07	1	$1/\sqrt{10}$
Tohoku earthquake (b)	2011	MYG014	NS (x)	0.5	1	$1/\sqrt{10}$
Kern County earthquake	1952	Taft Lincoln School	21 (x)	0.16	1	$1/\sqrt{10}$
			111 (y)	0.18	1.12	
			Up (z)	0.11	0.71	

1. Ground motion records of the El Centro, Chi-Chi, and Kern County Earthquakes are extracted from the PEER Ground Motion Database (http://ngawest2.berkeley.edu/, accessed on Jan. 12, 2019); records of the Hualien earthquake are provided by the National Center for Research on Earthquake Engineering, Taiwan; records of the Tohoku earthquake are extracted from Strong-motion Seismograph Networks (K-NET, KiK-net) (https://www.kyoshin.bosai.go.jp/, accessed on Mar. 18, 2019).
2. Directions based on the coordinates described in the dataset of the ground motion records; x, y, and z shown in the parentheses representing the input directions of the earthquake simulator (see Figure C.1)
3. Used in Figure C.2

Tables C.2 and C.3 list the inputs used for TS-1 and TS-2, respectively, including white noise, sine waves, full and five-second earthquake motions (identified by "5s"), and *isolated* motions (denoted by "IS#1", "IS#2", or "IS#3", referring to the three virtual isolation systems presented in Section 3.5.1). Table C.4 through Table C.6 present the input motions for the three test series of Phase II. The PGAs of the earthquake records were scaled to different intensities. The PGAs and the input orientations are identified, based on the coordinate system of Figure C.1.

(a) El Centro earthquake

(b) Hualien earthquake

(c) Chi-Chi earthquake

(d) Tohoku earthquake (AKT014_NS)

(e) Tohoku earthquake (MYG014_NS)

(f) Kern County earthquake
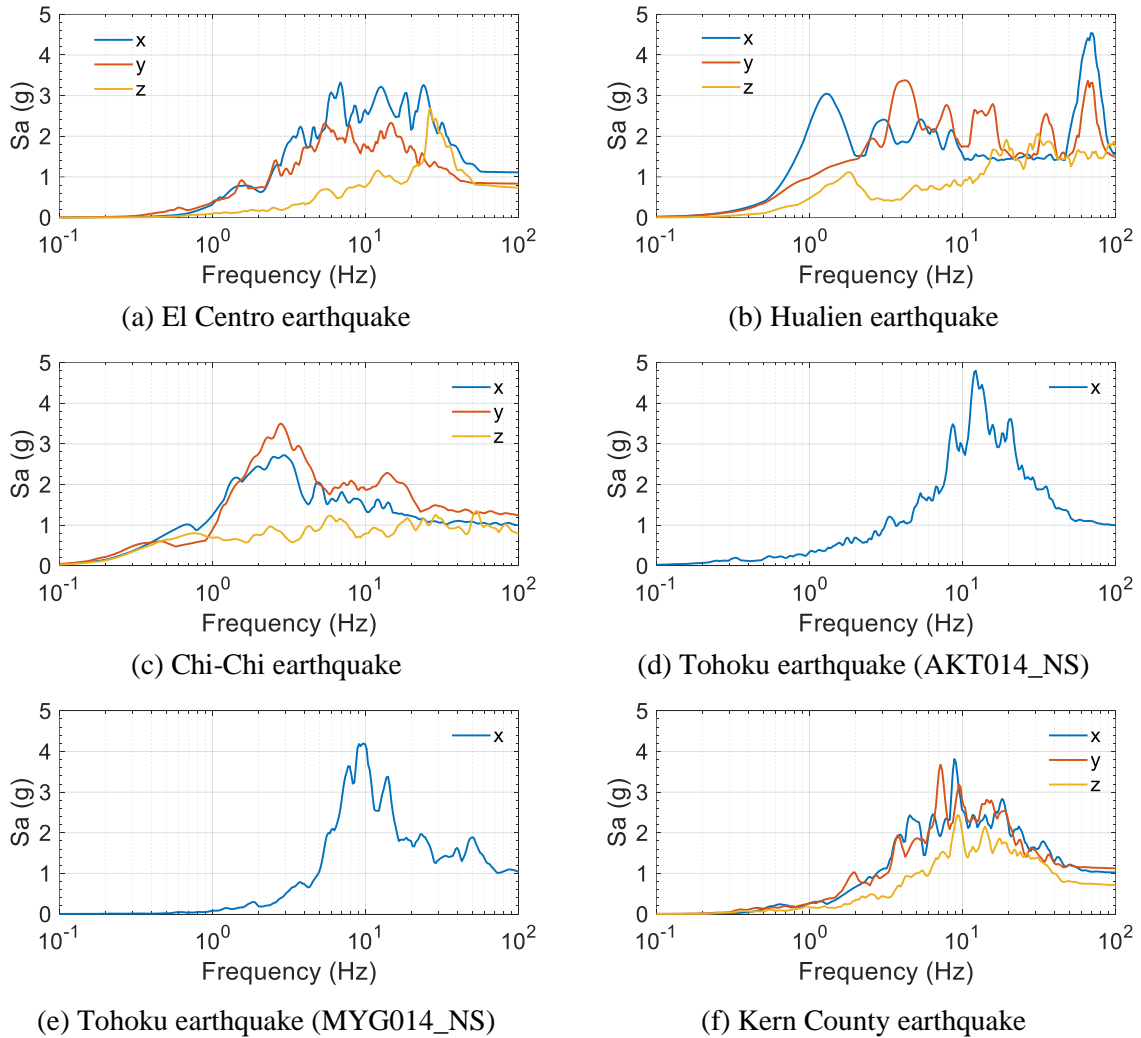
Figure C.2. Acceleration response spectra of input motions used for earthquake-simulator experiments, time and PGA scaled per Table C.1, damping ratio of 5%

Table C.2. Input motions for TS-1

Number	Motion	x-direction PGA (g)	y-direction PGA (g)	z-direction PGA (g)
1	White noise 1	0.1	-	-
2	White noise 2	0.1	-	-
3	Sine ($f = 0.5$ Hz)	0.01	-	-
4	Sine ($f = 1$ Hz)	0.04	-	-
5	Sine ($f = 10$ Hz)	0.1	-	-
6	Sine ($f = 10$ Hz)	0.2	-	-
7	Sine ($f = 10$ Hz)	0.4	-	-
8	Sine ($f = 10$ Hz)	1	-	-
9	Sine ($f = 1$ Hz)	0.4	-	-
10	Sine ($f = 10$ Hz)	1	-	-
11	Sine ($f = 20$ Hz)	0.1	-	-
12	Sine ($f = 20$ Hz)	0.2	-	-
13	Hualien earthquake	0.1	-	-
14	Chi-Chi earthquake	0.1	-	-
15	Chi-Chi earthquake	0.15	-	-
16	El Centro earthquake	0.1	-	-
17	El Centro earthquake	0.2	-	-
18	El Centro earthquake	0.4	-	-
19	Tohoku earthquake (a)	0.05	-	-
20	Tohoku earthquake (a)	0.075	-	-
21	Tohoku earthquake (b)	0.1	-	-
22	Tohoku earthquake (b)	0.2	-	-
23	Tohoku earthquake (b)	0.4	-	-
24	Tohoku earthquake (b)	0.6	-	-
25	Hualien earthquake 5s	0.1	-	-
26	Chi-Chi earthquake 5s	0.15	-	-
27	El Centro earthquake 5s	0.2	-	-

Table C.2. Input motions for TS-1 (continued)

Number	Motion	x-direction PGA (g)	y-direction PGA (g)	z-direction PGA (g)
28	El Centro earthquake 5s	0.4	-	-
29	Tohoku earthquake (b) 5s	0.2	-	-
30	Tohoku earthquake (b) 5s	0.6	-	-
31	Tohoku earthquake (b) 5s	0.2	-	-
32	Tohoku earthquake (b) 5s	0.6	-	-
33	El Centro earthquake 5s	1	-	-
34	El Centro earthquake	1	-	-
35	Sine ($f = 20$ Hz)	1	-	-
36	Sine ($f = 20$ Hz)	1	-	-
37	Hualien earthquake	0.1	0.094	-
38	Chi-Chi earthquake	0.1	0.125	-
39	Hualien earthquake	0.1	0.047	-
40	Chi-Chi earthquake	0.1	0.063	-
41	Hualien earthquake	0.1	0.023	-
42	Chi-Chi earthquake	0.1	0.031	-
43	Hualien earthquake 5s	0.1	0.094	-
44	Chi-Chi earthquake 5s	0.1	0.125	-
45	Hualien earthquake 5s	0.1	0.047	-
46	Chi-Chi earthquake 5s	0.1	0.063	-
47	Hualien earthquake 5s	0.1	0.023	-
48	Chi-Chi earthquake 5s	0.1	0.031	-
49	Hualien earthquake	0.1	0.094	0.058
50	Chi-Chi earthquake	0.1	0.125	0.055
51	Hualien earthquake 5s	0.1	0.094	0.058
52	Chi-Chi earthquake 5s	0.1	0.125	0.055
53	El Centro earthquake	0.13	0.097	-
54	El Centro earthquake	0.25	0.187	-

Table C.2. Input motions for TS-1 (continued)

Number	Motion	x-direction PGA (g)	y-direction PGA (g)	z-direction PGA (g)
55	El Centro earthquake	0.5	0.375	-
56	El Centro earthquake	1	0.751	-
57	El Centro earthquake	1	0.375	-
58	El Centro earthquake	1	0.187	-
59	El Centro earthquake 5s	1	0.751	-
60	El Centro earthquake 5s	1	0.375	-
61	El Centro earthquake 5s	1	0.187	-
62	El Centro earthquake	1	0.751	0.637
63	El Centro earthquake 5s	1	0.751	0.637
64	Sine ($f = 0.77$ Hz)	0.03	-	-
65	Sine ($f = 1.95$ Hz)	0.04	-	-
66	Sine ($f = 1.67$ Hz)	0.03	-	-
67	Sine ($f = 1.32$ Hz)	0.03	-	-
68	Sine ($f = 0.77$ Hz)	0.03	-	-

Table C.3. Input motions for TS-2[1]

Number	Motion	x-direction PGA (g)	y-direction PGA (g)	z-direction PGA (g)
1	White noise 1	0.1	-	-
2	White noise 2	0.1	-	-
3	Sine ($f = 0.5$ Hz)	0.01	-	-
4	Sine ($f = 1$ Hz)	0.04	-	-
5	Sine ($f = 10$ Hz)	0.2	-	-
6	Sine ($f = 10$ Hz)	1	-	-
7	Sine ($f = 20$ Hz)	0.1	-	-
8	Sine ($f = 20$ Hz)	0.4	-	-
9	Sine ($f = 0.77$ Hz)	0.01	-	-
10	Sine ($f = 1.32$ Hz)	0.04	-	-
11	Sine ($f = 1.67$ Hz)	0.05	-	-
12	Sine ($f = 1.95$ Hz)	0.06	-	-
13	Hualien earthquake	0.1	-	-
14	Chi-Chi earthquake	0.1	-	-
15	Chi-Chi earthquake	0.15	-	-
16	El Centro earthquake	0.1	-	-
17	El Centro earthquake	0.2	-	-
18	El Centro earthquake	0.4	-	-
19	Tohoku earthquake (a)	0.05	-	-
20	Tohoku earthquake (a)	0.075	-	-
21	Tohoku earthquake (b)	0.1	-	-
22	Tohoku earthquake (b)	0.2	-	-
23	Tohoku earthquake (b)	0.4	-	-
24	Tohoku earthquake (b)	0.6	-	-
25	Hualien earthquake 5s	0.1	-	-
26	Chi-Chi earthquake 5s	0.1	-	-
27	Hualien earthquake 5s	-	0.1	-

1. The setup of wave-height sensors TE, TW, TN, and TS shown in Figure 3.2c was applied to runs #71 to #114. For runs #1 to #70, TE and TW were 51 mm from the vessel wall and TN and TS were excluded (Yu and Whittaker, 2020a; Yu *et al*., 2021)

Table C.3 Input motions for TS-2[1] (continued)

Number	Motion	x-direction PGA (g)	y-direction PGA (g)	z-direction PGA (g)
28	Chi-Chi earthquake 5s	-	0.1	-
29	El Centro earthquake	1	-	-
30	El Centro earthquake 5s	1	-	-
31	Hualien earthquake	0.1	0.094	-
32	Chi-Chi earthquake	0.1	0.125	-
33	Hualien earthquake	0.1	0.047	-
34	Chi-Chi earthquake	0.1	0.063	-
35	Hualien earthquake 5s	0.1	0.094	-
36	Chi-Chi earthquake 5s	0.1	0.125	-
37	Hualien earthquake 5s	0.1	0.047	-
38	Chi-Chi earthquake 5s	0.1	0.063	-
39	Hualien earthquake	0.1	0.094	0.058
40	Chi-Chi earthquake	0.1	0.125	0.055
41	Hualien earthquake 5s	0.1	0.094	0.058
42	Chi-Chi earthquake 5s	0.1	0.125	0.055
43	El Centro earthquake	1	0.751	-
44	El Centro earthquake	1	0.375	-
45	El Centro earthquake 5s	1	0.751	-
46	El Centro earthquake 5s	1	0.375	-
47	El Centro earthquake	1	0.751	0.637
48	El Centro earthquake 5s	1	0.751	0.637
49	Hualien earthquake	0.1	-	-
50	Hualien earthquake 5s	0.1	-	-
51	Hualien earthquake	0.1	0.094	-
52	Hualien earthquake	0.1	0.047	-
53	Hualien earthquake 5s	0.1	0.094	-
54	Hualien earthquake 5s	0.1	0.047	-

Table C.3 Input motions for TS-2[1] (continued)

Number	Motion	x-direction PGA (g)	y-direction PGA (g)	z-direction PGA (g)
55	Hualien earthquake	0.1	0.094	0.058
56	Hualien earthquake 5s	0.1	0.094	0.058
57	Hualien earthquake	-	-	0.058
58	Hualien earthquake 5s	-	-	0.058
59	Chi-Chi earthquake	0.1	0.125	0.055
60	Chi-Chi earthquake 5s	0.1	0.125	0.055
61	Chi-Chi earthquake	-	-	0.055
62	Chi-Chi earthquake 5s	-	-	0.055
63	El Centro earthquake	1	0.751	0.637
64	El Centro earthquake 5s	1	0.751	0.637
65	El Centro earthquake	-	-	0.637
66	El Centro earthquake 5s	-	-	0.637
67	El Centro earthquake 5s	1	0.751	0.637
68	El Centro earthquake 5s	1	0.751	-
69	El Centro earthquake 5s	1	0.385	-
70	El Centro earthquake 5s	-	-	0.637
71	White noise	0.1	-	-
72	Sine ($f = 0.5$ Hz)	0.01	-	-
73	Sine ($f = 1$ Hz)	0.04	-	-
74	Chi-Chi earthquake	0.1	-	-
75	Chi-Chi earthquake	-	0.12	-
76	Chi-Chi earthquake	0.1	0.12	-
77	Chi-Chi earthquake	0.1	0.12	0.05
78	El Centro earthquake	0.5	-	-
79	El Centro earthquake	-	0.375	-
80	El Centro earthquake	0.5	0.375	-
81	El Centro earthquake	0.5	0.375	0.31

Table C.3 Input motions for TS-2[1] (continued)

Number	Motion	x-direction PGA (g)	y-direction PGA (g)	z-direction PGA (g)
82	El Centro earthquake	0.8	-	-
83	Kern County earthquake	0.4	-	-
84	Kern County earthquake	-	0.44	-
85	Kern County earthquake	0.4	0.44	-
86	Kern County earthquake	0.4	0.44	0.28
87	Kern County earthquake	0.8	-	-
88	IS#1 for motion 74 (CCE)	0.093	-	-
89	IS#1 for motion 76 (CCE)	0.084	0.145	-
90	IS#1 for motion 77 (CCE)	0.083	0.141	0.056
91	IS#1 for motion 82 (ECE)	0.356	-	-
92	IS#1 for motion 80 (ECE)	0.227	0.165	-
93	IS#1 for motion 81 (ECE)	0.226	0.173	0.187
94	IS#1 for motion 87 (KCE)	0.188	-	-
95	IS#1 for motion 85 (KCE)	0.123	0.136	-
96	IS#1 for motion 86 (KCE)	0.128	0.151	0.221
97	IS#2 for motion 74 (CCE)	0.084	-	-
98	IS#2 for motion 76 (CCE)	0.071	0.093	-
99	IS#2 for motion 77 (CCE)	0.070	0.091	0.056
100	IS#2 for motion 82 (ECE)	0.237	-	-
101	IS#2 for motion 80 (ECE)	0.168	0.112	-
102	IS#2 for motion 81 (ECE)	0.171	0.112	0.187
103	IS#2 for motion 87 (KCE)	0.140	-	-
104	IS#2 for motion 85 (KCE)	0.098	0.113	-
105	IS#2 for motion 86 (KCE)	0.112	0.123	0.221
106	IS#3 for motion 74 (CCE)	0.079	-	-
107	IS#3 for motion 76 (CCE)	0.070	0.073	-
108	IS#3 for motion 77 (CCE)	0.069	0.071	0.056

Table C.3 Input motions for TS-2[1] (continued)

Run #	Motion	x-direction PGA (g)	y-direction PGA (g)	z-direction PGA (g)
109	IS#3 for motion 82 (ECE)	0.161	-	-
110	IS#3 for motion 80 (ECE)	0.121	0.090	-
111	IS#3 for motion 81 (ECE)	0.123	0.095	0.187
112	IS#3 for motion 87 (KCE)	0.126	-	-
113	IS#3 for motion 85 (KCE)	0.090	0.096	-
114	IS#3 for motion 86 (KCE)	0.103	0.104	0.221

Table C.4. Input motions for test series 1, Phase II

Number	Motion	x-direction PGA (g)	y-direction PGA (g)	z-direction PGA (g)
1	White noise	0.1	-	-
2	Sine (f=0.5 Hz)	0.01	-	-
3	Sine (f=1 Hz)	0.04	-	-
4	Chi-Chi Earthquake	0.1	-	-
5	Chi-Chi Earthquake	-	0.12	-
6	Chi-Chi Earthquake	0.1	0.12	-
7	Chi-Chi Earthquake	0.1	0.12	0.05
8	El Centro Earthquake	0.5	-	-
9	El Centro Earthquake	-	0.375	-
10	El Centro Earthquake	0.5	0.375	-
11	El Centro Earthquake	0.5	0.375	0.31
12	El Centro Earthquake	0.8	-	-
13	Kern County Earthquake	0.4	-	-
14	Kern County Earthquake	-	0.44	-
15	Kern County Earthquake	0.4	0.44	-
16	Kern County Earthquake	0.4	0.44	0.28
17	Kern County Earthquake	0.8	-	-
18	IS#1 for motion 4 (CCE)	0.102	-	-
19	IS#1 for motion 6 (CCE)	0.148	0.147	-
20	IS#1 for motion 7 (CCE)	0.147	0.143	0.057
21	IS#1 for motion 12 (ECE)	0.365	-	-
22	IS#1 for motion 10 (ECE)	0.237	0.190	-
23	IS#1 for motion 11 (ECE)	0.234	0.217	0.315
24	IS#1 for motion 17 (KCE)	0.318	-	-
25	IS#1 for motion 15 (KCE)	0.166	0.139	-
26	IS#1 for motion 16 (KCE)	0.173	0.153	0.280
27	IS#2 for motion 4 (CCE)	0.086	-	-
28	IS#2 for motion 6 (CCE)	0.112	0.093	-
29	IS#2 for motion 7 (CCE)	0.111	0.091	0.057
30	IS#2 for motion 12 (ECE)	0.237	-	-

Table C.4. Input motions for test series 1, Phase II (continued)

Number	Motion	x-direction PGA (g)	y-direction PGA (g)	z-direction PGA (g)
31	IS#2 for motion 10 (ECE)	0.169	0.152	-
32	IS#2 for motion 11 (ECE)	0.171	0.162	0.315
33	IS#2 for motion 17 (KCE)	0.181	-	-
34	IS#2 for motion 15 (KCE)	0.110	0.114	-
35	IS#2 for motion 16 (KCE)	0.116	0.122	0.280
36	IS#3 for motion 4 (CCE)	0.080	-	-
37	IS#3 for motion 6 (CCE)	0.093	0.077	-
38	IS#3 for motion 7 (CCE)	0.093	0.076	0.057
39	IS#3 for motion 12 (ECE)	0.159	-	-
40	IS#3 for motion 10 (ECE)	0.120	0.122	-
41	IS#3 for motion 11 (ECE)	0.120	0.130	0.315
42	IS#3 for motion 17 (KCE)	0.127	-	-
43	IS#3 for motion 15 (KCE)	0.090	0.097	-
44	IS#3 for motion 16 (KCE)	0.103	0.104	0.280

Table C.5. Input motions for test series 2, Phase II

Number	Motion	x-direction PGA (g)	y-direction PGA (g)	z-direction PGA (g)
1	White noise	0.1	-	-
2	Sine (f=0.5 Hz)	0.01	-	-
3	Sine (f=1 Hz)	0.04	-	-
4	Chi-Chi Earthquake	0.1	-	-
5	El Centro Earthquake	0.4	-	-
6*	El Centro Earthquake	0.8	-	-
7	Kern County Earthquake	0.4	-	-
8*	Kern County Earthquake	0.8	-	-
9	IS#1 for motion 4 (CCE)	0.102	-	-
10	IS#1 for motion 5 (ECE)	0.174	-	-
11*	IS#1 for motion 6 (ECE)	0.365	-	-
12	IS#1 for motion 7 (KCE)	0.154	-	-
13*	IS#1 for motion 8 (KCE)	0.318	-	-
14	IS#2 for motion 4 (CCE)	0.086	-	-
15	IS#2 for motion 5 (ECE)	0.126	-	-
16*	IS#2 for motion 6 (ECE)	0.238	-	-
17	IS#2 for motion 7 (KCE)	0.113	-	-
18*	IS#2 for motion 8 (KCE)	0.182	-	-
19	IS#3 for motion 4 (CCE)	0.081	-	-
20	IS#3 for motion 5 (ECE)	0.101	-	-
21*	IS#3 for motion 6 (ECE)	0.160	-	-
22	IS#3 for motion 7 (KCE)	0.097	-	-
23*	IS#3 for motion 8 (KCE)	0.127	-	-

*Not run for configuration A.

Table C.6. Input motions for test series 3, Phase II

Number	Motion	x-direction PGA (g)	y-direction PGA (g)	z-direction PGA (g)
1	White noise	0.1	-	-
2	Sine (f=0.5 Hz)	0.01	-	-
3	Sine (f=1 Hz)	0.04	-	-
4	Chi-Chi Earthquake	0.1	-	-
5	Chi-Chi Earthquake	-	0.12	-
6	Chi-Chi Earthquake	0.1	0.12	-
7	Chi-Chi Earthquake	0.1	0.12	0.05
8	El Centro Earthquake	0.4	-	-
9	El Centro Earthquake	-	0.3	-
10	El Centro Earthquake	0.4	0.3	-
11	El Centro Earthquake	0.4	0.3	0.25
12*	El Centro Earthquake	0.8	-	-
13	Kern County Earthquake	0.4	-	-
14	Kern County Earthquake	-	0.44	-
15	Kern County Earthquake	0.4	0.44	-
16	Kern County Earthquake	0.4	0.44	0.28
17*	Kern County Earthquake	0.8	-	-
18	IS#1 for motion 4 (CCE)	0.102	-	-
19	IS#1 for motion 6 (CCE)	0.148	0.148	-
20	IS#1 for motion 7 (CCE)	0.147	0.143	0.057
21	IS#1 for motion 8 (ECE)	0.174	-	-
22*	IS#1 for motion 12 (ECE)	0.365	-	-
23	IS#1 for motion 10 (ECE)	0.177	0.154	-
24	IS#1 for motion 11 (ECE)	0.175	0.168	0.250
25	IS#1 for motion 13 (KCE)	0.154	-	-
26*	IS#1 for motion 17 (KCE)	0.318	-	-
27	IS#1 for motion 15 (KCE)	0.167	0.139	-
28	IS#1 for motion 16 (KCE)	0.173	0.153	0.280
29	IS#2 for motion 4 (CCE)	0.086	-	-
30	IS#2 for motion 6 (CCE)	0.112	0.094	-

Table C.6. Input motions for test series 3, Phase II (continued)

Number	Motion	x-direction PGA (g)	y-direction PGA (g)	z-direction PGA (g)
31	IS#2 for motion 7 (CCE)	0.111	0.091	0.057
32	IS#2 for motion 8 (ECE)	0.126	-	-
33*	IS#2 for motion 12 (ECE)	0.238	-	-
34	IS#2 for motion 10 (ECE)	0.138	0.114	-
35	IS#2 for motion 11 (ECE)	0.141	0.125	0.250
36	IS#2 for motion 13 (KCE)	0.113	-	-
37*	IS#2 for motion 17 (KCE)	0.182	-	-
38	IS#2 for motion 15 (KCE)	0.111	0.114	-
39	IS#2 for motion 16 (KCE)	0.116	0.122	0.280
40	IS#3 for motion 4 (CCE)	0.081	-	-
41	IS#3 for motion 6 (CCE)	0.093	0.077	-
42	IS#3 for motion 7 (CCE)	0.093	0.077	0.057
43	IS#3 for motion 8 (ECE)	0.101	-	-
44*	IS#3 for motion 12 (ECE)	0.160	-	-
45	IS#3 for motion 10 (ECE)	0.107	0.103	-
46	IS#3 for motion 11 (ECE)	0.109	0.108	0.250
47	IS#3 for motion 13 (KCE)	0.097	-	-
48*	IS#3 for motion 17 (KCE)	0.127	-	-
49	IS#3 for motion 15 (KCE)	0.090	0.097	-
50	IS#3 for motion 16 (KCE)	0.104	0.104	0.280

*Not run for configuration C.

C.2 References

Mir, F. U. H., Yu, C.-C., Cohen, M., Bardet, P., Coleman, J. L., and Whittaker, A. S. (2019). "Dataset generation for validation of fluid-structure interaction models." *Tran., 25th International Conference on Structural Mechanics in Reactor Technology (SMiRT-25)*, Charlotte, NC.

Mir, F. U. H., Yu, C.-C., Charkas, H., and Whittaker, A. S. (2020). "Validation of numerical models for seismic fluid-structure interaction analysis of advanced reactors." *Proc., International Congress on Advances in Nuclear Power Plants (ICAPP 2020)*, Abu Dhabi, United Arab Emirates.

Mir, F. U. H., Yu, C.-C., and Whittaker, A. S. (2021). "Validation of numerical models for seismic analysis of submerged components in advanced reactors." *Proc., 2021 International Topical Meeting on Probabilistic Safety Assessment and Analysis (PSA 2021)*, Columbus, OH.

Pacific Earthquake Engineering Research (PEER). "PEER ground motion database." <http://peer.berkeley.edu/peer_ground_motion_database>. (Jan. 12, 2019).

Yu, C.-C., and Whittaker, A. S. (2020a). "Analytical and numerical studies of seismic fluid-structure interaction in liquid-filled vessels." *MCEER-20-0003*, University at Buffalo, Buffalo, NY.

Yu, C.-C., and Whittaker, A. S. (2020b). "Analytical solutions for seismic fluid-structure interaction of head-supported cylindrical tanks." *Journal of Engineering Mechanics*, 146(10), 04020112.

Yu, C.-C., Mir, F. U. H., and Whittaker, A. S. (2021). "Validation of numerical models for seismic fluid-structure-interaction analysis of nuclear, safety-related equipment." *Nuclear Engineering and Design*, 379, 111179.

APPENDIX D

CHARACTERIZATION TESTS OF SINGLE FRICTION PENDULUM BEARINGS

D.1   Introduction

This appendix describes characterization tests for the four single concave friction pendulum (SFP) bearings used to seismically isolate the test specimen described in Section 7. The bearings are denoted SFP1, SFP2, SFP3, and SFP4 in this section. Each bearing consists of a sliding surface (concave plate), a housing plate, and a slider that is coated with a PTFE-type composite as shown in Figure D.1. Figure D.2 shows the fabrication drawings provided by the manufacturer (Earthquake Protection Systems).

This appendix comprises of four sections including this introduction. Section D.2 presents tests to determine the slow and fast coefficients of friction for the bearings, and the velocity dependence of the friction coefficient. Section D.3 describes the tests to determine the axial stiffness of the bearings. Section D.4 summarizes the test results.

Figure D.1. Components of an SFP bearing

28 cm

24.1 cm

6.4 cm

Elevation view

4.4 cm

1.3 cm

0.6 cm

3.8 cm dia slider

Radius = 47.3 cm

Section view
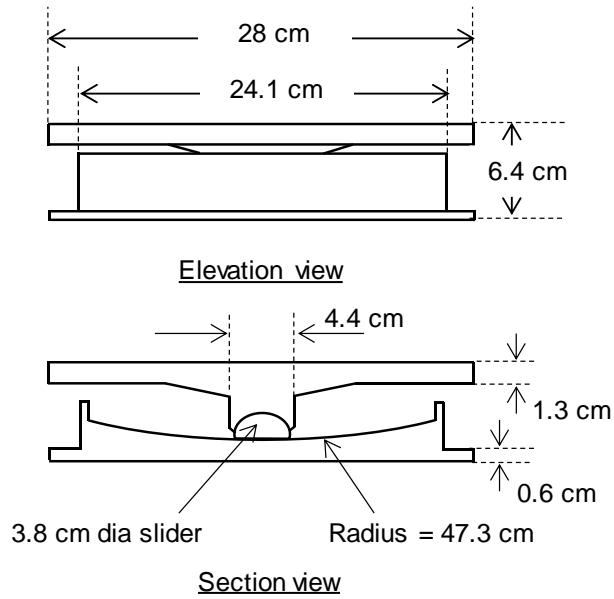
Figure D.2. Fabrication drawings provided by Earthquake Protection Systems

D.2 Characterization of behavior in the horizontal direction

The idealized force-displacement behavior of an SFP bearing, shown in Figure D.3, is characterized by the radius of curvature of the sliding surface (R) and the coefficient of friction at the sliding surface (μ). The characteristic strength (Q) and the post elastic stiffness (K_{pe}) are related to these parameters and the imposed instantaneous axial load (W) on the bearing as indicated in Figure D.3. The radius of curvature (R) is a known geometric property of the SFP bearing. The primary goal of the characterization tests is to determine the coefficient of friction (μ).

Horizontal force

$Q = \mu W$

$K_{pe} = \dfrac{W}{R}$
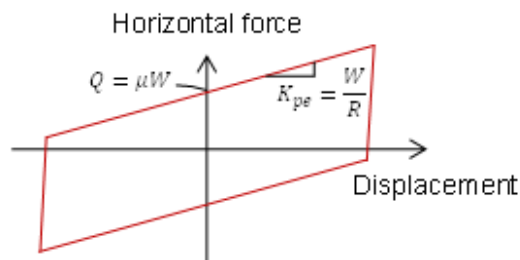
Displacement

Figure D.3. Idealized force-displacement behavior of an SFP bearing

The coefficient of friction is a function of the axial load on the bearing, the sliding velocity, and the temperature of the sliding surface (Constantinou *et al.* 2007). The dependence on axial load and sliding velocity is illustrated in Figure D.4. An increase in the axial load leads to a reduction in the coefficient of friction. The coefficient of friction at near zero sliding velocity is defined as the breakaway coefficient of friction (μ_B). As the sliding velocity increases, the coefficient of friction drops to a minimum value (μ_{min}) before attaining a maximum value (μ_{max}) at high velocities. In general, for a fixed value of axial load, the relation of the coefficient of friction and the sliding velocity (V) can be described by (Constantinou *et al.* 2007):

$$\mu = \mu_{max} - (\mu_{max} - \mu_{min})e^{-aV} \tag{D-1}$$

where a is a rate parameter. The coefficient of friction reduces with an increase in the temperature of the sliding surface. (The temperature dependence of the coefficient of friction is not characterized here.)
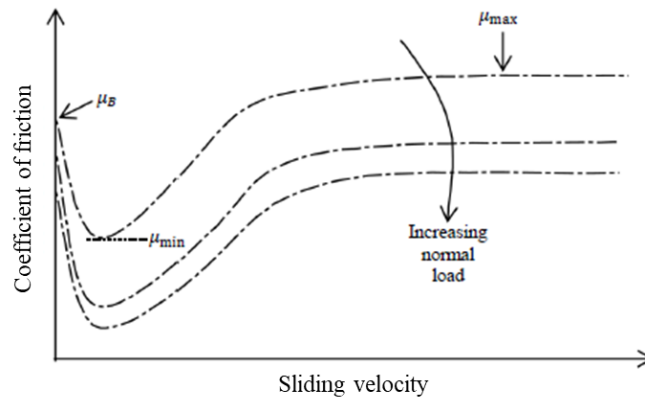
Figure D.4. Variation of the coefficient of friction with sliding velocity and axial load, adapted from Constantinou *et al.* (2007)

D.2.1. Test set-up and instrumentation

The single bearing testing machine (SBTM) at the University at Buffalo was used to test the bearings. The machine comprises a loading beam, a horizontal actuator, two vertical actuators, a load cell, and supporting frame structures, as shown in Figure D.5 and Figure D.6. The horizontal and vertical actuators transmit horizontal and axial forces or displacements, respectively, to the bearing via the loading beam. For the tests described herein, the vertical actuators were run under force control to accommodate changes in the bearing height while maintaining a predefined axial load on the bearings. The axial load recorded by

the load cell beneath the bearing was used to control the vertical actuators. The horizontal actuator was run in displacement control to impose a predefined displacement history.
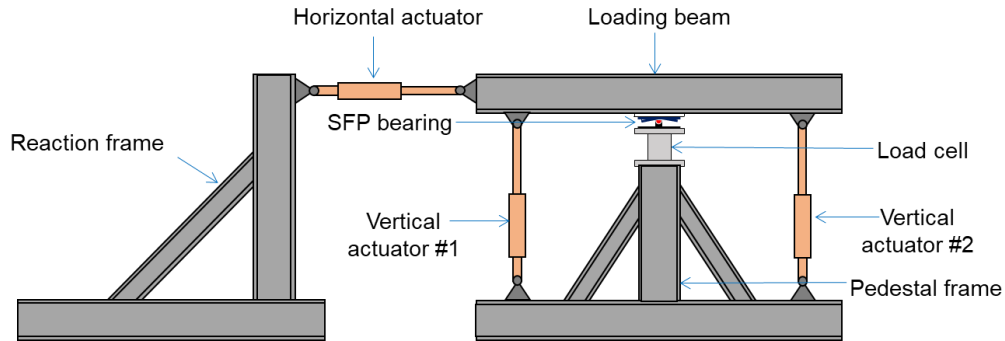
Figure D.5. Schematic of the SBTM at the University at Buffalo
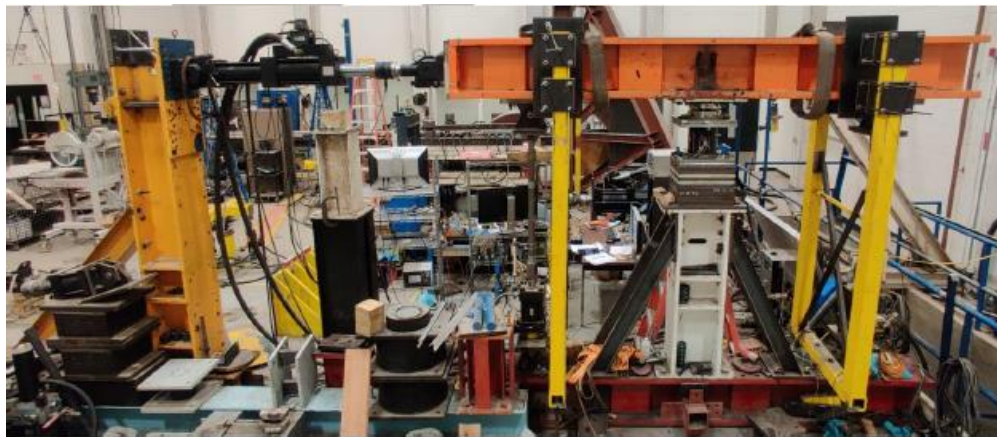
Figure D.6. SBTM at the University at Buffalo

Ten channels were used to record data in the tests. Each of the three actuators has an inline uniaxial load cell and an internal or an external displacement transducer to measure axial force and displacement, respectively. The shear force and axial force imposed on the bearing were recorded using the load cell. The acceleration of the loading beam and the command horizontal displacement (used as command for the horizontal actuator) were also recorded.

D.2.2. Test program

The goal of the characterization tests was to determine the coefficient of friction (μ_{max} and μ_{min}) and its velocity dependence for each bearing. A constant value of axial load (20 kN or 4.5 kips) was used

216

throughout the bearing characterization test program. This value is slightly higher than the axial load per bearing (17.2 kN or 3.9 kips) in the earthquake simulator tests described in Section 7.

Table D.1 describes the displacement histories used for testing the bearings. Tests S1 and S4 utilized low velocity triangular displacement histories (see Figure D.7) with different maximum displacements. These tests provide hysteresis loops with clearly defined transition points. Tests S2, S3, S5, and S6 utilized a displacement history first proposed by Constantinou *et al.* 2007. The profile of the displacement history is presented in Figure D.8. The displacement history (termed *cosine* in this section) begins with an idle time in which data is acquired to establish the breakaway friction force. A build-up time of 60 to 180 seconds follows, in which the displacement amplitude, u_o, is reached at a very low sliding velocity (less than 0.13 cm/sec). During this part of the imposed motion, $\mu_{\min}$ can be measured under truly quasi-static conditions. An idle time of 10 sec is then imposed to allow the temperature at the sliding interface to stabilize. The idle time is followed by 3.25 cycles of harmonic displacement, as shown in Figure D.8, which enables calculation of the maximum coefficient of friction ($\mu_{\max}$). The maximum coefficient of friction ($\mu_{\max}$) is attained in the first cycle of displacement, after which the coefficient of friction reduces due to heating. The reduced value of friction in the third cycle can be used to characterize heating effects in the bearings. Tests S2 and S5 have nearly equal peak velocities (4.8 cm/sec and 5.3 cm/sec) and tests S3 and S6 have the same peak velocity (31.9 cm/sec).

Figure D.9 presents the normalized force-displacement loop for test S2 of SFP2 and the different friction values computed per Constantinou *et al.* (2007) to illustrate the procedure used to determine the coefficients of friction. The minimum coefficient of friction ($\mu_{\min}$) occurs immediately after the initiation of sliding (when the sliding velocity is close to zero) as identified in Figure D.9. The maximum value of the coefficient of friction ($\mu_{\max} = \mu_{1st\_cycle}$) occurs in the first cycle of loading, at the time instant when the highest velocity is first attained. In the subsequent cycles, the coefficient of friction reduces due to heating of the sliding surface, characterized herein as the value of friction in the third cycle (μ_{3rd_cycle}).

Table D.1. Test program for the bearings, axial load = 20 kN (nominal axial pressure = 17.6 MPa)

Test	Signal	Frequency (Hz)	Build-up time (sec)	Max. displacement (cm)	Max. velocity (cm/sec)
S1	Triangular	-	-	2.54	0.13
S2	Cosine	0.3	60	2.54	4.8
S3	Cosine	2.0	60	2.54	31.9
S4	Triangular	-	-	8.4	0.13
S5	Cosine	0.1	180	8.4	5.3
S6	Cosine	0.6	180	8.4	31.9
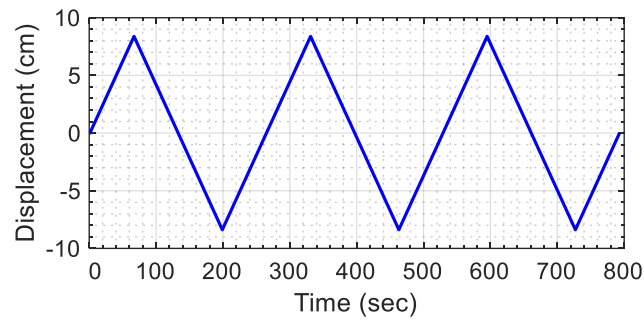
Figure D.7. Triangular displacement history, test S4
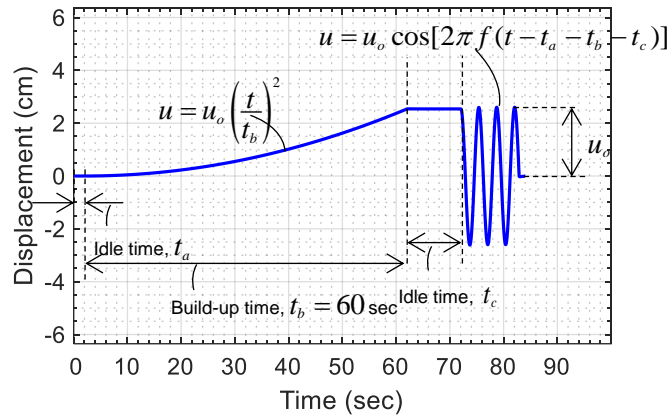
Figure D.8. Displacement history for test S2, u is displacement and f is frequency

218
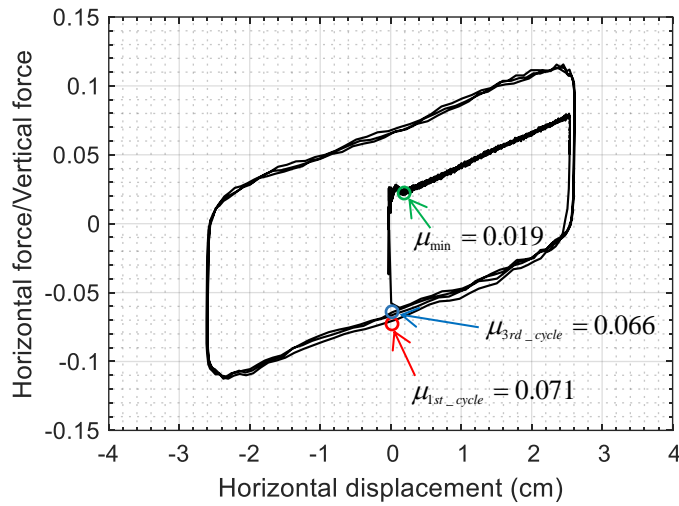
Figure D.9. Determining friction properties for SFP2 bearing, test S2

The velocity dependence of the friction coefficient is entirely characterized by μ_{max}, μ_{min}, and the rate parameter a in equation (D-1). The coefficients of friction, μ_{max} and μ_{min}, are determined from tests S2, S3, S5, and S6 using the procedure described above. To evaluate the parameter a for a bearing, a dataset comprising four pairs of velocity and friction is used. A curve per equation (D-1) is fit to the dataset to obtain a. The four pairs are:

1) velocity is zero, friction coefficient is equal to the average of μ_{min} from tests S2, S3, S5, and S6

2) velocity is 0.13 cm/sec (tests S1 and S4), friction coefficient is equal to the average of μ determined from tests S1 and S4

3) velocity is 5 cm/sec (average of velocities in tests S2 and S5), friction coefficient is equal to the average of μ_{1st_cycle} from tests S2 and S5

4) velocity is 31.9 cm/sec (tests S3 and S6), friction coefficient is equal to the average of μ_{1st_cycle} from tests S3 and S6

D.2.3. Results

Table D.2 presents the minimum (slow), first cycle, and third cycle values of the coefficient of friction, determined from the test data, for the four SFP bearings. The coefficients of friction increase with sliding velocity and reduce with heating of the sliding surface, which is consistent with the behavior of a PTFE-type composite and polished stainless-steel interface Constantinou *et al.* (2007). The variability in the estimated parameters for the four bearings here is typical for friction pendulum bearings at both model and prototype scales (e.g., see Sarlis *et al.* (2013) and McVitty and Constantinou (2015)).

Normalized force-displacement loops for all tests of the four bearings are presented in Figure D.10 through Figure D.13. The force-displacement behavior of the bearings for the high displacement, high velocity test S6 is erratic at high displacements because the axial load used in the tests is low (= 20 kN), which makes the control of the vertical actuators at high horizontal velocities and displacements challenging: the axial load reduces to near zero at multiple instants during the test. Similar outcomes are observed for the high horizontal velocity Test S3. Test S6 was repeated for SFP4 at a higher axial load of 62.3 kN (nominal axial pressure = 55 MPa). The resulting force-displacement loop is shown in Figure D.14. From the figure, it is evident that the behavior of the bearing is stable at the higher axial load.

Table D.2. Coefficients of friction (%) determined from tests, axial load = 20 kN (pressure = 17.6 MPa)

	Test	S1	S2	S3	S4	S5	S6
	Displacement (cm)	2.54	2.54	2.54	8.4	8.4	8.4
	Velocity (cm/sec)	0.13	4.8	31.9	0.13	5.3	31.9
SF1	Slow	-	3.7	3.4	-	3.1	4.5
SF1	1st cycle	4.9	10.5	12	5.2	10.5	13
SF1	3rd cycle	-	9.8	10.5	-	10.5	10
SF2	Slow	-	1.9	2.5	-	2.5	2.3
SF2	1st cycle	2.7	7.1	7.1	3.9	7.2	7.9
SF2	3rd cycle	-	6.6	6	-	7.2	6.9
SF3	Slow	-	2.4	2.7	-	2.8	2.6
SF3	1st cycle	3.3	8.2	9.2	4.7	8.9	11.8
SF3	3rd cycle	-	8.2	7.8	-	8.9	8.7
SF4	Slow	-	1.8	2.5	-	2.8	2.5
SF4	1st cycle	2.3	7.9	8.7	4.1	8.8	11.5
SF4	3rd cycle	-	7.9	7.5	-	8.8	8.2
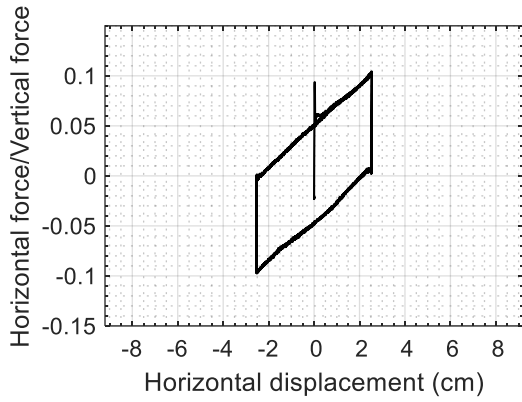
(a) test S1
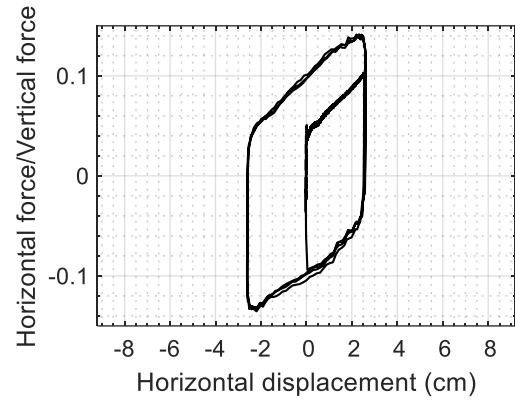
(b) test S2
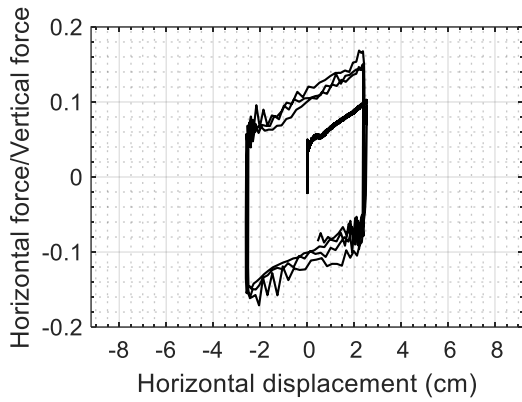
(c) test S3
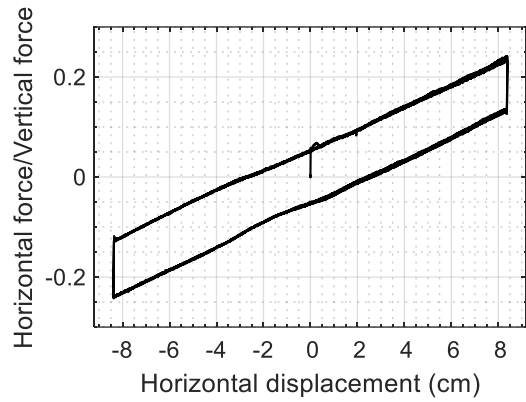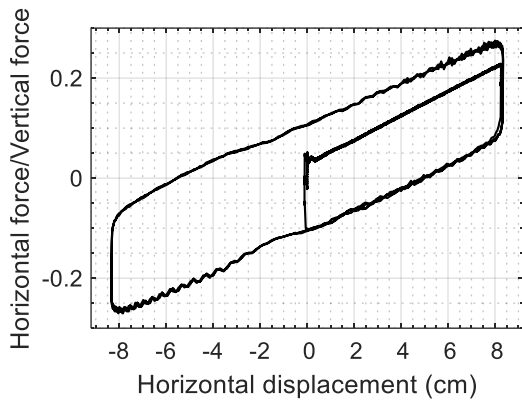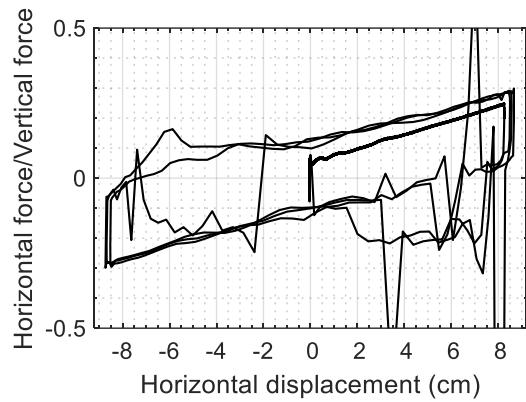
(d) test S4

(e) test S5

(f) test S6

Figure D.10. Normalized force-displacement loops for SFP1, axial load = 20 kN, nominal axial pressure = 17.6 MPa
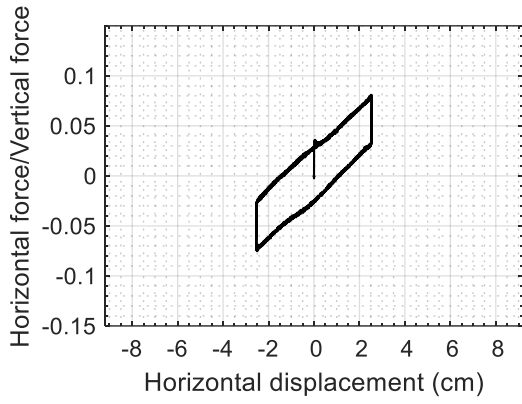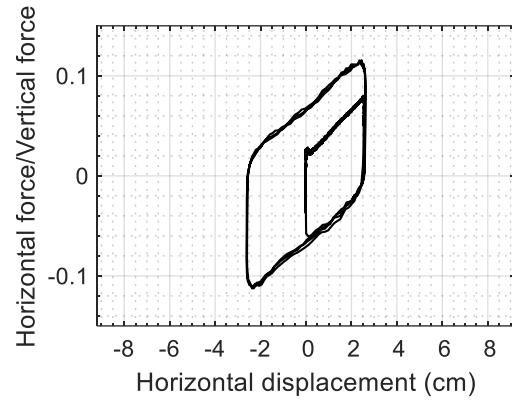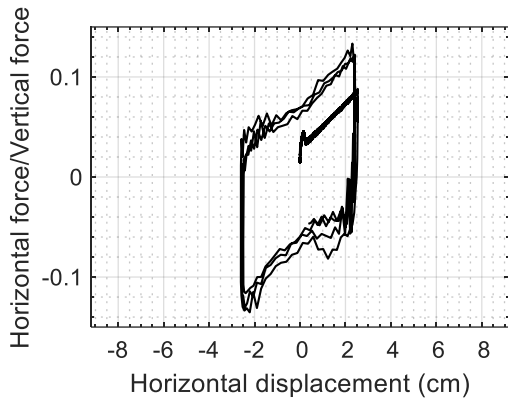
(a) test S1
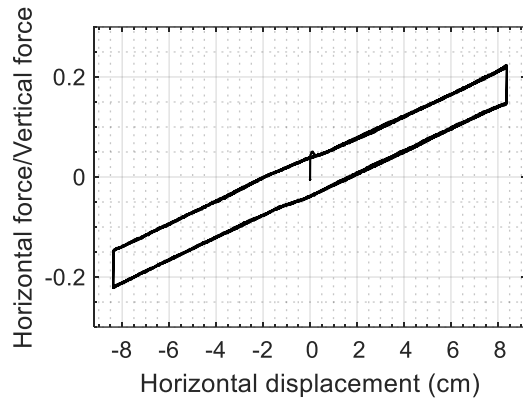
(b) test S2
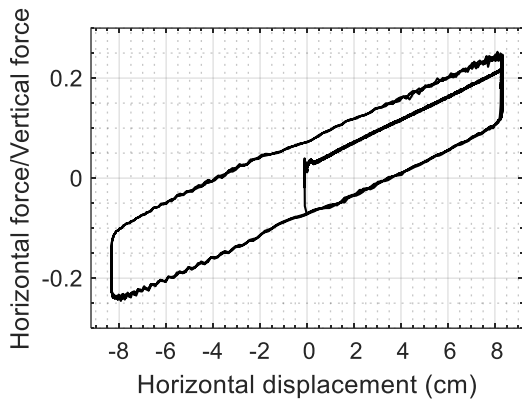
(c) test S3
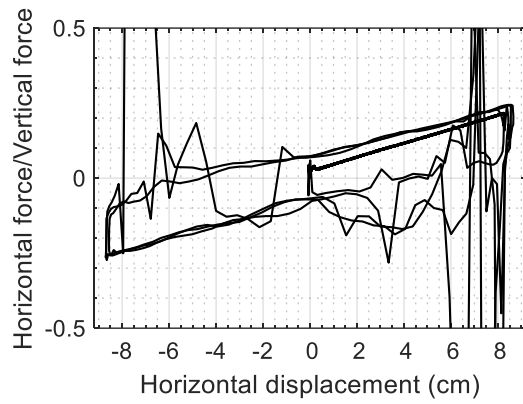
(d) test S4

(e) test S5

(f) test S6

Figure D.11. Normalized force-displacement loops for SFP2, axial load = 20 kN, nominal axial pressure = 17.6 MPa
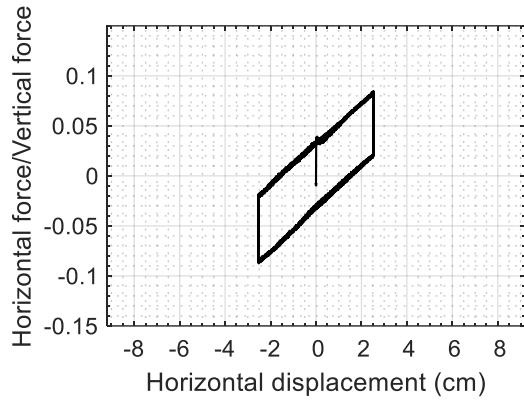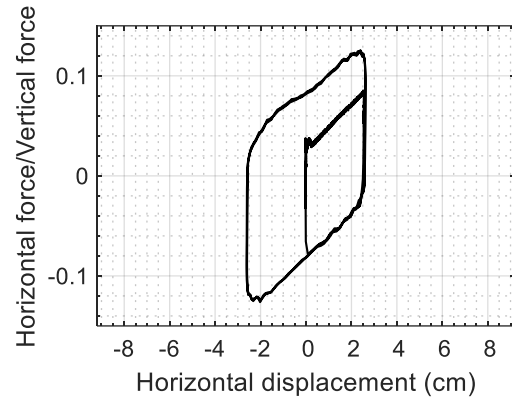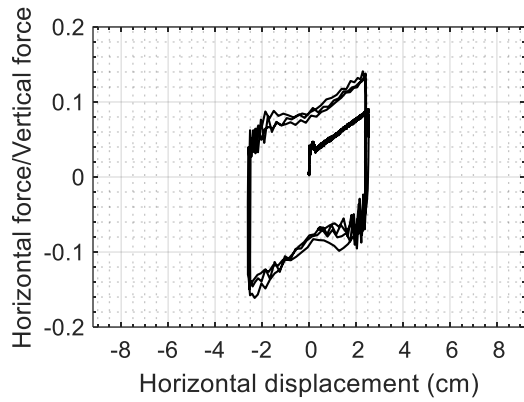
(a) test S1
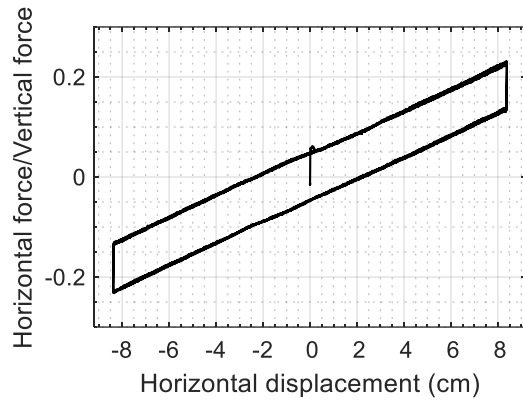
(b) test S2
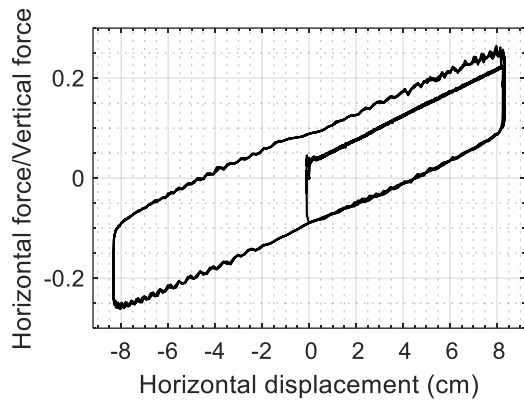
(c) test S3
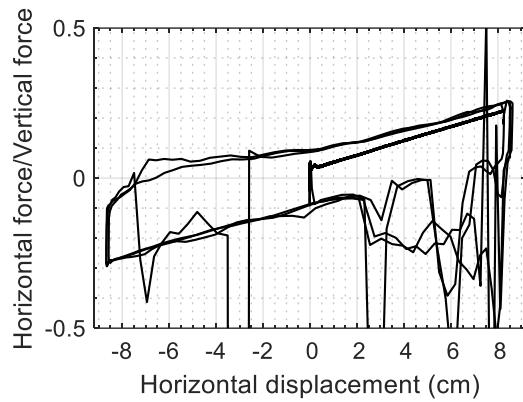
(d) test S4

(e) test S5

(f) test S6

Figure D.12. Normalized force-displacement loops for SFP3, axial load = 20 kN, nominal axial pressure = 17.6 MPa
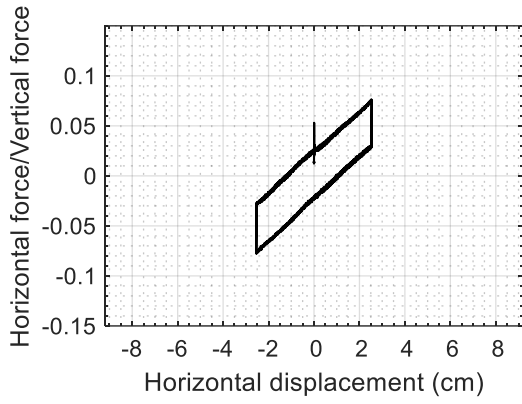
(a) test S1
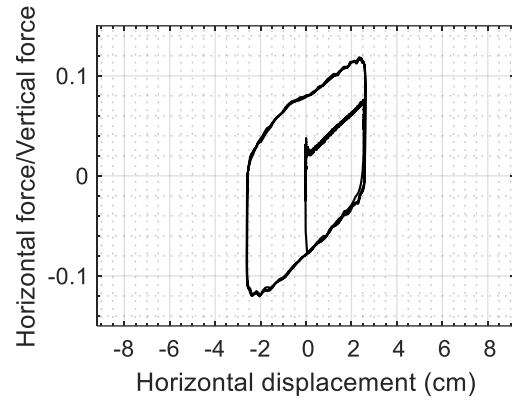
(b) test S2
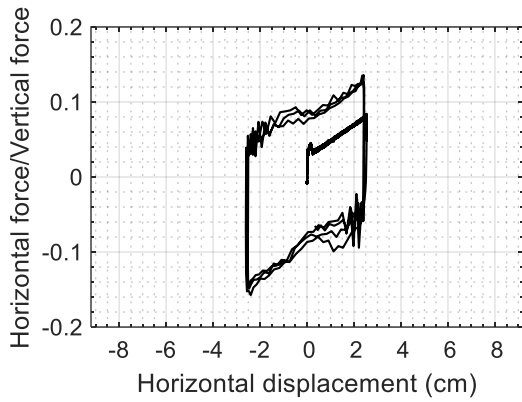
(c) test S3
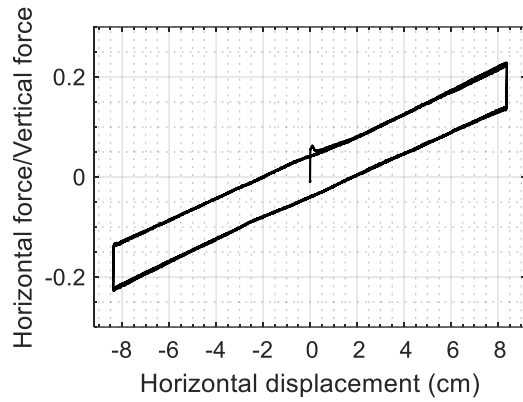
(d) test S4
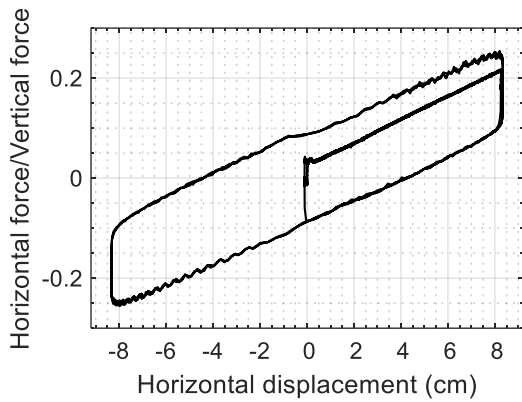
(e) test S5
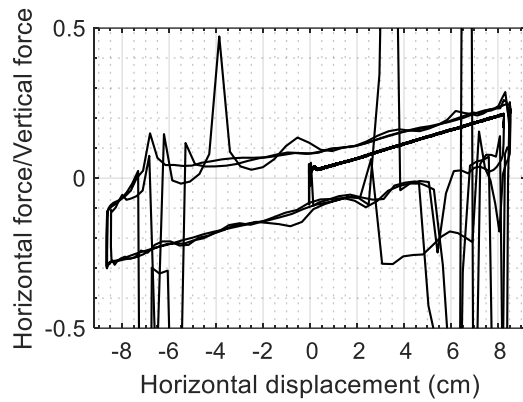
(f) test S6

Figure D.13. Normalized force-displacement loops for SFP4, axial load = 20 kN, nominal axial pressure = 17.6 MPa
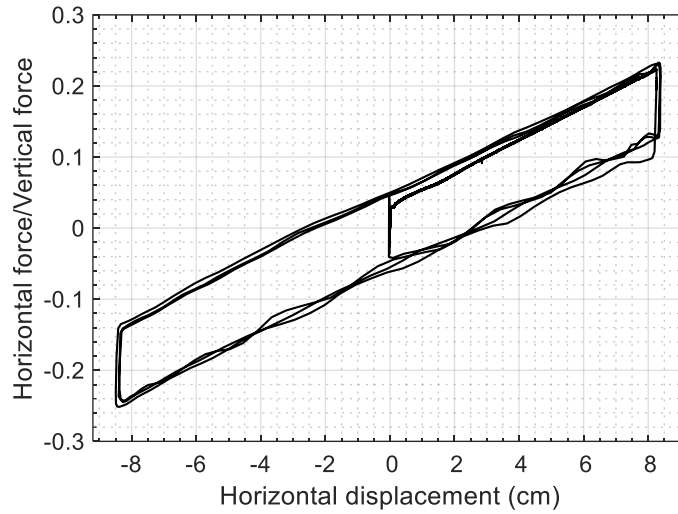
Figure D.14. Normalized force-displacement loop for SFP4, test S6, axial load = 62.3 kN, nominal
axial pressure = 55 MPa

Table D.3 presents friction coefficients for the four bearings at four velocities (evaluated as described
above). Figure D.15 presents best-fit curves per equation (D-1) plotted to determine the rate parameter. An
average rate parameter of 0.44 s/cm was obtained for the four bearings.

Table D.3. Average coefficients of friction (%) at different velocities,
axial load = 20 kN (nominal axial pressure = 17.6 MPa)

	Velocity (cm/sec)			
	0	0.13	5.0	31.9
SFP1	3.7	5.1	10.5	12.5
SFP2	2.3	3.3	7.2	7.5
SFP3	2.6	4.0	8.6	10.5
SFP4	2.4	3.2	8.4	10.1
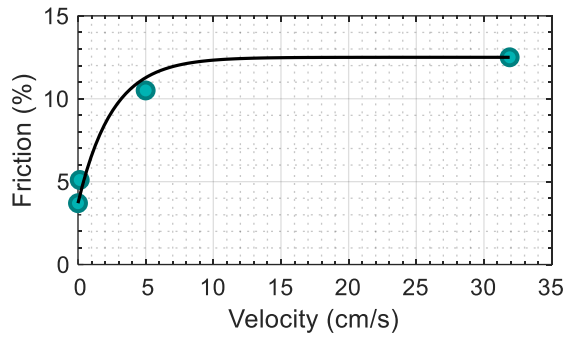
(a) SFP1, $a = 0.39$ s/cm
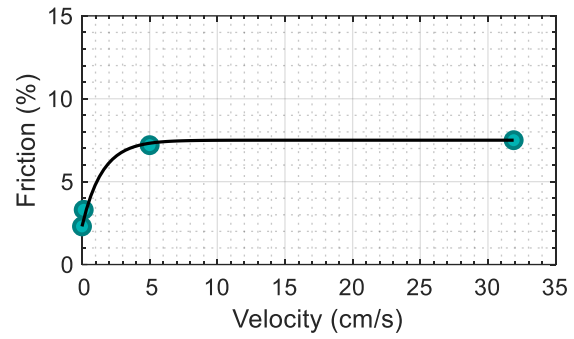
(b) SFP2, $a = 0.67$ s/cm
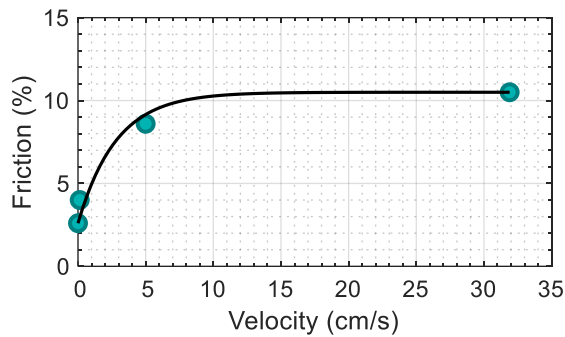
(c) SFP3, $a = 0.35$ s/cm
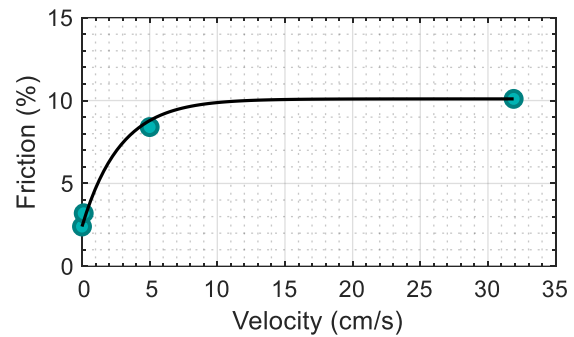
(d) SFP4, $a = 0.35$ s/cm

Figure D.15. Rate parameter a for the four bearings, average $a = 0.44$ s/cm

D.3   Characterization of behavior in the vertical direction

The representative force displacement behavior of an SFP bearing under axial compressive (vertical) load is shown in Figure D.16. The axial stiffness is low at low axial loads. The behavior at a particular axial load is characterized by the slope of the load-displacement curve at that load. The goal of the characterization tests described here was to estimate the axial stiffness of the four bearings at an axial load of 20 kN.
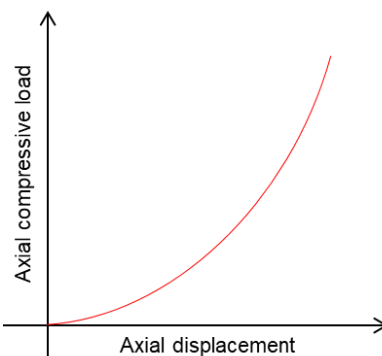
Figure D.16. Representative behavior of an SFP isolator in compression

226

The vertical stiffness characterization tests were carried out using the MTS tension-compression machine, manufactured by MTS Systems Corporation. Figure D.17 shows the setup used for testing. Linear potentiometers at the four corners of a bearing were used to record the relative movement of the concave and the housing plates. The tension-compression machine has an inbuilt load and displacement sensor. Six channels of data were recorded. The average of the displacements recorded by the four linear potentiometers and the actuator's displacement transducer was used as the measure of the axial displacement in the bearing.
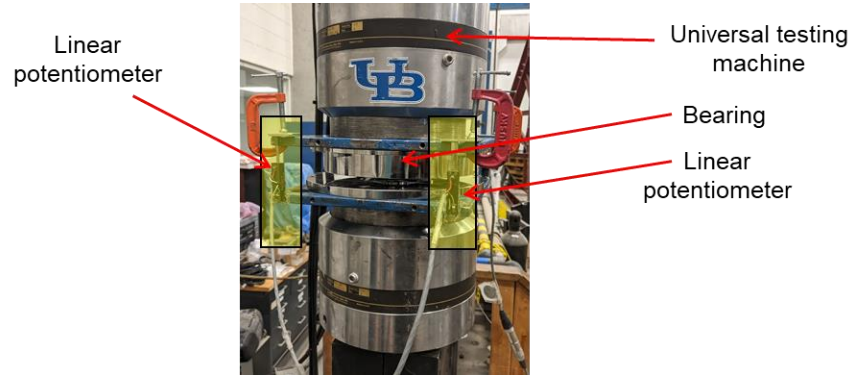
Figure D.17. Test setup used for vertical characterization tests

The loading history of Figure D.18 was used for testing. A pre-load of 5 kN was applied before the start of data acquisition, followed by a ramp up to a load of 20 kN (4.5 kips) in 10 sec and 2.75 cycles of ±8.9 kN (2 kips) at 0.1 Hz.
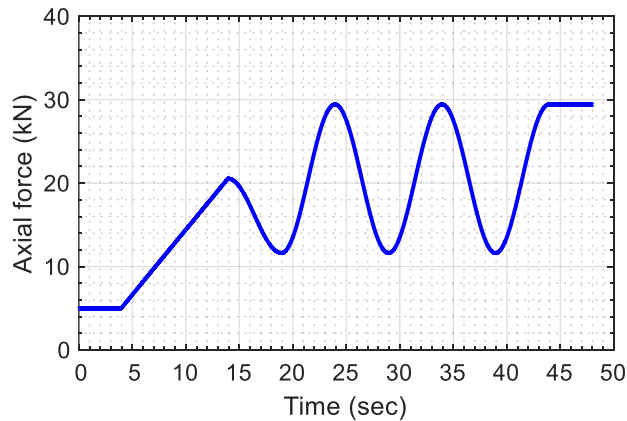
Figure D.18. Loading history used for characterizing vertical stiffness

Figure D.19 presents axial load – axial displacement plots for the four bearings. The estimated stiffness for each bearing is indicated on each plot. The average stiffness of the bearings is 1.07×10^5 kN/m at an axial load of 20 kN.
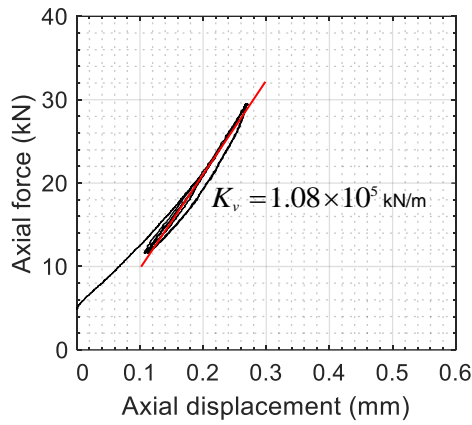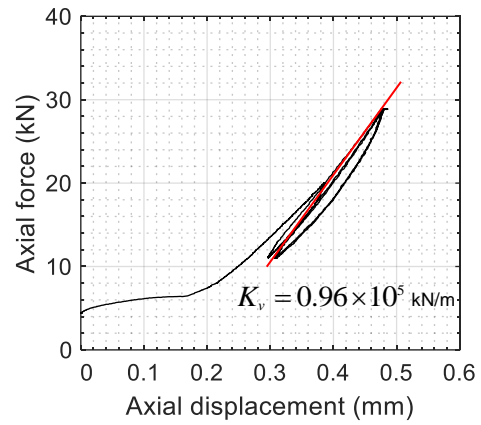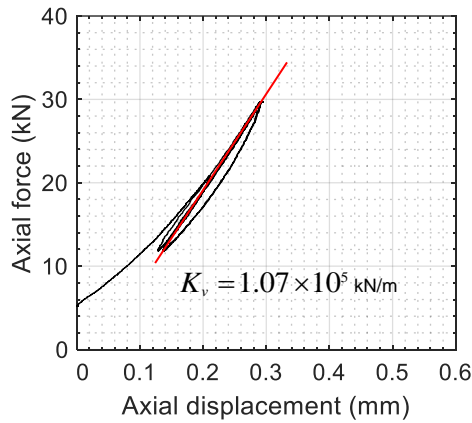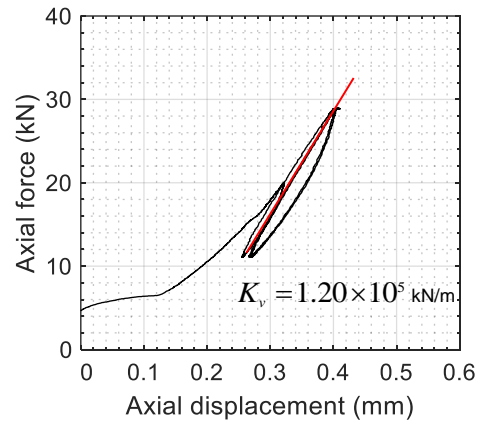
Figure D.19. Axial load vs displacement plots for SFP bearings, K_v is axial stiffness

The average stiffness of the bearings is approximately 3% of the axial stiffness of a cylindrical steel column with diameter equal to the slider diameter (= 3.8 cm) and height equal to that of the bearing (= 6.4 cm) at zero displacement. The size of the slider and the housing plate cavity in the bearings used here is small compared to bearings used in practice. Machining small-sized sliders and housing plate cavities to tight tolerances, required for achieving a high axial stiffness at low axial loads, is challenging. (A reasonable stiffness for larger diameter slider sizes is 10% to 20% of the *column stiffness.*)

D.4   Conclusions

The behavior of four SFP bearings under horizontal and vertical loads was characterized. An axial load of 20 kN (4.5 kips) was considered for the characterization tests. Behavior under horizontal loads was

characterized by estimating slow and fast coefficients of friction. The velocity dependence of the coefficient of friction for each bearing was characterized by a rate parameter. The behavior under vertical load was established by estimating the vertical stiffness of each bearing at an axial load of 20 kN. Table D.4 summarizes results.

Table D.4. Summary of characterization tests

Bearing	Friction coefficient, slow (%)	Friction coefficient, fast (%)	Rate parameter (s/cm)	Axial stiffness ($\times 10^5$ kN/m)
SFP1	3.7	12.5	0.39	1.08
SFP2	2.3	7.5	0.67	0.96
SFP3	2.6	10.5	0.35	1.07
SFP4	2.4	10.1	0.35	1.20
Average	2.8	10.2	0.44	1.07

D.5   References

Constantinou, M. C., Whittaker, A. S., Kalpakidis, Y., Fenz, D. M., and Warn, G. P. (2007). "Performance of seismic isolation hardware under service and seismic loading." *Report MCEER-07-0012*, The State University of New York at Buffalo, Buffalo, NY.

McVitty, W. J., and Constantinou, M. C. (2015). "Property modification factors for seismic isolators: design guidance for buildings." *Report MCEER 15-0005*, The State University of New York at Buffalo, Buffalo, NY.

Sarlis, A. A., Constantinou, M. C., and Reinhorn, A. M. (2013). "Shake table testing of triple friction pendulum isolators under extreme conditions." *Report MCEER-13-0011*, The State University of New York at Buffalo, Buffalo, NY.

APPENDIX E

ROCKING RESPONSE OF LIQUID FILLED CYLINDRICAL VESSLES

E.1   Introduction

This appendix examines an existing analytical solution for predicting hydrodynamic responses in rigid cylindrical vessels due to rotational seismic inputs. Analytical solutions for pressure in the fluid and on the vessel wall, and base moment, are modified to account for the effects of angular displacements at the base. A finite element model of a water-filled cylindrical vessel, using the Arbitrary Lagrangian and Eulerian (ALE) solver in LS-DYNA, is used to demonstrate the efficacy of the proposed expressions for three base rocking motions.

Section E.2 introduces the existing analytical solution. Section E.3 and Section E.4 describe modifications to the analytical solution to account for the effect of angular displacements in the calculated moment and hydrodynamic pressure, respectively. Section E.5 describes a finite element study to demonstrate the efficacy of the proposed modifications to the solution. A summary of the study is presented in Section E.6.

E.2   Existing analytical solution for hydrodynamic responses due to rocking inputs

The hydrodynamic responses of liquid-filled cylindrical vessels to horizontal base excitation have been the subject of a number of studies, beginning in the 1930s, as discussed in Section 2. Approximate and exact analytical solutions for evaluating the hydrodynamic responses in such vessels are available and have been implemented in design guidelines for decades. These solutions assume that the base of the vessel moves horizontally without rotation. In service, vessels may also experience rotational inputs due to 1) flexibility of the foundation or support, and 2) rotational components of ground motion, regardless of whether the vessel has a flexible or rigid support.

Basu *et al.* (2012) report peak rocking accelerations of about 0.2 rad/sec^2 in ground motions. Trifunac (2009) describes earthquake rocking acceleration records with peak amplitudes between 0.0001 and 0.1 rad/sec^2, and rotational displacements ranging from 10^{-6} rad to 10^{-3} rad (0.00006° to 0.05°). Graizer (2006) presents examples of earthquake-induced rotational displacements as high as 0.054 rad (3.1°). (The peak rotational displacements used as inputs later in this appendix are on the higher side of the range reported in the literature for earthquake ground motions but may be smaller than those for a vessel supported on a flexible foundation or inside a structure on flexible supports.)

Veletsos and Tang (1987) propose an analytical solution for estimating hydrodynamic responses in a rigid cylindrical vessel subjected to rocking motion at the base. The derivation presented therein closely follows

their approach to develop similar expressions for cylindrical vessels subjected to lateral base excitation (Veletsos 1984) wherein the hydrodynamic responses are parsed into impulsive and convective components. The impulsive component represents the effects of the part of the fluid that is assumed to move with the vessel as a rigidly attached mass. The convective component represents the effects of the part of the fluid that sloshes. The sloshing response is further parsed into contributions from different sloshing modes. Such an approach of parsing the hydrodynamic responses into impulsive and convective components makes it straightforward to combine solutions for rocking and lateral base excitations under the assumption of linearity and small displacements.

The system considered in Veletsos and Tang (1987) is shown in Figure B.1: an upright cylindrical vessel of radius R filled with fluid to a height H subjected to a time (t) dependent rocking motion $\theta_b''(t)$ at its base. The associated angular velocity and displacement of the base are denoted as $\theta_b'(t)$ and $\theta_b(t)$, respectively. A cylindrical coordinate system (r, θ, z) is used to specify points in the fluid domain. The angle θ is measured in the circumferential direction while as θ_b is measured about a horizontal axis normal to the plane defined by $\theta = 0$. A counter-clockwise direction is considered positive for both θ and θ_b.
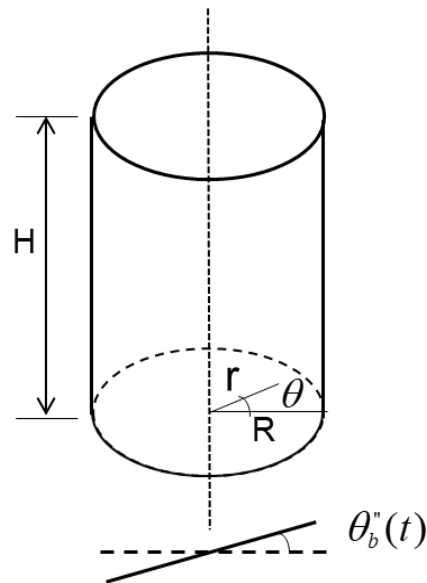
Figure E.1. Upright cylindrical vessel subjected to base rocking (Veletsos and Tang 1987)

The hydrodynamic responses are calculated by solving Laplace's equation for velocity potential, $\phi(r, \theta, z, t)$, assuming an incompressible and inviscid fluid:

$$\nabla^2\phi(r,\theta,z,t)=0 \tag{E-1}$$

Three boundary conditions are used to solve the above equation: 1) the vertical velocity of the fluid at the base must equal the corresponding velocity of the base, 2) the radial velocities of the fluid and the vessel wall near the wall must be the same, and 3) a linearized pressure boundary condition at the free surface. These are listed below (g denotes the acceleration due to gravity):

$$\left(-\frac{\partial\phi(r,\theta,z,t)}{\partial z}\right)_{z=0}=\theta_b^{\cdot}(t)r\cos\theta \tag{E-2}$$

$$\left(-\frac{\partial\phi(r,\theta,z,t)}{\partial r}\right)_{r=R}=-\theta_b^{\cdot}(t)z\cos\theta \tag{E-3}$$

$$\left(\frac{\partial^2\phi(r,\theta,z,t)}{\partial t^2}+g\frac{\partial\phi(r,\theta,z,t)}{\partial z}\right)_{z=H}=0 \tag{E-4}$$

The corresponding solutions for hydrodynamic pressure, base shear, base moment, and wave height are then obtained as functions of the input rocking motion. As an example, the expression for hydrodynamic pressure, p, is as follows:

$$p(r,\theta,z,t)=[c_o^r(r,z)H\theta_b^{\cdot\cdot}(t)+\sum_{j=1}^{\infty}c_j^r(r,z)A_j^r(t)]\rho_l R\cos\theta \tag{E-5}$$

where c_o^r and c_j^r are dimensionless coefficients, $A_j^r(t)$ is the acceleration of a single-degree-of-freedom oscillator with frequency equal to the jth sloshing mode of vibration subjected to an acceleration equal to $H\theta_b^{\cdot\cdot}(t)$, and ρ_l is the density of the fluid. Expressions for other response quantities can be found in Veletsos and Tang (1987). Although the instantaneous angular displacement $\theta_b(t)$ does not appear in the proposed expressions, it does affect the hydrodynamic pressure and the base moment as discussed next. Approximate approaches to account for such effects are described in the following sections.

E.3   Pressure due to rotational displacement at base

A sectional view of an open cylindrical vessel of radius R with fluid filled to height H, rotated at its base by angle θ_b, is shown in Figure E.2. A horizontal free surface is assumed herein, making the expressions valid for small values of z/H. It is clear from the shown displaced shape that the fluid height above any point, and thus the gravity head (or hydrostatic pressure), changes with $\theta_b(t)$. For an arbitrary point with coordinates r, θ, and z in the original configuration, the following expression for pressure head in the displaced configuration can be derived by the use of geometry:

$$p_{head}(r,\theta,z,t) = \rho_l g[(-1)^\alpha \{|r\cos\theta| + (-1)^{\alpha+1}(H-z)\tan\theta_b(t)\}\sin\theta_b(t) + (H-z)\sec\theta_b(t)] \quad \text{(E-6)}$$

where $\alpha = 1$ for $(-\pi/2) \le \theta < (\pi/2)$ and $\alpha = 2$ for $(\pi/2) \le \theta < (3\pi/2)$. The displacement field used to derive this expression is shown in Figure E.2 for the point marked in yellow. For small values of $\theta_b(t)$, $\sin\theta_b(t) \approx \tan\theta_b(t) \approx \theta_b(t)$, $\sec\theta_b(t) \approx 1$, and $\theta_b^2 \approx 0$. Using these approximations, equation (E-6) is simplified to:

$$p_{head}(r,\theta,z,t) \approx \rho_l g[(-1)^\alpha |r\cos\theta|\theta_b(t) + (H-z)] \quad \text{(E-7)}$$

The time dependence of the pressure head at a point, as evident in equations (E-6) and (E-7), needs to be accounted for in the analytical solution when comparing results with those recorded in an experiment or predicted by analysis of a numerical model.
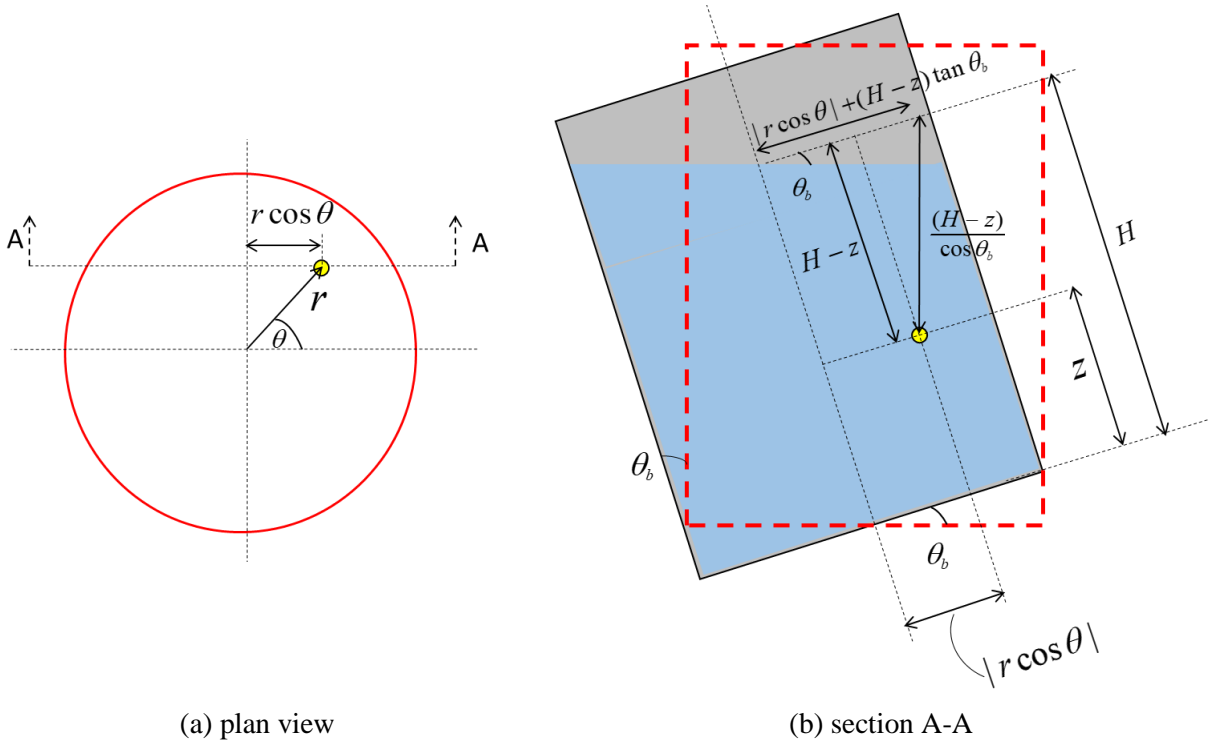
(a) plan view   (b) section A-A

Figure E.2. Pressure head at an arbitrary point in a base-rotated vessel

E.4 Moment due to rotational displacement at base

In addition to the hydrodynamic base moment associated with the impulsive and convective modes, as derived in Veletsos and Tang (1987), there is an additional base moment due to the weight of the fluid (and

also the vessel, if the vessel weight is significant) in the base-rotated configuration. See Figure E.3a. The incremental moment, $M_{\theta_b}(t)$, can be expressed as:

$$M_{\theta_b}(t) = \left(W_f \sin\theta_b(t)\right)h_c + \left(W_f \cos\theta_b(t)\right)\bar{x} \tag{E-8}$$

where W_f is the total weight of the contained fluid, and $\bar{x}$ and h_c locate the center of gravity of the fluid mass in the displaced configuration. Expressions for $\bar{x}$ and h_c can be obtained using Figure E.3b wherein the fluid is divided into two regions, I and II, and the distances to the respective centers of mass (marked in red) are indicated. Region I is cylindrical in shape and Region II is a truncated cylinder. The masses $m_{f,1}$ and $m_{f,2}$ of the two regions are:

$$m_{f,1} = \frac{W_f\left(H - R|\sin\theta_b(t)|\right)}{gH} \quad \text{and} \quad m_{f,2} = \frac{W_f R|\sin\theta_b(t)|}{gH}$$

(a) shifted center of gravity (CG) in the base-rotated configuration

(b) center of gravity for Regions I and II
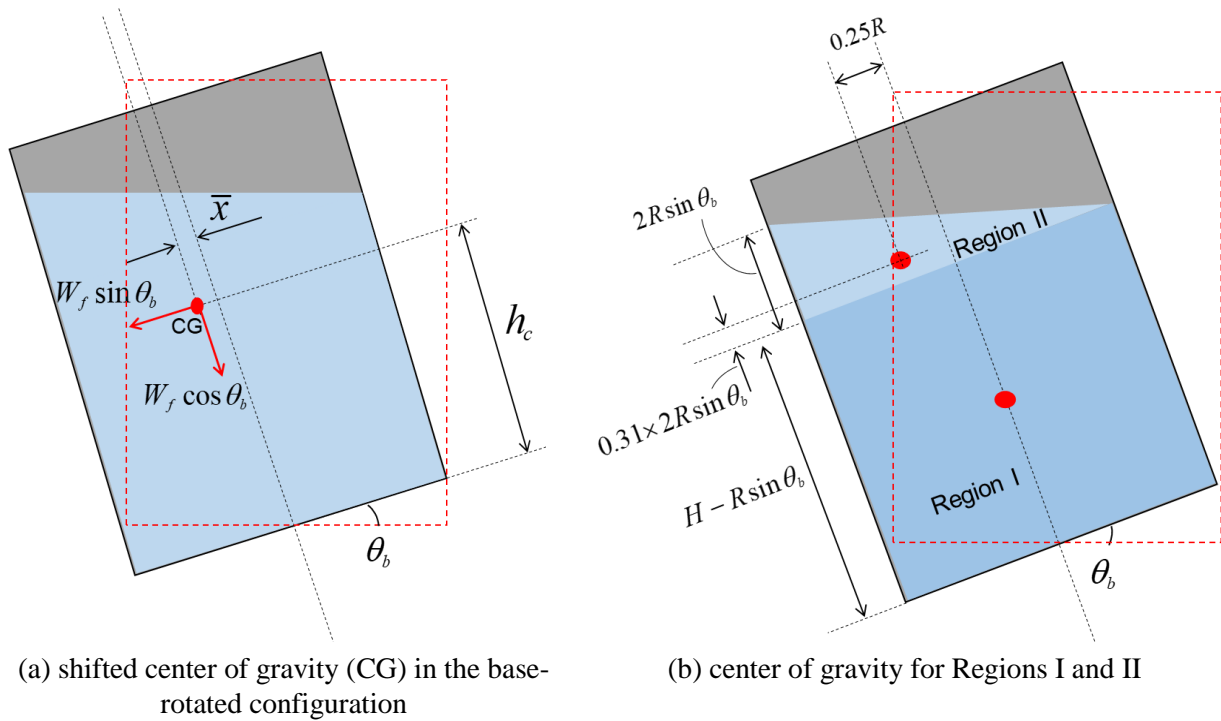
Figure E.3. Calculation of moment due to rotation at the base

The distances $\bar{x}$ and h_c are:

$$\bar{x} = \frac{R^2 \sin\theta_b(t)}{4H} \quad \text{and} \quad h_c = \frac{H}{2} + \frac{0.12R^2 \sin^2\theta_b(t)}{H}$$

For small $\theta_b(t)$, the expressions for $\bar{x}$ and h_c simplify to:

$$\bar{x} \approx \frac{R^2\theta_b(t)}{4H} \text{ and } h_c \approx \frac{H}{2}$$

Equation (E-8) then simplifies to:

$$M_{\theta_b}(t) \approx W_f \frac{H}{2}\theta_b(t) + W_f \frac{R^2\theta_b(t)}{4H} \tag{E-9}$$

E.5   Finite element study

The ALE model in LS-DYNA (LSTC 2017), validated in Section 4, was used to check the efficacy of the proposed modifications to the existing Veletsos and Tang solution. A finite element (FE) model closely following the geometry of a vessel described in Section 3 was prepared. The model consists of a carbon steel vessel with a radius of 0.76 m, height of 2 m, and wall thickness of 7.9 mm, filled with water to a height of 1.62 m above the base. The first mode frequency of the vessel wall fixed at the bottom rim (no fluid mass is added) is 207 Hz and the frequency of the impulsive mode for the fluid-filled vessel is 140 Hz, as evaluated using the procedure outlined in Malhotra *et al.* (2000). For such high natural frequencies, the vessel wall can be treated as rigid. The base of the vessel was modeled using a rigid material with negligible mass density. The mass of the vessel wall is 615 kg and that of the contained fluid is 2932 kg. In the finite element (FE) model, the structural domain (i.e., the vessel wall and base) was Lagrangian and the fluid domain was Eulerian. Nodes at the interface of the Lagrangian and Eulerian domains were merged. The elements in the space above the water level were modeled as a *void* using the *INITIAL_VOID_PART card in the LS-DYNA card deck. The properties of water were assigned via *MAT (material) and *EOS (equation-of-state) cards. Figure E.4 shows an isometric view of the model. The vessel is shown in grey and the water is shown in blue. Elements of the void space are not shown. The sizes of the elements as shown in Figure E.4 were optimized, resulting in smaller elements for the fluid domain adjacent to the vessel wall, above and below the free surface, and along the *x*-direction diameter of the vessel.
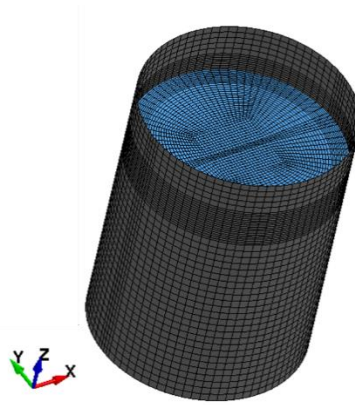
Figure E.4. ALE model in LS-DYNA.

Results of response-history analyses for two rocking inputs (about the *y*-axis, see Figure E.4), identified here as R-1 and R-2, are described first. The inputs are shown in Figure E.5. The analytical solution of Veletsos and Tang, and the additional terms for pressure and moment response proposed above, are valid for small amplitude rotational inputs. The amplitudes of motions R-1 and R-2 were therefore chosen to be small. Motion R-1 is a sinusoid with an amplitude of 0.1 rad/s^2 and a frequency of 1 Hz. Motion R-2 is a rocking motion of amplitude 0.16 rad/s^2 recorded during an earthquake-simulator test at the base of the vessel. The normalized power spectral density plot for R-2, shown in Figure E.5e, shows that the input comprises a wide range of frequencies (0 - 30 Hz). The two inputs correspond to peak horizontal accelerations of 0.02g and 0.03g at the top of the vessel (the height of the vessel is 2 m) and peak base rotations of 0.016 rad (0.92°) and 0.011 rad (0.63°) (see Figure E.5b and Figure E.5d).

The results of analysis of the ALE model are compared with the analytical solution of Veletsos and Tang for base reactions (shear along the *x*-direction and base moment about the *y*-axis), wave height, and pressure at two points (one point each in regions defined by $(-\pi/2) \leq \theta < (\pi/2)$ and $(\pi/2) \leq \theta < (3\pi/2)$). For pressure and base moment, a comparison with the analytical solution considering additional responses per equations (E-7) and (E-9), respectively, is also made. The hydrostatic pressure at $t = 0$ is ignored in all of the pressure histories. The contribution of the rigid vessel wall to base reactions is included in the analytical solutions. A base shear equal to $0.5 m_t L \theta_g''(t)$ and a base moment equal to $0.33 m_t L^2 \theta_g''(t)$, where m_t and L are the mass and height of the vessel wall, respectively, is added to the corresponding hydrodynamic time series, as suggested in Veletsos and Tang (1987). The moment contributed by the weight of the vessel wall due to shifting of the center of gravity ($0.5 m_t g L \theta_g(t)$) in the displaced configuration is also included in the modification to base moment. Figure E.6 presents results for the two inputs considered and Table E.1

237

presents a summary of the differences in the maximum values of the considered responses. Responses obtained using the analytical solution of Veletsos and Tang are referred to as 'Analytical (V+T)' and those obtained using the analytical solution with the proposed modifications as 'Analytical (herein)'.
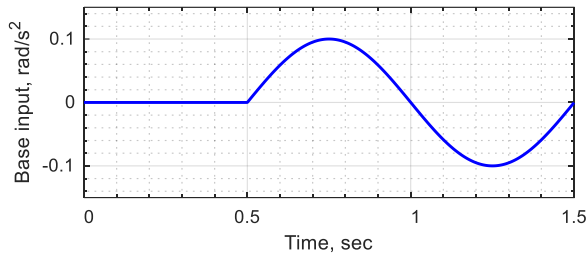
(a) R-1, angular acceleration, peak amplitude = 0.10 rad/s^2
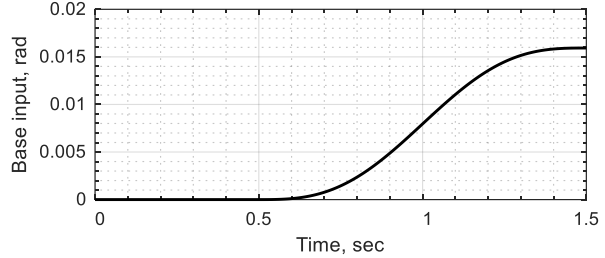
(b) R-1, angular displacement, peak amplitude = 0.016 rad
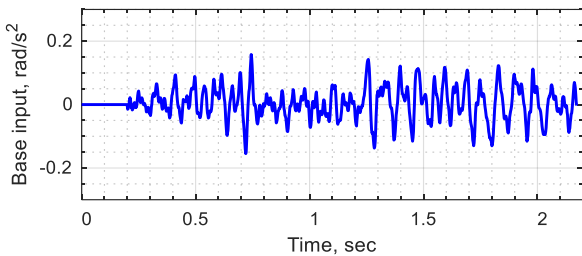
(c) R-2, angular acceleration, peak amplitude = 0.16 rad/s^2
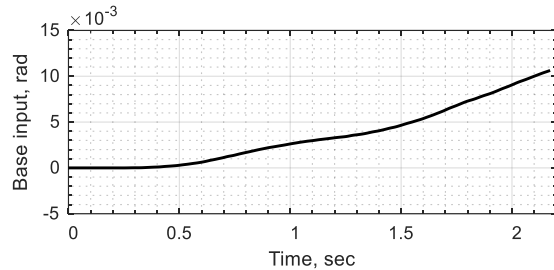
(d) R-2, angular displacement, peak amplitude = 0.011 rad
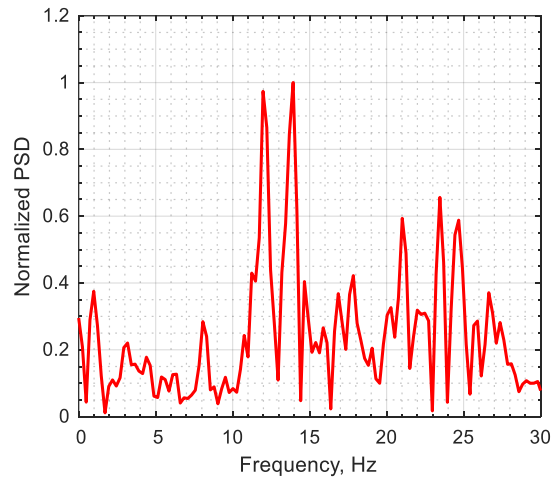
(e) R-2, normalized PSD plot

Figure E.5. Rocking inputs for response-history analyses

238

Input R-1   Input R-2

(a) base shear

(b) wave height at $(r,\theta,z) = (0.62, \pi, 1.62)$; r and z in meters.

(c) pressure at $(r,\theta,z) = (0.62, \pi/6, 0.21)$; r and z in meters.

(d) pressure at $(r,\theta,z) = (0.62, 5\pi/6, 0.21)$; r and z in meters.

(e) base moment
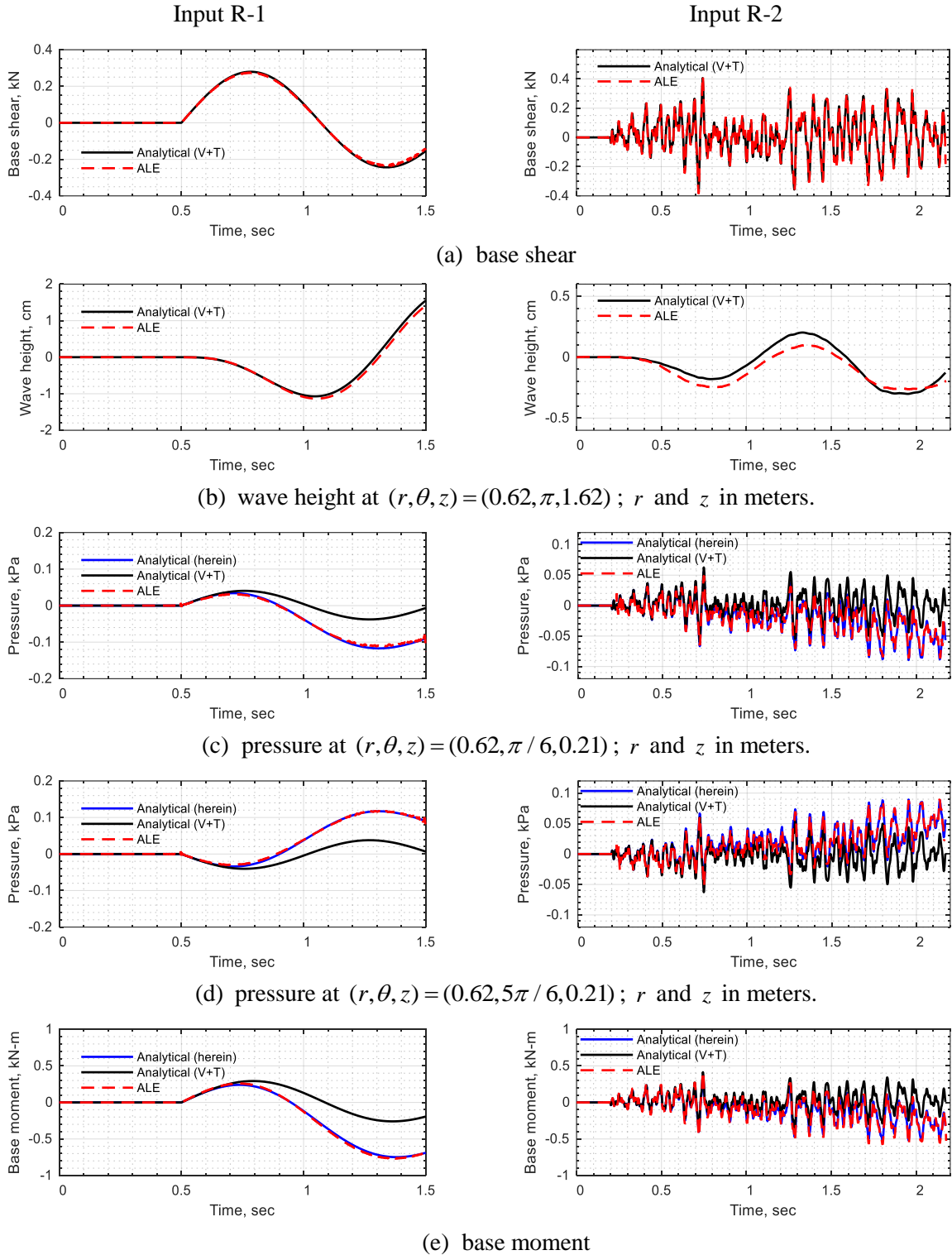
Figure E.6. Comparison of original and modified analytical solution with ALE model

Table E.1. Differences in peak responses with respect to the ALE model

Response quantity (r and z in meters)	R-1		R-2	
	Analytical (V+T)	Analytical (herein)	Analytical (V+T)	Analytical (herein)
Base shear	1%	NA[†]	-3%	NA
Wave height at $(r,\theta,z)=(0.62,\pi,1.62)$	10%	NA	14%	NA
Pressure at $(r,\theta,z)=(0.62,\pi/6,0.21)$	-68%	-2%	-65%	3%
Pressure at $(r,\theta,z)=(0.62,5\pi/6,0.21)$	-66%	-6%	-30%	-1%
Base moment	-62%	-3%	-28%	-9%

[†]Not applicable

The large percentage differences between the ALE predictions and the V+T analytical solutions show clearly that neglecting the contribution of rotational displacement at the base can lead to significant errors in pressure and base moment in certain cases. For the peak values of rotational acceleration and displacement considered here, the maximum contribution (to pressure or base moment) from rotational displacement (per equations (E-7) and (E-9) for pressure and base moment, respectively) is of the same order of magnitude as that of the corresponding maximum value predicted by Veletsos and Tang (1987), considering rotational acceleration only.

The two inputs, R-1 and R-2, are such that the corresponding rotational displacements increase monotonically with time, and they end with residual rotational displacements (see Figure E.5b and Figure E.5d). As a consequence (see equations (E-7) and (E-9)), the pressure and base moment histories from the ALE analysis and the modified analytical solution have non-zero end values (see Figure E.6). The effects of rotational displacement on pressure and base moment are easily visualized for such inputs.[23]

Consider now a 10-second, synthetic rocking acceleration input, R-3, with a zero residual rotational displacement. The acceleration and displacement time series are shown in Figure E.7a and Figure E.7b, respectively. The peak rotational acceleration is 0.07 rad/sec^2 and the peak rotational displacement is 0.0017 rad (0.1°); the peaks occur at 3.9 sec and 4.8 sec, respectively. Response histories (for input R-3) obtained from the ALE model, and the V+T and modified analytical solutions, for pressure and base moment are presented in Figure E.7c and Figure E.7d, respectively. Plots are shown only for the duration of significant

[23] The error introduced in the peak value of pressure (or base moment) by neglecting rotational displacements depends on the amplitude and temporal phasing of *significant* rotational displacements in the time series thereof.

rotational displacement (identified here as 3 sec to 7 sec, as highlighted in Figure E.7b). The difference between the peak values of pressure (base moment) predicted by the existing analytical solution and the ALE model is -20% (-26%). The modified analytical solutions presented herein reduce the differences to less than 1% for both pressure and base moment.
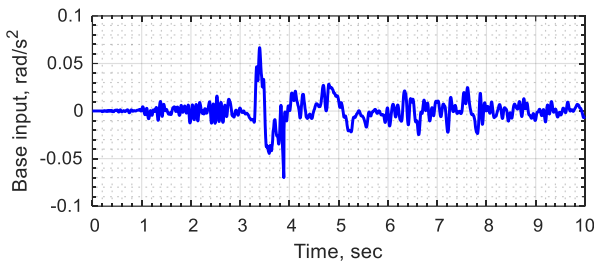
(a) angular acceleration, peak amplitude = 0.07 rad/s^2
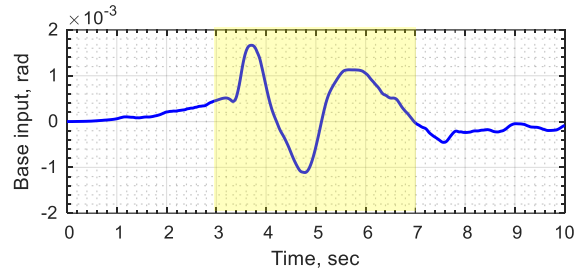
(b) angular displacement, peak amplitude = 0.0017 rad
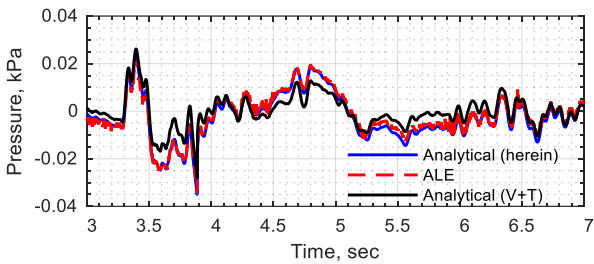
(c) comparison of pressure histories for $(r, \theta, z) = (0.62, \pi / 6, 0.21)$; r and z in meters
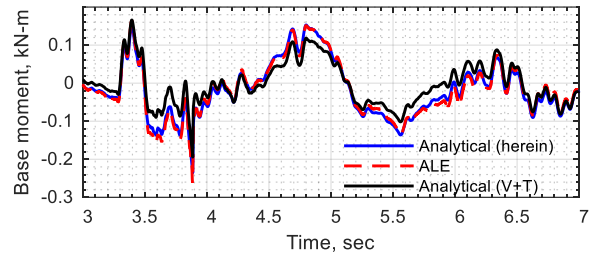
(d) comparison of base moment

Figure E.7. Analysis for rocking input R-3

E.6 Closing remarks

Rotational inputs at the base of a fluid-filled cylindrical vessel affect the hydrodynamic responses (e.g., base reactions, wave height, and pressure). Rocking inputs can result from rotational components of ground motion and/or foundation or support flexibility. The analytical solution of Veletsos and Tang (1987) for evaluating such responses in a fluid-filled rigid cylindrical vessel was examined. Base shear and wave height histories predicted by the Veletsos and Tang solution for two small-amplitude rocking inputs were in close agreement with predictions from analysis of a FE model, as seen in Figure E.6, Figure E.7, and Table E.1. The pressure and base moment histories predicted by the analytical solution do not agree well with the FE predictions because the effects of rotational displacements at the base are not addressed. Modifications are made to the analytical solution to account for these effects per equations ((E-7): pressure)

and ((E-9): base moment), respectively. The revised analytical solutions for hydrodynamic pressure and base moment are in very close agreement with results of finite element analysis.

E.7   References

Basu, D., Whittaker, A. S., and Constantinou, M. C. (2012). "Characterizing the rotational components of earthquake ground motion." *Report MCEER-12-0005*, The State University of New York at Buffalo, Buffalo, NY.

Graizer, V. (2006). "Tilts in strong ground motion." *Bulletin of the Seismological Society of America*, 96(6), 2090-2102.

LSTC. (2017). "LS-DYNA user's manual – Version R 11.0." Livermore Software Technology Corporation, Livermore, CA, USA.

Malhotra, P. K., Wenk, T., and Wieland, M. (2000). "Simple procedure for seismic analysis of liquid-storage tanks." *Structural Engineering International*, 10(3), 197-201.

Trifunac, M. D. (2009). "Review: rotations in structural response." *Bulletin of the Seismological Society of America*, 99(2B), 968-979.

Veletsos, A. S. (1984). "Seismic response and design of liquid storage tanks." *Guidelines for the seismic design of oil and gas pipeline systems*, Committee on Gas and Liquid Fuel Lifelines, American Society of Civil Engineers (ASCE), Reston, VA, 255-370.

Veletsos, A. S., and Tang, Y. (1987). "Rocking response of liquid storage tanks." *Journal of Engineering Mechanics*, 113(11), 1774-1792.

MCEER Technical Reports

MCEER publishes technical reports on a variety of subjects written by authors funded through MCEER. These reports can be downloaded from the MCEER website at http://www.buffalo.edu/mceer. They can also be requested through NTIS, P.O. Box 1425, Springfield, Virginia 22151. NTIS accession numbers are shown in parenthesis, if available.

NCEER-87-0001 "First-Year Program in Research, Education and Technology Transfer," 3/5/87, (PB88-134275, A04, MF-A01).

NCEER-87-0002 "Experimental Evaluation of Instantaneous Optimal Algorithms for Structural Control," by R.C. Lin, T.T. Soong and A.M. Reinhorn, 4/20/87, (PB88-134341, A04, MF-A01).

NCEER-87-0003 "Experimentation Using the Earthquake Simulation Facilities at University at Buffalo," by A.M. Reinhorn and R.L. Ketter, not available.

NCEER-87-0004 "The System Characteristics and Performance of a Shaking Table," by J.S. Hwang, K.C. Chang and G.C. Lee, 6/1/87, (PB88-134259, A03, MF-A01). This report is available only through NTIS (see address given above).

NCEER-87-0005 "A Finite Element Formulation for Nonlinear Viscoplastic Material Using a Q Model," by O. Gyebi and G. Dasgupta, 11/2/87, (PB88-213764, A08, MF-A01).

NCEER-87-0006 "Symbolic Manipulation Program (SMP) - Algebraic Codes for Two and Three Dimensional Finite Element Formulations," by X. Lee and G. Dasgupta, 11/9/87, (PB88-218522, A05, MF-A01).

NCEER-87-0007 "Instantaneous Optimal Control Laws for Tall Buildings Under Seismic Excitations," by J.N. Yang, A. Akbarpour and P. Ghaemmaghami, 6/10/87, (PB88-134333, A06, MF-A01). This report is only available through NTIS (see address given above).

NCEER-87-0008 "IDARC: Inelastic Damage Analysis of Reinforced Concrete Frame - Shear-Wall Structures," by Y.J. Park, A.M. Reinhorn and S.K. Kunnath, 7/20/87, (PB88-134325, A09, MF-A01). This report is only available through NTIS (see address given above).

NCEER-87-0009 "Liquefaction Potential for New York State: A Preliminary Report on Sites in Manhattan and Buffalo," by M. Budhu, V. Vijayakumar, R.F. Giese and L. Baumgras, 8/31/87, (PB88-163704, A03, MF-A01). This report is available only through NTIS (see address given above).

NCEER-87-0010 "Vertical and Torsional Vibration of Foundations in Inhomogeneous Media," by A.S. Veletsos and K.W. Dotson, 6/1/87, (PB88-134291, A03, MF-A01). This report is only available through NTIS (see address given above).

NCEER-87-0011 "Seismic Probabilistic Risk Assessment and Seismic Margins Studies for Nuclear Power Plants," by Howard H.M. Hwang, 6/15/87, (PB88-134267, A03, MF-A01). This report is only available through NTIS (see address given above).

NCEER-87-0012 "Parametric Studies of Frequency Response of Secondary Systems Under Ground-Acceleration Excitations," by Y. Yong and Y.K. Lin, 6/10/87, (PB88-134309, A03, MF-A01). This report is only available through NTIS (see address given above).

NCEER-87-0013 "Frequency Response of Secondary Systems Under Seismic Excitation," by J.A. HoLung, J. Cai and Y.K. Lin, 7/31/87, (PB88-134317, A05, MF-A01). This report is only available through NTIS (see address given above).

NCEER-87-0014 "Modelling Earthquake Ground Motions in Seismically Active Regions Using Parametric Time Series Methods," by G.W. Ellis and A.S. Cakmak, 8/25/87, (PB88-134283, A08, MF-A01). This report is only available through NTIS (see address given above).

NCEER-87-0015 "Detection and Assessment of Seismic Structural Damage," by E. DiPasquale and A.S. Cakmak, 8/25/87, (PB88-163712, A05, MF-A01). This report is only available through NTIS (see address given above).

NCEER-87-0016   "Pipeline Experiment at Parkfield, California," by J. Isenberg and E. Richardson, 9/15/87, (PB88-163720, A03, MF-A01). This report is available only through NTIS (see address given above).

NCEER-87-0017   "Digital Simulation of Seismic Ground Motion," by M. Shinozuka, G. Deodatis and T. Harada, 8/31/87, (PB88-155197, A04, MF-A01). This report is available only through NTIS (see address given above).

NCEER-87-0018   "Practical Considerations for Structural Control: System Uncertainty, System Time Delay and Truncation of Small Control Forces," J.N. Yang and A. Akbarpour, 8/10/87, (PB88-163738, A08, MF-A01). This report is only available through NTIS (see address given above).

NCEER-87-0019   "Modal Analysis of Nonclassically Damped Structural Systems Using Canonical Transformation," by J.N. Yang, S. Sarkani and F.X. Long, 9/27/87, (PB88-187851, A04, MF-A01).

NCEER-87-0020   "A Nonstationary Solution in Random Vibration Theory," by J.R. Red-Horse and P.D. Spanos, 11/3/87, (PB88-163746, A03, MF-A01).

NCEER-87-0021   "Horizontal Impedances for Radially Inhomogeneous Viscoelastic Soil Layers," by A.S. Veletsos and K.W. Dotson, 10/15/87, (PB88-150859, A04, MF-A01).

NCEER-87-0022   "Seismic Damage Assessment of Reinforced Concrete Members," by Y.S. Chung, C. Meyer and M. Shinozuka, 10/9/87, (PB88-150867, A05, MF-A01). This report is available only through NTIS (see address given above).

NCEER-87-0023   "Active Structural Control in Civil Engineering," by T.T. Soong, 11/11/87, (PB88-187778, A03, MF-A01).

NCEER-87-0024   "Vertical and Torsional Impedances for Radially Inhomogeneous Viscoelastic Soil Layers," by K.W. Dotson and A.S. Veletsos, 12/87, (PB88-187786, A03, MF-A01).

NCEER-87-0025   "Proceedings from the Symposium on Seismic Hazards, Ground Motions, Soil-Liquefaction and Engineering Practice in Eastern North America," October 20-22, 1987, edited by K.H. Jacob, 12/87, (PB88-188115, A23, MF-A01). This report is available only through NTIS (see address given above).

NCEER-87-0026   "Report on the Whittier-Narrows, California, Earthquake of October 1, 1987," by J. Pantelic and A. Reinhorn, 11/87, (PB88-187752, A03, MF-A01). This report is available only through NTIS (see address given above).

NCEER-87-0027   "Design of a Modular Program for Transient Nonlinear Analysis of Large 3-D Building Structures," by S. Srivastav and J.F. Abel, 12/30/87, (PB88-187950, A05, MF-A01). This report is only available through NTIS (see address given above).

NCEER-87-0028   "Second-Year Program in Research, Education and Technology Transfer," 3/8/88, (PB88-219480, A04, MF-A01).

NCEER-88-0001   "Workshop on Seismic Computer Analysis and Design of Buildings With Interactive Graphics," by W. McGuire, J.F. Abel and C.H. Conley, 1/18/88, (PB88-187760, A03, MF-A01). This report is only available through NTIS (see address given above).

NCEER-88-0002   "Optimal Control of Nonlinear Flexible Structures," by J.N. Yang, F.X. Long and D. Wong, 1/22/88, (PB88-213772, A06, MF-A01).

NCEER-88-0003   "Substructuring Techniques in the Time Domain for Primary-Secondary Structural Systems," by G.D. Manolis and G. Juhn, 2/10/88, (PB88-213780, A04, MF-A01).

NCEER-88-0004   "Iterative Seismic Analysis of Primary-Secondary Systems," by A. Singhal, L.D. Lutes and P.D. Spanos, 2/23/88, (PB88-213798, A04, MF-A01).

NCEER-88-0005   "Stochastic Finite Element Expansion for Random Media," by P.D. Spanos and R. Ghanem, 3/14/88, (PB88-213806, A03, MF-A01).

NCEER-88-0006   "Combining Structural Optimization and Structural Control," by F.Y. Cheng and C.P. Pantelides, 1/10/88, (PB88-213814, A05, MF-A01).

NCEER-88-0007 "Seismic Performance Assessment of Code-Designed Structures," by H.H-M. Hwang, J-W. Jaw and H-J. Shau, 3/20/88, (PB88-219423, A04, MF-A01). This report is only available through NTIS (see address given above).

NCEER-88-0008 "Reliability Analysis of Code-Designed Structures Under Natural Hazards," by H.H-M. Hwang, H. Ushiba and M. Shinozuka, 2/29/88, (PB88-229471, A07, MF-A01). This report is only available through NTIS (see address given above).

NCEER-88-0009 "Seismic Fragility Analysis of Shear Wall Structures," by J-W Jaw and H.H-M. Hwang, 4/30/88, (PB89-102867, A04, MF-A01).

NCEER-88-0010 "Base Isolation of a Multi-Story Building Under a Harmonic Ground Motion - A Comparison of Performances of Various Systems," by F-G Fan, G. Ahmadi and I.G. Tadjbakhsh, 5/18/88, (PB89-122238, A06, MF-A01). This report is only available through NTIS (see address given above).

NCEER-88-0011 "Seismic Floor Response Spectra for a Combined System by Green's Functions," by F.M. Lavelle, L.A. Bergman and P.D. Spanos, 5/1/88, (PB89-102875, A03, MF-A01).

NCEER-88-0012 "A New Solution Technique for Randomly Excited Hysteretic Structures," by G.Q. Cai and Y.K. Lin, 5/16/88, (PB89-102883, A03, MF-A01).

NCEER-88-0013 "A Study of Radiation Damping and Soil-Structure Interaction Effects in the Centrifuge," by K. Weissman, supervised by J.H. Prevost, 5/24/88, (PB89-144703, A06, MF-A01).

NCEER-88-0014 "Parameter Identification and Implementation of a Kinematic Plasticity Model for Frictional Soils," by J.H. Prevost and D.V. Griffiths, not available.

NCEER-88-0015 "Two- and Three- Dimensional Dynamic Finite Element Analyses of the Long Valley Dam," by D.V. Griffiths and J.H. Prevost, 6/17/88, (PB89-144711, A04, MF-A01).

NCEER-88-0016 "Damage Assessment of Reinforced Concrete Structures in Eastern United States," by A.M. Reinhorn, M.J. Seidel, S.K. Kunnath and Y.J. Park, 6/15/88, (PB89-122220, A04, MF-A01). This report is only available through NTIS (see address given above).

NCEER-88-0017 "Dynamic Compliance of Vertically Loaded Strip Foundations in Multilayered Viscoelastic Soils," by S. Ahmad and A.S.M. Israil, 6/17/88, (PB89-102891, A04, MF-A01).

NCEER-88-0018 "An Experimental Study of Seismic Structural Response With Added Viscoelastic Dampers," by R.C. Lin, Z. Liang, T.T. Soong and R.H. Zhang, 6/30/88, (PB89-122212, A05, MF-A01). This report is available only through NTIS (see address given above).

NCEER-88-0019 "Experimental Investigation of Primary - Secondary System Interaction," by G.D. Manolis, G. Juhn and A.M. Reinhorn, 5/27/88, (PB89-122204, A04, MF-A01).

NCEER-88-0020 "A Response Spectrum Approach For Analysis of Nonclassically Damped Structures," by J.N. Yang, S. Sarkani and F.X. Long, 4/22/88, (PB89-102909, A04, MF-A01).

NCEER-88-0021 "Seismic Interaction of Structures and Soils: Stochastic Approach," by A.S. Veletsos and A.M. Prasad, 7/21/88, (PB89-122196, A04, MF-A01). This report is only available through NTIS (see address given above).

NCEER-88-0022 "Identification of the Serviceability Limit State and Detection of Seismic Structural Damage," by E. DiPasquale and A.S. Cakmak, 6/15/88, (PB89-122188, A05, MF-A01). This report is available only through NTIS (see address given above).

NCEER-88-0023 "Multi-Hazard Risk Analysis: Case of a Simple Offshore Structure," by B.K. Bhartia and E.H. Vanmarcke, 7/21/88, (PB89-145213, A05, MF-A01).

NCEER-88-0024   "Automated Seismic Design of Reinforced Concrete Buildings," by Y.S. Chung, C. Meyer and M. Shinozuka, 7/5/88, (PB89-122170, A06, MF-A01). This report is available only through NTIS (see address given above).

NCEER-88-0025   "Experimental Study of Active Control of MDOF Structures Under Seismic Excitations," by L.L. Chung, R.C. Lin, T.T. Soong and A.M. Reinhorn, 7/10/88, (PB89-122600, A04, MF-A01).

NCEER-88-0026   "Earthquake Simulation Tests of a Low-Rise Metal Structure," by J.S. Hwang, K.C. Chang, G.C. Lee and R.L. Ketter, 8/1/88, (PB89-102917, A04, MF-A01).

NCEER-88-0027   "Systems Study of Urban Response and Reconstruction Due to Catastrophic Earthquakes," by F. Kozin and H.K. Zhou, 9/22/88, (PB90-162348, A04, MF-A01).

NCEER-88-0028   "Seismic Fragility Analysis of Plane Frame Structures," by H.H-M. Hwang and Y.K. Low, 7/31/88, (PB89-131445, A06, MF-A01).

NCEER-88-0029   "Response Analysis of Stochastic Structures," by A. Kardara, C. Bucher and M. Shinozuka, 9/22/88, (PB89-174429, A04, MF-A01).

NCEER-88-0030   "Nonnormal Accelerations Due to Yielding in a Primary Structure," by D.C.K. Chen and L.D. Lutes, 9/19/88, (PB89-131437, A04, MF-A01).

NCEER-88-0031   "Design Approaches for Soil-Structure Interaction," by A.S. Veletsos, A.M. Prasad and Y. Tang, 12/30/88, (PB89-174437, A03, MF-A01). This report is available only through NTIS (see address given above).

NCEER-88-0032   "A Re-evaluation of Design Spectra for Seismic Damage Control," by C.J. Turkstra and A.G. Tallin, 11/7/88, (PB89-145221, A05, MF-A01).

NCEER-88-0033   "The Behavior and Design of Noncontact Lap Splices Subjected to Repeated Inelastic Tensile Loading," by V.E. Sagan, P. Gergely and R.N. White, 12/8/88, (PB89-163737, A08, MF-A01).

NCEER-88-0034   "Seismic Response of Pile Foundations," by S.M. Mamoon, P.K. Banerjee and S. Ahmad, 11/1/88, (PB89-145239, A04, MF-A01).

NCEER-88-0035   "Modeling of R/C Building Structures With Flexible Floor Diaphragms (IDARC2)," by A.M. Reinhorn, S.K. Kunnath and N. Panahshahi, 9/7/88, (PB89-207153, A07, MF-A01).

NCEER-88-0036   "Solution of the Dam-Reservoir Interaction Problem Using a Combination of FEM, BEM with Particular Integrals, Modal Analysis, and Substructuring," by C-S. Tsai, G.C. Lee and R.L. Ketter, 12/31/88, (PB89-207146, A04, MF-A01).

NCEER-88-0037   "Optimal Placement of Actuators for Structural Control," by F.Y. Cheng and C.P. Pantelides, 8/15/88, (PB89-162846, A05, MF-A01).

NCEER-88-0038   "Teflon Bearings in Aseismic Base Isolation: Experimental Studies and Mathematical Modeling," by A. Mokha, M.C. Constantinou and A.M. Reinhorn, 12/5/88, (PB89-218457, A10, MF-A01). This report is available only through NTIS (see address given above).

NCEER-88-0039   "Seismic Behavior of Flat Slab High-Rise Buildings in the New York City Area," by P. Weidlinger and M. Ettouney, 10/15/88, (PB90-145681, A04, MF-A01).

NCEER-88-0040   "Evaluation of the Earthquake Resistance of Existing Buildings in New York City," by P. Weidlinger and M. Ettouney, 10/15/88, not available.

NCEER-88-0041   "Small-Scale Modeling Techniques for Reinforced Concrete Structures Subjected to Seismic Loads," by W. Kim, A. El-Attar and R.N. White, 11/22/88, (PB89-189625, A05, MF-A01).

NCEER-88-0042   "Modeling Strong Ground Motion from Multiple Event Earthquakes," by G.W. Ellis and A.S. Cakmak, 10/15/88, (PB89-174445, A03, MF-A01).

NCEER-88-0043   "Nonstationary Models of Seismic Ground Acceleration," by M. Grigoriu, S.E. Ruiz and E. Rosenblueth, 7/15/88, (PB89-189617, A04, MF-A01).

NCEER-88-0044   "SARCF User's Guide: Seismic Analysis of Reinforced Concrete Frames," by Y.S. Chung, C. Meyer and M. Shinozuka, 11/9/88, (PB89-174452, A08, MF-A01).

NCEER-88-0045   "First Expert Panel Meeting on Disaster Research and Planning," edited by J. Pantelic and J. Stoyle, 9/15/88, (PB89-174460, A05, MF-A01).

NCEER-88-0046   "Preliminary Studies of the Effect of Degrading Infill Walls on the Nonlinear Seismic Response of Steel Frames," by C.Z. Chrysostomou, P. Gergely and J.F. Abel, 12/19/88, (PB89-208383, A05, MF-A01).

NCEER-88-0047   "Reinforced Concrete Frame Component Testing Facility - Design, Construction, Instrumentation and Operation," by S.P. Pessiki, C. Conley, T. Bond, P. Gergely and R.N. White, 12/16/88, (PB89-174478, A04, MF-A01).

NCEER-89-0001   "Effects of Protective Cushion and Soil Compliancy on the Response of Equipment Within a Seismically Excited Building," by J.A. HoLung, 2/16/89, (PB89-207179, A04, MF-A01).

NCEER-89-0002   "Statistical Evaluation of Response Modification Factors for Reinforced Concrete Structures," by H.H-M. Hwang and J-W. Jaw, 2/17/89, (PB89-207187, A05, MF-A01).

NCEER-89-0003   "Hysteretic Columns Under Random Excitation," by G-Q. Cai and Y.K. Lin, 1/9/89, (PB89-196513, A03, MF-A01).

NCEER-89-0004   "Experimental Study of `Elephant Foot Bulge' Instability of Thin-Walled Metal Tanks," by Z-H. Jia and R.L. Ketter, 2/22/89, (PB89-207195, A03, MF-A01).

NCEER-89-0005   "Experiment on Performance of Buried Pipelines Across San Andreas Fault," by J. Isenberg, E. Richardson and T.D. O'Rourke, 3/10/89, (PB89-218440, A04, MF-A01). This report is available only through NTIS (see address given above).

NCEER-89-0006   "A Knowledge-Based Approach to Structural Design of Earthquake-Resistant Buildings," by M. Subramani, P. Gergely, C.H. Conley, J.F. Abel and A.H. Zaghw, 1/15/89, (PB89-218465, A06, MF-A01).

NCEER-89-0007   "Liquefaction Hazards and Their Effects on Buried Pipelines," by T.D. O'Rourke and P.A. Lane, 2/1/89, (PB89-218481, A09, MF-A01).

NCEER-89-0008   "Fundamentals of System Identification in Structural Dynamics," by H. Imai, C-B. Yun, O. Maruyama and M. Shinozuka, 1/26/89, (PB89-207211, A04, MF-A01).

NCEER-89-0009   "Effects of the 1985 Michoacan Earthquake on Water Systems and Other Buried Lifelines in Mexico," by A.G. Ayala and M.J. O'Rourke, 3/8/89, (PB89-207229, A06, MF-A01).

NCEER-89-R010   "NCEER Bibliography of Earthquake Education Materials," by K.E.K. Ross, Second Revision, 9/1/89, (PB90-125352, A05, MF-A01). This report is replaced by NCEER-92-0018.

NCEER-89-0011   "Inelastic Three-Dimensional Response Analysis of Reinforced Concrete Building Structures (IDARC-3D), Part I - Modeling," by S.K. Kunnath and A.M. Reinhorn, 4/17/89, (PB90-114612, A07, MF-A01). This report is available only through NTIS (see address given above).

NCEER-89-0012   "Recommended Modifications to ATC-14," by C.D. Poland and J.O. Malley, 4/12/89, (PB90-108648, A15, MF-A01).

NCEER-89-0013   "Repair and Strengthening of Beam-to-Column Connections Subjected to Earthquake Loading," by M. Corazao and A.J. Durrani, 2/28/89, (PB90-109885, A06, MF-A01).

NCEER-89-0014   "Program EXKAL2 for Identification of Structural Dynamic Systems," by O. Maruyama, C-B. Yun, M. Hoshiya and M. Shinozuka, 5/19/89, (PB90-109877, A09, MF-A01).

NCEER-89-0015 "Response of Frames With Bolted Semi-Rigid Connections, Part I - Experimental Study and Analytical Predictions," by P.J. DiCorso, A.M. Reinhorn, J.R. Dickerson, J.B. Radziminski and W.L. Harper, 6/1/89, not available.

NCEER-89-0016 "ARMA Monte Carlo Simulation in Probabilistic Structural Analysis," by P.D. Spanos and M.P. Mignolet, 7/10/89, (PB90-109893, A03, MF-A01).

NCEER-89-P017 "Preliminary Proceedings from the Conference on Disaster Preparedness - The Place of Earthquake Education in Our Schools," Edited by K.E.K. Ross, 6/23/89, (PB90-108606, A03, MF-A01).

NCEER-89-0017 "Proceedings from the Conference on Disaster Preparedness - The Place of Earthquake Education in Our Schools," Edited by K.E.K. Ross, 12/31/89, (PB90-207895, A012, MF-A02). This report is available only through NTIS (see address given above).

NCEER-89-0018 "Multidimensional Models of Hysteretic Material Behavior for Vibration Analysis of Shape Memory Energy Absorbing Devices, by E.J. Graesser and F.A. Cozzarelli, 6/7/89, (PB90-164146, A04, MF-A01).

NCEER-89-0019 "Nonlinear Dynamic Analysis of Three-Dimensional Base Isolated Structures (3D-BASIS)," by S. Nagarajaiah, A.M. Reinhorn and M.C. Constantinou, 8/3/89, (PB90-161936, A06, MF-A01). This report has been replaced by NCEER-93-0011.

NCEER-89-0020 "Structural Control Considering Time-Rate of Control Forces and Control Rate Constraints," by F.Y. Cheng and C.P. Pantelides, 8/3/89, (PB90-120445, A04, MF-A01).

NCEER-89-0021 "Subsurface Conditions of Memphis and Shelby County," by K.W. Ng, T-S. Chang and H-H.M. Hwang, 7/26/89, (PB90-120437, A03, MF-A01).

NCEER-89-0022 "Seismic Wave Propagation Effects on Straight Jointed Buried Pipelines," by K. Elhmadi and M.J. O'Rourke, 8/24/89, (PB90-162322, A10, MF-A02).

NCEER-89-0023 "Workshop on Serviceability Analysis of Water Delivery Systems," edited by M. Grigoriu, 3/6/89, (PB90-127424, A03, MF-A01).

NCEER-89-0024 "Shaking Table Study of a 1/5 Scale Steel Frame Composed of Tapered Members," by K.C. Chang, J.S. Hwang and G.C. Lee, 9/18/89, (PB90-160169, A04, MF-A01).

NCEER-89-0025 "DYNA1D: A Computer Program for Nonlinear Seismic Site Response Analysis - Technical Documentation," by Jean H. Prevost, 9/14/89, (PB90-161944, A07, MF-A01). This report is available only through NTIS (see address given above).

NCEER-89-0026 "1:4 Scale Model Studies of Active Tendon Systems and Active Mass Dampers for Aseismic Protection," by A.M. Reinhorn, T.T. Soong, R.C. Lin, Y.P. Yang, Y. Fukao, H. Abe and M. Nakai, 9/15/89, (PB90-173246, A10, MF-A02). This report is available only through NTIS (see address given above).

NCEER-89-0027 "Scattering of Waves by Inclusions in a Nonhomogeneous Elastic Half Space Solved by Boundary Element Methods," by P.K. Hadley, A. Askar and A.S. Cakmak, 6/15/89, (PB90-145699, A07, MF-A01).

NCEER-89-0028 "Statistical Evaluation of Deflection Amplification Factors for Reinforced Concrete Structures," by H.H.M. Hwang, J-W. Jaw and A.L. Ch'ng, 8/31/89, (PB90-164633, A05, MF-A01).

NCEER-89-0029 "Bedrock Accelerations in Memphis Area Due to Large New Madrid Earthquakes," by H.H.M. Hwang, C.H.S. Chen and G. Yu, 11/7/89, (PB90-162330, A04, MF-A01).

NCEER-89-0030 "Seismic Behavior and Response Sensitivity of Secondary Structural Systems," by Y.Q. Chen and T.T. Soong, 10/23/89, (PB90-164658, A08, MF-A01).

NCEER-89-0031 "Random Vibration and Reliability Analysis of Primary-Secondary Structural Systems," by Y. Ibrahim, M. Grigoriu and T.T. Soong, 11/10/89, (PB90-161951, A04, MF-A01).

NCEER-89-0032   "Proceedings from the Second U.S. - Japan Workshop on Liquefaction, Large Ground Deformation and Their Effects on Lifelines, September 26-29, 1989," Edited by T.D. O'Rourke and M. Hamada, 12/1/89, (PB90-209388, A22, MF-A03).

NCEER-89-0033   "Deterministic Model for Seismic Damage Evaluation of Reinforced Concrete Structures," by J.M. Bracci, A.M. Reinhorn, J.B. Mander and S.K. Kunnath, 9/27/89, (PB91-108803, A06, MF-A01).

NCEER-89-0034   "On the Relation Between Local and Global Damage Indices," by E. DiPasquale and A.S. Cakmak, 8/15/89, (PB90-173865, A05, MF-A01).

NCEER-89-0035   "Cyclic Undrained Behavior of Nonplastic and Low Plasticity Silts," by A.J. Walker and H.E. Stewart, 7/26/89, (PB90-183518, A10, MF-A01).

NCEER-89-0036   "Liquefaction Potential of Surficial Deposits in the City of Buffalo, New York," by M. Budhu, R. Giese and L. Baumgrass, 1/17/89, (PB90-208455, A04, MF-A01).

NCEER-89-0037   "A Deterministic Assessment of Effects of Ground Motion Incoherence," by A.S. Veletsos and Y. Tang, 7/15/89, (PB90-164294, A03, MF-A01).

NCEER-89-0038   "Workshop on Ground Motion Parameters for Seismic Hazard Mapping," July 17-18, 1989, edited by R.V. Whitman, 12/1/89, (PB90-173923, A04, MF-A01).

NCEER-89-0039   "Seismic Effects on Elevated Transit Lines of the New York City Transit Authority," by C.J. Costantino, C.A. Miller and E. Heymsfield, 12/26/89, (PB90-207887, A06, MF-A01).

NCEER-89-0040   "Centrifugal Modeling of Dynamic Soil-Structure Interaction," by K. Weissman, Supervised by J.H. Prevost, 5/10/89, (PB90-207879, A07, MF-A01).

NCEER-89-0041   "Linearized Identification of Buildings With Cores for Seismic Vulnerability Assessment," by I-K. Ho and A.E. Aktan, 11/1/89, (PB90-251943, A07, MF-A01).

NCEER-90-0001   "Geotechnical and Lifeline Aspects of the October 17, 1989 Loma Prieta Earthquake in San Francisco," by T.D. O'Rourke, H.E. Stewart, F.T. Blackburn and T.S. Dickerman, 1/90, (PB90-208596, A05, MF-A01).

NCEER-90-0002   "Nonnormal Secondary Response Due to Yielding in a Primary Structure," by D.C.K. Chen and L.D. Lutes, 2/28/90, (PB90-251976, A07, MF-A01).

NCEER-90-0003   "Earthquake Education Materials for Grades K-12," by K.E.K. Ross, 4/16/90, (PB91-251984, A05, MF-A05). This report has been replaced by NCEER-92-0018.

NCEER-90-0004   "Catalog of Strong Motion Stations in Eastern North America," by R.W. Busby, 4/3/90, (PB90-251984, A05, MF-A01).

NCEER-90-0005   "NCEER Strong-Motion Data Base: A User Manual for the GeoBase Release (Version 1.0 for the Sun3)," by P. Friberg and K. Jacob, 3/31/90 (PB90-258062, A04, MF-A01).

NCEER-90-0006   "Seismic Hazard Along a Crude Oil Pipeline in the Event of an 1811-1812 Type New Madrid Earthquake," by H.H.M. Hwang and C-H.S. Chen, 4/16/90, (PB90-258054, A04, MF-A01).

NCEER-90-0007   "Site-Specific Response Spectra for Memphis Sheahan Pumping Station," by H.H.M. Hwang and C.S. Lee, 5/15/90, (PB91-108811, A05, MF-A01).

NCEER-90-0008   "Pilot Study on Seismic Vulnerability of Crude Oil Transmission Systems," by T. Ariman, R. Dobry, M. Grigoriu, F. Kozin, M. O'Rourke, T. O'Rourke and M. Shinozuka, 5/25/90, (PB91-108837, A06, MF-A01).

NCEER-90-0009   "A Program to Generate Site Dependent Time Histories: EQGEN," by G.W. Ellis, M. Srinivasan and A.S. Cakmak, 1/30/90, (PB91-108829, A04, MF-A01).

NCEER-90-0010   "Active Isolation for Seismic Protection of Operating Rooms," by M.E. Talbott, Supervised by M. Shinozuka, 6/8/9, (PB91-110205, A05, MF-A01).

NCEER-90-0011   "Program LINEARID for Identification of Linear Structural Dynamic Systems," by C-B. Yun and M. Shinozuka, 6/25/90, (PB91-110312, A08, MF-A01).

NCEER-90-0012   "Two-Dimensional Two-Phase Elasto-Plastic Seismic Response of Earth Dams," by A.N. Yiagos, Supervised by J.H. Prevost, 6/20/90, (PB91-110197, A13, MF-A02).

NCEER-90-0013   "Secondary Systems in Base-Isolated Structures: Experimental Investigation, Stochastic Response and Stochastic Sensitivity," by G.D. Manolis, G. Juhn, M.C. Constantinou and A.M. Reinhorn, 7/1/90, (PB91-110320, A08, MF-A01).

NCEER-90-0014   "Seismic Behavior of Lightly-Reinforced Concrete Column and Beam-Column Joint Details," by S.P. Pessiki, C.H. Conley, P. Gergely and R.N. White, 8/22/90, (PB91-108795, A11, MF-A02).

NCEER-90-0015   "Two Hybrid Control Systems for Building Structures Under Strong Earthquakes," by J.N. Yang and A. Danielians, 6/29/90, (PB91-125393, A04, MF-A01).

NCEER-90-0016   "Instantaneous Optimal Control with Acceleration and Velocity Feedback," by J.N. Yang and Z. Li, 6/29/90, (PB91-125401, A03, MF-A01).

NCEER-90-0017   "Reconnaissance Report on the Northern Iran Earthquake of June 21, 1990," by M. Mehrain, 10/4/90, (PB91-125377, A03, MF-A01).

NCEER-90-0018   "Evaluation of Liquefaction Potential in Memphis and Shelby County," by T.S. Chang, P.S. Tang, C.S. Lee and H. Hwang, 8/10/90, (PB91-125427, A09, MF-A01).

NCEER-90-0019   "Experimental and Analytical Study of a Combined Sliding Disc Bearing and Helical Steel Spring Isolation System," by M.C. Constantinou, A.S. Mokha and A.M. Reinhorn, 10/4/90, (PB91-125385, A06, MF-A01). This report is available only through NTIS (see address given above).

NCEER-90-0020   "Experimental Study and Analytical Prediction of Earthquake Response of a Sliding Isolation System with a Spherical Surface," by A.S. Mokha, M.C. Constantinou and A.M. Reinhorn, 10/11/90, (PB91-125419, A05, MF-A01).

NCEER-90-0021   "Dynamic Interaction Factors for Floating Pile Groups," by G. Gazetas, K. Fan, A. Kaynia and E. Kausel, 9/10/90, (PB91-170381, A05, MF-A01).

NCEER-90-0022   "Evaluation of Seismic Damage Indices for Reinforced Concrete Structures," by S. Rodriguez-Gomez and A.S. Cakmak, 9/30/90, PB91-171322, A06, MF-A01).

NCEER-90-0023   "Study of Site Response at a Selected Memphis Site," by H. Desai, S. Ahmad, E.S. Gazetas and M.R. Oh, 10/11/90, (PB91-196857, A03, MF-A01).

NCEER-90-0024   "A User's Guide to Strongmo: Version 1.0 of NCEER's Strong-Motion Data Access Tool for PCs and Terminals," by P.A. Friberg and C.A.T. Susch, 11/15/90, (PB91-171272, A03, MF-A01).

NCEER-90-0025   "A Three-Dimensional Analytical Study of Spatial Variability of Seismic Ground Motions," by L-L. Hong and A.H.-S. Ang, 10/30/90, (PB91-170399, A09, MF-A01).

NCEER-90-0026   "MUMOID User's Guide - A Program for the Identification of Modal Parameters," by S. Rodriguez-Gomez and E. DiPasquale, 9/30/90, (PB91-171298, A04, MF-A01).

NCEER-90-0027   "SARCF-II User's Guide - Seismic Analysis of Reinforced Concrete Frames," by S. Rodriguez-Gomez, Y.S. Chung and C. Meyer, 9/30/90, (PB91-171280, A05, MF-A01).

NCEER-90-0028   "Viscous Dampers: Testing, Modeling and Application in Vibration and Seismic Isolation," by N. Makris and M.C. Constantinou, 12/20/90 (PB91-190561, A06, MF-A01).

NCEER-90-0029   "Soil Effects on Earthquake Ground Motions in the Memphis Area," by H. Hwang, C.S. Lee, K.W. Ng and T.S. Chang, 8/2/90, (PB91-190751, A05, MF-A01).

NCEER-91-0001   "Proceedings from the Third Japan-U.S. Workshop on Earthquake Resistant Design of Lifeline Facilities and Countermeasures for Soil Liquefaction, December 17-19, 1990," edited by T.D. O'Rourke and M. Hamada, 2/1/91, (PB91-179259, A99, MF-A04).

NCEER-91-0002   "Physical Space Solutions of Non-Proportionally Damped Systems," by M. Tong, Z. Liang and G.C. Lee, 1/15/91, (PB91-179242, A04, MF-A01).

NCEER-91-0003   "Seismic Response of Single Piles and Pile Groups," by K. Fan and G. Gazetas, 1/10/91, (PB92-174994, A04, MF-A01).

NCEER-91-0004   "Damping of Structures: Part 1 - Theory of Complex Damping," by Z. Liang and G. Lee, 10/10/91, (PB92-197235, A12, MF-A03).

NCEER-91-0005   "3D-BASIS - Nonlinear Dynamic Analysis of Three Dimensional Base Isolated Structures: Part II," by S. Nagarajaiah, A.M. Reinhorn and M.C. Constantinou, 2/28/91, (PB91-190553, A07, MF-A01). This report has been replaced by NCEER-93-0011.

NCEER-91-0006   "A Multidimensional Hysteretic Model for Plasticity Deforming Metals in Energy Absorbing Devices," by E.J. Graesser and F.A. Cozzarelli, 4/9/91, (PB92-108364, A04, MF-A01).

NCEER-91-0007   "A Framework for Customizable Knowledge-Based Expert Systems with an Application to a KBES for Evaluating the Seismic Resistance of Existing Buildings," by E.G. Ibarra-Anaya and S.J. Fenves, 4/9/91, (PB91-210930, A08, MF-A01).

NCEER-91-0008   "Nonlinear Analysis of Steel Frames with Semi-Rigid Connections Using the Capacity Spectrum Method," by G.G. Deierlein, S-H. Hsieh, Y-J. Shen and J.F. Abel, 7/2/91, (PB92-113828, A05, MF-A01).

NCEER-91-0009   "Earthquake Education Materials for Grades K-12," by K.E.K. Ross, 4/30/91, (PB91-212142, A06, MF-A01). This report has been replaced by NCEER-92-0018.

NCEER-91-0010   "Phase Wave Velocities and Displacement Phase Differences in a Harmonically Oscillating Pile," by N. Makris and G. Gazetas, 7/8/91, (PB92-108356, A04, MF-A01).

NCEER-91-0011   "Dynamic Characteristics of a Full-Size Five-Story Steel Structure and a 2/5 Scale Model," by K.C. Chang, G.C. Yao, G.C. Lee, D.S. Hao and Y.C. Yeh," 7/2/91, (PB93-116648, A06, MF-A02).

NCEER-91-0012   "Seismic Response of a 2/5 Scale Steel Structure with Added Viscoelastic Dampers," by K.C. Chang, T.T. Soong, S-T. Oh and M.L. Lai, 5/17/91, (PB92-110816, A05, MF-A01).

NCEER-91-0013   "Earthquake Response of Retaining Walls; Full-Scale Testing and Computational Modeling," by S. Alampalli and A-W.M. Elgamal, 6/20/91, not available.

NCEER-91-0014   "3D-BASIS-M: Nonlinear Dynamic Analysis of Multiple Building Base Isolated Structures," by P.C. Tsopelas, S. Nagarajaiah, M.C. Constantinou and A.M. Reinhorn, 5/28/91, (PB92-113885, A09, MF-A02).

NCEER-91-0015   "Evaluation of SEAOC Design Requirements for Sliding Isolated Structures," by D. Theodossiou and M.C. Constantinou, 6/10/91, (PB92-114602, A11, MF-A03).

NCEER-91-0016   "Closed-Loop Modal Testing of a 27-Story Reinforced Concrete Flat Plate-Core Building," by H.R. Somaprasad, T. Toksoy, H. Yoshiyuki and A.E. Aktan, 7/15/91, (PB92-129980, A07, MF-A02).

NCEER-91-0017   "Shake Table Test of a 1/6 Scale Two-Story Lightly Reinforced Concrete Building," by A.G. El-Attar, R.N. White and P. Gergely, 2/28/91, (PB92-222447, A06, MF-A02).

NCEER-91-0018   "Shake Table Test of a 1/8 Scale Three-Story Lightly Reinforced Concrete Building," by A.G. El-Attar, R.N. White and P. Gergely, 2/28/91, (PB93-116630, A08, MF-A02).

NCEER-91-0019   "Transfer Functions for Rigid Rectangular Foundations," by A.S. Veletsos, A.M. Prasad and W.H. Wu, 7/31/91, not available.

NCEER-91-0020   "Hybrid Control of Seismic-Excited Nonlinear and Inelastic Structural Systems," by J.N. Yang, Z. Li and A. Danielians, 8/1/91, (PB92-143171, A06, MF-A02).

NCEER-91-0021   "The NCEER-91 Earthquake Catalog: Improved Intensity-Based Magnitudes and Recurrence Relations for U.S. Earthquakes East of New Madrid," by L. Seeber and J.G. Armbruster, 8/28/91, (PB92-176742, A06, MF-A02).

NCEER-91-0022   "Proceedings from the Implementation of Earthquake Planning and Education in Schools: The Need for Change - The Roles of the Changemakers," by K.E.K. Ross and F. Winslow, 7/23/91, (PB92-129998, A12, MF-A03).

NCEER-91-0023   "A Study of Reliability-Based Criteria for Seismic Design of Reinforced Concrete Frame Buildings," by H.H.M. Hwang and H-M. Hsu, 8/10/91, (PB92-140235, A09, MF-A02).

NCEER-91-0024   "Experimental Verification of a Number of Structural System Identification Algorithms," by R.G. Ghanem, H. Gavin and M. Shinozuka, 9/18/91, (PB92-176577, A18, MF-A04).

NCEER-91-0025   "Probabilistic Evaluation of Liquefaction Potential," by H.H.M. Hwang and C.S. Lee," 11/25/91, (PB92-143429, A05, MF-A01).

NCEER-91-0026   "Instantaneous Optimal Control for Linear, Nonlinear and Hysteretic Structures - Stable Controllers," by J.N. Yang and Z. Li, 11/15/91, (PB92-163807, A04, MF-A01).

NCEER-91-0027   "Experimental and Theoretical Study of a Sliding Isolation System for Bridges," by M.C. Constantinou, A. Kartoum, A.M. Reinhorn and P. Bradford, 11/15/91, (PB92-176973, A10, MF-A03).

NCEER-92-0001   "Case Studies of Liquefaction and Lifeline Performance During Past Earthquakes, Volume 1: Japanese Case Studies," Edited by M. Hamada and T. O'Rourke, 2/17/92, (PB92-197243, A18, MF-A04).

NCEER-92-0002   "Case Studies of Liquefaction and Lifeline Performance During Past Earthquakes, Volume 2: United States Case Studies," Edited by T. O'Rourke and M. Hamada, 2/17/92, (PB92-197250, A20, MF-A04).

NCEER-92-0003   "Issues in Earthquake Education," Edited by K. Ross, 2/3/92, (PB92-222389, A07, MF-A02).

NCEER-92-0004   "Proceedings from the First U.S. - Japan Workshop on Earthquake Protective Systems for Bridges," Edited by I.G. Buckle, 2/4/92, (PB94-142239, A99, MF-A06).

NCEER-92-0005   "Seismic Ground Motion from a Haskell-Type Source in a Multiple-Layered Half-Space," A.P. Theoharis, G. Deodatis and M. Shinozuka, 1/2/92, not available.

NCEER-92-0006   "Proceedings from the Site Effects Workshop," Edited by R. Whitman, 2/29/92, (PB92-197201, A04, MF-A01).

NCEER-92-0007   "Engineering Evaluation of Permanent Ground Deformations Due to Seismically-Induced Liquefaction," by M.H. Baziar, R. Dobry and A-W.M. Elgamal, 3/24/92, (PB92-222421, A13, MF-A03).

NCEER-92-0008   "A Procedure for the Seismic Evaluation of Buildings in the Central and Eastern United States," by C.D. Poland and J.O. Malley, 4/2/92, (PB92-222439, A20, MF-A04).

NCEER-92-0009   "Experimental and Analytical Study of a Hybrid Isolation System Using Friction Controllable Sliding Bearings," by M.Q. Feng, S. Fujii and M. Shinozuka, 5/15/92, (PB93-150282, A06, MF-A02).

NCEER-92-0010   "Seismic Resistance of Slab-Column Connections in Existing Non-Ductile Flat-Plate Buildings," by A.J. Durrani and Y. Du, 5/18/92, (PB93-116812, A06, MF-A02).

NCEER-92-0011   "The Hysteretic and Dynamic Behavior of Brick Masonry Walls Upgraded by Ferrocement Coatings Under Cyclic Loading and Strong Simulated Ground Motion," by H. Lee and S.P. Prawel, 5/11/92, not available.

NCEER-92-0012   "Study of Wire Rope Systems for Seismic Protection of Equipment in Buildings," by G.F. Demetriades, M.C. Constantinou and A.M. Reinhorn, 5/20/92, (PB93-116655, A08, MF-A02).

NCEER-92-0013   "Shape Memory Structural Dampers: Material Properties, Design and Seismic Testing," by P.R. Witting and F.A. Cozzarelli, 5/26/92, (PB93-116663, A05, MF-A01).

NCEER-92-0014   "Longitudinal Permanent Ground Deformation Effects on Buried Continuous Pipelines," by M.J. O'Rourke, and C. Nordberg, 6/15/92, (PB93-116671, A08, MF-A02).

NCEER-92-0015   "A Simulation Method for Stationary Gaussian Random Functions Based on the Sampling Theorem," by M. Grigoriu and S. Balopoulou, 6/11/92, (PB93-127496, A05, MF-A01).

NCEER-92-0016   "Gravity-Load-Designed Reinforced Concrete Buildings: Seismic Evaluation of Existing Construction and Detailing Strategies for Improved Seismic Resistance," by G.W. Hoffmann, S.K. Kunnath, A.M. Reinhorn and J.B. Mander, 7/15/92, (PB94-142007, A08, MF-A02).

NCEER-92-0017   "Observations on Water System and Pipeline Performance in the Limón Area of Costa Rica Due to the April 22, 1991 Earthquake," by M. O'Rourke and D. Ballantyne, 6/30/92, (PB93-126811, A06, MF-A02).

NCEER-92-0018   "Fourth Edition of Earthquake Education Materials for Grades K-12," Edited by K.E.K. Ross, 8/10/92, (PB93-114023, A07, MF-A02).

NCEER-92-0019   "Proceedings from the Fourth Japan-U.S. Workshop on Earthquake Resistant Design of Lifeline Facilities and Countermeasures for Soil Liquefaction," Edited by M. Hamada and T.D. O'Rourke, 8/12/92, (PB93-163939, A99, MF-E11).

NCEER-92-0020   "Active Bracing System: A Full Scale Implementation of Active Control," by A.M. Reinhorn, T.T. Soong, R.C. Lin, M.A. Riley, Y.P. Wang, S. Aizawa and M. Higashino, 8/14/92, (PB93-127512, A06, MF-A02).

NCEER-92-0021   "Empirical Analysis of Horizontal Ground Displacement Generated by Liquefaction-Induced Lateral Spreads," by S.F. Bartlett and T.L. Youd, 8/17/92, (PB93-188241, A06, MF-A02).

NCEER-92-0022   "IDARC Version 3.0: Inelastic Damage Analysis of Reinforced Concrete Structures," by S.K. Kunnath, A.M. Reinhorn and R.F. Lobo, 8/31/92, (PB93-227502, A07, MF-A02).

NCEER-92-0023   "A Semi-Empirical Analysis of Strong-Motion Peaks in Terms of Seismic Source, Propagation Path and Local Site Conditions, by M. Kamiyama, M.J. O'Rourke and R. Flores-Berrones, 9/9/92, (PB93-150266, A08, MF-A02).

NCEER-92-0024   "Seismic Behavior of Reinforced Concrete Frame Structures with Nonductile Details, Part I: Summary of Experimental Findings of Full Scale Beam-Column Joint Tests," by A. Beres, R.N. White and P. Gergely, 9/30/92, (PB93-227783, A05, MF-A01).

NCEER-92-0025   "Experimental Results of Repaired and Retrofitted Beam-Column Joint Tests in Lightly Reinforced Concrete Frame Buildings," by A. Beres, S. El-Borgi, R.N. White and P. Gergely, 10/29/92, (PB93-227791, A05, MF-A01).

NCEER-92-0026   "A Generalization of Optimal Control Theory: Linear and Nonlinear Structures," by J.N. Yang, Z. Li and S. Vongchavalitkul, 11/2/92, (PB93-188621, A05, MF-A01).

NCEER-92-0027   "Seismic Resistance of Reinforced Concrete Frame Structures Designed Only for Gravity Loads: Part I - Design and Properties of a One-Third Scale Model Structure," by J.M. Bracci, A.M. Reinhorn and J.B. Mander, 12/1/92, (PB94-104502, A08, MF-A02).

NCEER-92-0028   "Seismic Resistance of Reinforced Concrete Frame Structures Designed Only for Gravity Loads: Part II - Experimental Performance of Subassemblages," by L.E. Aycardi, J.B. Mander and A.M. Reinhorn, 12/1/92, (PB94-104510, A08, MF-A02).

NCEER-92-0029   "Seismic Resistance of Reinforced Concrete Frame Structures Designed Only for Gravity Loads: Part III - Experimental Performance and Analytical Study of a Structural Model," by J.M. Bracci, A.M. Reinhorn and J.B. Mander, 12/1/92, (PB93-227528, A09, MF-A01).

NCEER-92-0030 "Evaluation of Seismic Retrofit of Reinforced Concrete Frame Structures: Part I - Experimental Performance of Retrofitted Subassemblages," by D. Choudhuri, J.B. Mander and A.M. Reinhorn, 12/8/92, (PB93-198307, A07, MF-A02).

NCEER-92-0031 "Evaluation of Seismic Retrofit of Reinforced Concrete Frame Structures: Part II - Experimental Performance and Analytical Study of a Retrofitted Structural Model," by J.M. Bracci, A.M. Reinhorn and J.B. Mander, 12/8/92, (PB93-198315, A09, MF-A03).

NCEER-92-0032 "Experimental and Analytical Investigation of Seismic Response of Structures with Supplemental Fluid Viscous Dampers," by M.C. Constantinou and M.D. Symans, 12/21/92, (PB93-191435, A10, MF-A03). This report is available only through NTIS (see address given above).

NCEER-92-0033 "Reconnaissance Report on the Cairo, Egypt Earthquake of October 12, 1992," by M. Khater, 12/23/92, (PB93-188621, A03, MF-A01).

NCEER-92-0034 "Low-Level Dynamic Characteristics of Four Tall Flat-Plate Buildings in New York City," by H. Gavin, S. Yuan, J. Grossman, E. Pekelis and K. Jacob, 12/28/92, (PB93-188217, A07, MF-A02).

NCEER-93-0001 "An Experimental Study on the Seismic Performance of Brick-Infilled Steel Frames With and Without Retrofit," by J.B. Mander, B. Nair, K. Wojtkowski and J. Ma, 1/29/93, (PB93-227510, A07, MF-A02).

NCEER-93-0002 "Social Accounting for Disaster Preparedness and Recovery Planning," by S. Cole, E. Pantoja and V. Razak, 2/22/93, (PB94-142114, A12, MF-A03).

NCEER-93-0003 "Assessment of 1991 NEHRP Provisions for Nonstructural Components and Recommended Revisions," by T.T. Soong, G. Chen, Z. Wu, R-H. Zhang and M. Grigoriu, 3/1/93, (PB93-188639, A06, MF-A02).

NCEER-93-0004 "Evaluation of Static and Response Spectrum Analysis Procedures of SEAOC/UBC for Seismic Isolated Structures," by C.W. Winters and M.C. Constantinou, 3/23/93, (PB93-198299, A10, MF-A03).

NCEER-93-0005 "Earthquakes in the Northeast - Are We Ignoring the Hazard? A Workshop on Earthquake Science and Safety for Educators," edited by K.E.K. Ross, 4/2/93, (PB94-103066, A09, MF-A02).

NCEER-93-0006 "Inelastic Response of Reinforced Concrete Structures with Viscoelastic Braces," by R.F. Lobo, J.M. Bracci, K.L. Shen, A.M. Reinhorn and T.T. Soong, 4/5/93, (PB93-227486, A05, MF-A02).

NCEER-93-0007 "Seismic Testing of Installation Methods for Computers and Data Processing Equipment," by K. Kosar, T.T. Soong, K.L. Shen, J.A. HoLung and Y.K. Lin, 4/12/93, (PB93-198299, A07, MF-A02).

NCEER-93-0008 "Retrofit of Reinforced Concrete Frames Using Added Dampers," by A. Reinhorn, M. Constantinou and C. Li, not available.

NCEER-93-0009 "Seismic Behavior and Design Guidelines for Steel Frame Structures with Added Viscoelastic Dampers," by K.C. Chang, M.L. Lai, T.T. Soong, D.S. Hao and Y.C. Yeh, 5/1/93, (PB94-141959, A07, MF-A02).

NCEER-93-0010 "Seismic Performance of Shear-Critical Reinforced Concrete Bridge Piers," by J.B. Mander, S.M. Waheed, M.T.A. Chaudhary and S.S. Chen, 5/12/93, (PB93-227494, A08, MF-A02).

NCEER-93-0011 "3D-BASIS-TABS: Computer Program for Nonlinear Dynamic Analysis of Three Dimensional Base Isolated Structures," by S. Nagarajaiah, C. Li, A.M. Reinhorn and M.C. Constantinou, 8/2/93, (PB94-141819, A09, MF-A02).

NCEER-93-0012 "Effects of Hydrocarbon Spills from an Oil Pipeline Break on Ground Water," by O.J. Helweg and H.H.M. Hwang, 8/3/93, (PB94-141942, A06, MF-A02).

NCEER-93-0013 "Simplified Procedures for Seismic Design of Nonstructural Components and Assessment of Current Code Provisions," by M.P. Singh, L.E. Suarez, E.E. Matheu and G.O. Maldonado, 8/4/93, (PB94-141827, A09, MF-A02).

NCEER-93-0014 "An Energy Approach to Seismic Analysis and Design of Secondary Systems," by G. Chen and T.T. Soong, 8/6/93, (PB94-142767, A11, MF-A03).

NCEER-93-0015   "Proceedings from School Sites: Becoming Prepared for Earthquakes - Commemorating the Third Anniversary of the Loma Prieta Earthquake," Edited by F.E. Winslow and K.E.K. Ross, 8/16/93, (PB94-154275, A16, MF-A02).

NCEER-93-0016   "Reconnaissance Report of Damage to Historic Monuments in Cairo, Egypt Following the October 12, 1992 Dahshur Earthquake," by D. Sykora, D. Look, G. Croci, E. Karaesmen and E. Karaesmen, 8/19/93, (PB94-142221, A08, MF-A02).

NCEER-93-0017   "The Island of Guam Earthquake of August 8, 1993," by S.W. Swan and S.K. Harris, 9/30/93, (PB94-141843, A04, MF-A01).

NCEER-93-0018   "Engineering Aspects of the October 12, 1992 Egyptian Earthquake," by A.W. Elgamal, M. Amer, K. Adalier and A. Abul-Fadl, 10/7/93, (PB94-141983, A05, MF-A01).

NCEER-93-0019   "Development of an Earthquake Motion Simulator and its Application in Dynamic Centrifuge Testing," by I. Krstelj, Supervised by J.H. Prevost, 10/23/93, (PB94-181773, A-10, MF-A03).

NCEER-93-0020   "NCEER-Taisei Corporation Research Program on Sliding Seismic Isolation Systems for Bridges: Experimental and Analytical Study of a Friction Pendulum System (FPS)," by M.C. Constantinou, P. Tsopelas, Y-S. Kim and S. Okamoto, 11/1/93, (PB94-142775, A08, MF-A02).

NCEER-93-0021   "Finite Element Modeling of Elastomeric Seismic Isolation Bearings," by L.J. Billings, Supervised by R. Shepherd, 11/8/93, not available.

NCEER-93-0022   "Seismic Vulnerability of Equipment in Critical Facilities: Life-Safety and Operational Consequences," by K. Porter, G.S. Johnson, M.M. Zadeh, C. Scawthorn and S. Eder, 11/24/93, (PB94-181765, A16, MF-A03).

NCEER-93-0023   "Hokkaido Nansei-oki, Japan Earthquake of July 12, 1993, by P.I. Yanev and C.R. Scawthorn, 12/23/93, (PB94-181500, A07, MF-A01).

NCEER-94-0001   "An Evaluation of Seismic Serviceability of Water Supply Networks with Application to the San Francisco Auxiliary Water Supply System," by I. Markov, Supervised by M. Grigoriu and T. O'Rourke, 1/21/94, (PB94-204013, A07, MF-A02).

NCEER-94-0002   "NCEER-Taisei Corporation Research Program on Sliding Seismic Isolation Systems for Bridges: Experimental and Analytical Study of Systems Consisting of Sliding Bearings, Rubber Restoring Force Devices and Fluid Dampers," Volumes I and II, by P. Tsopelas, S. Okamoto, M.C. Constantinou, D. Ozaki and S. Fujii, 2/4/94, (PB94-181740, A09, MF-A02 and PB94-181757, A12, MF-A03).

NCEER-94-0003   "A Markov Model for Local and Global Damage Indices in Seismic Analysis," by S. Rahman and M. Grigoriu, 2/18/94, (PB94-206000, A12, MF-A03).

NCEER-94-0004   "Proceedings from the NCEER Workshop on Seismic Response of Masonry Infills," edited by D.P. Abrams, 3/1/94, (PB94-180783, A07, MF-A02).

NCEER-94-0005   "The Northridge, California Earthquake of January 17, 1994: General Reconnaissance Report," edited by J.D. Goltz, 3/11/94, (PB94-193943, A10, MF-A03).

NCEER-94-0006   "Seismic Energy Based Fatigue Damage Analysis of Bridge Columns: Part I - Evaluation of Seismic Capacity," by G.A. Chang and J.B. Mander, 3/14/94, (PB94-219185, A11, MF-A03).

NCEER-94-0007   "Seismic Isolation of Multi-Story Frame Structures Using Spherical Sliding Isolation Systems," by T.M. Al-Hussaini, V.A. Zayas and M.C. Constantinou, 3/17/94, (PB94-193745, A09, MF-A02).

NCEER-94-0008   "The Northridge, California Earthquake of January 17, 1994: Performance of Highway Bridges," edited by I.G. Buckle, 3/24/94, (PB94-193851, A06, MF-A02).

NCEER-94-0009   "Proceedings of the Third U.S.-Japan Workshop on Earthquake Protective Systems for Bridges," edited by I.G. Buckle and I. Friedland, 3/31/94, (PB94-195815, A99, MF-A06).

NCEER-94-0010   "3D-BASIS-ME: Computer Program for Nonlinear Dynamic Analysis of Seismically Isolated Single and Multiple Structures and Liquid Storage Tanks," by P.C. Tsopelas, M.C. Constantinou and A.M. Reinhorn, 4/12/94, (PB94-204922, A09, MF-A02).

NCEER-94-0011   "The Northridge, California Earthquake of January 17, 1994: Performance of Gas Transmission Pipelines," by T.D. O'Rourke and M.C. Palmer, 5/16/94, (PB94-204989, A05, MF-A01).

NCEER-94-0012   "Feasibility Study of Replacement Procedures and Earthquake Performance Related to Gas Transmission Pipelines," by T.D. O'Rourke and M.C. Palmer, 5/25/94, (PB94-206638, A09, MF-A02).

NCEER-94-0013   "Seismic Energy Based Fatigue Damage Analysis of Bridge Columns: Part II - Evaluation of Seismic Demand," by G.A. Chang and J.B. Mander, 6/1/94, (PB95-18106, A08, MF-A02).

NCEER-94-0014   "NCEER-Taisei Corporation Research Program on Sliding Seismic Isolation Systems for Bridges: Experimental and Analytical Study of a System Consisting of Sliding Bearings and Fluid Restoring Force/Damping Devices," by P. Tsopelas and M.C. Constantinou, 6/13/94, (PB94-219144, A10, MF-A03).

NCEER-94-0015   "Generation of Hazard-Consistent Fragility Curves for Seismic Loss Estimation Studies," by H. Hwang and J-R. Huo, 6/14/94, (PB95-181996, A09, MF-A02).

NCEER-94-0016   "Seismic Study of Building Frames with Added Energy-Absorbing Devices," by W.S. Pong, C.S. Tsai and G.C. Lee, 6/20/94, (PB94-219136, A10, A03).

NCEER-94-0017   "Sliding Mode Control for Seismic-Excited Linear and Nonlinear Civil Engineering Structures," by J. Yang, J. Wu, A. Agrawal and Z. Li, 6/21/94, (PB95-138483, A06, MF-A02).

NCEER-94-0018   "3D-BASIS-TABS Version 2.0: Computer Program for Nonlinear Dynamic Analysis of Three Dimensional Base Isolated Structures," by A.M. Reinhorn, S. Nagarajaiah, M.C. Constantinou, P. Tsopelas and R. Li, 6/22/94, (PB95-182176, A08, MF-A02).

NCEER-94-0019   "Proceedings of the International Workshop on Civil Infrastructure Systems: Application of Intelligent Systems and Advanced Materials on Bridge Systems," Edited by G.C. Lee and K.C. Chang, 7/18/94, (PB95-252474, A20, MF-A04).

NCEER-94-0020   "Study of Seismic Isolation Systems for Computer Floors," by V. Lambrou and M.C. Constantinou, 7/19/94, (PB95-138533, A10, MF-A03).

NCEER-94-0021   "Proceedings of the U.S.-Italian Workshop on Guidelines for Seismic Evaluation and Rehabilitation of Unreinforced Masonry Buildings," Edited by D.P. Abrams and G.M. Calvi, 7/20/94, (PB95-138749, A13, MF-A03).

NCEER-94-0022   "NCEER-Taisei Corporation Research Program on Sliding Seismic Isolation Systems for Bridges: Experimental and Analytical Study of a System Consisting of Lubricated PTFE Sliding Bearings and Mild Steel Dampers," by P. Tsopelas and M.C. Constantinou, 7/22/94, (PB95-182184, A08, MF-A02).

NCEER-94-0023   "Development of Reliability-Based Design Criteria for Buildings Under Seismic Load," by Y.K. Wen, H. Hwang and M. Shinozuka, 8/1/94, (PB95-211934, A08, MF-A02).

NCEER-94-0024   "Experimental Verification of Acceleration Feedback Control Strategies for an Active Tendon System," by S.J. Dyke, B.F. Spencer, Jr., P. Quast, M.K. Sain, D.C. Kaspari, Jr. and T.T. Soong, 8/29/94, (PB95-212320, A05, MF-A01).

NCEER-94-0025   "Seismic Retrofitting Manual for Highway Bridges," Edited by I.G. Buckle and I.F. Friedland, published by the Federal Highway Administration (PB95-212676, A15, MF-A03).

NCEER-94-0026   "Proceedings from the Fifth U.S.-Japan Workshop on Earthquake Resistant Design of Lifeline Facilities and Countermeasures Against Soil Liquefaction," Edited by T.D. O'Rourke and M. Hamada, 11/7/94, (PB95-220802, A99, MF-E08).

NCEER-95-0001 "Experimental and Analytical Investigation of Seismic Retrofit of Structures with Supplemental Damping: Part 1 - Fluid Viscous Damping Devices," by A.M. Reinhorn, C. Li and M.C. Constantinou, 1/3/95, (PB95-266599, A09, MF-A02).

NCEER-95-0002 "Experimental and Analytical Study of Low-Cycle Fatigue Behavior of Semi-Rigid Top-And-Seat Angle Connections," by G. Pekcan, J.B. Mander and S.S. Chen, 1/5/95, (PB95-220042, A07, MF-A02).

NCEER-95-0003 "NCEER-ATC Joint Study on Fragility of Buildings," by T. Anagnos, C. Rojahn and A.S. Kiremidjian, 1/20/95, (PB95-220026, A06, MF-A02).

NCEER-95-0004 "Nonlinear Control Algorithms for Peak Response Reduction," by Z. Wu, T.T. Soong, V. Gattulli and R.C. Lin, 2/16/95, (PB95-220349, A05, MF-A01).

NCEER-95-0005 "Pipeline Replacement Feasibility Study: A Methodology for Minimizing Seismic and Corrosion Risks to Underground Natural Gas Pipelines," by R.T. Eguchi, H.A. Seligson and D.G. Honegger, 3/2/95, (PB95-252326, A06, MF-A02).

NCEER-95-0006 "Evaluation of Seismic Performance of an 11-Story Frame Building During the 1994 Northridge Earthquake," by F. Naeim, R. DiSulio, K. Benuska, A. Reinhorn and C. Li, not available.

NCEER-95-0007 "Prioritization of Bridges for Seismic Retrofitting," by N. Basöz and A.S. Kiremidjian, 4/24/95, (PB95-252300, A08, MF-A02).

NCEER-95-0008 "Method for Developing Motion Damage Relationships for Reinforced Concrete Frames," by A. Singhal and A.S. Kiremidjian, 5/11/95, (PB95-266607, A06, MF-A02).

NCEER-95-0009 "Experimental and Analytical Investigation of Seismic Retrofit of Structures with Supplemental Damping: Part II - Friction Devices," by C. Li and A.M. Reinhorn, 7/6/95, (PB96-128087, A11, MF-A03).

NCEER-95-0010 "Experimental Performance and Analytical Study of a Non-Ductile Reinforced Concrete Frame Structure Retrofitted with Elastomeric Spring Dampers," by G. Pekcan, J.B. Mander and S.S. Chen, 7/14/95, (PB96-137161, A08, MF-A02).

NCEER-95-0011 "Development and Experimental Study of Semi-Active Fluid Damping Devices for Seismic Protection of Structures," by M.D. Symans and M.C. Constantinou, 8/3/95, (PB96-136940, A23, MF-A04).

NCEER-95-0012 "Real-Time Structural Parameter Modification (RSPM): Development of Innervated Structures," by Z. Liang, M. Tong and G.C. Lee, 4/11/95, (PB96-137153, A06, MF-A01).

NCEER-95-0013 "Experimental and Analytical Investigation of Seismic Retrofit of Structures with Supplemental Damping: Part III - Viscous Damping Walls," by A.M. Reinhorn and C. Li, 10/1/95, (PB96-176409, A11, MF-A03).

NCEER-95-0014 "Seismic Fragility Analysis of Equipment and Structures in a Memphis Electric Substation," by J-R. Huo and H.H.M. Hwang, 8/10/95, (PB96-128087, A09, MF-A02).

NCEER-95-0015 "The Hanshin-Awaji Earthquake of January 17, 1995: Performance of Lifelines," Edited by M. Shinozuka, 11/3/95, (PB96-176383, A15, MF-A03).

NCEER-95-0016 "Highway Culvert Performance During Earthquakes," by T.L. Youd and C.J. Beckman, available as NCEER-96-0015.

NCEER-95-0017 "The Hanshin-Awaji Earthquake of January 17, 1995: Performance of Highway Bridges," Edited by I.G. Buckle, 12/1/95, not available.

NCEER-95-0018 "Modeling of Masonry Infill Panels for Structural Analysis," by A.M. Reinhorn, A. Madan, R.E. Valles, Y. Reichmann and J.B. Mander, 12/8/95, (PB97-110886, MF-A01, A06).

NCEER-95-0019 "Optimal Polynomial Control for Linear and Nonlinear Structures," by A.K. Agrawal and J.N. Yang, 12/11/95, (PB96-168737, A07, MF-A02).

NCEER-95-0020   "Retrofit of Non-Ductile Reinforced Concrete Frames Using Friction Dampers," by R.S. Rao, P. Gergely and R.N. White, 12/22/95, (PB97-133508, A10, MF-A02).

NCEER-95-0021   "Parametric Results for Seismic Response of Pile-Supported Bridge Bents," by G. Mylonakis, A. Nikolaou and G. Gazetas, 12/22/95, (PB97-100242, A12, MF-A03).

NCEER-95-0022   "Kinematic Bending Moments in Seismically Stressed Piles," by A. Nikolaou, G. Mylonakis and G. Gazetas, 12/23/95, (PB97-113914, MF-A03, A13).

NCEER-96-0001   "Dynamic Response of Unreinforced Masonry Buildings with Flexible Diaphragms," by A.C. Costley and D.P. Abrams," 10/10/96, (PB97-133573, MF-A03, A15).

NCEER-96-0002   "State of the Art Review: Foundations and Retaining Structures," by I. Po Lam, not available.

NCEER-96-0003   "Ductility of Rectangular Reinforced Concrete Bridge Columns with Moderate Confinement," by N. Wehbe, M. Saiidi, D. Sanders and B. Douglas, 11/7/96, (PB97-133557, A06, MF-A02).

NCEER-96-0004   "Proceedings of the Long-Span Bridge Seismic Research Workshop," edited by I.G. Buckle and I.M. Friedland, not available.

NCEER-96-0005   "Establish Representative Pier Types for Comprehensive Study: Eastern United States," by J. Kulicki and Z. Prucz, 5/28/96, (PB98-119217, A07, MF-A02).

NCEER-96-0006   "Establish Representative Pier Types for Comprehensive Study: Western United States," by R. Imbsen, R.A. Schamber and T.A. Osterkamp, 5/28/96, (PB98-118607, A07, MF-A02).

NCEER-96-0007   "Nonlinear Control Techniques for Dynamical Systems with Uncertain Parameters," by R.G. Ghanem and M.I. Bujakov, 5/27/96, (PB97-100259, A17, MF-A03).

NCEER-96-0008   "Seismic Evaluation of a 30-Year Old Non-Ductile Highway Bridge Pier and Its Retrofit," by J.B. Mander, B. Mahmoodzadegan, S. Bhadra and S.S. Chen, 5/31/96, (PB97-110902, MF-A03, A10).

NCEER-96-0009   "Seismic Performance of a Model Reinforced Concrete Bridge Pier Before and After Retrofit," by J.B. Mander, J.H. Kim and C.A. Ligozio, 5/31/96, (PB97-110910, MF-A02, A10).

NCEER-96-0010   "IDARC2D Version 4.0: A Computer Program for the Inelastic Damage Analysis of Buildings," by R.E. Valles, A.M. Reinhorn, S.K. Kunnath, C. Li and A. Madan, 6/3/96, (PB97-100234, A17, MF-A03).

NCEER-96-0011   "Estimation of the Economic Impact of Multiple Lifeline Disruption: Memphis Light, Gas and Water Division Case Study," by S.E. Chang, H.A. Seligson and R.T. Eguchi, 8/16/96, (PB97-133490, A11, MF-A03).

NCEER-96-0012   "Proceedings from the Sixth Japan-U.S. Workshop on Earthquake Resistant Design of Lifeline Facilities and Countermeasures Against Soil Liquefaction, Edited by M. Hamada and T. O'Rourke, 9/11/96, (PB97-133581, A99, MF-A06).

NCEER-96-0013   "Chemical Hazards, Mitigation and Preparedness in Areas of High Seismic Risk: A Methodology for Estimating the Risk of Post-Earthquake Hazardous Materials Release," by H.A. Seligson, R.T. Eguchi, K.J. Tierney and K. Richmond, 11/7/96, (PB97-133565, MF-A02, A08).

NCEER-96-0014   "Response of Steel Bridge Bearings to Reversed Cyclic Loading," by J.B. Mander, D-K. Kim, S.S. Chen and G.J. Premus, 11/13/96, (PB97-140735, A12, MF-A03).

NCEER-96-0015   "Highway Culvert Performance During Past Earthquakes," by T.L. Youd and C.J. Beckman, 11/25/96, (PB97-133532, A06, MF-A01).

NCEER-97-0001   "Evaluation, Prevention and Mitigation of Pounding Effects in Building Structures," by R.E. Valles and A.M. Reinhorn, 2/20/97, (PB97-159552, A14, MF-A03).

NCEER-97-0002   "Seismic Design Criteria for Bridges and Other Highway Structures," by C. Rojahn, R. Mayes, D.G. Anderson, J. Clark, J.H. Hom, R.V. Nutt and M.J. O'Rourke, 4/30/97, (PB97-194658, A06, MF-A03).

NCEER-97-0003   "Proceedings of the U.S.-Italian Workshop on Seismic Evaluation and Retrofit," Edited by D.P. Abrams and G.M. Calvi, 3/19/97, (PB97-194666, A13, MF-A03).

NCEER-97-0004   "Investigation of Seismic Response of Buildings with Linear and Nonlinear Fluid Viscous Dampers," by A.A. Seleemah and M.C. Constantinou, 5/21/97, (PB98-109002, A15, MF-A03).

NCEER-97-0005   "Proceedings of the Workshop on Earthquake Engineering Frontiers in Transportation Facilities," edited by G.C. Lee and I.M. Friedland, 8/29/97, (PB98-128911, A25, MR-A04).

NCEER-97-0006   "Cumulative Seismic Damage of Reinforced Concrete Bridge Piers," by S.K. Kunnath, A. El-Bahy, A. Taylor and W. Stone, 9/2/97, (PB98-108814, A11, MF-A03).

NCEER-97-0007   "Structural Details to Accommodate Seismic Movements of Highway Bridges and Retaining Walls," by R.A. Imbsen, R.A. Schamber, E. Thorkildsen, A. Kartoum, B.T. Martin, T.N. Rosser and J.M. Kulicki, 9/3/97, (PB98-108996, A09, MF-A02).

NCEER-97-0008   "A Method for Earthquake Motion-Damage Relationships with Application to Reinforced Concrete Frames," by A. Singhal and A.S. Kiremidjian, 9/10/97, (PB98-108988, A13, MF-A03).

NCEER-97-0009   "Seismic Analysis and Design of Bridge Abutments Considering Sliding and Rotation," by K. Fishman and R. Richards, Jr., 9/15/97, (PB98-108897, A06, MF-A02).

NCEER-97-0010   "Proceedings of the FHWA/NCEER Workshop on the National Representation of Seismic Ground Motion for New and Existing Highway Facilities," edited by I.M. Friedland, M.S. Power and R.L. Mayes, 9/22/97, (PB98-128903, A21, MF-A04).

NCEER-97-0011   "Seismic Analysis for Design or Retrofit of Gravity Bridge Abutments," by K.L. Fishman, R. Richards, Jr. and R.C. Divito, 10/2/97, (PB98-128937, A08, MF-A02).

NCEER-97-0012   "Evaluation of Simplified Methods of Analysis for Yielding Structures," by P. Tsopelas, M.C. Constantinou, C.A. Kircher and A.S. Whittaker, 10/31/97, (PB98-128929, A10, MF-A03).

NCEER-97-0013   "Seismic Design of Bridge Columns Based on Control and Repairability of Damage," by C-T. Cheng and J.B. Mander, 12/8/97, (PB98-144249, A11, MF-A03).

NCEER-97-0014   "Seismic Resistance of Bridge Piers Based on Damage Avoidance Design," by J.B. Mander and C-T. Cheng, 12/10/97, (PB98-144223, A09, MF-A02).

NCEER-97-0015   "Seismic Response of Nominally Symmetric Systems with Strength Uncertainty," by S. Balopoulou and M. Grigoriu, 12/23/97, (PB98-153422, A11, MF-A03).

NCEER-97-0016   "Evaluation of Seismic Retrofit Methods for Reinforced Concrete Bridge Columns," by T.J. Wipf, F.W. Klaiber and F.M. Russo, 12/28/97, (PB98-144215, A12, MF-A03).

NCEER-97-0017   "Seismic Fragility of Existing Conventional Reinforced Concrete Highway Bridges," by C.L. Mullen and A.S. Cakmak, 12/30/97, (PB98-153406, A08, MF-A02).

NCEER-97-0018   "Loss Asssessment of Memphis Buildings," edited by D.P. Abrams and M. Shinozuka, 12/31/97, (PB98-144231, A13, MF-A03).

NCEER-97-0019   "Seismic Evaluation of Frames with Infill Walls Using Quasi-static Experiments," by K.M. Mosalam, R.N. White and P. Gergely, 12/31/97, (PB98-153455, A07, MF-A02).

NCEER-97-0020   "Seismic Evaluation of Frames with Infill Walls Using Pseudo-dynamic Experiments," by K.M. Mosalam, R.N. White and P. Gergely, 12/31/97, (PB98-153430, A07, MF-A02).

NCEER-97-0021   "Computational Strategies for Frames with Infill Walls: Discrete and Smeared Crack Analyses and Seismic Fragility," by K.M. Mosalam, R.N. White and P. Gergely, 12/31/97, (PB98-153414, A10, MF-A02).

NCEER-97-0022   "Proceedings of the NCEER Workshop on Evaluation of Liquefaction Resistance of Soils," edited by T.L. Youd and I.M. Idriss, 12/31/97, (PB98-155617, A15, MF-A03).

MCEER-98-0001   "Extraction of Nonlinear Hysteretic Properties of Seismically Isolated Bridges from Quick-Release Field Tests," by Q. Chen, B.M. Douglas, E.M. Maragakis and I.G. Buckle, 5/26/98, (PB99-118838, A06, MF-A01).

MCEER-98-0002   "Methodologies for Evaluating the Importance of Highway Bridges," by A. Thomas, S. Eshenaur and J. Kulicki, 5/29/98, (PB99-118846, A10, MF-A02).

MCEER-98-0003   "Capacity Design of Bridge Piers and the Analysis of Overstrength," by J.B. Mander, A. Dutta and P. Goel, 6/1/98, (PB99-118853, A09, MF-A02).

MCEER-98-0004   "Evaluation of Bridge Damage Data from the Loma Prieta and Northridge, California Earthquakes," by N. Basoz and A. Kiremidjian, 6/2/98, (PB99-118861, A15, MF-A03).

MCEER-98-0005   "Screening Guide for Rapid Assessment of Liquefaction Hazard at Highway Bridge Sites," by T. L. Youd, 6/16/98, (PB99-118879, A06, not available on microfiche).

MCEER-98-0006   "Structural Steel and Steel/Concrete Interface Details for Bridges," by P. Ritchie, N. Kauhl and J. Kulicki, 7/13/98, (PB99-118945, A06, MF-A01).

MCEER-98-0007   "Capacity Design and Fatigue Analysis of Confined Concrete Columns," by A. Dutta and J.B. Mander, 7/14/98, (PB99-118960, A14, MF-A03).

MCEER-98-0008   "Proceedings of the Workshop on Performance Criteria for Telecommunication Services Under Earthquake Conditions," edited by A.J. Schiff, 7/15/98, (PB99-118952, A08, MF-A02).

MCEER-98-0009   "Fatigue Analysis of Unconfined Concrete Columns," by J.B. Mander, A. Dutta and J.H. Kim, 9/12/98, (PB99-123655, A10, MF-A02).

MCEER-98-0010   "Centrifuge Modeling of Cyclic Lateral Response of Pile-Cap Systems and Seat-Type Abutments in Dry Sands," by A.D. Gadre and R. Dobry, 10/2/98, (PB99-123606, A13, MF-A03).

MCEER-98-0011   "IDARC-BRIDGE: A Computational Platform for Seismic Damage Assessment of Bridge Structures," by A.M. Reinhorn, V. Simeonov, G. Mylonakis and Y. Reichman, 10/2/98, (PB99-162919, A15, MF-A03).

MCEER-98-0012   "Experimental Investigation of the Dynamic Response of Two Bridges Before and After Retrofitting with Elastomeric Bearings," by D.A. Wendichansky, S.S. Chen and J.B. Mander, 10/2/98, (PB99-162927, A15, MF-A03).

MCEER-98-0013   "Design Procedures for Hinge Restrainers and Hinge Sear Width for Multiple-Frame Bridges," by R. Des Roches and G.L. Fenves, 11/3/98, (PB99-140477, A13, MF-A03).

MCEER-98-0014   "Response Modification Factors for Seismically Isolated Bridges," by M.C. Constantinou and J.K. Quarshie, 11/3/98, (PB99-140485, A14, MF-A03).

MCEER-98-0015   "Proceedings of the U.S.-Italy Workshop on Seismic Protective Systems for Bridges," edited by I.M. Friedland and M.C. Constantinou, 11/3/98, (PB2000-101711, A22, MF-A04).

MCEER-98-0016   "Appropriate Seismic Reliability for Critical Equipment Systems: Recommendations Based on Regional Analysis of Financial and Life Loss," by K. Porter, C. Scawthorn, C. Taylor and N. Blais, 11/10/98, (PB99-157265, A08, MF-A02).

MCEER-98-0017   "Proceedings of the U.S. Japan Joint Seminar on Civil Infrastructure Systems Research," edited by M. Shinozuka and A. Rose, 11/12/98, (PB99-156713, A16, MF-A03).

MCEER-98-0018   "Modeling of Pile Footings and Drilled Shafts for Seismic Design," by I. PoLam, M. Kapuskar and D. Chaudhuri, 12/21/98, (PB99-157257, A09, MF-A02).

MCEER-99-0001 "Seismic Evaluation of a Masonry Infilled Reinforced Concrete Frame by Pseudodynamic Testing," by S.G. Buonopane and R.N. White, 2/16/99, (PB99-162851, A09, MF-A02).

MCEER-99-0002 "Response History Analysis of Structures with Seismic Isolation and Energy Dissipation Systems: Verification Examples for Program SAP2000," by J. Scheller and M.C. Constantinou, 2/22/99, (PB99-162869, A08, MF-A02).

MCEER-99-0003 "Experimental Study on the Seismic Design and Retrofit of Bridge Columns Including Axial Load Effects," by A. Dutta, T. Kokorina and J.B. Mander, 2/22/99, (PB99-162877, A09, MF-A02).

MCEER-99-0004 "Experimental Study of Bridge Elastomeric and Other Isolation and Energy Dissipation Systems with Emphasis on Uplift Prevention and High Velocity Near-source Seismic Excitation," by A. Kasalanati and M. C. Constantinou, 2/26/99, (PB99-162885, A12, MF-A03).

MCEER-99-0005 "Truss Modeling of Reinforced Concrete Shear-flexure Behavior," by J.H. Kim and J.B. Mander, 3/8/99, (PB99-163693, A12, MF-A03).

MCEER-99-0006 "Experimental Investigation and Computational Modeling of Seismic Response of a 1:4 Scale Model Steel Structure with a Load Balancing Supplemental Damping System," by G. Pekcan, J.B. Mander and S.S. Chen, 4/2/99, (PB99-162893, A11, MF-A03).

MCEER-99-0007 "Effect of Vertical Ground Motions on the Structural Response of Highway Bridges," by M.R. Button, C.J. Cronin and R.L. Mayes, 4/10/99, (PB2000-101411, A10, MF-A03).

MCEER-99-0008 "Seismic Reliability Assessment of Critical Facilities: A Handbook, Supporting Documentation, and Model Code Provisions," by G.S. Johnson, R.E. Sheppard, M.D. Quilici, S.J. Eder and C.R. Scawthorn, 4/12/99, (PB2000-101701, A18, MF-A04).

MCEER-99-0009 "Impact Assessment of Selected MCEER Highway Project Research on the Seismic Design of Highway Structures," by C. Rojahn, R. Mayes, D.G. Anderson, J.H. Clark, D'Appolonia Engineering, S. Gloyd and R.V. Nutt, 4/14/99, (PB99-162901, A10, MF-A02).

MCEER-99-0010 "Site Factors and Site Categories in Seismic Codes," by R. Dobry, R. Ramos and M.S. Power, 7/19/99, (PB2000-101705, A08, MF-A02).

MCEER-99-0011 "Restrainer Design Procedures for Multi-Span Simply-Supported Bridges," by M.J. Randall, M. Saiidi, E. Maragakis and T. Isakovic, 7/20/99, (PB2000-101702, A10, MF-A02).

MCEER-99-0012 "Property Modification Factors for Seismic Isolation Bearings," by M.C. Constantinou, P. Tsopelas, A. Kasalanati and E. Wolff, 7/20/99, (PB2000-103387, A11, MF-A03).

MCEER-99-0013 "Critical Seismic Issues for Existing Steel Bridges," by P. Ritchie, N. Kauhl and J. Kulicki, 7/20/99, (PB2000-101697, A09, MF-A02).

MCEER-99-0014 "Nonstructural Damage Database," by A. Kao, T.T. Soong and A. Vender, 7/24/99, (PB2000-101407, A06, MF-A01).

MCEER-99-0015 "Guide to Remedial Measures for Liquefaction Mitigation at Existing Highway Bridge Sites," by H.G. Cooke and J. K. Mitchell, 7/26/99, (PB2000-101703, A11, MF-A03).

MCEER-99-0016 "Proceedings of the MCEER Workshop on Ground Motion Methodologies for the Eastern United States," edited by N. Abrahamson and A. Becker, 8/11/99, (PB2000-103385, A07, MF-A02).

MCEER-99-0017 "Quindío, Colombia Earthquake of January 25, 1999: Reconnaissance Report," by A.P. Asfura and P.J. Flores, 10/4/99, (PB2000-106893, A06, MF-A01).

MCEER-99-0018 "Hysteretic Models for Cyclic Behavior of Deteriorating Inelastic Structures," by M.V. Sivaselvan and A.M. Reinhorn, 11/5/99, (PB2000-103386, A08, MF-A02).

MCEER-99-0019   "Proceedings of the 7th U.S.- Japan Workshop on Earthquake Resistant Design of Lifeline Facilities and Countermeasures Against Soil Liquefaction," edited by T.D. O'Rourke, J.P. Bardet and M. Hamada, 11/19/99, (PB2000-103354, A99, MF-A06).

MCEER-99-0020   "Development of Measurement Capability for Micro-Vibration Evaluations with Application to Chip Fabrication Facilities," by G.C. Lee, Z. Liang, J.W. Song, J.D. Shen and W.C. Liu, 12/1/99, (PB2000-105993, A08, MF-A02).

MCEER-99-0021   "Design and Retrofit Methodology for Building Structures with Supplemental Energy Dissipating Systems," by G. Pekcan, J.B. Mander and S.S. Chen, 12/31/99, (PB2000-105994, A11, MF-A03).

MCEER-00-0001   "The Marmara, Turkey Earthquake of August 17, 1999: Reconnaissance Report," edited by C. Scawthorn; with major contributions by M. Bruneau, R. Eguchi, T. Holzer, G. Johnson, J. Mander, J. Mitchell, W. Mitchell, A. Papageorgiou, C. Scaethorn, and G. Webb, 3/23/00, (PB2000-106200, A11, MF-A03).

MCEER-00-0002   "Proceedings of the MCEER Workshop for Seismic Hazard Mitigation of Health Care Facilities," edited by G.C. Lee, M. Ettouney, M. Grigoriu, J. Hauer and J. Nigg, 3/29/00, (PB2000-106892, A08, MF-A02).

MCEER-00-0003   "The Chi-Chi, Taiwan Earthquake of September 21, 1999: Reconnaissance Report," edited by G.C. Lee and C.H. Loh, with major contributions by G.C. Lee, M. Bruneau, I.G. Buckle, S.E. Chang, P.J. Flores, T.D. O'Rourke, M. Shinozuka, T.T. Soong, C-H. Loh, K-C. Chang, Z-J. Chen, J-S. Hwang, M-L. Lin, G-Y. Liu, K-C. Tsai, G.C. Yao and C-L. Yen, 4/30/00, (PB2001-100980, A10, MF-A02).

MCEER-00-0004   "Seismic Retrofit of End-Sway Frames of Steel Deck-Truss Bridges with a Supplemental Tendon System: Experimental and Analytical Investigation," by G. Pekcan, J.B. Mander and S.S. Chen, 7/1/00, (PB2001-100982, A10, MF-A02).

MCEER-00-0005   "Sliding Fragility of Unrestrained Equipment in Critical Facilities," by W.H. Chong and T.T. Soong, 7/5/00, (PB2001-100983, A08, MF-A02).

MCEER-00-0006   "Seismic Response of Reinforced Concrete Bridge Pier Walls in the Weak Direction," by N. Abo-Shadi, M. Saiidi and D. Sanders, 7/17/00, (PB2001-100981, A17, MF-A03).

MCEER-00-0007   "Low-Cycle Fatigue Behavior of Longitudinal Reinforcement in Reinforced Concrete Bridge Columns," by J. Brown and S.K. Kunnath, 7/23/00, (PB2001-104392, A08, MF-A02).

MCEER-00-0008   "Soil Structure Interaction of Bridges for Seismic Analysis," I. PoLam and H. Law, 9/25/00, (PB2001-105397, A08, MF-A02).

MCEER-00-0009   "Proceedings of the First MCEER Workshop on Mitigation of Earthquake Disaster by Advanced Technologies (MEDAT-1), edited by M. Shinozuka, D.J. Inman and T.D. O'Rourke, 11/10/00, (PB2001-105399, A14, MF-A03).

MCEER-00-0010   "Development and Evaluation of Simplified Procedures for Analysis and Design of Buildings with Passive Energy Dissipation Systems, Revision 01," by O.M. Ramirez, M.C. Constantinou, C.A. Kircher, A.S. Whittaker, M.W. Johnson, J.D. Gomez and C. Chrysostomou, 11/16/01, (PB2001-105523, A23, MF-A04).

MCEER-00-0011   "Dynamic Soil-Foundation-Structure Interaction Analyses of Large Caissons," by C-Y. Chang, C-M. Mok, Z-L. Wang, R. Settgast, F. Waggoner, M.A. Ketchum, H.M. Gonnermann and C-C. Chin, 12/30/00, (PB2001-104373, A07, MF-A02).

MCEER-00-0012   "Experimental Evaluation of Seismic Performance of Bridge Restrainers," by A.G. Vlassis, E.M. Maragakis and M. Saiid Saiidi, 12/30/00, (PB2001-104354, A09, MF-A02).

MCEER-00-0013   "Effect of Spatial Variation of Ground Motion on Highway Structures," by M. Shinozuka, V. Saxena and G. Deodatis, 12/31/00, (PB2001-108755, A13, MF-A03).

MCEER-00-0014   "A Risk-Based Methodology for Assessing the Seismic Performance of Highway Systems," by S.D. Werner, C.E. Taylor, J.E. Moore, II, J.S. Walton and S. Cho, 12/31/00, (PB2001-108756, A14, MF-A03).

MCEER-01-0001 "Experimental Investigation of P-Delta Effects to Collapse During Earthquakes," by D. Vian and M. Bruneau, 6/25/01, (PB2002-100534, A17, MF-A03).

MCEER-01-0002 "Proceedings of the Second MCEER Workshop on Mitigation of Earthquake Disaster by Advanced Technologies (MEDAT-2)," edited by M. Bruneau and D.J. Inman, 7/23/01, (PB2002-100434, A16, MF-A03).

MCEER-01-0003 "Sensitivity Analysis of Dynamic Systems Subjected to Seismic Loads," by C. Roth and M. Grigoriu, 9/18/01, (PB2003-100884, A12, MF-A03).

MCEER-01-0004 "Overcoming Obstacles to Implementing Earthquake Hazard Mitigation Policies: Stage 1 Report," by D.J. Alesch and W.J. Petak, 12/17/01, (PB2002-107949, A07, MF-A02).

MCEER-01-0005 "Updating Real-Time Earthquake Loss Estimates: Methods, Problems and Insights," by C.E. Taylor, S.E. Chang and R.T. Eguchi, 12/17/01, (PB2002-107948, A05, MF-A01).

MCEER-01-0006 "Experimental Investigation and Retrofit of Steel Pile Foundations and Pile Bents Under Cyclic Lateral Loadings," by A. Shama, J. Mander, B. Blabac and S. Chen, 12/31/01, (PB2002-107950, A13, MF-A03).

MCEER-02-0001 "Assessment of Performance of Bolu Viaduct in the 1999 Duzce Earthquake in Turkey" by P.C. Roussis, M.C. Constantinou, M. Erdik, E. Durukal and M. Dicleli, 5/8/02, (PB2003-100883, A08, MF-A02).

MCEER-02-0002 "Seismic Behavior of Rail Counterweight Systems of Elevators in Buildings," by M.P. Singh, Rildova and L.E. Suarez, 5/27/02. (PB2003-100882, A11, MF-A03).

MCEER-02-0003 "Development of Analysis and Design Procedures for Spread Footings," by G. Mylonakis, G. Gazetas, S. Nikolaou and A. Chauncey, 10/02/02, (PB2004-101636, A13, MF-A03, CD-A13).

MCEER-02-0004 "Bare-Earth Algorithms for Use with SAR and LIDAR Digital Elevation Models," by C.K. Huyck, R.T. Eguchi and B. Houshmand, 10/16/02, (PB2004-101637, A07, CD-A07).

MCEER-02-0005 "Review of Energy Dissipation of Compression Members in Concentrically Braced Frames," by K.Lee and M. Bruneau, 10/18/02, (PB2004-101638, A10, CD-A10).

MCEER-03-0001 "Experimental Investigation of Light-Gauge Steel Plate Shear Walls for the Seismic Retrofit of Buildings" by J. Berman and M. Bruneau, 5/2/03, (PB2004-101622, A10, MF-A03, CD-A10).

MCEER-03-0002 "Statistical Analysis of Fragility Curves," by M. Shinozuka, M.Q. Feng, H. Kim, T. Uzawa and T. Ueda, 6/16/03, (PB2004-101849, A09, CD-A09).

MCEER-03-0003 "Proceedings of the Eighth U.S.-Japan Workshop on Earthquake Resistant Design f Lifeline Facilities and Countermeasures Against Liquefaction," edited by M. Hamada, J.P. Bardet and T.D. O'Rourke, 6/30/03, (PB2004-104386, A99, CD-A99).

MCEER-03-0004 "Proceedings of the PRC-US Workshop on Seismic Analysis and Design of Special Bridges," edited by L.C. Fan and G.C. Lee, 7/15/03, (PB2004-104387, A14, CD-A14).

MCEER-03-0005 "Urban Disaster Recovery: A Framework and Simulation Model," by S.B. Miles and S.E. Chang, 7/25/03, (PB2004-104388, A07, CD-A07).

MCEER-03-0006 "Behavior of Underground Piping Joints Due to Static and Dynamic Loading," by R.D. Meis, M. Maragakis and R. Siddharthan, 11/17/03, (PB2005-102194, A13, MF-A03, CD-A00).

MCEER-04-0001 "Experimental Study of Seismic Isolation Systems with Emphasis on Secondary System Response and Verification of Accuracy of Dynamic Response History Analysis Methods," by E. Wolff and M. Constantinou, 1/16/04 (PB2005-102195, A99, MF-E08, CD-A00).

MCEER-04-0002 "Tension, Compression and Cyclic Testing of Engineered Cementitious Composite Materials," by K. Kesner and S.L. Billington, 3/1/04, (PB2005-102196, A08, CD-A08).

MCEER-04-0003   "Cyclic Testing of Braces Laterally Restrained by Steel Studs to Enhance Performance During Earthquakes," by O.C. Celik, J.W. Berman and M. Bruneau, 3/16/04, (PB2005-102197, A13, MF-A03, CD-A00).

MCEER-04-0004   "Methodologies for Post Earthquake Building Damage Detection Using SAR and Optical Remote Sensing: Application to the August 17, 1999 Marmara, Turkey Earthquake," by C.K. Huyck, B.J. Adams, S. Cho, R.T. Eguchi, B. Mansouri and B. Houshmand, 6/15/04, (PB2005-104888, A10, CD-A00).

MCEER-04-0005   "Nonlinear Structural Analysis Towards Collapse Simulation: A Dynamical Systems Approach," by M.V. Sivaselvan and A.M. Reinhorn, 6/16/04, (PB2005-104889, A11, MF-A03, CD-A00).

MCEER-04-0006   "Proceedings of the Second PRC-US Workshop on Seismic Analysis and Design of Special Bridges," edited by G.C. Lee and L.C. Fan, 6/25/04, (PB2005-104890, A16, CD-A00).

MCEER-04-0007   "Seismic Vulnerability Evaluation of Axially Loaded Steel Built-up Laced Members," by K. Lee and M. Bruneau, 6/30/04, (PB2005-104891, A16, CD-A00).

MCEER-04-0008   "Evaluation of Accuracy of Simplified Methods of Analysis and Design of Buildings with Damping Systems for Near-Fault and for Soft-Soil Seismic Motions," by E.A. Pavlou and M.C. Constantinou, 8/16/04, (PB2005-104892, A08, MF-A02, CD-A00).

MCEER-04-0009   "Assessment of Geotechnical Issues in Acute Care Facilities in California," by M. Lew, T.D. O'Rourke, R. Dobry and M. Koch, 9/15/04, (PB2005-104893, A08, CD-A00).

MCEER-04-0010   "Scissor-Jack-Damper Energy Dissipation System," by A.N. Sigaher-Boyle and M.C. Constantinou, 12/1/04 (PB2005-108221).

MCEER-04-0011   "Seismic Retrofit of Bridge Steel Truss Piers Using a Controlled Rocking Approach," by M. Pollino and M. Bruneau, 12/20/04 (PB2006-105795).

MCEER-05-0001   "Experimental and Analytical Studies of Structures Seismically Isolated with an Uplift-Restraint Isolation System," by P.C. Roussis and M.C. Constantinou, 1/10/05 (PB2005-108222).

MCEER-05-0002   "A Versatile Experimentation Model for Study of Structures Near Collapse Applied to Seismic Evaluation of Irregular Structures," by D. Kusumastuti, A.M. Reinhorn and A. Rutenberg, 3/31/05 (PB2006-101523).

MCEER-05-0003   "Proceedings of the Third PRC-US Workshop on Seismic Analysis and Design of Special Bridges," edited by L.C. Fan and G.C. Lee, 4/20/05, (PB2006-105796).

MCEER-05-0004   "Approaches for the Seismic Retrofit of Braced Steel Bridge Piers and Proof-of-Concept Testing of an Eccentrically Braced Frame with Tubular Link," by J.W. Berman and M. Bruneau, 4/21/05 (PB2006-101524).

MCEER-05-0005   "Simulation of Strong Ground Motions for Seismic Fragility Evaluation of Nonstructural Components in Hospitals," by A. Wanitkorkul and A. Filiatrault, 5/26/05 (PB2006-500027).

MCEER-05-0006   "Seismic Safety in California Hospitals: Assessing an Attempt to Accelerate the Replacement or Seismic Retrofit of Older Hospital Facilities," by D.J. Alesch, L.A. Arendt and W.J. Petak, 6/6/05 (PB2006-105794).

MCEER-05-0007   "Development of Seismic Strengthening and Retrofit Strategies for Critical Facilities Using Engineered Cementitious Composite Materials," by K. Kesner and S.L. Billington, 8/29/05 (PB2006-111701).

MCEER-05-0008   "Experimental and Analytical Studies of Base Isolation Systems for Seismic Protection of Power Transformers," by N. Murota, M.Q. Feng and G-Y. Liu, 9/30/05 (PB2006-111702).

MCEER-05-0009   "3D-BASIS-ME-MB: Computer Program for Nonlinear Dynamic Analysis of Seismically Isolated Structures," by P.C. Tsopelas, P.C. Roussis, M.C. Constantinou, R. Buchanan and A.M. Reinhorn, 10/3/05 (PB2006-111703).

MCEER-05-0010   "Steel Plate Shear Walls for Seismic Design and Retrofit of Building Structures," by D. Vian and M. Bruneau, 12/15/05 (PB2006-111704).

MCEER-05-0011 "The Performance-Based Design Paradigm," by M.J. Astrella and A. Whittaker, 12/15/05 (PB2006-111705).

MCEER-06-0001 "Seismic Fragility of Suspended Ceiling Systems," H. Badillo-Almaraz, A.S. Whittaker, A.M. Reinhorn and G.P. Cimellaro, 2/4/06 (PB2006-111706).

MCEER-06-0002 "Multi-Dimensional Fragility of Structures," by G.P. Cimellaro, A.M. Reinhorn and M. Bruneau, 3/1/06 (PB2007-106974, A09, MF-A02, CD A00).

MCEER-06-0003 "Built-Up Shear Links as Energy Dissipators for Seismic Protection of Bridges," by P. Dusicka, A.M. Itani and I.G. Buckle, 3/15/06 (PB2006-111708).

MCEER-06-0004 "Analytical Investigation of the Structural Fuse Concept," by R.E. Vargas and M. Bruneau, 3/16/06 (PB2006-111709).

MCEER-06-0005 "Experimental Investigation of the Structural Fuse Concept," by R.E. Vargas and M. Bruneau, 3/17/06 (PB2006-111710).

MCEER-06-0006 "Further Development of Tubular Eccentrically Braced Frame Links for the Seismic Retrofit of Braced Steel Truss Bridge Piers," by J.W. Berman and M. Bruneau, 3/27/06 (PB2007-105147).

MCEER-06-0007 "REDARS Validation Report," by S. Cho, C.K. Huyck, S. Ghosh and R.T. Eguchi, 8/8/06 (PB2007-106983).

MCEER-06-0008 "Review of Current NDE Technologies for Post-Earthquake Assessment of Retrofitted Bridge Columns," by J.W. Song, Z. Liang and G.C. Lee, 8/21/06 (PB2007-106984).

MCEER-06-0009 "Liquefaction Remediation in Silty Soils Using Dynamic Compaction and Stone Columns," by S. Thevanayagam, G.R. Martin, R. Nashed, T. Shenthan, T. Kanagalingam and N. Ecemis, 8/28/06 (PB2007-106985).

MCEER-06-0010 "Conceptual Design and Experimental Investigation of Polymer Matrix Composite Infill Panels for Seismic Retrofitting," by W. Jung, M. Chiewanichakorn and A.J. Aref, 9/21/06 (PB2007-106986).

MCEER-06-0011 "A Study of the Coupled Horizontal-Vertical Behavior of Elastomeric and Lead-Rubber Seismic Isolation Bearings," by G.P. Warn and A.S. Whittaker, 9/22/06 (PB2007-108679).

MCEER-06-0012 "Proceedings of the Fourth PRC-US Workshop on Seismic Analysis and Design of Special Bridges: Advancing Bridge Technologies in Research, Design, Construction and Preservation," Edited by L.C. Fan, G.C. Lee and L. Ziang, 10/12/06 (PB2007-109042).

MCEER-06-0013 "Cyclic Response and Low Cycle Fatigue Characteristics of Plate Steels," by P. Dusicka, A.M. Itani and I.G. Buckle, 11/1/06 06 (PB2007-106987).

MCEER-06-0014 "Proceedings of the Second US-Taiwan Bridge Engineering Workshop," edited by W.P. Yen, J. Shen, J-Y. Chen and M. Wang, 11/15/06 (PB2008-500041).

MCEER-06-0015 "User Manual and Technical Documentation for the REDARS™ Import Wizard," by S. Cho, S. Ghosh, C.K. Huyck and S.D. Werner, 11/30/06 (PB2007-114766).

MCEER-06-0016 "Hazard Mitigation Strategy and Monitoring Technologies for Urban and Infrastructure Public Buildings: Proceedings of the China-US Workshops," edited by X.Y. Zhou, A.L. Zhang, G.C. Lee and M. Tong, 12/12/06 (PB2008-500018).

MCEER-07-0001 "Static and Kinetic Coefficients of Friction for Rigid Blocks," by C. Kafali, S. Fathali, M. Grigoriu and A.S. Whittaker, 3/20/07 (PB2007-114767).

MCEER-07-0002 "Hazard Mitigation Investment Decision Making: Organizational Response to Legislative Mandate," by L.A. Arendt, D.J. Alesch and W.J. Petak, 4/9/07 (PB2007-114768).

MCEER-07-0003 "Seismic Behavior of Bidirectional-Resistant Ductile End Diaphragms with Unbonded Braces in Straight or Skewed Steel Bridges," by O. Celik and M. Bruneau, 4/11/07 (PB2008-105141).

MCEER-07-0004 "Modeling Pile Behavior in Large Pile Groups Under Lateral Loading," by A.M. Dodds and G.R. Martin, 4/16/07(PB2008-105142).

MCEER-07-0005 "Experimental Investigation of Blast Performance of Seismically Resistant Concrete-Filled Steel Tube Bridge Piers," by S. Fujikura, M. Bruneau and D. Lopez-Garcia, 4/20/07 (PB2008-105143).

MCEER-07-0006 "Seismic Analysis of Conventional and Isolated Liquefied Natural Gas Tanks Using Mechanical Analogs," by I.P. Christovasilis and A.S. Whittaker, 5/1/07, not available.

MCEER-07-0007 "Experimental Seismic Performance Evaluation of Isolation/Restraint Systems for Mechanical Equipment – Part 1: Heavy Equipment Study," by S. Fathali and A. Filiatrault, 6/6/07 (PB2008-105144).

MCEER-07-0008 "Seismic Vulnerability of Timber Bridges and Timber Substructures," by A.A. Sharma, J.B. Mander, I.M. Friedland and D.R. Allicock, 6/7/07 (PB2008-105145).

MCEER-07-0009 "Experimental and Analytical Study of the XY-Friction Pendulum (XY-FP) Bearing for Bridge Applications," by C.C. Marin-Artieda, A.S. Whittaker and M.C. Constantinou, 6/7/07 (PB2008-105191).

MCEER-07-0010 "Proceedings of the PRC-US Earthquake Engineering Forum for Young Researchers," Edited by G.C. Lee and X.Z. Qi, 6/8/07 (PB2008-500058).

MCEER-07-0011 "Design Recommendations for Perforated Steel Plate Shear Walls," by R. Purba and M. Bruneau, 6/18/07, (PB2008-105192).

MCEER-07-0012 "Performance of Seismic Isolation Hardware Under Service and Seismic Loading," by M.C. Constantinou, A.S. Whittaker, Y. Kalpakidis, D.M. Fenz and G.P. Warn, 8/27/07, (PB2008-105193).

MCEER-07-0013 "Experimental Evaluation of the Seismic Performance of Hospital Piping Subassemblies," by E.R. Goodwin, E. Maragakis and A.M. Itani, 9/4/07, (PB2008-105194).

MCEER-07-0014 "A Simulation Model of Urban Disaster Recovery and Resilience: Implementation for the 1994 Northridge Earthquake," by S. Miles and S.E. Chang, 9/7/07, (PB2008-106426).

MCEER-07-0015 "Statistical and Mechanistic Fragility Analysis of Concrete Bridges," by M. Shinozuka, S. Banerjee and S-H. Kim, 9/10/07, (PB2008-106427).

MCEER-07-0016 "Three-Dimensional Modeling of Inelastic Buckling in Frame Structures," by M. Schachter and AM. Reinhorn, 9/13/07, (PB2008-108125).

MCEER-07-0017 "Modeling of Seismic Wave Scattering on Pile Groups and Caissons," by I. Po Lam, H. Law and C.T. Yang, 9/17/07 (PB2008-108150).

MCEER-07-0018 "Bridge Foundations: Modeling Large Pile Groups and Caissons for Seismic Design," by I. Po Lam, H. Law and G.R. Martin (Coordinating Author), 12/1/07 (PB2008-111190).

MCEER-07-0019 "Principles and Performance of Roller Seismic Isolation Bearings for Highway Bridges," by G.C. Lee, Y.C. Ou, Z. Liang, T.C. Niu and J. Song, 12/10/07 (PB2009-110466).

MCEER-07-0020 "Centrifuge Modeling of Permeability and Pinning Reinforcement Effects on Pile Response to Lateral Spreading," by L.L Gonzalez-Lagos, T. Abdoun and R. Dobry, 12/10/07 (PB2008-111191).

MCEER-07-0021 "Damage to the Highway System from the Pisco, Perú Earthquake of August 15, 2007," by J.S. O'Connor, L. Mesa and M. Nykamp, 12/10/07, (PB2008-108126).

MCEER-07-0022 "Experimental Seismic Performance Evaluation of Isolation/Restraint Systems for Mechanical Equipment – Part 2: Light Equipment Study," by S. Fathali and A. Filiatrault, 12/13/07 (PB2008-111192).

MCEER-07-0023 "Fragility Considerations in Highway Bridge Design," by M. Shinozuka, S. Banerjee and S.H. Kim, 12/14/07 (PB2008-111193).

MCEER-07-0024 "Performance Estimates for Seismically Isolated Bridges," by G.P. Warn and A.S. Whittaker, 12/30/07 (PB2008-112230).

MCEER-08-0001 "Seismic Performance of Steel Girder Bridge Superstructures with Conventional Cross Frames," by L.P. Carden, A.M. Itani and I.G. Buckle, 1/7/08, (PB2008-112231).

MCEER-08-0002 "Seismic Performance of Steel Girder Bridge Superstructures with Ductile End Cross Frames with Seismic Isolators," by L.P. Carden, A.M. Itani and I.G. Buckle, 1/7/08 (PB2008-112232).

MCEER-08-0003 "Analytical and Experimental Investigation of a Controlled Rocking Approach for Seismic Protection of Bridge Steel Truss Piers," by M. Pollino and M. Bruneau, 1/21/08 (PB2008-112233).

MCEER-08-0004 "Linking Lifeline Infrastructure Performance and Community Disaster Resilience: Models and Multi-Stakeholder Processes," by S.E. Chang, C. Pasion, K. Tatebe and R. Ahmad, 3/3/08 (PB2008-112234).

MCEER-08-0005 "Modal Analysis of Generally Damped Linear Structures Subjected to Seismic Excitations," by J. Song, Y-L. Chu, Z. Liang and G.C. Lee, 3/4/08 (PB2009-102311).

MCEER-08-0006 "System Performance Under Multi-Hazard Environments," by C. Kafali and M. Grigoriu, 3/4/08 (PB2008-112235).

MCEER-08-0007 "Mechanical Behavior of Multi-Spherical Sliding Bearings," by D.M. Fenz and M.C. Constantinou, 3/6/08 (PB2008-112236).

MCEER-08-0008 "Post-Earthquake Restoration of the Los Angeles Water Supply System," by T.H.P. Tabucchi and R.A. Davidson, 3/7/08 (PB2008-112237).

MCEER-08-0009 "Fragility Analysis of Water Supply Systems," by A. Jacobson and M. Grigoriu, 3/10/08 (PB2009-105545).

MCEER-08-0010 "Experimental Investigation of Full-Scale Two-Story Steel Plate Shear Walls with Reduced Beam Section Connections," by B. Qu, M. Bruneau, C-H. Lin and K-C. Tsai, 3/17/08 (PB2009-106368).

MCEER-08-0011 "Seismic Evaluation and Rehabilitation of Critical Components of Electrical Power Systems," S. Ersoy, B. Feizi, A. Ashrafi and M. Ala Saadeghvaziri, 3/17/08 (PB2009-105546).

MCEER-08-0012 "Seismic Behavior and Design of Boundary Frame Members of Steel Plate Shear Walls," by B. Qu and M. Bruneau, 4/26/08 . (PB2009-106744).

MCEER-08-0013 "Development and Appraisal of a Numerical Cyclic Loading Protocol for Quantifying Building System Performance," by A. Filiatrault, A. Wanitkorkul and M. Constantinou, 4/27/08 (PB2009-107906).

MCEER-08-0014 "Structural and Nonstructural Earthquake Design: The Challenge of Integrating Specialty Areas in Designing Complex, Critical Facilities," by W.J. Petak and D.J. Alesch, 4/30/08 (PB2009-107907).

MCEER-08-0015 "Seismic Performance Evaluation of Water Systems," by Y. Wang and T.D. O'Rourke, 5/5/08 (PB2009-107908).

MCEER-08-0016 "Seismic Response Modeling of Water Supply Systems," by P. Shi and T.D. O'Rourke, 5/5/08 (PB2009-107910).

MCEER-08-0017 "Numerical and Experimental Studies of Self-Centering Post-Tensioned Steel Frames," by D. Wang and A. Filiatrault, 5/12/08 (PB2009-110479).

MCEER-08-0018 "Development, Implementation and Verification of Dynamic Analysis Models for Multi-Spherical Sliding Bearings," by D.M. Fenz and M.C. Constantinou, 8/15/08 (PB2009-107911).

MCEER-08-0019 "Performance Assessment of Conventional and Base Isolated Nuclear Power Plants for Earthquake Blast Loadings," by Y.N. Huang, A.S. Whittaker and N. Luco, 10/28/08 (PB2009-107912).

MCEER-08-0020 "Remote Sensing for Resilient Multi-Hazard Disaster Response – Volume I: Introduction to Damage Assessment Methodologies," by B.J. Adams and R.T. Eguchi, 11/17/08 (PB2010-102695).

MCEER-08-0021 "Remote Sensing for Resilient Multi-Hazard Disaster Response – Volume II: Counting the Number of Collapsed Buildings Using an Object-Oriented Analysis: Case Study of the 2003 Bam Earthquake," by L. Gusella, C.K. Huyck and B.J. Adams, 11/17/08 (PB2010-100925).

MCEER-08-0022 "Remote Sensing for Resilient Multi-Hazard Disaster Response – Volume III: Multi-Sensor Image Fusion Techniques for Robust Neighborhood-Scale Urban Damage Assessment," by B.J. Adams and A. McMillan, 11/17/08 (PB2010-100926).

MCEER-08-0023 "Remote Sensing for Resilient Multi-Hazard Disaster Response – Volume IV: A Study of Multi-Temporal and Multi-Resolution SAR Imagery for Post-Katrina Flood Monitoring in New Orleans," by A. McMillan, J.G. Morley, B.J. Adams and S. Chesworth, 11/17/08 (PB2010-100927).

MCEER-08-0024 "Remote Sensing for Resilient Multi-Hazard Disaster Response – Volume V: Integration of Remote Sensing Imagery and VIEWS^{TM} Field Data for Post-Hurricane Charley Building Damage Assessment," by J.A. Womble, K. Mehta and B.J. Adams, 11/17/08 (PB2009-115532).

MCEER-08-0025 "Building Inventory Compilation for Disaster Management: Application of Remote Sensing and Statistical Modeling," by P. Sarabandi, A.S. Kiremidjian, R.T. Eguchi and B. J. Adams, 11/20/08 (PB2009-110484).

MCEER-08-0026 "New Experimental Capabilities and Loading Protocols for Seismic Qualification and Fragility Assessment of Nonstructural Systems," by R. Retamales, G. Mosqueda, A. Filiatrault and A. Reinhorn, 11/24/08 (PB2009-110485).

MCEER-08-0027 "Effects of Heating and Load History on the Behavior of Lead-Rubber Bearings," by I.V. Kalpakidis and M.C. Constantinou, 12/1/08 (PB2009-115533).

MCEER-08-0028 "Experimental and Analytical Investigation of Blast Performance of Seismically Resistant Bridge Piers," by S.Fujikura and M. Bruneau, 12/8/08 (PB2009-115534).

MCEER-08-0029 "Evolutionary Methodology for Aseismic Decision Support," by Y. Hu and G. Dargush, 12/15/08.

MCEER-08-0030 "Development of a Steel Plate Shear Wall Bridge Pier System Conceived from a Multi-Hazard Perspective," by D. Keller and M. Bruneau, 12/19/08 (PB2010-102696).

MCEER-09-0001 "Modal Analysis of Arbitrarily Damped Three-Dimensional Linear Structures Subjected to Seismic Excitations," by Y.L. Chu, J. Song and G.C. Lee, 1/31/09 (PB2010-100922).

MCEER-09-0002 "Air-Blast Effects on Structural Shapes," by G. Ballantyne, A.S. Whittaker, A.J. Aref and G.F. Dargush, 2/2/09 (PB2010-102697).

MCEER-09-0003 "Water Supply Performance During Earthquakes and Extreme Events," by A.L. Bonneau and T.D. O'Rourke, 2/16/09 (PB2010-100923).

MCEER-09-0004 "Generalized Linear (Mixed) Models of Post-Earthquake Ignitions," by R.A. Davidson, 7/20/09 (PB2010-102698).

MCEER-09-0005 "Seismic Testing of a Full-Scale Two-Story Light-Frame Wood Building: NEESWood Benchmark Test," by I.P. Christovasilis, A. Filiatrault and A. Wanitkorkul, 7/22/09 (PB2012-102401).

MCEER-09-0006 "IDARC2D Version 7.0: A Program for the Inelastic Damage Analysis of Structures," by A.M. Reinhorn, H. Roh, M. Sivaselvan, S.K. Kunnath, R.E. Valles, A. Madan, C. Li, R. Lobo and Y.J. Park, 7/28/09 (PB2010-103199).

MCEER-09-0007 "Enhancements to Hospital Resiliency: Improving Emergency Planning for and Response to Hurricanes," by D.B. Hess and L.A. Arendt, 7/30/09 (PB2010-100924).

MCEER-09-0008 "Assessment of Base-Isolated Nuclear Structures for Design and Beyond-Design Basis Earthquake Shaking," by Y.N. Huang, A.S. Whittaker, R.P. Kennedy and R.L. Mayes, 8/20/09 (PB2010-102699).

MCEER-09-0009 "Quantification of Disaster Resilience of Health Care Facilities," by G.P. Cimellaro, C. Fumo, A.M Reinhorn and M. Bruneau, 9/14/09 (PB2010-105384).

MCEER-09-0010 "Performance-Based Assessment and Design of Squat Reinforced Concrete Shear Walls," by C.K. Gulec and A.S. Whittaker, 9/15/09 (PB2010-102700).

MCEER-09-0011 "Proceedings of the Fourth US-Taiwan Bridge Engineering Workshop," edited by W.P. Yen, J.J. Shen, T.M. Lee and R.B. Zheng, 10/27/09 (PB2010-500009).

MCEER-09-0012 "Proceedings of the Special International Workshop on Seismic Connection Details for Segmental Bridge Construction," edited by W. Phillip Yen and George C. Lee, 12/21/09 (PB2012-102402).

MCEER-10-0001 "Direct Displacement Procedure for Performance-Based Seismic Design of Multistory Woodframe Structures," by W. Pang and D. Rosowsky, 4/26/10 (PB2012-102403).

MCEER-10-0002 "Simplified Direct Displacement Design of Six-Story NEESWood Capstone Building and Pre-Test Seismic Performance Assessment," by W. Pang, D. Rosowsky, J. van de Lindt and S. Pei, 5/28/10 (PB2012-102404).

MCEER-10-0003 "Integration of Seismic Protection Systems in Performance-Based Seismic Design of Woodframed Structures," by J.K. Shinde and M.D. Symans, 6/18/10 (PB2012-102405).

MCEER-10-0004 "Modeling and Seismic Evaluation of Nonstructural Components: Testing Frame for Experimental Evaluation of Suspended Ceiling Systems," by A.M. Reinhorn, K.P. Ryu and G. Maddaloni, 6/30/10 (PB2012-102406).

MCEER-10-0005 "Analytical Development and Experimental Validation of a Structural-Fuse Bridge Pier Concept," by S. El-Bahey and M. Bruneau, 10/1/10 (PB2012-102407).

MCEER-10-0006 "A Framework for Defining and Measuring Resilience at the Community Scale: The PEOPLES Resilience Framework," by C.S. Renschler, A.E. Frazier, L.A. Arendt, G.P. Cimellaro, A.M. Reinhorn and M. Bruneau, 10/8/10 (PB2012-102408).

MCEER-10-0007 "Impact of Horizontal Boundary Elements Design on Seismic Behavior of Steel Plate Shear Walls," by R. Purba and M. Bruneau, 11/14/10 (PB2012-102409).

MCEER-10-0008 "Seismic Testing of a Full-Scale Mid-Rise Building: The NEESWood Capstone Test," by S. Pei, J.W. van de Lindt, S.E. Pryor, H. Shimizu, H. Isoda and D.R. Rammer, 12/1/10 (PB2012-102410).

MCEER-10-0009 "Modeling the Effects of Detonations of High Explosives to Inform Blast-Resistant Design," by P. Sherkar, A.S. Whittaker and A.J. Aref, 12/1/10 (PB2012-102411).

MCEER-10-0010 "L'Aquila Earthquake of April 6, 2009 in Italy: Rebuilding a Resilient City to Withstand Multiple Hazards," by G.P. Cimellaro, I.P. Christovasilis, A.M. Reinhorn, A. De Stefano and T. Kirova, 12/29/10.

MCEER-11-0001 "Numerical and Experimental Investigation of the Seismic Response of Light-Frame Wood Structures," by I.P. Christovasilis and A. Filiatrault, 8/8/11 (PB2012-102412).

MCEER-11-0002 "Seismic Design and Analysis of a Precast Segmental Concrete Bridge Model," by M. Anagnostopoulou, A. Filiatrault and A. Aref, 9/15/11.

MCEER-11-0003 'Proceedings of the Workshop on Improving Earthquake Response of Substation Equipment," Edited by A.M. Reinhorn, 9/19/11 (PB2012-102413).

MCEER-11-0004 "LRFD-Based Analysis and Design Procedures for Bridge Bearings and Seismic Isolators," by M.C. Constantinou, I. Kalpakidis, A. Filiatrault and R.A. Ecker Lay, 9/26/11.

MCEER-11-0005 "Experimental Seismic Evaluation, Model Parameterization, and Effects of Cold-Formed Steel-Framed Gypsum Partition Walls on the Seismic Performance of an Essential Facility," by R. Davies, R. Retamales, G. Mosqueda and A. Filiatrault, 10/12/11.

MCEER-11-0006 "Modeling and Seismic Performance Evaluation of High Voltage Transformers and Bushings," by A.M. Reinhorn, K. Oikonomou, H. Roh, A. Schiff and L. Kempner, Jr., 10/3/11.

MCEER-11-0007 "Extreme Load Combinations: A Survey of State Bridge Engineers," by G.C. Lee, Z. Liang, J.J. Shen and J.S. O'Connor, 10/14/11.

MCEER-12-0001 "Simplified Analysis Procedures in Support of Performance Based Seismic Design," by Y.N. Huang and A.S. Whittaker.

MCEER-12-0002 "Seismic Protection of Electrical Transformer Bushing Systems by Stiffening Techniques," by M. Koliou, A. Filiatrault, A.M. Reinhorn and N. Oliveto, 6/1/12.

MCEER-12-0003 "Post-Earthquake Bridge Inspection Guidelines," by J.S. O'Connor and S. Alampalli, 6/8/12.

MCEER-12-0004 "Integrated Design Methodology for Isolated Floor Systems in Single-Degree-of-Freedom Structural Fuse Systems," by S. Cui, M. Bruneau and M.C. Constantinou, 6/13/12.

MCEER-12-0005 "Characterizing the Rotational Components of Earthquake Ground Motion," by D. Basu, A.S. Whittaker and M.C. Constantinou, 6/15/12.

MCEER-12-0006 "Bayesian Fragility for Nonstructural Systems," by C.H. Lee and M.D. Grigoriu, 9/12/12.

MCEER-12-0007 "A Numerical Model for Capturing the In-Plane Seismic Response of Interior Metal Stud Partition Walls," by R.L. Wood and T.C. Hutchinson, 9/12/12.

MCEER-12-0008 "Assessment of Floor Accelerations in Yielding Buildings," by J.D. Wieser, G. Pekcan, A.E. Zaghi, A.M. Itani and E. Maragakis, 10/5/12.

MCEER-13-0001 "Experimental Seismic Study of Pressurized Fire Sprinkler Piping Systems," by Y. Tian, A. Filiatrault and G. Mosqueda, 4/8/13.

MCEER-13-0002 "Enhancing Resource Coordination for Multi-Modal Evacuation Planning," by D.B. Hess, B.W. Conley and C.M. Farrell, 2/8/13.

MCEER-13-0003 "Seismic Response of Base Isolated Buildings Considering Pounding to Moat Walls," by A. Masroor and G. Mosqueda, 2/26/13.

MCEER-13-0004 "Seismic Response Control of Structures Using a Novel Adaptive Passive Negative Stiffness Device," by D.T.R. Pasala, A.A. Sarlis, S. Nagarajaiah, A.M. Reinhorn, M.C. Constantinou and D.P. Taylor, 6/10/13.

MCEER-13-0005 "Negative Stiffness Device for Seismic Protection of Structures," by A.A. Sarlis, D.T.R. Pasala, M.C. Constantinou, A.M. Reinhorn, S. Nagarajaiah and D.P. Taylor, 6/12/13.

MCEER-13-0006 "Emilia Earthquake of May 20, 2012 in Northern Italy: Rebuilding a Resilient Community to Withstand Multiple Hazards," by G.P. Cimellaro, M. Chiriatti, A.M. Reinhorn and L. Tirca, June 30, 2013.

MCEER-13-0007 "Precast Concrete Segmental Components and Systems for Accelerated Bridge Construction in Seismic Regions," by A.J. Aref, G.C. Lee, Y.C. Ou and P. Sideris, with contributions from K.C. Chang, S. Chen, A. Filiatrault and Y. Zhou, June 13, 2013.

MCEER-13-0008 "A Study of U.S. Bridge Failures (1980-2012)," by G.C. Lee, S.B. Mohan, C. Huang and B.N. Fard, June 15, 2013.

MCEER-13-0009 "Development of a Database Framework for Modeling Damaged Bridges," by G.C. Lee, J.C. Qi and C. Huang, June 16, 2013.

MCEER-13-0010   "Model of Triple Friction Pendulum Bearing for General Geometric and Frictional Parameters and for Uplift Conditions," by A.A. Sarlis and M.C. Constantinou, July 1, 2013.

MCEER-13-0011   "Shake Table Testing of Triple Friction Pendulum Isolators under Extreme Conditions," by A.A. Sarlis, M.C. Constantinou and A.M. Reinhorn, July 2, 2013.

MCEER-13-0012   "Theoretical Framework for the Development of MH-LRFD," by G.C. Lee (coordinating author), H.A Capers, Jr., C. Huang, J.M. Kulicki, Z. Liang, T. Murphy, J.J.D. Shen, M. Shinozuka and P.W.H. Yen, July 31, 2013.

MCEER-13-0013   "Seismic Protection of Highway Bridges with Negative Stiffness Devices," by N.K.A. Attary, M.D. Symans, S. Nagarajaiah, A.M. Reinhorn, M.C. Constantinou, A.A. Sarlis, D.T.R. Pasala, and D.P. Taylor, September 3, 2014.

MCEER-14-0001   "Simplified Seismic Collapse Capacity-Based Evaluation and Design of Frame Buildings with and without Supplemental Damping Systems," by M. Hamidia, A. Filiatrault, and A. Aref, May 19, 2014.

MCEER-14-0002   "Comprehensive Analytical Seismic Fragility of Fire Sprinkler Piping Systems," by Siavash Soroushian, Emmanuel "Manos" Maragakis, Arash E. Zaghi, Alicia Echevarria, Yuan Tian and Andre Filiatrault, August 26, 2014.

MCEER-14-0003   "Hybrid Simulation of the Seismic Response of a Steel Moment Frame Building Structure through Collapse," by M. Del Carpio Ramos, G. Mosqueda and D.G. Lignos, October 30, 2014.

MCEER-14-0004   "Blast and Seismic Resistant Concrete-Filled Double Skin Tubes and Modified Steel Jacketed Bridge Columns," by P.P. Fouche and M. Bruneau, June 30, 2015.

MCEER-14-0005   "Seismic Performance of Steel Plate Shear Walls Considering Various Design Approaches," by R. Purba and M. Bruneau, October 31, 2014.

MCEER-14-0006   "Air-Blast Effects on Civil Structures," by Jinwon Shin, Andrew S. Whittaker, Amjad J. Aref and David Cormie, October 30, 2014.

MCEER-14-0007   "Seismic Performance Evaluation of Precast Girders with Field-Cast Ultra High Performance Concrete (UHPC) Connections," by G.C. Lee, C. Huang, J. Song, and J. S. O'Connor, July 31, 2014.

MCEER-14-0008   "Post-Earthquake Fire Resistance of Ductile Concrete-Filled Double-Skin Tube Columns," by Reza Imani, Gilberto Mosqueda and Michel Bruneau, December 1, 2014.

MCEER-14-0009   "Cyclic Inelastic Behavior of Concrete Filled Sandwich Panel Walls Subjected to In-Plane Flexure," by Y. Alzeni and M. Bruneau, December 19, 2014.

MCEER-14-0010   "Analytical and Experimental Investigation of Self-Centering Steel Plate Shear Walls," by D.M. Dowden and M. Bruneau, December 19, 2014.

MCEER-15-0001   "Seismic Analysis of Multi-story Unreinforced Masonry Buildings with Flexible Diaphragms," by J. Aleman, G. Mosqueda and A.S. Whittaker, June 12, 2015.

MCEER-15-0002   "Site Response, Soil-Structure Interaction and Structure-Soil-Structure Interaction for Performance Assessment of Buildings and Nuclear Structures," by C. Bolisetti and A.S. Whittaker, June 15, 2015.

MCEER-15-0003   "Stress Wave Attenuation in Solids for Mitigating Impulsive Loadings," by R. Rafiee-Dehkharghani, A.J. Aref and G. Dargush, August 15, 2015.

MCEER-15-0004   "Computational, Analytical, and Experimental Modeling of Masonry Structures," by K.M. Dolatshahi and A.J. Aref, November 16, 2015.

MCEER-15-0005   "Property Modification Factors for Seismic Isolators: Design Guidance for Buildings," by W.J. McVitty and M.C. Constantinou, June 30, 2015.

271

MCEER-15-0006   "Seismic Isolation of Nuclear Power Plants using Sliding Bearings," by Manish Kumar, Andrew S. Whittaker and Michael C. Constantinou, December 27, 2015.

MCEER-15-0007   "Quintuple Friction Pendulum Isolator Behavior, Modeling and Validation," by Donghun Lee and Michael C. Constantinou, December 28, 2015.

MCEER-15-0008   "Seismic Isolation of Nuclear Power Plants using Elastomeric Bearings," by Manish Kumar, Andrew S. Whittaker and Michael C. Constantinou, December 29, 2015.

MCEER-16-0001   "Experimental, Numerical and Analytical Studies on the Seismic Response of Steel-Plate Concrete (SC) Composite Shear Walls," by Siamak Epackachi and Andrew S. Whittaker, June 15, 2016.

MCEER-16-0002   "Seismic Demand in Columns of Steel Frames," by Lisa Shrestha and Michel Bruneau, June 17, 2016.

MCEER-16-0003   "Development and Evaluation of Procedures for Analysis and Design of Buildings with Fluidic Self-Centering Systems" by Shoma Kitayama and Michael C. Constantinou, July 21, 2016.

MCEER-16-0004   "Real Time Control of Shake Tables for Nonlinear Hysteretic Systems," by Ki Pung Ryu and Andrei M. Reinhorn, October 22, 2016.

MCEER-16-0006   "Seismic Isolation of High Voltage Electrical Power Transformers," by Kostis Oikonomou, Michael C. Constantinou, Andrei M. Reinhorn and Leon Kemper, Jr., November 2, 2016.

MCEER-16-0007   "Open Space Damping System Theory and Experimental Validation," by Erkan Polat and Michael C. Constantinou, December 13, 2016.

MCEER-16-0008   "Seismic Response of Low Aspect Ratio Reinforced Concrete Walls for Buildings and Safety-Related Nuclear Applications," by Bismarck N. Luna and Andrew S. Whittaker.

MCEER-16-0009   "Buckling Restrained Braces Applications for Superstructure and Substructure Protection in Bridges," by Xiaone Wei and Michel Bruneau, December 28, 2016.

MCEER-16-0010   "Procedures and Results of Assessment of Seismic Performance of Seismically Isolated Electrical Transformers with Due Consideration for Vertical Isolation and Vertical Ground Motion Effects," by Shoma Kitayama, Michael C. Constantinou and Donghun Lee, December 31, 2016.

MCEER-17-0001   "Diagonal Tension Field Inclination Angle in Steel Plate Shear Walls," by Yushan Fu, Fangbo Wang and Michel Bruneau, February 10, 2017.

MCEER-17-0002   "Behavior of Steel Plate Shear Walls Subjected to Long Duration Earthquakes," by Ramla Qureshi and Michel Bruneau, September 1, 2017.

MCEER-17-0003   "Response of Steel-plate Concrete (SC) Wall Piers to Combined In-plane and Out-of-plane Seismic Loadings," by Brian Terranova, Andrew S. Whittaker, Siamak Epackachi and Nebojsa Orbovic, July 17, 2017.

MCEER-17-0004   "Design of Reinforced Concrete Panels for Wind-borne Missile Impact," by Brian Terranova, Andrew S. Whittaker and Len Schwer, July 18, 2017.

MCEER-17-0005   "A Simple Strategy for Dynamic Substructuring and its Application to Soil-Foundation-Structure Interaction," by Aikaterini Stefanaki and Metttupalayam V. Sivaselvan, December 15, 2017.

MCEER-17-0006   "Dynamics of Cable Structures: Modeling and Applications," by Nicholas D. Oliveto and Mettupalayam V. Sivaselvan, December 1, 2017.

MCEER-17-0007   "Development and Validation of a Combined Horizontal-Vertical Seismic Isolation System for High-Voltage-Power Transformers," by Donghun Lee and Michael C. Constantinou, November 3, 2017.

MCEER-18-0001   "Reduction of Seismic Acceleration Parameters for Temporary Bridge Design," by Conor Stucki and Michel Bruneau, March 22, 2018.

MCEER-18-0002   "Seismic Response of Low Aspect Ratio Reinforced Concrete Walls," by Bismarck N. Luna, Jonathan P. Rivera, Siamak Epackachi and Andrew S. Whittaker, April 21, 2018.

MCEER-18-0003   "Seismic Damage Assessment of Low Aspect Ratio Reinforced Concrete Shear Walls," by Jonathan P. Rivera, Bismarck N. Luna and Andrew S. Whittaker, April 16, 2018.

MCEER-18-0004   "Seismic Performance Assessment of Seismically Isolated Buildings Designed by the Procedures of ASCE/SEI 7," by Shoma Kitayama and Michael C. Constantinou, April 14, 2018.

MCEER-19-0001   MCEER-19-0001   "Development and Validation of a Seismic Isolation System for Lightweight Residential Construction," by Huseyin Cisalar and Michael C. Constantinou, March 24, 2019.

MCEER-20-0001   "A Multiscale Study of Reinforced Concrete Shear Walls Subjected to Elevated Temperatures," by Alok Deshpande and Andrew S. Whittaker, June 26, 2020.

MCEER-20-0002   "Further Results on the Assessment of Performance of Seismically Isolated Electrical Transformers," by Shoma Kitayama and Michael C. Constantinou, June 30, 2020.

MCEER-20-0003   "Analytical and Numerical Studies of Seismic Fluid-Structure Interaction in Liquid-Filled Vessels," by Ching-Ching Yu and Andrew S. Whittaker, August 1, 2020.

MCEER-22-0001   "Modeling Triple Friction Pendulum Bearings in Program OpenSees Including Frictional Heating Effects," by Hyun-Myung Kim and Michael C. Constantinou, April 18, 2022.

MCEER-22-0002   "Physical and Numerical Simulations of Seismic Fluid-Structure Interaction in Advanced Nuclear Reactors," by Faizan Ul Haq Mir, Ching-Ching Yu, Andrew S. Whittaker and Michael C. Constantinou, July 8, 2022.

MCEER: Earthquake Engineering to Extreme Events